Annual Report

of

The Institute Of Physics

Academia Sinica

Volume 10 October 1980

IN COMMEMORATION OF
THE SEVENTIETH ANNIVERSARY YEAR OF
THE REPUBLIC OF CHINA

The Institute of Physics, Academia Sinica
Taipei, Taiwan, Republic of China

中央研究院物理研究所集刊

編輯委員會

The Annual Report is published annually by the Institute of Physics, Academia Sinica, Taipei, Taiwan 115, Republic of China.

本集刊每年出版一次

非　賣　品

中央研究院

物理研究所集刊

第十卷

(中華民國建國七十年紀念)

發行人：林　爾　康

編輯者：中央研究院物理研究所集刊編輯委員會

出版者：中央研究院物理研究所　臺北市南港區

印刷者：大　地　印　刷　廠

電　話：九七一二二四四・九七一二二六六

中華民國六十九年十月出版

中央研究院物理研究所集刊

第 十 卷

中央研究院物理研究所印行

CONTENTS 目 錄

ARTICLES

Further Investigations On "A Simple Nuclear E2 Transition Model of $2_1^+ \rightarrow 0_1^+$ Transition For Even-Even Nuclei."..... .....C. W. Wang, G. C. Kiang, L. L. Kiang, C. C. Hsu, and E. K. Lin..... 1

Exact Angular Momentum Projection and Excited Bands in 160 Yb. .....Lu Lin and Amand Faessler..... 15

Proposal For Improvement of Vertical Solar Cell. .....Yu-Tung Yang..... 25

Magnetoresistivity of Some Amorphous Metals. ....Y. D. Yao, S. Arajs, and S. T. Lin..... 29

Structural and Electrical Properties of Fe-Rich Fe-Pd Alloys. .....Y. D. Yao and S. Arajs..... 37

Electrical Resistivity of Amorphous $Fe_{80}B_{20-x-y}Si_xC_y$ Alloys..... .....Y. D. Yao, S. Arajs and S. T. Lin..... 55

On the Concept of Negative Correlation Energy and Process of Deflect Formation In Chalcogenide Glasses.....Chun Chiang..... 61

A Simple Method to Study The Ionic Condition of Muscle. .....Wei Kung Wang..... 65

Inhibition of Catecholamine Biosynthesis by α-Methyl-Tyrosine, 3-Iodotyrosine and Diethyldithiocarbamic Acid In Rat Brain .....Wei Kung Wang and Yi Chiang..... 69

Further Studies on The Interference Effect of Catamaran Planing Hulls. ..... Chun-Tsung Wang..... 77

Predictions of Temperature Distribution Resulting From The Surface Discharge of Heated Water Into Large Bodies of Water. .....Robert R. Hwang and Shain-Way Jang..... 87

The Buoyant Rise of Plumes In a Stratified Environment. ……Robert R. Hwang……103
A New Time Integration Scheme For Primitive Equation Model Over East Asia Area.……Lai-Chen Chien……115
客觀分析程式之驗證 …… 劉玉龍、曾忠一……129
臺北市二氧化硫時序預報模式之研究 …… 梁文傑、蔡豐智……173
有限元素法之客觀分析 …… 梁文傑、謝全生……211
空氣污染之聚合平均佳化理論與應用 …… 梁文傑、楊佩華……241

ABSTRACT

(α, αp) Quasifree Proton Knockout Reaction on ^{2}H, ^{6}Li, and ^{19}F.……A. Nadasen, T. A. Carey, P. G. Roos, N. S. Chant, C. W. Wang, and H. L. Chen……279
Quasi-free (α, 2α) Reaction Induced By 140 MeV Alpha Particles on ^{9}Be, ^{12}C, ^{16}O, and ^{20}Ne Targets……C. W. Wang, N. S. Chant, P. G. Roos, A. Nadasen, and T. A. Carey……279
Variation of Photovoltaic Effect In Vertical n/p-Junction Solar Cells.……Yu-Tung Yang……280
Diffusion and P-type Conduction of Magnesium Impurities In Germanium.……L. T. Ho……280
Anisotropy of Magnetoresistivity In Ni-Rich Ni-Cu and Ni-Si Alloys.……Yeong Der Yao……281
Electrical Resistivity and Crystallization of Metallic Glasses $Fe_{84}B_{16}$ and $Fe_{84}B_{13}Si_3$……Yeong Der Yao and Shui Tien Lin……281
An Artificial Upwelling Experiment-Laboratory and Field Investigation.……Nai-Kuang, Liang, Shiang-Maw Tzeng, Fung-I Chen, Yeong-Chen Lin and Nai-Tsung Liang……282
Percolation Theory and Experiments On Ultra Thin Metallic Films.……Shou-Yih Wang and T. T. Chen and N. T. Liang……282
A Proposed Dynamic Mechanism of Nerve Action Potentical. …… Chun Chiang……283
Membrane Potential and Active Transport-An Information Theory Approach.……Yuh Ying L. Wang and Wei-Kung Wang……283
Inhibition of Dopamine Formation By Dopa, Dopamine and Apormorphine In Presvnaptic Nerve Terminal…… ……Wei-Kung Wang, Tsung-Yung Hai and Yi-Chiang……284

Study of Catecholamine Biosynthesis In Hypothalamus By a Continuous Measuring Method. ····· W. K. Wang, T. Y. Hai and Y. Chiang ····· 285
A Representation of an Instantaneous Unit Hydrograph From Geomorphology. ····· V. K. Gupta, E. Waymire and C. T. Wang ····· 286
A Geomorphologic Approach To Study Basin Hydrologic Response. ····· C. T. Wang and V. K. Gupta ····· 286
On The Wedge Effect On Planing Hulls. ····· Chun-Tsung Wang ····· 287
Laboratory Study On The Two-Dimensional Flow of A Stratified Fluid Over An Obstacle. ····· Robert R. Hwang and Shain-Way Jang ····· 287
Generalization of Kuo's Parameterization of Cumulus Convection. ····· Wen-Jey Liang ····· 288
A Theory For Parameterization of Cumulus Convection. ····· Wen-Jey Liang ····· 288
The Variational Optimization of Wind Field For The Estimation of Vertical Velocity. ····· Wen-Jey Liang ····· 289
The Optimization Theories For Air Pollution Estimation And Their Applications. ····· Wen-Jey Liang ····· 289
Flow Past An Impulsively Started Circular Cylinder. ····· Lai-Chen Chien ····· 290
Time Dependent of The Flow Over An Impulsively Started Circular Cylinder. ····· Lai-Chen Chien ····· 291
模型重量對波擊壓力之影響 ····· 莊生侖、汪群從、陳生平、林志清 ····· 292
用有限元素法求大氣垂直速度 ····· 曾忠一 ····· 292
臺北市一氧化碳污染與偵測網之佳化評估 ····· 梁文傑、李克堂 ····· 293
組合模式數值天氣預報之研究 ····· 梁文傑、蕭錫璋、胡仲英、陳熙揚、徐月娟 ····· 293
高雄地區二氧化硫污染與偵測網之佳化評估 ····· 梁文傑、李崇德 ····· 294

FURTHER STUDIES ON "A SIMPLE NUCLEAR E2 TRANSITION MODEL OF $2_1^+ \rightarrow 0_1^+$ TRANSITION FOR EVEN-EVEN NUCLEI"+

by

C.W. WANG (王 建 萬), G.C. KIANG (江 紀 成), L.L. KIANG*,
C.C. HSU, and E.K. LIN (林 爾 康)

Abstract

A simple, parameter free model for nuclear E2 transition from 2_1^+ to 0_1^+ states for even-even nuclei has been proposed. Transition rates based on this model have been deduced and calculated. The lifetimes of the 2_1^+ states for 214 nuclei have been caluulated and compared with experimental results. The ratios of these two values fall in to a region from 0.2 to 1.67 for most nuclei. The deformation parameters for 49 vibrational nuclei have also been calculated. These values are found to consist with the experimental values to within 50%.

1. INTRODUCTION

The electromagnetic transitions in nuclei have long become a powerful tool for the nuclear structure investigation. Numerous experimental results and theoretical calculations have been reported on this field. These results and calculations had been summaried and discussed in the review articles, such as that by Yoshida and Zamick[1]. The results of each calculation depend on the nuclear structure model. Due to the lack of a unified nuclear model, there is no general nuclear electromagnetic transition expression that applies to most of the nuclei. However, despite of this difficulty, many attempts have been made on this subject. The single particle model of Weisskopf[2] is so far the most systematic one that predicts the nuclear electromagnetic multipole transitions some one or two order of magnitude deviated from the experimental results for the low nonvanishing multipole transitions. Approximations that in terms of collective variables are also widely investigated[3]. However, the results of these calculations are mostly determined by parameters such as the deformation parameters. Refined shell model calculations for specific nucleus are also intensively investigated[4].

Recently, Hsu et. al.[5] suggested that pure vibrational nuclear states were due to the vibration of the nuclear center-of mass. These authors also proposed a size parameter of $\lambda = M\omega_A/(2\hbar) = 0.083A^{1/3}$ fm^{-2} from an averaging point of view. The validity of that proposition need to be checked. In this report, we want to present a simple, parameter free approximation for the $2_1^+ \rightarrow 0_1^+$ nuclear electromagnetic transitions for even-even nuclei.

+ 發表於紀念王唯農博士之原子核物理研討會（南港，69年7月28日）

* Department of Physics, Tsing Hua University, Hsinchu, Taiwan, R.O.C.

2. THE MODEL

Since the 2_1^+ state energies of the most even-even nuclei are far below the single particle separation energy and the wavelengths of the $2_1^+ \rightarrow 0_1^+$ transitions are much larger than that of the nuclear dimensions. We assume that, in the case of $2_1^+ \rightarrow 0_1^+$ transitions, the nuclear Hamiltonian of the even-even nuclei can be approximated by the combination of a spin zero point charge and a simple harmonic oscillator with interaction $V(r) = -V_0 + {}^1/_2 M\omega_0^2 r^2$, where $M = Am$ is the nuclear mass and ω_0 is the characteristic angular freguency of the oscillator. The term $-V_0$ is a negative potential that is designed to ensure that the nucleus is bounded. According to this approximation, the electric quadrupole operator is

$$\hat{Q}_{2\mu} = \sum_{j=1}^{A} \left[e_j r_j^2 \, Y_{2\mu}^* (\theta_j, \phi_j) + i \, g_{sj} \, \mu_0 \left(\frac{\omega}{c}\right) (2+1)^{-1} \vec{\sigma}_j \times \vec{r}_j \cdot \vec{\nabla} (r^2 Y_{2\mu}^*)_j \right]$$

$$\sim \sum_{j=1}^{Z} \left[e r_j^2 \, Y_{2\mu}^* (\theta_j, \phi_j) \right] = Z e r^2 Y_{2\mu}^* (\theta, \phi) \qquad (1)$$

The nuclear E2 transition, $2_1^+ \rightarrow 0_1^+$, is then corresponding to the transition of this sytem from two oscillator quanta state ($n=2$), to the ground state ($n=0$). By using the well known oscillator wave function

$$|n\ell m> = R_n (r) \, Y_m (\theta, \phi) \qquad (2)$$

the $2_1^+ \rightarrow 0_1^+$ transition rate become

$$T_{fi} = \frac{8(2+1)}{2[(2\cdot 2+1)!!]} \frac{1}{\hbar} \left(\frac{\hbar\omega}{\hbar c}\right)^5 |<000 | (Z e r^2 Y_{2\mu}^*) | 22m>|^2 \qquad (3)$$

for specific magnetic quantum numbers m and μ. The orbital quantum number of the 2_1^+ state is assigned to consistent with the angular momentum of that nuclear state. By carrying out expression (3) and averaging over the initial substates and summing over the final substates, one obtains the transition rate

$$T(2_1^+ \rightarrow 0_1^+) = \frac{cZ^2}{80} \frac{e^2}{\hbar c} \left(\frac{\hbar\omega}{\hbar c}\right)^5 \cdot 1/\alpha^2 \qquad (4)$$

where $\alpha = M\omega_0/(2\hbar)$. The characteristic angular frequency ω_0 can be determined by considering that the energy of the emitted gamma ray is $\hbar\omega = E(n=2) - E(n=0) = 2\hbar\omega_0$. That is $\omega_0 = \omega/2$. Inserting these relations and the universal constants in expression (4), the transition rate can be denoted by

$$T(2_1^+ \rightarrow 0_1^+) = 2.5199 \times 10^{12} \, Z^2 (\hbar\omega)^3 / A^2 \cdot \sec^{-1} \qquad (5)$$

with $\hbar\omega$ measured in MeV. The potential $-V_0$ plays no role in the transition rate calculations. It is worth noticing that equation (5) contains no free parameter.

3. RESULTS AND DISCUSSIONS

The $2_1^+ \rightarrow 0_1^+$ transition rates of the even-even nuclei have been calculated based on equation (5) in the range of A=12 to A=206. A total of 214 nuclei, stable and unstable, has been investiged. The lifetimes of the 2_1^+ states are, after the correction due to the internal conversion, also made. The conversion coefficients are taken from the compilation listed in the book edited by K. Siegbahn[6]. For all of these nuclei, that the lifetime of the 2^+ states are experimentally avialable[6-8], the ratios of the calculated and experimental lifetimes, τcal/τexp, are listed in the fourth column of Table 1. These ratios are also plotted in Fig. 1 against the mass number A. It is found that the ratios are fallen in between 0.15 and 6. That is we obtained the correct order for the $2^+ \rightarrow 0^+$ transition rates. Moreover, 204 of these ratios, i.e. 95.3% of the investigated nuclei, have the values from 0.2 to 1.67. Besides, the average of these 214 values is found to be 0.851, quite close to the expected value 1. Especially, the average value of the range $^{96}_{44}$Ru to $^{204}_{80}$Hg is 0.992, lest than 1% deviated from the expected result. We thus believe that this approximation is reasonable although correction for specific nucleus is needed.

One may argue that this approximation is by no means a simple single particle model. However, there are several essential differences between these two approximations. Firstly, the present approximation is a parameter free one while the single particle model depends on the radius parameter. Secondly, the proposed approximation suggests that there is no change in the nuclear internal structure during the transition $2_1^+ \rightarrow 0_1^+$ while the single particle orbit do changed in the single particle model. In order to investigate this approximation further, we consider the mean square deformations of the ground state β_0^2 of the vibrational nuclei which related to the change of the mean square radius in various excited states by[3]

$$\begin{aligned} \delta\langle r^2\rangle_N &= \frac{1}{Z}\left[\langle r_N^2\rangle - \langle r_0^2\rangle\right] \\ &= \frac{2}{5} N \beta_0^2 \frac{3}{4\pi} R_0^2 \end{aligned} \tag{6}$$

where N is the number of phonon of the excited state. Similar change of the mean square radius can be found in the pressent approximation. It has the form

$$\delta\langle r_n^2\rangle = \frac{n}{Z}\frac{\hbar}{M\omega_0} = \frac{4\hbar^2c^2}{Amc^2\hbar\omega}\cdot\frac{1}{Z}, \text{ for } n=2 \tag{7}$$

By combining exprssions (6) and (7) for the vibrational nuclei and considering the 2_1^+ state (N=1) with $R_0 = 1.2\ A^{1/3}$fm, one obtains

$$\beta_0^2 = 1.216 \times 10^3/(A^{5/3}Z\hbar\omega) \tag{8}$$

TABLE 1

Element	Ex(2_1^+) (MeV)	T($2_1^+ \rightarrow 0_1^+$) (10^{12}sec^{-1})	rcal/rexpt
$^{12}_{6}C$	4.43	53.66	0.466
$^{14}_{6}C$	7.012	159.6	0.485
$^{16}_{8}O$	6.916	208.4	0.792
$^{18}_{8}O$	1.98	3.864	0.193
$^{18}_{10}Ne$	1.8873	5.228	0.288
$^{20}_{10}Ne$	1.63	2.728	0.459
$^{22}_{10}Ne$	1.2746	1.078	0.321
$^{24}_{10}Ne$	1.9808	3.400	0.291
$^{22}_{12}Mg$	1.2463	1.451	0.320
$^{24}_{12}Mg$	1.36853	1.615	0.478
$^{26}_{12}Mg$	1.81	3.183	0.544
$^{28}_{12}Mg$	1.4734	1.480	0.397
$^{26}_{14}Si$	1.7959	4.232	0.169
$^{28}_{14}Si$	1.780	3.553	0.557
$^{30}_{14}Si$	2.23	6.086	0.456
$^{32}_{14}Si$	1.9414	3.529	0.456
$^{30}_{16}S$	2.2106	7.743	0.697
$^{32}_{16}S$	2.2303	6.989	0.901
$^{34}_{16}S$	2.1273	5.372	0.465
$^{36}_{16}S$	3.291	17.74	0.513
$^{34}_{18}Ar$	2.0909	6.456	0.674
$^{36}_{18}Ar$	1.97	4.816	0.514
$^{38}_{18}Ar$	2.168	5.762	0.301
$^{40}_{18}Ar$	1.461	1.591	0.390
$^{42}_{18}Ar$	1.2082	0.8163	0.314
$^{40}_{20}Ca$	3.9045	37.50	0.544
$^{42}_{20}Ca$	1.525	2.027	0.544
$^{44}_{20}Ca$	1.157	0.8064	0.295
$^{46}_{20}Ca$	1.347	1.164	0.153
$^{48}_{20}Ca$	3.832	24.62	0.704

A Simple Nucuear E2 Transition Model of $2_1^+ \rightarrow 0_1^+$ Transition for Even-Even Nuclel

Element	Ex(2_1^+) (MeV)	T($2_1^+ \rightarrow 0_1^+$) (10^{12}sec^{-1})	τcal/τexpt
$^{42}_{22}$Ti	1.555	2.600	0.663
$^{44}_{22}$Ti	1.083	0.8002	0.278
$^{46}_{22}$Ti	0.8894	0.4055	0.425
$^{48}_{22}$Ti	0.9833	0.5033	0.459
$^{50}_{22}$Ti	1.55	1.817	0.545
$^{52}_{22}$Ti	1.047	0.5177	0.449
$^{48}_{24}$Cr	0.7524	0.2683	0.287
$^{50}_{24}$Cr	0.79	0.2863	0.391
$^{52}_{24}$Cr	1.4336	1.582	0.684
$^{54}_{24}$Cr	0.8353	0.2901	0.292
$^{54}_{26}$Fe	1.409	1.634	0.425
$^{56}_{26}$Fe	0.8469	0.3300	0.350
$^{58}_{26}$Fe	0.8105	0.2696	0.956
$^{56}_{28}$Ni	2.701	12.41	1.12
$^{58}_{28}$Ni	1.45	1.790	1.02
$^{60}_{28}$Ni	1.3326	1.299	1.16
$^{62}_{28}$Ni	1.172	0.8274	0.598
$^{64}_{28}$Ni	1.34	1.161	0.853
$^{64}_{30}$Zn	0.992	0.5405	0.754
$^{66}_{30}$Zn	1.039	0.5840	0.742
$^{68}_{30}$Zn	1.078	0.6144	0.705
$^{70}_{30}$Zn	0.884	0.3197	0.677
$^{70}_{32}$Ge	1.040	0.5924	0.900
$^{72}_{32}$Ge	0.835	0.2898	0.797
$^{74}_{32}$Ge	0.596	0.09976	0.579
$^{76}_{32}$Ge	0.567	0.08537	0.451
$^{72}_{34}$Se	0.862	0.3599	0.550
$^{74}_{34}$Se	0.635	0.1362	0.848
$^{76}_{34}$Se	0.5593	0.08824	0.734
$^{78}_{34}$Se	0.6142	0.1109	0.727
$^{80}_{34}$Se	0.6662	0.1346	0.644

Element	Ex(2_1^+) (MeV)	T($2_1^+ \rightarrow 0_1^+$) (10^{12}sec^{-1})	τcal/τexpt
$^{82}_{34}$Se	0.6554	0.1220	0.619
$^{76}_{36}$Kr	0.424	0.04310	0.435
$^{78}_{36}$Kr	0.455	0.05056	0.548
$^{80}_{36}$Kr	0.618	0.1204	0.851
$^{82}_{36}$Kr	0.7769	0.2277	0.610
$^{84}_{36}$Kr	0.88	0.3154	0.666
$^{80}_{38}$Sr	0.3854	0.02606	0.665
$^{84}_{38}$Sr	0.795	0.2591	1.03
$^{86}_{38}$Sr	1.078	0.6163	1.13
$^{88}_{38}$Sr	1.8362	2.909	1.49
$^{90}_{40}$Sr	2.18	5.157	1.45
$^{92}_{40}$Zr	0.934	0.3881	0.357
$^{94}_{40}$Zr	0.92	0.3553	0.390
$^{96}_{40}$Zr	1.59	1.759	1.31
$^{100}_{40}$Zr	0.2125	0.003869	0.257
$^{102}_{40}$Zr	0.1519	0.001358	0.237
$^{92}_{42}$Mo	1.54	1.918	0.903
$^{94}_{42}$Mo	0.871	0.3324	1.04
$^{96}_{42}$Mo	0.778	0.2271	0.898
$^{98}_{42}$Mo	0.7868	0.2254	0.932
$^{100}_{42}$Mo	0.5355	0.06826	0.923
$^{102}_{42}$Mo	0.2960	0.01108	0.586
$^{104}_{42}$Mo	0.192	0.002909	0.270
$^{106}_{42}$Mo	0.1717	0.002003	0.297
$^{96}_{44}$Ru	0.84	0.3138	0.818
$^{98}_{44}$Ru	0.66	0.1460	0.949
$^{100}_{44}$Ru	0.5396	0.07660	0.822
$^{102}_{44}$Ru	0.4748	0.05020	0.863
$^{104}_{44}$Ru	0.3577	0.02640	0.646
$^{108}_{44}$Ru	0.2424	0.005957	0.342
$^{110}_{44}$Ru	0.24067	0.005620	0.388

A Simple Nuclear E2 Transition Model of $2_1^+ \rightarrow 0_1^+$ Transition for Even-Even Nuclei

Element	Ex(2_1^+) (MeV)	T($2_1^+ \rightarrow 0_1^+$) ($10^{12}sec^{-1}$)	$\tau cal/\tau expt$
$^{112}_{44}Ru$	0.2368	0.005160	0.420
$^{104}_{46}Pd$	0.5555	0.08451	0.820
$^{106}_{46}Pd$	0.5118	0.06362	0.908
$^{108}_{46}Pd$	0.4338	0.03732	0.473
$^{110}_{46}Pd$	0.3738	0.02302	0.753
$^{112}_{46}Pd$	0.3489	0.01800	0.385
$^{114}_{46}Pd$	0.333	0.01515	0.229
$^{116}_{46}Pd$	0.341	0.01571	0.401
$^{106}_{48}Cd$	0.63	0.1292	0.894
$^{108}_{48}Cd$	0.7332	0.1264	1.10
$^{110}_{48}Cd$	0.6576	0.1364	1.10
$^{112}_{48}Cd$	0.6174	0.1089	1.06
$^{114}_{48}Cd$	0.5581	0.07766	0.992
$^{116}_{48}Cd$	0.5131	0.05828	0.991
$^{112}_{50}Sn$	1.257	0.9975	1.99
$^{114}_{50}Sn$	1.299	1.063	2.18
$^{116}_{50}Sn$	1.2933	1.013	1.71
$^{118}_{50}Sn$	1.230	0.8419	1.65
$^{120}_{50}Sn$	1.171	0.7025	1.57
$^{122}_{50}Sn$	1.14	0.6271	1.48
$^{124}_{50}Sn$	1.131	0.5927	1.27
$^{120}_{52}Te$	0.562	0.08399	0.825
$^{122}_{52}Te$	0.564	0.08213	1.06
$^{124}_{52}Te$	0.603	0.09716	1.15
$^{126}_{52}Te$	0.667	0.1274	1.21
$^{128}_{52}Te$	0.743	0.1706	1.27
$^{130}_{52}Te$	0.84	0.2390	1.26
$^{120}_{54}Xe$	0.3218	0.01700	0.453
$^{122}_{54}Xe$	0.332	0.01810	0.619
$^{124}_{54}Xe$	0.3543	0.02125	0.582
$^{126}_{54}Xe$	0.386	0.02662	0.651

Element	$Ex(2_1^+)$ (MeV)	$T(2_1^+ \rightarrow 0_1^+)$ ($10^{12}sec^{-1}$)	$\tau cal/\tau expt$
$^{128}_{54}Xe$	0.443	0.03899	0.741
$^{130}_{54}Xe$	0.538	0.06771	1.46
$^{132}_{54}Xe$	0.6678	0.1256	1.13
$^{126}_{56}Ba$	0.256	0.008350	0.476
$^{128}_{56}Ba$	0.283	0.01090	0.678
$^{130}_{56}Ba$	0.356	0.02110	0.821
$^{132}_{56}Ba$	0.464	0.04530	0.900
$^{134}_{56}Ba$	0.6046	0.09726	1.37
$^{136}_{56}Ba$	0.818	0.2338	1.56
$^{138}_{56}Ba$	1.4359	1.229	2.56
$^{142}_{56}Ba$	0.3595	0.01820	0.566
$^{144}_{56}Ba$	0.1993	0.003017	0.341
$^{146}_{56}Ba$	0.181	0.002198	0.364
$^{132}_{58}Ce$	0.325	0.01670	0.880
$^{134}_{58}Ce$	0.4092	0.03235	0.932
$^{140}_{58}Ce$	1.496	1.758	2.53
$^{142}_{58}Ce$	0.6412	0.1108	1.10
$^{146}_{58}Ce$	0.2586	0.006877	0.388
$^{150}_{58}Ce$	0.098	0.0003546	0.582
$^{142}_{60}Nd$	1.57	1.741	5.63
$^{144}_{60}Nd$	0.695	0.1469	1.39
$^{146}_{60}Nd$	0.453	0.03970	0.876
$^{148}_{60}Nd$	0.300	0.01118	0.756
$^{150}_{60}Nd$	0.132	0.0009270	0.449
$^{152}_{60}Nd$	0.0759	0.0001717	<1.32
$^{154}_{60}Nd$	0.0728	0.0001476	0.881
$^{144}_{62}Sm$	1.6601	2.137	3.60
$^{148}_{62}Sm$	0.550	0.07600	1.25
$^{150}_{62}Sm$	0.334	0.01600	0.890
$^{152}_{62}Sm$	0.12178	0.0007570	0.564
$^{154}_{62}Sm$	0.08199	0.0002250	0.808

Element	Ex(2_1^+) (MeV)	T($2_1^+ \rightarrow 0_1^+$) ($10^{12}sec^{-1}$)	$\tau cal/\tau expt$
$^{152}_{64}Gd$	0.34424	0.01822	1.31
$^{154}_{64}Gd$	0.12307	0.0008110	0.630
$^{156}_{64}Gd$	0.088967	0.0002987	0.776
$^{158}_{64}Gd$	0.07951	0.0002078	0.988
$^{160}_{64}Gd$	0.0753	0.0001720	1.05
$^{156}_{66}Dy$	0.1378	0.001180	0.795
$^{158}_{66}Dy$	0.099	0.0004266	1.24
$^{160}_{66}Dy$	0.08679	0.0002803	0.865
$^{162}_{66}Dy$	0.0807	0.0002198	0.958
$^{164}_{66}Dy$	0.073392	0.0001613	1.12
$^{166}_{68}Er$	0.3446	0.01959	1.07
$^{168}_{68}Er$	0.1921	0.003309	0.740
$^{160}_{68}Er$	0.1257	0.0009040	0.952
$^{162}_{68}Er$	0.1020	0.0004712	0.901
$^{164}_{68}Er$	0.0915	0.0003320	1.01
$^{166}_{68}Er$	0.08056	0.0002210	1.12
$^{168}_{68}Er$	0.0798	0.0002098	1.14
$^{170}_{68}Er$	0.0793	0.0002011	1.20
$^{162}_{70}Yb$	0.1663	0.002160	0.735
$^{164}_{70}Yb$	0.1233	0.008398	0.782
$^{166}_{70}Yb$	0.1022	0.0004783	0.950
$^{168}_{70}Yb$	0.08773	0.0002954	1.10
$^{170}_{70}Yb$	0.084262	0.0002556	1.17
$^{172}_{70}Yb$	0.0787	0.0002034	1.30
$^{174}_{70}Yb$	0.0765	0.0001826	1.28
$^{176}_{70}Yb$	0.0821	0.0002206	1.05
$^{166}_{72}Hf$	0.1587	0.001895	0.665
$^{168}_{72}Hf$	0.1239	0.0008803	0.743
$^{170}_{72}Hf$	0.1008	0.0004629	0.959
$^{172}_{72}Hf$	0.0945	0.0003726	0.905
$^{174}_{72}Hf$	0.0909	0.0003241	0.956

Element	$Ex(2_1^+)$ (MeV)	$T(2_1^+ \rightarrow 0_1^+)$ ($10^{12}sec^{-1}$)	$\tau cal/\tau expt$
$^{176}_{72}Hf$	0.08836	0.0002909	1.19
$^{178}_{72}Hf$	0.0932	0.0003338	1.01
$^{180}_{72}Hf$	0.09333	0.0003278	1.03
$^{180}_{74}W$	0.103	0.0004653	0.965
$^{182}_{74}W$	0.1001	0.0004088	0.951
$^{184}_{74}W$	0.112	0.0005604	0.772
$^{186}_{74}W$	0.1226	0.0007350	0.785
$^{182}_{76}Os$	0.1271	0.0009022	0.804
$^{184}_{76}Os$	0.120	0.0007429	0.654
$^{186}_{76}Os$	0.12716	0.001086	0.662
$^{188}_{76}Os$	0.155	0.001534	0.579
$^{190}_{76}Os$	0.1867	0.002624	1.03
$^{192}_{76}Os$	0.20579	0.003441	0.907
$^{184}_{78}Pt$	0.163	0.001961	0.901
$^{186}_{78}Pt$	0.1915	0.003112	0.808
$^{188}_{78}Pt$	0.2656	0.008127	1.22
$^{190}_{78}Pt$	0.2957	0.01098	1.26
$^{192}_{78}Pt$	0.31649	0.01318	1.31
$^{194}_{78}Pt$	0.3285	0.01444	1.07
$^{196}_{78}Pt$	0.3557	0.01796	1.10
$^{198}_{78}Pt$	0.408	0.0256	1.09
$^{194}_{80}Hg$	0.427	0.03336	0.670
$^{196}_{80}Hg$	0.4261	0.03248	1.52
$^{198}_{80}Hg$	0.4118	0.02873	1.10
$^{200}_{80}Hg$	0.36797	0.02009	0.822
$^{202}_{80}Hg$	0.439	0.03344	0.829
$^{204}_{80}Hg$	0.43	0.03081	0.625
$^{204}_{82}Pb$	0.8993	0.2960	0.731
$^{206}_{82}Pb$	0.8033	0.2070	0.419

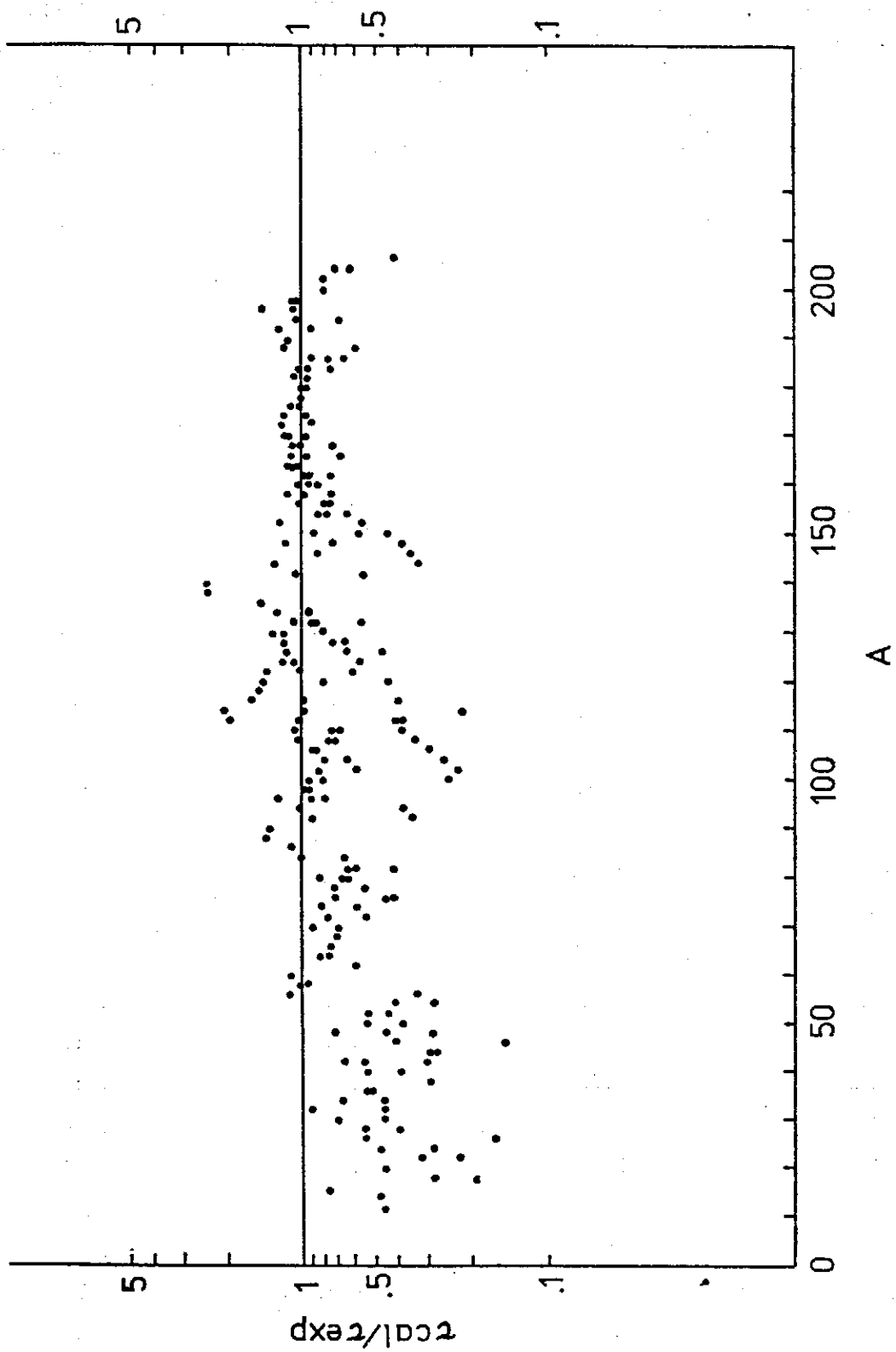

FIG 1.

with $\hbar\omega$ measured in MeV. The absolute values of β_0 for 49 vibrational nuclei are calculated based on equation (8) and are shown in the fourth column of Table 2 together with the experimental values[9, 10, 11] which are shown in the third column. The calculated and experimental β_0 are quite nicely consistent with each other. The largest inconsistency comes from $^{192}_{79}$Pt and $^{204}_{80}$Hg with $|\beta_0^{cal}-\beta_0^{exp}|/\beta_0^{exp}=0.51$.

From these results, we believe that the present approximation, although in its simple structure, is a resonable approach to the nuclear $2_1^+ \rightarrow 0_1^+$ transition.

TABLE 2

Element	E_{21}^+ (MeV)	β_0 expt	β_0 cal
$^{54}_{26}$F	1.41	0.18	0.207
$^{56}_{26}$Fe	0.835	0.23	0.260
$^{58}_{26}$Fe	0.805	0.27	0.259
$^{64}_{30}$Zn	0.990	0.250	0.200
$^{66}_{30}$Zn	1.039	0.227	0.190
$^{68}_{30}$Zn	1.078	0.205	0.182
$^{70}_{30}$Zn	0.887	0.229	0.196
$^{74}_{34}$Se	0.635	0.337	0.208
$^{76}_{34}$Se	0.559	0.326	0.217
$^{78}_{34}$Se	0.614	0.287	0.202
$^{80}_{34}$Se	0.666	0.240	0.190
$^{96}_{44}$Ru	0.833	0.159	0.128
$^{98}_{44}$Ru	0.654	0.215	0.142
$^{100}_{44}$Ru	0.540	0.232	0.154
$^{102}_{44}$Ru	0.473	0.264	0.162
$^{104}_{44}$Ru	0.358	0.288	0.183
$^{104}_{46}$Pd	0.555	0.212	0.144
$^{106}_{46}$Pd	0.512	0.224	0.147
$^{108}_{46}$Pd	0.434	0.243	0.158
$^{110}_{46}$Pd	0.374	0.252	0.167
$^{106}_{48}$Cd	0.633	0.186	0.130
$^{108}_{48}$Cd	0.633	0.195	0.128

Element	E_{21}^+ (MeV)	β_0 expt	β_0 cal
$^{110}_{48}$Cd	0.658	0.183	0.123
$^{112}_{48}$Cd	0.617	0.186	0.126
$^{114}_{48}$Cd	0.558	0.193	0.130
$^{116}_{48}$Cd	0.513	0.201	0.134
$^{120}_{52}$Te	0.560	0.170	0.120
$^{122}_{52}$Te	0.564	0.183	0.118
$^{124}_{52}$Te	0.603	0.174	0.112
$^{126}_{52}$Te	0.667	0.163	0.105
$^{128}_{52}$Te	0.743	0.142	0.098
$^{130}_{52}$Te	0.840	0.127	0.091
$^{142}_{60}$Nd	1.570	0.104	0.058
$^{144}_{60}$Nd	0.695	0.111	0.086
$^{146}_{60}$Nd	0.455	0.161	0.105
$^{148}_{60}$Nd	0.300	0.197	0.128
$^{188}_{76}$Os	0.155	0.193	0.129
$^{190}_{76}$Os	0.186	0.185	0.117
$^{192}_{78}$Pt	0.316	0.179	0.088
$^{194}_{78}$Pt	0.328	0.156	0.085
$^{196}_{78}$Pt	0.356	0.125	0.081
$^{198}_{78}$Pt	0.405	0.134	0.076
$^{196}_{80}$Hg	0.426	0.129	0.073
$^{198}_{80}$Hg	0.412	0.109	0.074
$^{200}_{80}$Hg	0.368	0.098	0.078
$^{202}_{80}$Hg	0.440	0.086	0.071
$^{204}_{80}$Hg	0.430	0.047	0.071
$^{204}_{82}$Pb	0.899	0.048	0.048
$^{206}_{82}$Pt	0.803	0.037	0.051

REFERENCES

(1) S. Yoshida and L. Zamick, Ann. Rev. Nucl. Sci., Vol. 22 (1972) 121
(2) V. F. Weisskopf, Phys. Rev. 83, 1073 (1951).
(3) e.q. J. M. Eisenberg and W. Greiner, Nuclear Models, North-Holland Publishing, 1970, and the references cited therein.
(4) H. C. Chiang et. al., J. Phys. G: Nuclear Physi. 6 (1980) 345 and the references cited therein.
(5) C. C. Hsu et. al., to be published.
(6) K. Siegbahn, α, β, γ Ray Spectroscopy, North-Holland, 1979.
(7) P. M. Endt & C. Van der Lenn, N. P. A310 (1978), Nos. 1,2.
(8) C. M. Lederer and V. S. Shirley, Table of Isotopes, 7th edition, John Wiley & Sons, Inc. 1978.
(9) Landalt-Bornstein, Neue Serie Vol. 1 (Springer, Berlin, 1961).
(10) E. K. Warburton, D. E. Alburger and D. H. Wilkinson, Phys. Rev. 129 (1963) 2180.
(11) Nuclear Data Sheets (Nuclear Data Group, Oak Ridge National Lab., Oak Ridge, Tenn. 1966).

EXACT ANGULAR MOMENTUM PROJECTION AND EXCITED BANDS IN ^{160}Yb*

LU LIN+

Physics Dept., National Central University
Chung-Li, Taiwan, Republic of China

and

AMAND FAESSLER

Institute für Theoretische Physik der Universität Tübingen
D-7400 Tübingen, West Germany

Abstract

The method of exact angular momentum projection is reviewed. Experimental excited bands in $^{160}_{70}Yb_{90}$ are studied using the method of exact angular momentum and particle number projection for excited rotational states. The results are compared to a description of an angular momentum non-conserving cranking approach.

Angular momentum projection for a Hartree-Bogoliubov ground state wave function has been formulated many years ago (see for instance ref. (1). Here we shall only summarize the relevant formalism. The ground state Hartree-Bogoliubov wave function can be written in the canonical representation

$$|\phi\rangle = \prod_{k>0} (u_k + v_k\, b_k^+\, b_{\bar{k}}^+)\,|0\rangle = (\prod_{k>0} u_k)\,\exp\Big[\tfrac{1}{2}\sum_{i,k} f_{ik}\, b_i^+\, b_k^+\Big]|0\rangle, \qquad (1)$$

where the f_{ik} 's can be expressed in matrix representation by the matrices U and V as:

$$f_{ik} = (V \cdot U^{-1})_{ik}\,. \qquad (2)$$

The relevant quantities in the calculation as functions of the rotation angle are:

$$n(\Omega) = [\det X(\Omega)]^{\frac{1}{2}},\ X(\Omega) = U^T \cdot R(\Omega) \cdot U + V^T \cdot R(\Omega) \cdot V,$$
$$K(\Omega) = [R(\Omega) \cdot V \cdot X^{-1} \cdot U^T],\quad \sigma(\Omega) = R(\Omega) \cdot U \cdot X^{-1} \cdot V^T,$$
$$\rho(\Omega) = R(\Omega) \cdot V \cdot X^{-1} \cdot V^T,$$

$$E_J = \frac{\sum_{kk'} \int d\Omega\, D^{J*}_{kk'}(\Omega)\ \langle\phi|HR(\Omega)|\phi\rangle}{\sum_{kk'} \int d\Omega\, D^{J*}_{kk'}(\Omega)\ \langle\phi|R(\Omega)|\phi\rangle} = \frac{\sum_{kk'} \int d\Omega\, D^{J*}_{kk'}(\Omega) n(\Omega) \tilde{h}(\Omega)}{\sum_{kk'} \int d\Omega\, D^{J*}_{kk'}(\Omega) n(\Omega)}\,. \qquad (3)$$

The quantities above are defined in ref. (1), except that we write them in the canonical representation for convenience. In deriving this formalism, the following mathematical artifice was used:

+ Work partially supported by the National Science Council of the Republic of China.
* 發表於紀念王唯農博士之原子核物理研討會（南港，69年7月28日）。

$$n^2(\Omega) = (\det\ U^T)\ (\det\ U)\ \det\left[1 + (V\cdot U^{-1})^T \cdot R(\Omega) \cdot (V\cdot U^{-1}) \cdot R(\Omega)^T\right],$$
$$= \det\left[U^T \cdot R(\Omega) \cdot U + V^T \cdot R(\Omega) V\right] \equiv \det\ X(\Omega)\ . \qquad (4)$$

Concerning the excited states, we shall describe here briefly the method of Lin and Faessler[2] for the readers' convenience. Let us denote a set of Nilsson single-particle states by $(\alpha, \beta, \ldots)$. Among them, we use $(\mu, \nu, \ldots)$ for the excited single-particle states, and (i, j, k, ...) for those in the pairing phase. A two-quasiparticle excited state can be written as

$$|\psi> = b_1^+ b_2^+ \mid \psi_0> = \lim_{\varepsilon\to 0} (\varepsilon + b_1^+ b_2^+) \prod_{k>0} (u_k + v_k b_k^+ b_{\bar{k}}^+) |0> \equiv \lim_{\varepsilon\to 0} |\psi(\varepsilon)>. \qquad (5)$$

Before taking the limit $\varepsilon \to 0$, we can write

$$|\psi(\varepsilon)> = \varepsilon \left(\prod_{k>0} u_k\right) \exp\left[\tfrac{1}{2} \sum_{\alpha\beta} F_{\alpha\beta}(\varepsilon) b_\alpha^+ b_\beta^+\right] |0>. \qquad (6)$$

The matrix $F_{\alpha\beta}(\varepsilon)$ can be written as

$$F_{\alpha\beta}(\varepsilon) = [V \cdot U(\varepsilon)^{-1}]_{\alpha\beta}\ , \qquad (7)$$

with $V_{i\bar{i}} = 1,\ V_{\bar{i}i} = -1,\ U_{\bar{i}i} = U_{i\bar{i}} = 1,\ U_{12} = U_{\bar{2}\bar{1}} = \varepsilon\ ,$

$$U_{\mu\nu} = V_{\mu\nu} = 0 \quad \text{otherwise}, \qquad (8)$$

U_{ik} and V_{ik} are exactly those defined in ref. (1)

Now, it is important to note that:

(i) The inverse of $U(\varepsilon)$ does exist, and

$$\det\left[V(\varepsilon)\cdot U(\varepsilon)^T\right] = \det\left[U(\varepsilon)\cdot U(\varepsilon)^T\right]_{\mu\nu} \det\left[U\cdot U^T\right]_{ik} = \varepsilon^4 \prod_{k>0} U_k U_k\ , \qquad (9)$$

$$n^2(\Omega, \varepsilon) = \det\left[U(\varepsilon)^T \cdot R(\Omega) \cdot U(\varepsilon) + V^T \cdot R(\Omega) \cdot V\right] \equiv \det[X_{\alpha\beta}(\Omega, \varepsilon)]\ . \qquad (10)$$

(ii) The limit of $X(\Omega, \varepsilon)$ also exists when ε goes to zero. Therefore we have

$$\lim_{\varepsilon\to 0} n^2(\Omega, \varepsilon) = \lim_{\varepsilon\to 0} \det\left[X(\Omega, \varepsilon)\right] = \det\left[X(\Omega, \varepsilon = 0)\right]\ . \qquad (11)$$

The energy E_J then becomes

$$E_J = \lim_{\varepsilon\to 0} \frac{\sum_{kk'} \int d\Omega\ D^J_{kk'}(\Omega) n(\Omega, \varepsilon) \tilde{h}(\Omega, \varepsilon)}{\sum_{kk'} \int d\Omega\ D^J_{kk'}(\Omega) n(\Omega, \varepsilon)} = \frac{\sum_{kk'} \int d\Omega\ D^J_{kk'}(\Omega) n(\Omega, \varepsilon = 0) \tilde{h}(\Omega, \varepsilon = 0)}{\sum_{kk'} \int d\Omega\ D^J_{kk'}(\Omega) n(\Omega, \varepsilon = 0)}\ . \qquad (12)$$

Finally, the whole calculation reduces to the calculation of the overlap functions at $\varepsilon = 0$, which practically amounts to what we have to do for the ground state calculation with a slight modification.

There is another kind of two-quasiparticle states similar to that of eq. (5), that is $|\psi> = b_1^+ b_2^+ \mid \psi_0>$. The formalism for such states can be worked out in a straightforward manner in analogy to the arguments above.

The matrix $X_{\alpha\beta}(\Omega, \varepsilon = 0)$ can be written in the form

$$X_{\alpha\beta} = \begin{bmatrix} X_{ik} & X_{i\nu} \\ X_{\mu k} & X_{\mu\nu} \end{bmatrix} \tag{13}$$

The explicit form of the matrix elements can be obtained directly from eqs. (3) and (8). Let us write the inverse of $X_{\alpha\beta}$ in the form

$$X^{-1}_{\alpha\beta} = Z_{\alpha\beta} = \begin{bmatrix} Z_{ik} & Z_{i\nu} \\ Z_{\mu k} & Z_{\mu\nu} \end{bmatrix} \tag{14}$$

It is straightforward to show by simply matrix algebra that

$$\begin{gathered} Z_{ik} = X^{-1}_{ik} + (X^{-1}_{ij} X_{j\mu}) Z_{\mu\nu} (X_{\nu l} X^{-1}_{lk}) , \\ Z_{i\nu} = -(X^{-1}_{ij} X_{j\mu}) Z_{\mu\nu} , \qquad Z_{\mu k} = -Z_{\mu\nu} (X_{\nu j} X^{-1}_{jk}) , \\ Z_{\mu\nu} = [X_{\mu\nu} - X_{\mu j} (X^{-1}_{jl} X_{l\nu})]^{-1} , \end{gathered} \tag{15}$$

and

$$n^2(\Omega,\ \varepsilon=0) = \det [X_{\alpha\beta}(\Omega,\ \varepsilon=0)] = \det (X_{ik}) \det [X_{\mu\nu} - X_{\mu j} (X^{-1}_{jl} X_{l\nu})] . \tag{16}$$

Recently, the spectra of ^{160}Yb with three negative-parity and two positive-parity bands have been obtained experimentally by Riedinger et al.[3] Based on the study of single particle motion in rotating potentials, Mottelson[4] has discussed the most striking and fundamental features revealed by this data. A much more detailed discussion of these spectra is also given by Riedinger et al.[3]. With this rather simple model, the authors are able to explain the main features of the observed bands and their crossings. There is no doubt that the analysis of ref. (3) and ref. (4) is highly valuable, but it is also desirable to have a more quantitative description based on an angular momentum conserving theory. Recently, the authors[5] have developed a method to project a Hartree-Fock-Bogoliubov wave function and 2, 4, 6, ... quasi particle states before variation of the pairing and shape degrees of freedom onto good angular momentum and particle number. In this letter we shall report on application of this method to the new data in ^{160}Yb. The calculations are performed in the way described in ref. (5), therefore we shall not repeat the details of the treatment here. We include all the 2 qp states which lie close to the Fermi surface. These include also those 2 qp configurations which are discussed in refs, (3) and, (4). Altogether, the single particle states we choose for our calculation are: $(i_{13/2,\ 1/2})$, $(i_{13/2,\ 3/2})$, $(h_{11/2,\ 11/2})$, $(h_{9/2,\ 3/2})$, $(f_{7/2,\ 3/2})$, $(f_{7/2,\ 1/2})$ (where we indicated, only the major component for the Nilsson wave function). From these single particle levels, we form all the possible combinations to construct two quasi particle excited states (including also $K=0$ pairs as described in ref, (5)). For each of these states we perform angular momentum and particle number projection. The equation $\delta(\psi_J | H | \psi_J) = 0$ is then solved

by varying pairing gap parameters Δ_N, Δ_P and the deformation β for each J. Two strinking facts are found from all the two quasi particle excited bands we have calculated. First, there are only a few bands which can be compared with the data, all the others are either too high in energy or have too narrow spacings companet to the observed values, the ground state band has the minimum energy at the deformation around $\beta=0.28$, and for the excited bands at $\beta=0.31$. These values for the deformation vary slightly from band to band, from one J to the other, they change a little also when we change the values of the pairing force constants $G_{P/N}$ and the quadrupole force strength. However, all thses small variations never become large enough to change the results by some significant magnitudes. Therefore, in order to save computer time, in our final calculations we simply fix $\beta=0.28$ for all J-states in the ground state band, and $\beta=0.31$ for all J-states in all the excited bands. Throughout the calculations the pairing strength constant for neutrons is taken as $G_N=24/A$ MeV, and for the quadrupole strength constants $X_N=X_P=X_{NP}=78/A^{1.4}$ MeV.

For positive parity excited bands, we have calculated the $(i_{13/2\pm3/2}, K=0)$ two quasi particle excited band, and the $(i_{13/2\pm3/2}, K=0)$ two particle excited band. The excited band with $(i_{13/2\pm1/2}, K=0)$ is too high in energy, For the negative parity excited bands there are only four bands among all the possible combinations formed from the single particle states which are in the same energy range as the experiments. They are:

Theor. 1: $(i_{13/2,\,3/2}) \times (h_{11/2,\,11/2})$ $K=7^-$
Theor. 2: $(i_{13/2,\,3/2}) \times (f_{7/2,\,3/2})$ $K=3^-$
Theor. 3: $(i_{13/2,\,3/2}) \times (f_{7/2,\,3/2})$ $K=0^-$
Theor. 4: $(i_{13/2,\,3/2}) \times (h_{11/2,\,11/2})$ $K=4^-$

In the following, we shall report and discuss the results of our calculations in three parts: I. Negative parity odd-J, II. Negative parity even-J, III. positive parity bands. This last part includes the ground and the S band.

I. NEGATIVE PARITY ODD-J STATES

The theoretically calculated excited bands together with two experimental bands, exp. 2 and exp. 3[3, 4], are shown in Fig. 1. It can be seen clearly that the first three theoretical bands are very close in energy for each J, but Theor. 4 is distinctively higher in energy about 150 to 250 keV than all the other three for every J. Also, Theor. 4 agrees excellently well with exp. 3 when $J \geq 11^-$. Therefore, we wish to suggest that the experimental band 3 in ref. (3) could be indentified with Theor. 4 in our calculation. For lower spin states ($J=9^-$ and 7^-), Theor. 4 does agree not so well with exp. 3. This could be

due to mixing with other bands. So far as exp. 2 is concerned, the first three theoretical bands are all very close to it. But Theor. 3 is the closest one. We may suggest that exp. 2 should contain Theor. 3 as the main component plus the mixing of Theor. 1 and Theor. 2. (It is interesting to see that if we arbitrarily mix Theor. 1, Theor. 2 and Theor. 3 with the amplitude ratios 1 : 2 : 2 (see Th. 5 in Fig. 1), it agrees very well with exp. 2 for $J \geq 13^-$. At lower spin states, as already discussed above, it should also contain some mixing from Theor. (4) Thus, we have come to the conclusion that, from our calculation exp. 3 should be mainly a pure two quasi particle excited band, and exp. 2 should be a more collective band superposed by Theor. 1, Theor. 2 and Theor. 3. To identify exp. 2 as mainly the Theor. 3 is in agreement with ref. (3) and ref. (4) suggesting that the lower spin states of exp. 3 should also contain Theor. 2 and Theor 3 is also to some extent consistent with ref. (3) and ref. 4). A further improved theory should therefore, in addition to angular momentum and particle number conservation (included in our approach), contain also the possibility of band mixing. This kind of work is presently in progress.

II. NEGATIVE PARITY EVEN-J STATES

The negative parity even-J states of our four theoretical bands together with the experimental band 1 of ref. (3) are shown in Fig. 2. In the figure it shows that all the first three theoretical bands, Theor. 1, Theor. 2. and Theor. 3, are quite good in comparison to the observed exp. 1. Theor. 4 is a little farther away. Theor. 3 agrees with the experiments the best among all four theoretical bands for $J \geqq 10^-$. Besides it agrees with the observed backbending at $J = 20^-$ to 22^-. It is reasonable to suggest that exp. 1 should be identified as having Theor. 3 to be the major component as already discussed for the negative parity odd spin states. This is again consistent with the suggestion by ref. (3) and ref. (4). However, it should also contain some finite amount of mixture from other bands, especially from Theor. 4. For $J = 6^-$ and 8^-, Fig. 2 shows that exp. 1 should contain mainly Th. 4. In contrast to exp. 3 Theor. 4, the situation here for exp. 1 is similar to exp. 2 that it should be more a mixed than just a pure two quasi particle excited band.

III. POSITIVE PARITY STATES

The calculation for the ground state band is performed exactly the same way as described in ref. (6) except one little technical detail. In ref. (6) a small correction for the moment of inertia for the core is introduced to fit the first 2^+ energy. This is as a result practically the same as decreasing G_N A or G_P A by approximately one MeV. This reduction of the pairing force

strength was used in this calculation. But we have less degrees of freedom than it may seem at the first moment. After the pairing force strength $G_{P/N}$ and the quadrupole force constant x are fixed, we can calculate all the excited bands parameter free.

The calculated ground state band and the positive parity excited band together with the experiments of ref. (3) are shown in Fig. 3. As one sees in this figure, we find the worst agreement of our calculations for the ground state band. This is due to the fact that $^{160}_{70}Yb_{90}$ is a poor rotor in ground state band and cannot be fully described without including vibrations. The calculated excited band in Fig. 3 is a superposition, with equal amplitudes, of the $(i_{13/2,\ \pm 3/2},\ k=0)$ two quasi particle excited band and the $(i_{13/2,\ \pm 3/2},\ k=0)$ two particle excited band. As it is straightforward to show that a $k=0$ two particle excited band is a superposition of a $k=0$ two quasi particle excited band and the ground state band, therefore our calculated excited band is also a mixture of the ground state band and the $k=0$ two quasi particle excited band. The results of this band seem to agree with the experiments reasonably well. This is again in principle consistent with the suggestion of ref. (3) and ref. (4).

From all the discussions above, we are led to draw the following conclusions. The analysis based on the study of single particle motion in rotating potentials is qualitatively consistent in most parts with the calculation with exact angular momentum and particle number projection. The former can be used as a first guide to study the excited rotational bands. However, for more detailed quantitative invertigation, especially in the backbending region, an angular momentum and particle number conserving theory is superior.

REFERENCES

(1) K. Goeke, A. Faessler and H. H. Wolter, Nucl. Phys. A183 (1972) 352.
(2) Lu Lin and A. Faessler, Phys. Lett. (1978) to be published.
(3) L. L. Riedinger, O. Anderson, S. Frauendorf, J. D. Garrett, J. J. Gaardhøje, G. B. Hagemann, B. Herskind, Y. V. Makovetzky, J. C. Waddington, M. Guttormson, and P. O. Tjøm, to be published, and contributed paper to the Symposium on High-Spin Phenomena in Nuclei at Argonne National Lab., USA, March 1979.
(4) B. Mottelson, lecture given at the Symposium on High-Spin Phenomena in Nuclei at Argonne National Lab., USA March 1979.
(5) L. Lin and A. Faessler, Phys. Lett. 78B (1978) 533; L. Lin, A. Faessler, and R. M. Dreizler, Nucl. Phys. A318 (1979) 287.
(6) F. Grümmer, K. W. Schmid and A. Faessler, Nucl. Phys. A239 (1975) 289.

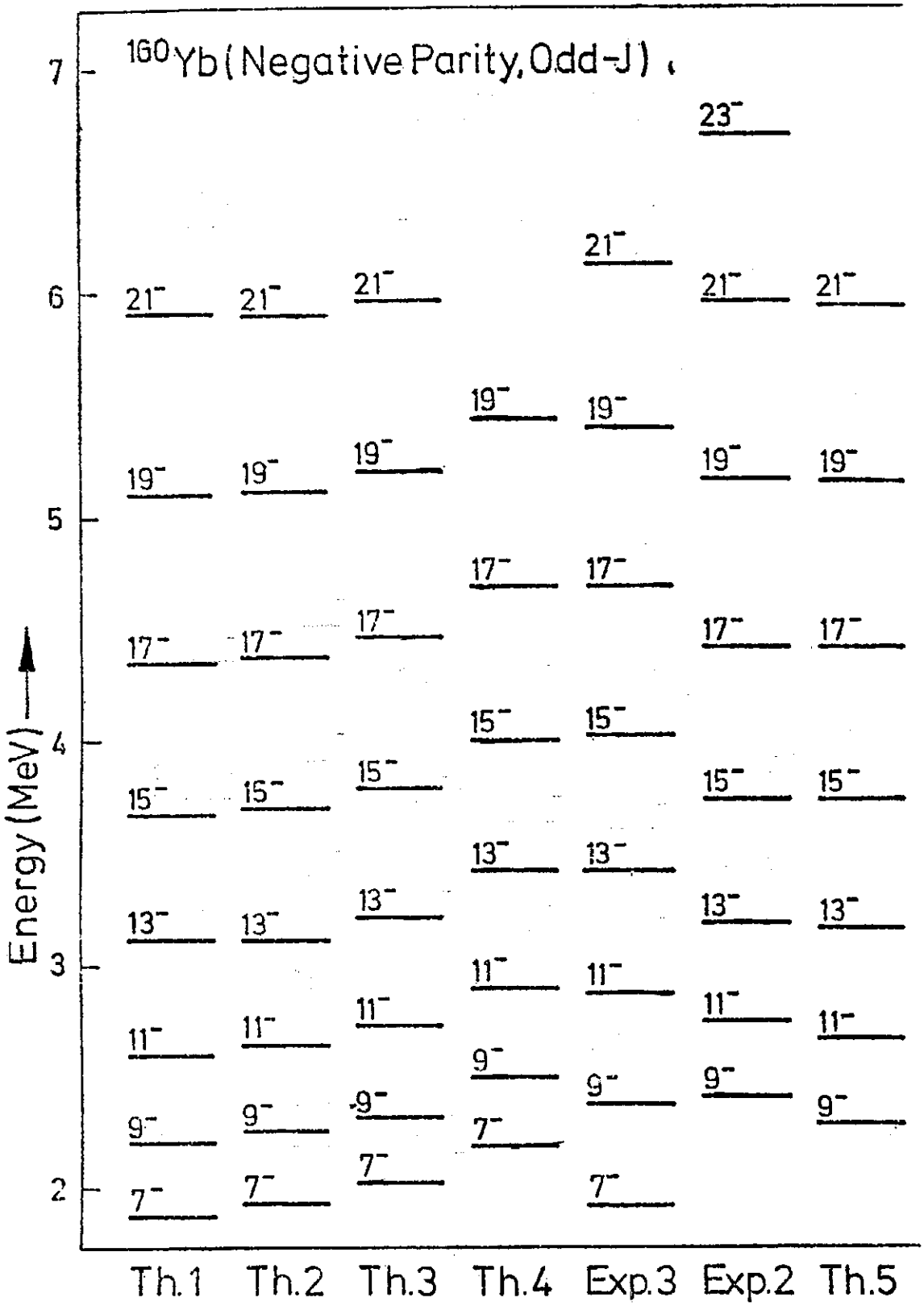

FIG. 1. Calculated energies compared to experiments for negative parity odd-J states in ^{160}Yb. See text for details.

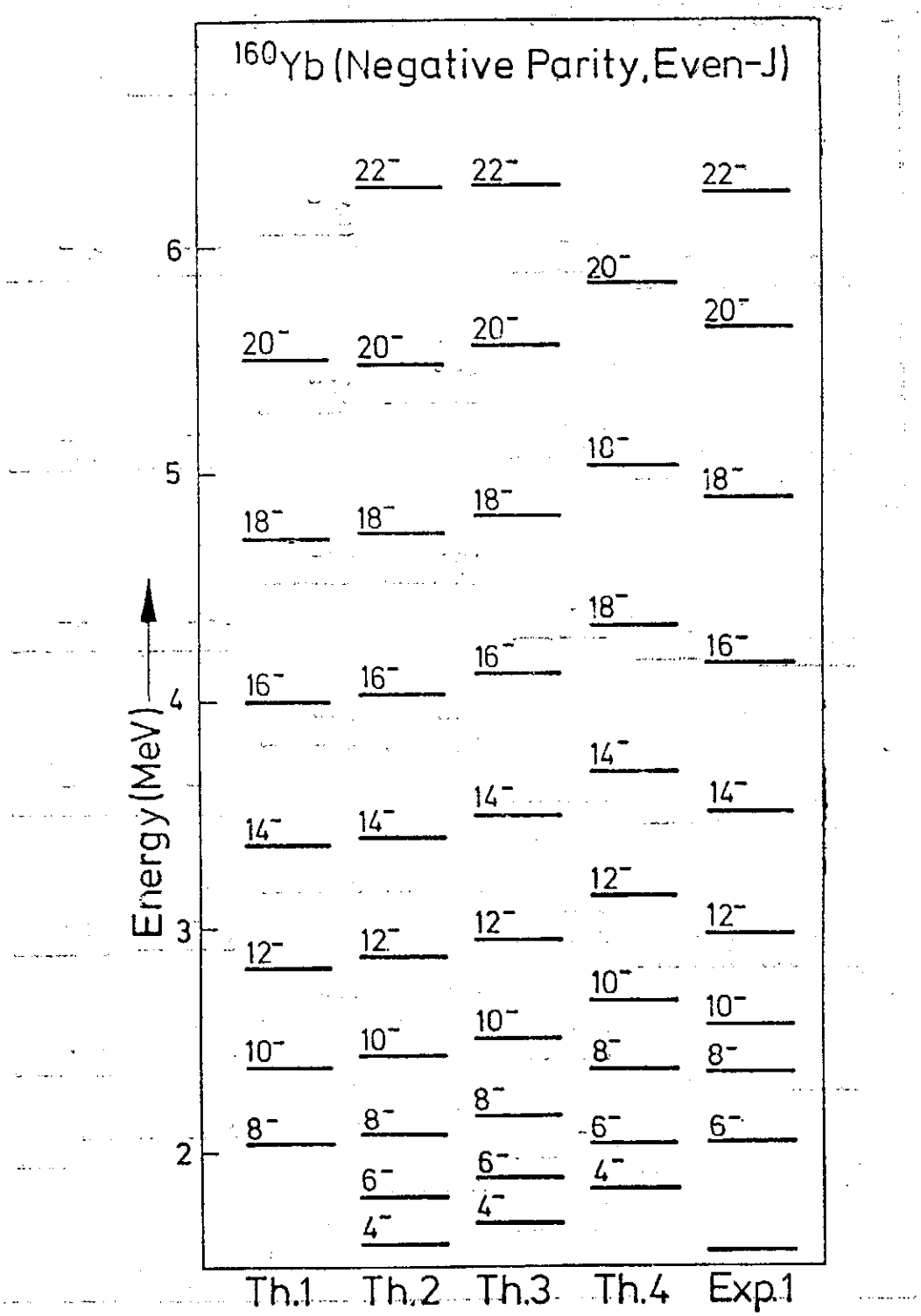

FIG. 2. Calculated energies compared to experiments for negative parity even-J states in ^{160}Yb. See text for details.

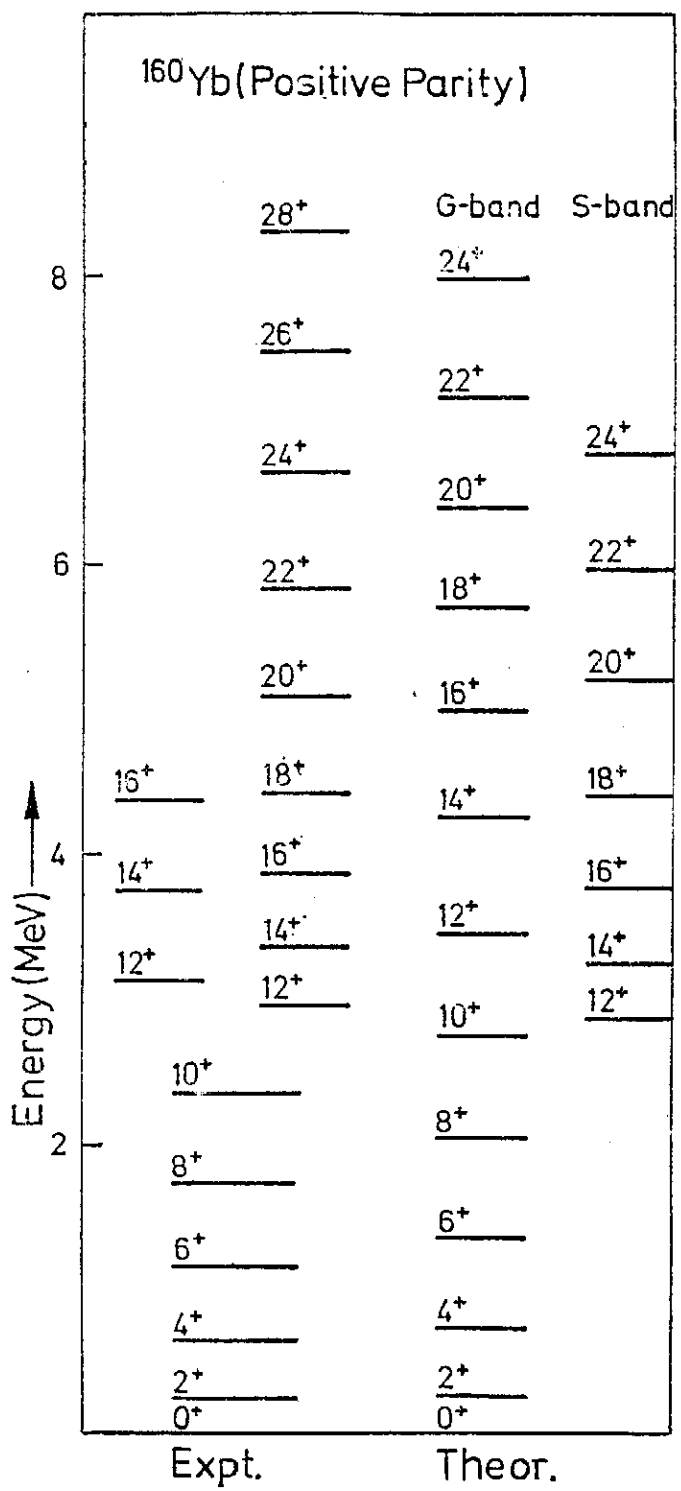

FIG. 3. Calculated energies compared to experiments for positive parity states in ^{160}Yb. See text for details.

PROPOSAL FOR IMPROVEMENT OF VERTICAL SOLAR CELL

YU-TUNG YANG (楊 毓 東)

Institute of Physics, Academia Sinica
Nankang, Taipei, Taiwan, Republic of China

Abstract

The solar cells produced by the Comsat Corporation[1, 2] were serrated surface solar cells, and the announced efficiency was 15%. The serrated surface sollar cells may be viewed as a combination of the horizontal-and the vertical-solar cells. The multi-layer vertical planar-junction solar cells produced by the Solarex Corporation[3] may have over 13% AMO efficiency. Recently, it was found in this laboratory that the absorption of light by a vertical planar-junction solar cell is "polarization direction of light" selective, i.e., the vertical solar cell prefers the absorption of light with its E-wave vector parallel to the built-in E_{dc}-vector of the vertical solar cell. The light absorption becomes almost zero when the E-wave vector is perpendicular to the E_{dc}-vector. When the V_{oc} vs. $\angle(\vec{E}_{h\nu}, \vec{E}_{dc})$ was measured, it was found that the ratio of the maximum V_{oc} to the average V_{oc} due to angular variation is about 1.5. The square of the above ratio, which is also the solar energy conversion recovery factor, is about 2.25. Thus, if the solar energy is fully recovered, the efficiency of the vertical solar cell should be over 30%. Circular vertical solar cell of proper size may be able to eliminate the polarization direction of light selective absorption effect.

1. INTRODUCTION

Vertical solar cell has been considered more efficient than horizontal solar cell[1, 2]. However, the former may be even more efficient if my recent discovery of the "polarization of light direction selective absorption effect" is taken into account[4]. As far as the solar energy to electrical energy conversion is concerned, the above effect is a bad one because a lot of the solar energy is simply wasted if the E-wave vector of the incident light is not in the direction of the built-in electrostatic field E_{dc} vector of the vertically-oriented planar-junction diode.

2. THEORETICAL IMPROVEMENT OF VERTICAL-JUNCTION SOLAR CELL

The basic idea of the improvement is to make the E_{dc}-vector of the vertical solar cell everywhere parallel to the $E_{h\nu}$-vector of an unpolarized incident light. This is only an idea because it can only be fulfilled if the unit vertical solar cell of circular cross-section is shrunken to almost zero in diameter, and the density of the vertical solar cells becomes infinity. It is almost impossible to make such a densely packed vertical solar cell at this moment. However,

the next best thing one can do is to reduce the cross-section to a tolerable size of the order of the wave lengths of the incident light. This approximation is based on the Heisenberg uncertainty principle. Since

$$p_x \cdot x \geqslant h, \tag{1}$$

and for photon,

$$p_x = \frac{h\nu}{c}. \tag{2}$$

By substituting (2) into (1), the result is

$$X \geqslant \frac{c}{\nu} \quad \text{or} \quad x \gtrsim \lambda \tag{3}$$

If λ is the wave length of the incident light and X is the approximate diameter of the circular cross-section of the vertical solar cell, then the solar cell is within the region of vibration of the light. Since the unit vertical solar cell and the region of the light oscillation may coincide under the uncertainty principle, therefore the E-wave vector and the E_{dc} vector may be considered as in the same direction. Since the silicon cell responds to about 0.1 to one micron wave lengths of light, therefore, the diameters of the circular cross-section of the vertical solar cells must also be of the order of 0.1 to one micron in order to match the uncertainty principle.

One unit of the vertical solar cell is shown in Fig. 1. The ohmic contacts are made as usual. The unit can be repeated as many times as desired to make a multiplet. Other advantages of the vertical solar cell are kept as usual and needed not be mentioned.

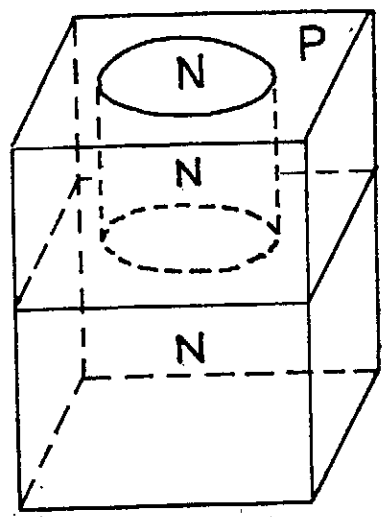

Fig. 1. Proposed one unit circular-junction vertical solar cell. As many such unit cells may be piled together as one desires.

Fig. 2 shows: If both a vertical planar-junction solar cell (a) and a vertical circular-junction solar cell (b_1) have the same top area for receiving the sun light and have the same depth, if the circumference of the circle in (b_1)

is spread out to become a straight line, the length of the line may be ℓ if the diameter of the circle is ℓ/π, ($\ell \sim \lambda$), then without considering the "polarization direction of light selective absorption effect", the physical properties of both (a) and (b_1) would be about the same. However, if the "polarization effect" is taken into consideration and if the diameter of the circle is somewhat larger than ℓ/π, then for the same top-area and depth of the vertical solar cell, the unit cell (b_1) may be physically superior than (a). (b_2) is the equivalence of (b_1) when the diameter of the circle is larger than ℓ/π, and the area of the unit cell remains the same as (b_1). Detail calculation, based on the diffusion-continuity equation in both Cartesian coordinates and cylindrical coordinates form, may show the relations between (a), (b_1), and (b_2).

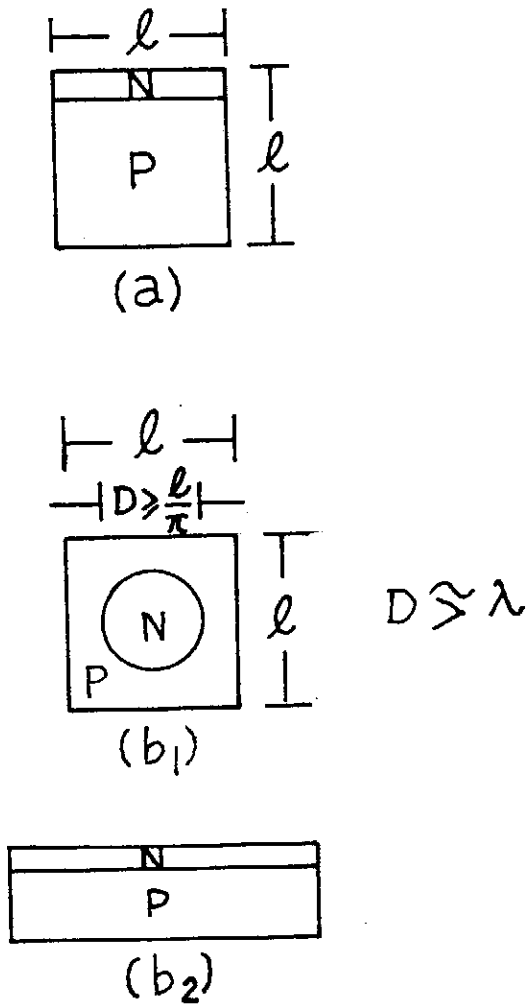

Fig. 2. (a) Vertical planar-junction solar cell, (b_1) Vertical circular-junction solar cell, the design of which can be made in such a way that the circumference of the circle in (b_1) is longer than ℓ if the diameter of the circle is larger than ℓ/π. (b_2) The spread out form of (b_1). (a), (b_2), and (b_1) have the same top area for receiving the sun light and have the same depth.

REFERENCES

(1) H. J. Hovel, "Solar cells", p. 225, Addendum, (Semiconductors and semimetals, Vol. 11, 1975), Academic Press, New York
(2) Science News, p263, Oct. 26, 1974
(3) J. Lindmayer and C. Wrigley, IEEE, Conf. record, 12th photovoltaic specialists conf., Baton Rouge, Louisiana, Nov. 1976
(4) Y. T. Yang, Ann. report, Institute of physics, Academia Sinica, Nankang, Taipei, Taiwan, Republic of China, 1979

MAGNETORESISTIVITY OF SOME AMORPHOUS METALS

Y. D. YAO (姚 永 德)
Institute of Physics, Academia Sinica
Nankang, Taipei, 115, R.O.C.

S. ARAJS
Department of Physics, Clarkson College of Technology
Potsdam, N.Y. 13676, U.S.A.

and

S. T. LIN
Department of Physics, Cheng Kung University
Tainan, Taiwan, 700, R.O.C.

Abstract

The magnetoresistivity of amorphous $Cu_{60}Zr_{40}$, $Fe_{80}B_{20}$, $Fe_{80}B_{18}Si_2$ and $Fe_{80}B_{13}Si_4C_3$ alloys was studied for three different orientations of the ribbon plane to the magnetic field direction. The magnetoresistivity of $Cu_{60}Zr_{40}$ is negligible at least within our experimental error. For ferromagnetic metallic Fe-B-Si-C glasses, the longitudinal magnetoresistivity is positive and the transverse one negative. When the magnetic field is perpendicular to the ribbon plane of $Fe_{80}B_{13}Si_4C_3$, a small resistivity increase is observed for small fields up to a few hundreds of Oersted, thereafter a hysteresis behavior is followed. This can be understood qualitatively by the influence of the demagnetizing effect.

INTRODUCTION

In recent years interest in the mechanism of conduction of amorphous metallic alloys to the presence of a magnetic field has been stimulated by the following two facts: (1) the fast development of metallic glasses in the 1970's and (2) the recent development of two-current model[1-4] in ferromagnetic metals and alloys. The magnetoresistance has recently been observed in a variety of amorphous metallic alloys such as $Fe_{80}B_{20}$[5-7], $Fe_{78}Mo_2B_{20}$[5-7], $Fe_{40}Ni_{40}P_{14}B_6$[6,7], $Fe_{32}Ni_{36}Cr_{14}P_{12}B_6$[6], $Pd_{80}Si_{20}$[8] and $Gd_{67}Co_{33}$[8]. In this investigation we reports measurements of the field dependence of magnetoresistivity on amorphous non-magnetic alloy $Cu_{60}Zr_{40}$ and amorphous ferromagnetic alloys $Fe_{80}B_{20}$, $Fe_{80}B_{18}Si_2$ and $Fe_{80}B_{13}Si_4C_3$. Our experimental results are briefly described below. This is just a beginning of our systematic investigations about the field dependence of the resistivity in metallic glasses.

EXPERIMENTAL CONSIDERATION

One amorphous non-magnetic alloy $Cu_{60}Zr_{40}$ and three amorphous magnetic alloys $Fe_{80}B_{20}$, $Fe_{80}B_{18}Si_2$ and $Fe_{80}B_{13}Si_4C_3$ were prepared by the technique of solidifying a stream of molten metal against the outside of a rapidly rotating

copper drum. The samples were roughly in a form of ribbon 1-2 mm wide, 20-40 μm thick and 1-2 cm in length. Four copper electrodes were lightly spot welded to each sample, the two central electrodes being used as potential leads and the other two as current leads. The electrical resistivity of these samples was determined using the conventional fourpoint probe technique. A seven inches laboratory electromagnet (O. S. Walker Company) was used to produce the magnetic fields. The magnetic field was applied to the ribbon sample with three different orientations as shown in Fig. 1. The potentiometer used for this study is accurate to 0.1 μV. The current was maintained constant to about one part in 10^5.

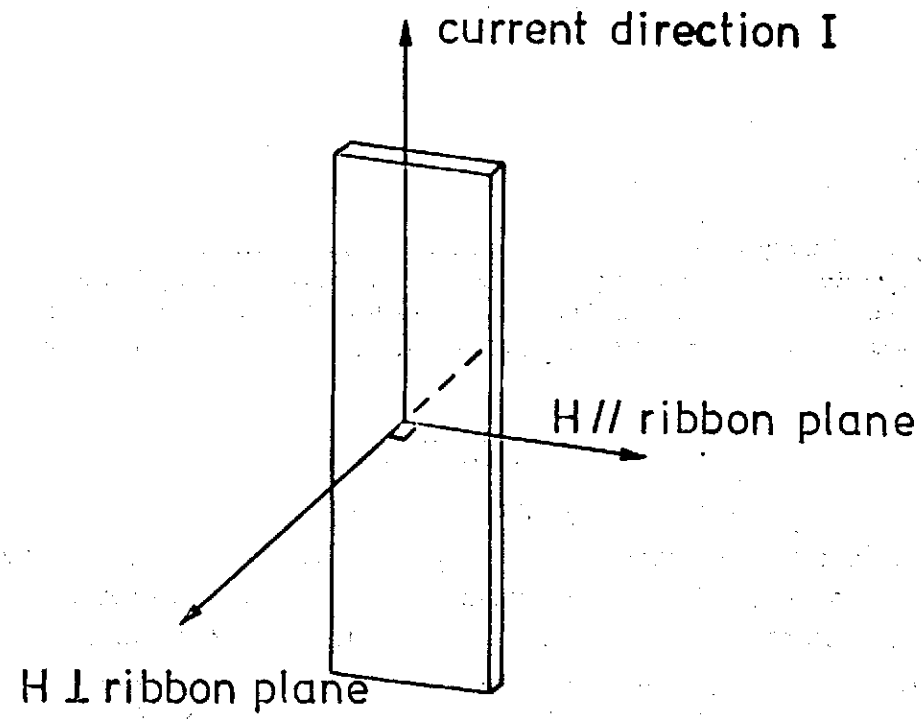

FIG. 1. Schematic representation of the directions between ribbon sample and magnetic field etc..

RESULTS AND DISCUSSION

Fig. 2 shows the electrical resistivity of $Cu_{60}Z_{40}$ at 78 and 300 K as a function of the magnetic field. We find that the resistivity of $Cu_{60}Zr_{40}$ is not sensitive to the presence of a magnetic field. The magnetoresistivity of $Cu_{60}Zr_{40}$ is negligible at least within our experimental error. The value of electrical resistivity at 78 K is a little higher than that at 300 K, this means that the temperature coefficient of resistivity, $\alpha \equiv (1/\rho)d\rho/dT$, is small and negative for $Cu_{60}Zr_{40}$ between 78 and 300 K. In general, charge carriers drifting in a material under the combined action of transverse electric and magnetic vectors are subject

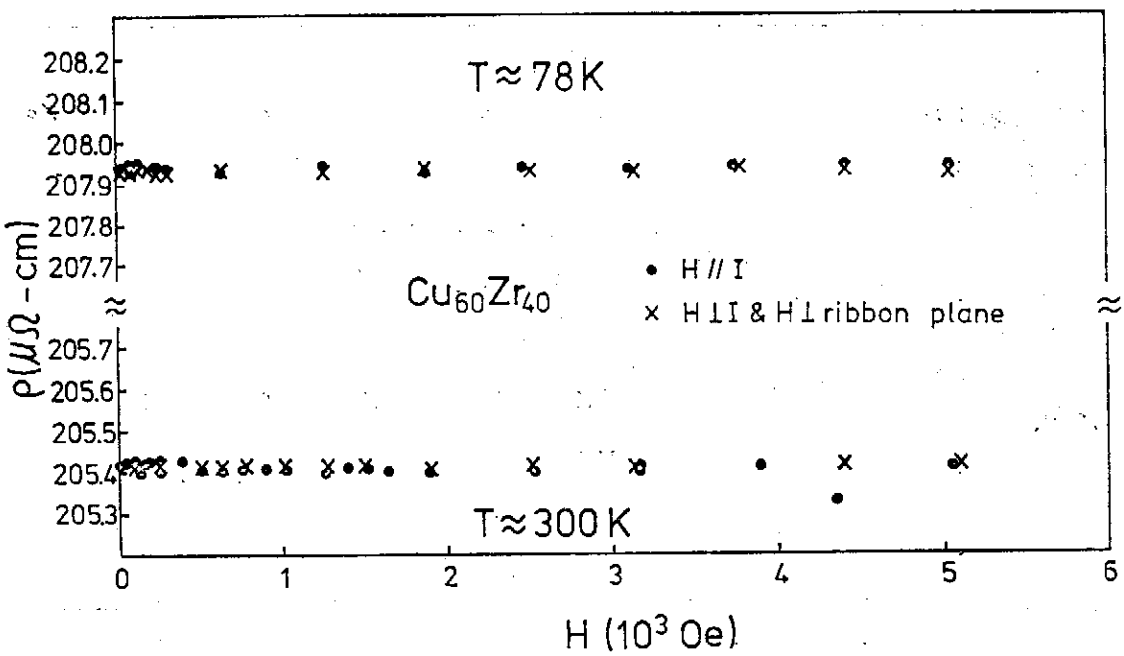

FIG. 2. Electrical resistivity of $Cu_{60}Zr_{40}$ as a function of the magnetic field at 78 and 300 K.

to the Lorentz force which deflects some of them producing the Hall field. If all the charge carriers are identical and can be described by a spherical Fermi surface and by a single isotropic relaxation time then the Hall field compensates the Lorentz force, the current streamlines are invariant with magnetic field, and in consequence, the magnetoresistivity is zero. If the charge carriers are not of the same charge type, if their effective masses are different or their relaxation times are energy dependent then the Lorentz force is not fully compensated by the Hall field. This produces a current transverse to the electrical and magnetic vectors and a change in the resistivity of a sample which can be measured along its longitudinal direction of current flow. According to our data, we conclude that the Hall field compensates the Lorentz force in $Cu_{60}Zr_{40}$.

The field dependence of the resistivity for $Fe_{80}B_{20}$, $Fe_{80}B_{18}Si_2$ and $Fe_{80}B_{13}Si_4C_3$ is shown in Fig. 3, 4, and 5, respectively. Here $\Delta\rho_{\parallel}$ and $\Delta\rho_{\perp}$ are the resistivity changes in magnetic fields parallel and perpendicular to the current direction, respectively. For the $\Delta\rho_{\perp}$ measurements, the direction of the magnetic field is parallel to the ribbon plane for the samples of $Fe_{80}B_{20}$ and $Fe_{80}B_{18}Si_2$; however, for the sample of $Fe_{80}B_{13}Si_4C_3$, we chose the perpendicular situation between the magnetic field and the ribbon plane. Generally speaking, the longitudinal magnetoresistivity is positive and the transverse one negative, which according to Potter[9] means that the resistivity is dominated by scattering of minority-spin electrons. Both $\Delta\rho_{\parallel}$ and $\Delta\rho_{\perp}$ tend to saturate with increasing magnetic field. For comparison purpose, Fig. 6 shows the normalized longitudinal

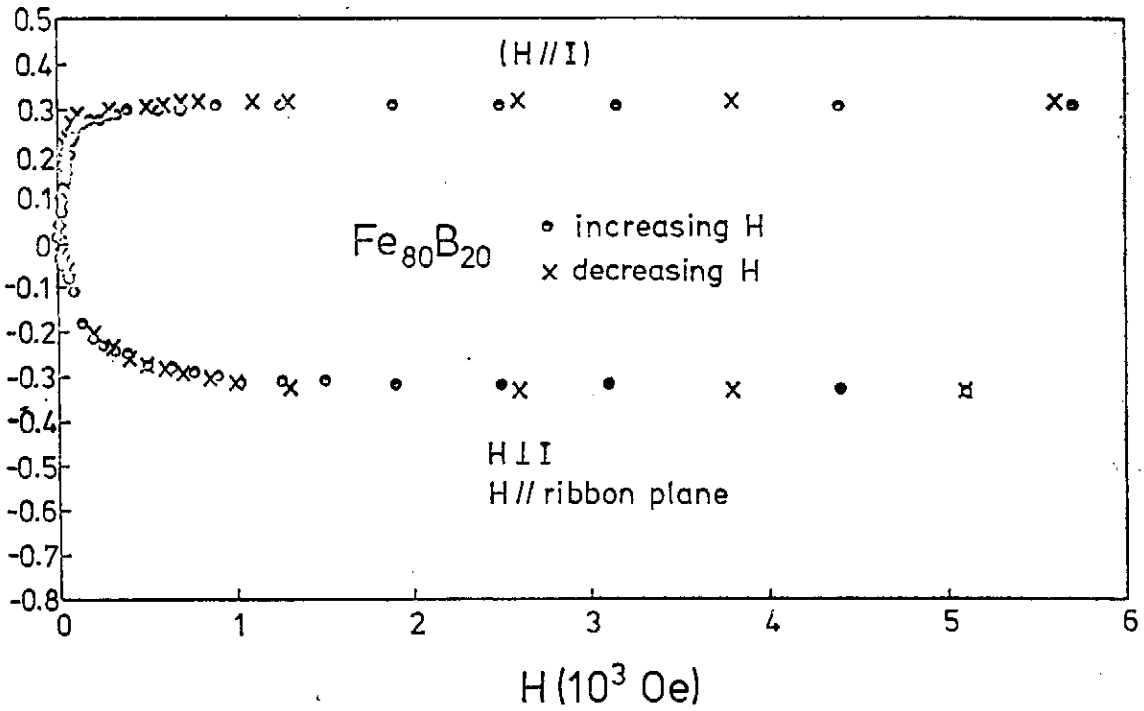

FIG. 3. $\Delta\rho_{\parallel}$ and $\Delta\rho_{\perp}$ of $Fe_{80}B_{20}$ as a function of the magnetic field.

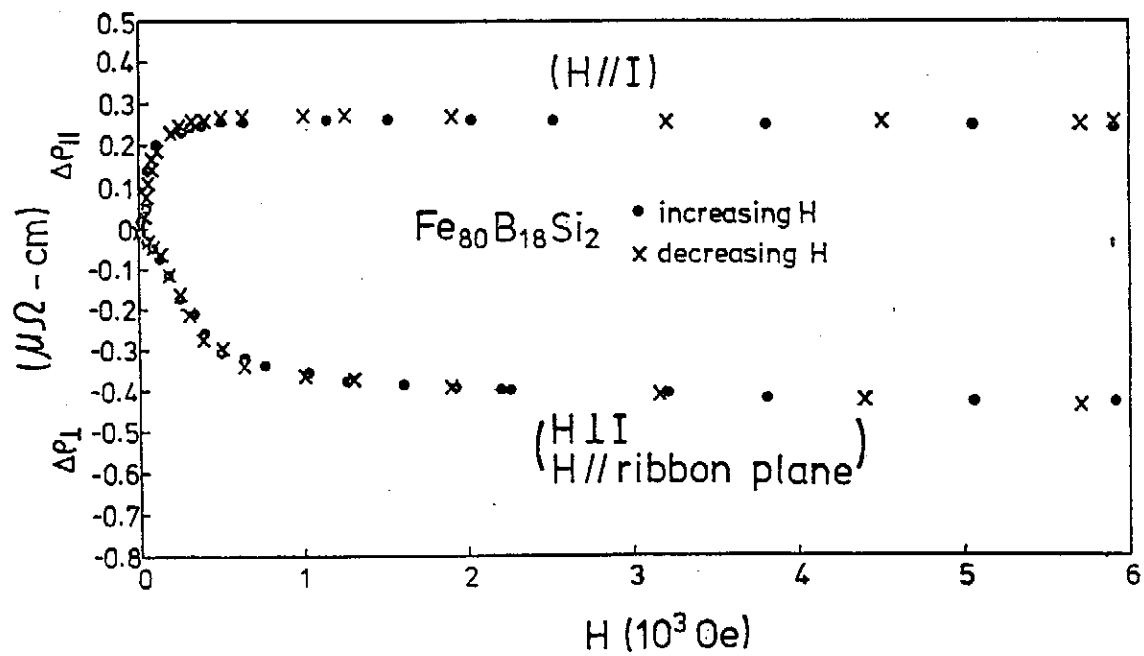

FIG. 4. $\Delta\rho_{\parallel}$ and $\Delta\rho_{\perp}$ of $Fe_{80}B_{18}Si_2$ as a function of the magnetic field.

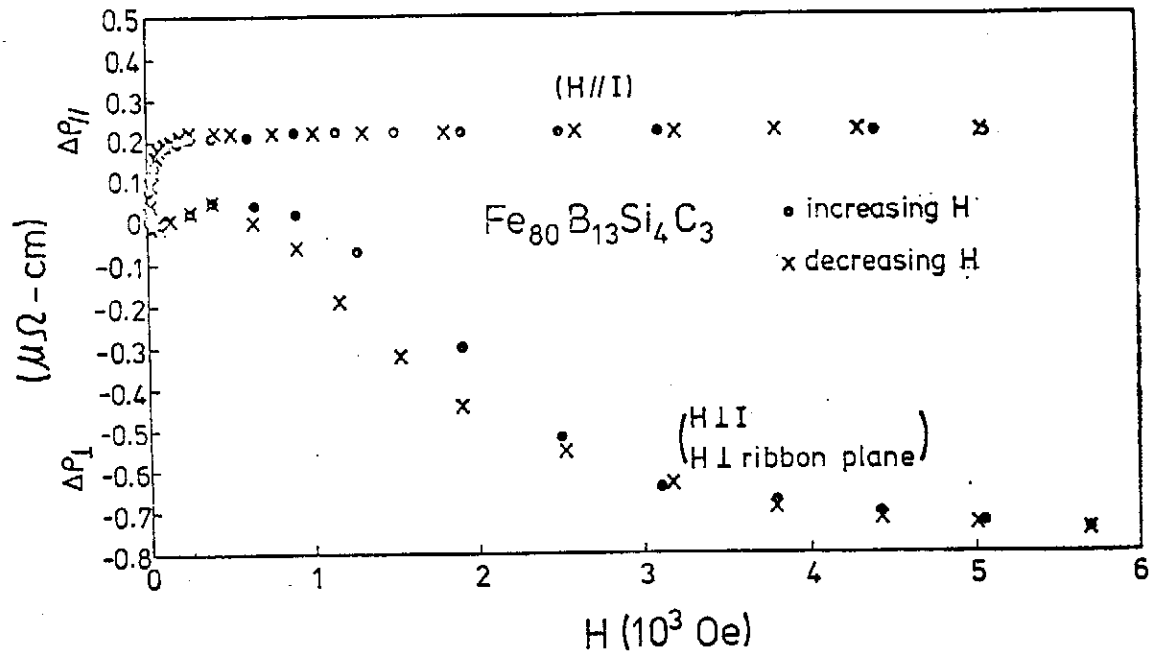

FIG. 5. $\Delta\rho_{//}$ and $\Delta\rho_{\perp}$ of $Fe_{80}B_{13}Si_4C_3$ as a function of the magnetic field.

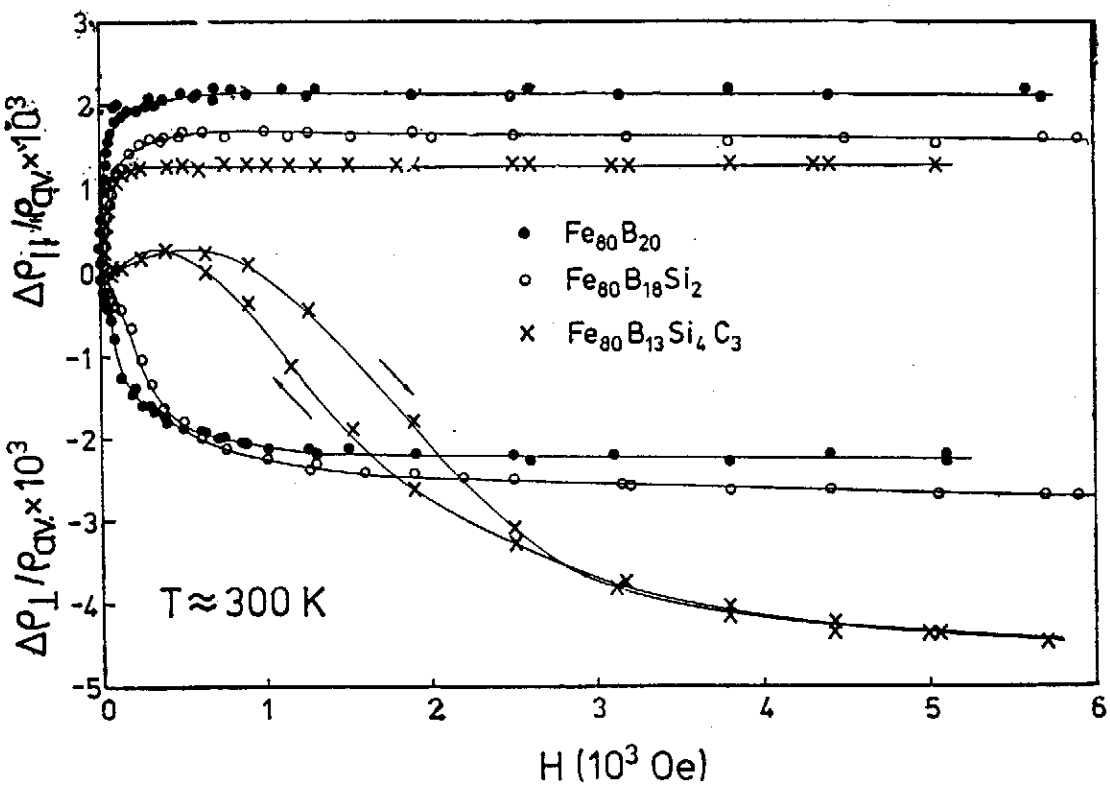

FIG. 6. Normalized longitudinal and transverse magnetoresistivity as a function of the magnetic field for $Fe_{80}B_{20}$, $Fe_{80}B_{18}Si_2$ and $Fe_{80}B_{13}Si_4C_3$.

and transverse magnetoresistivity at 300 K as a function of the magnetic field for all the amorphous ferromagnetic samples we used for this study. Here, $\rho_{av}=\rho_{\parallel}/3+2\rho_{\perp}/3$, and $\rho_{\parallel}$ and $\rho_{\perp}$ are the resistivities in saturating magnetic fields applied parallel and normal to the current, respectively. As can be seen, the value of the saturated longitudinal magnetoresistivity $\Delta\rho_{\parallel}/\rho_{av.}$ of the $Fe_{80}B_{20-x-y}Si_xC_y$ system is decreased with increasing the impurities of silicon and carbon. On the other hand, the absolute value of the saturated transverse magnetoresistivity $|\Delta\rho_{\perp}/\rho_{av.}|$ of this system is increased by adding the silicon and carbon impurities. The difference of the magnetoresistivity is small between $Fe_{80}B_{20}$ and $Fe_{80}B_{18}Si_2$ (Table 1). The large negative value of $\Delta\rho_{\perp}$ for $Fe_{80}B_{13}Si_4C_3$ could be qualitatively understood if the negative magnetoresistance[10] of glassy carbon is taken into account.

TABLE I: Experimental values of $\rho_{av.}$, $\Delta\rho_{\parallel}$, $\Delta\rho_{\perp}$, $\Delta\rho$ and $\Delta\rho/\rho_{av.}$ for $Fe_{80}B_{20}$, $Fe_{80}B_{18}Si_2$ and $Fe_{80}B_{13}Si_4C_3$ in saturating magnetic fields.

Samples	$\rho_{av.}$ ($\mu\Omega$-cm)	$\Delta\rho_{\parallel}$ ($\mu\Omega$-cm)	$\Delta\rho_{\perp}$ ($\mu\Omega$-cm)	$\Delta\rho$ ($\mu\Omega$-cm)	$\Delta\rho/\rho_{av.}(\times10^3)$
$Fe_{80}B_{20}$	144.64±0.01	0.32±0.02	−0.33±0.02	0.65±0.04	4.49±0.27
$Fe_{80}B_{18}Si_2$	160.85±0.01	0.26±0.02	−0.43±0.02	0.69±0.04	4.29±0.25
$Fe_{80}B_{13}Si_4C_3$	169.44±0.01	0.22±0.02	−0.75±0.02	0.97±0.04	5.72±0.23

When the magnetic field is parallel to the current direction, a strong positive $\Delta\rho_{\parallel}$ up to fields roughly of hundred Oersted is observed. $\Delta\rho_{\parallel}$ is then gradually saturated after a few hundreds of Oersted. When the magnetic field is normal to the current direction; two directions have to be considered: i.e H $\parallel$ ribbon plane and H $\perp$ ribbon plane. This is due to the large ratio width/thickness of the ribbon samples. For samples of $Fe_{80}B_{20}$ and $Fe_{80}B_{18}Si_2$, we chose H $\parallel$ ribbon plane and found that $\Delta\rho_{\perp}$ was strong negative up to fields of a few hundreds of Oersted and then saturated for higher magnetic fields. For the $Fe_{80}B_{18}Si_4C_3$ sample, we let H $\perp$ ribbon plane. The results are that $\Delta\rho_{\perp}$ is slightly positive at small magnetic fields below a few hundreds of Oersted. It seems that parts of the domains align first perpendicular to the magnetic field direction and parallel to the current, which leads to a resistivity increase. This small resistivity increase at low magnetic fields we observed in $Fe_{80}B_{13}Si_4C_3$ sample as qualitatively consistent with that due to Bergmann and Marquardt[11] and Kern and Gonser[7]. The hysteresis behavior of $\Delta\rho_{\perp}$ roughly between 300 and 3000 Oe can also be qualitatively understood by the influence of the demagnetizing field.

Further systematic investigations on a variety of glassy systems are now in progress in our laboratories and will be reported later.

REFERENCES

(1) N. F. Mott, Adv. Phys. **13,** 325 (1964).
(2) I. A. Campbell, A. Fert and A. R. Pomeroy, Phil. Mag. **15,** 977 (1967).
(3) A. I. Fert and I. A. Campbell, Phys. Rev. Lett. **21,** 1190 (1968).
(4) J. W. F. Dorleijn and A. R. Miedema, J. Phys. F: Metal Phys. **5,** 487 and 1543 (1975); also **7,** L23 (1977).
(5) G. Bohnke, N. Croitoriu, M. Rosenberg and M. Sostarich, IEEE Transactions on Magnetics, Vol. Mag. — 14, No. 5 p. 955 (1978).
(6) A. K. Nigan and A. K. Majumdar, Physica **95B,** 385 (1978).
(7) R. Kern and V. Gonser, J. Magnetism and Magnetic Materials **13,** 74 (1979).
(8) J. Kästner, H. J. Schink and E. F. Wassermann, Solid St. Comm. **33,** 527 (1980).
(9) R. I. Potter, Phys. Rev. **B10,** 4626 (1974).
(10) A. A. Bright, Phys. Rev. **B20,** 5142 (1979).
(11) G. Bergmann and P. Marquardt, Phys. Rev. **B18,** 326 (1978).

STRUCTURAL AND ELECTRICAL PROPERTIES OF Fe-rich Fe-Pd ALLOYS

Y. D. YAO (姚 永 德)
Institute of Physics, Academia Sinica
Nankang, Taipei, 115 Taiwan, R.O.C.
and
S. ARAJS
Department of Physics, Clarkson College of Technology
Potsdam, N.Y. 13676 U. S. A.

Abstract

The structural and electrical properties of a series of Fe-rich Fe-Pd alloys has been studied by means of the electrical resistivity technique. Special attention is given to these anomalies due to the magnetic phase transition, the α-ν transition and the metastable phase which exists in higher Pd concentration Fe-Pd samples.

INTRODUCTION

The fundamental properties of iron and iron-rich alloys have drawn an increasing interest because of their huge technological importance. In general, there exists two different crystal structures in pure metallic iron; the B.C.C. (α or δ phases) and F.C.C. (ν phase) structures. Roughly speaking, the α-phase is stable below 1183 K; ν-phase is stable between 1,183 K and 1,663 K; above 1,663 K and up to the melting temperature of iron ($\sim$ 1807 K) δ-phase is stable. The α-phase iron is ferromagnetic below the Curie temperature (T_c), and is paramagnetic, above T_c. The ν-phase iron is a quite mysterious metal whose magnetic properties are not quite clear yet. In iron-rich alloys the changes of these fundamental properties will depend on the kind and concentration of foreign atoms dissolved. But any changes due to these foreign atoms should affect the scattering behavior of the conduction electrons and thus be observed in measurements of the electrical resistivity. In a previous publication[1], we have reported on a study of the electrical resistivity of FePd alloys with 3.0 and 7.9 at.% Pd in the temperature range of 800-1200 K. The interesting hysteresis anomalous feature of the electrical resistivity near the magnetic phase transition has been explained by the overlapping effect between magnetic and α-ν transitions.

In this paper the complete electrical resistivity data of iron-palladium alloys containing 0.5, 1.0, 3.0, 7.9, 10.0 and 11.9 at.% Pd as a function of the absolute temperature (T) between 77 and 1250 K are reported. Special attention is given to these anomalies due to the magnetic phase transition, the α-ν transition and the metastable phase which exists in higher concentration Pd alloys. Our experimental results and their significance are presented below.

EXPERIMENTAL PROCEDURE

Except the sample containing 0.5 at.% Pd, all the Fe-Pd samples used for this study were cut from the same homogenized ingots prepared for the high temperature magnetic susceptibility study before[2]. All samples were in the from of rectangular parallelepiped. The surfaces of these samples were polished by using files and sandpapes. Typical sample dimensions were roughly $2.3 \times 2.3 \times 20$ (units is mm^3).

The electrical resistivity data of these Fe-Pd samples were measured by means of the standard four-point probe technique. Temperatures between 77 and 300 K were achieved in a cryostat; temperatures between 300 and 1250 K were achieved in a Marshall furnace. Both cryostat and Marshall furnace can be either high vacuumed or filled with helium gases. Below 300 K, two Pt resistance thermometers were used to measure the temperature; above 300K, two chromal-alumel thermocouples were used. These sensors were placed very close to the end of the two potential leads on the sample. Spotwelded molybdenum wires with 0.0178 cm diameter were used as potential and current leads. The electrical resistivity data were recorded at various small temperature intervals of roughly 0.5 K in the vicinity of the magnetic and the α-ν phase transformations, and large temperature intervals of roughly 10 to 20 K in the remainder of the temperature rauge studied. The DC current was maintained constant to about one part in 10^5 and the potential was measured with a precision of 0.1 microvolts. For each sample $d\rho/dT$ was obtained from the $\rho(T)$ data by point-by-point differentiation using a computer. To facilitate the critical analysis, $d^2\rho/dT^2$ the second derivative of $\rho(T)$, was also computer generated from the heating run $d\rho/dT$ data in a similar manner.

RESULTS AND DISCUSSION

Fig. 1 shows the residual electrical resistivity measured at 4.2 K before this study. This plot can be explained according to Nordheim's rule. The value of the increase in the electrical resistivity is gradually changed roughly from 2.3 $\mu\Omega$cm/at.% for very dilute Fe-Pd alloys to 0.7 $\mu\Omega$cm/at.% for Fe-Pd alloys containing 12 at.% Pd.

Fig. 2 shows the electrical resistivity data of our Fe-Pd alloys containing 0.5, 1.0, 3.0, 7.9, 10.0 11.9 at.% Pd with increasing and decreasing temperatures between 77 and 1250 K. At least two different runs were taken for each sample. The various types of points (open, closed, etc.) shown in Fig. 2 are associated with different heating and cooling runs. For clarity not all the data are presented. The dashed curves in Fig. 2 means no experimental data were taken in that temperature region. The electrical resistivity data for these Fe-Pd

samples containing 0.5, 1.0 and 3.0 at.% Pd are consistant between different runs. However, for temperature roughly below 900 K, the electrical resistivity of the heating run of those Fe-Pd samples containing 7.9, 10.0 and 11.9 at.% Pd are dramatically different between Run 1 and Run 2. This irreversible shift phenomenon of the electrical resistivity from higher value in Run 1 to lower value in Run 2 can be considered (even not quite) similar to the transformation from a metastable phase to stable state in metallic glasses. It is well known that, when metalloid dissolved in either iron or palladium under very fast quench rate, an amorphous metallic glass is formed. Even we have not found any reports or papers yet to show that FePd system is an amorphous alloy. However, it has been shown that two transition metals not containing a metalloid, for example the Cu-Zr and Nb-Ni systems[3], can also be an amorphous metallic glass. This is because that binary transition alloys may produce a complex intermetallic compound in equilibrium. Now let us consider the FePd system with higher Pd concentration, when samples quenched from liquid state to solid state, some complex atomically disordered metastable intermetallic compound of FePd may be produced. These metastable phases will easily tend to the atomically ordered stable state if the temperature is increased. Our experimental results show that the shift of the electricial resistivity does

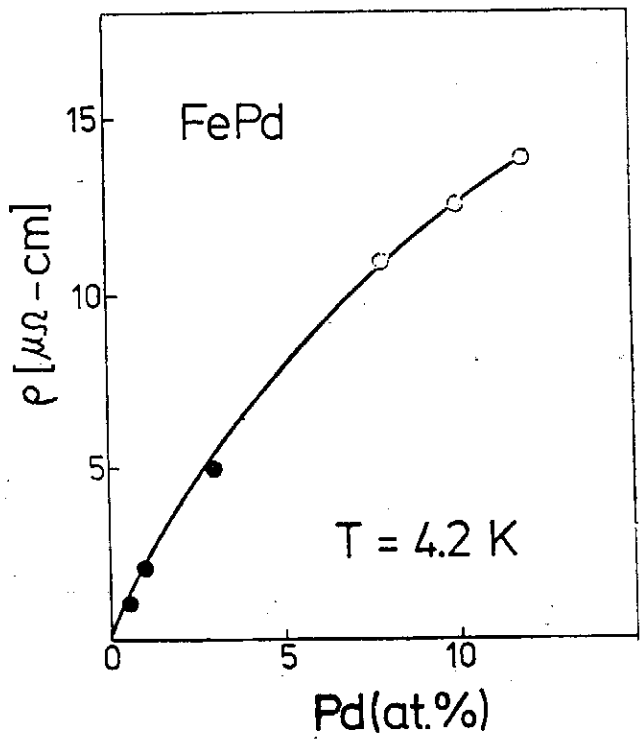

FIG. 1. Residual electrical resistivity of iron-palladium alloys as a function of the palladium concentration.

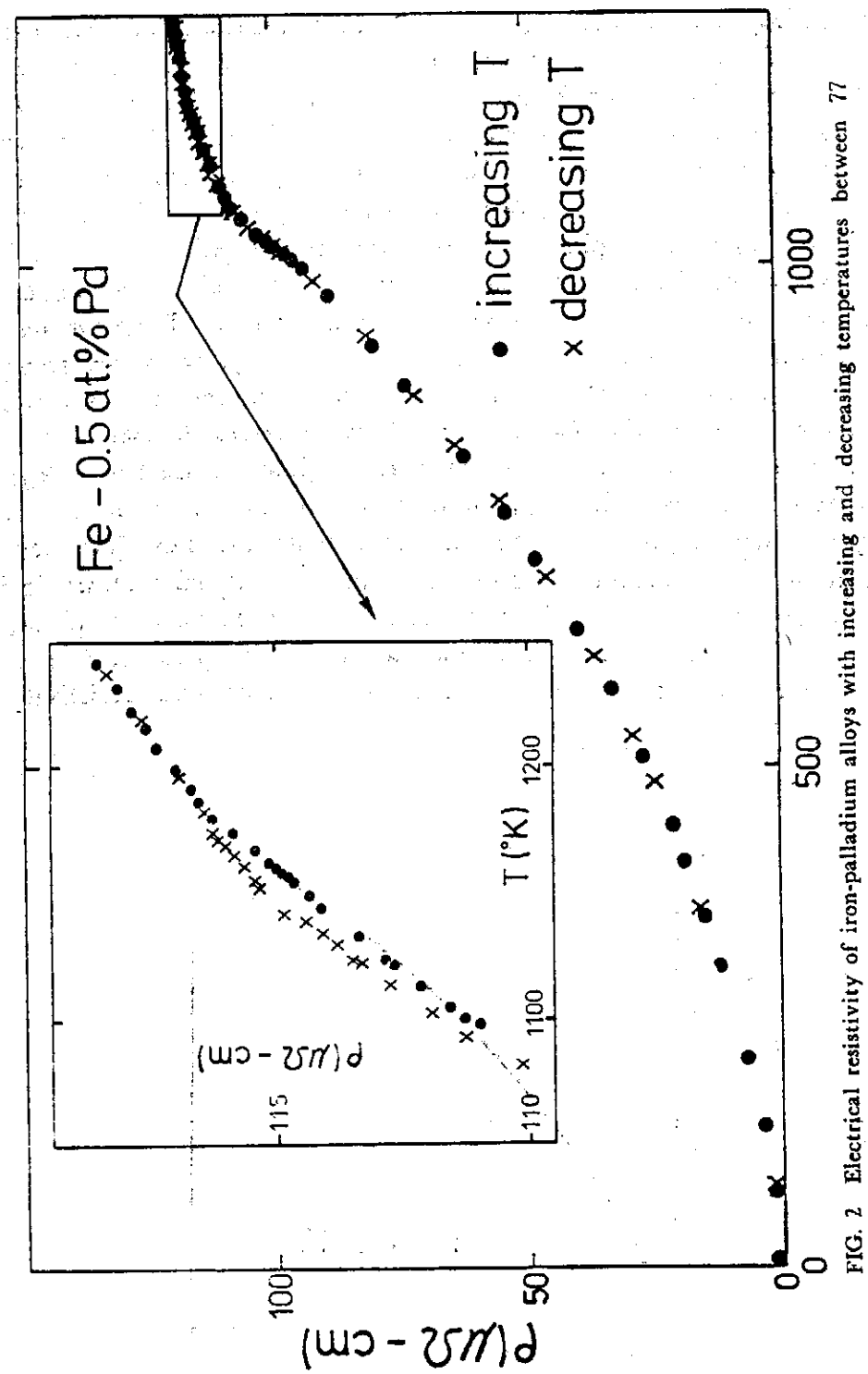

FIG. 2 Electrical resistivity of iron-palladium alloys with increasing and decreasing temperatures between 77 and 1250 K.
(a) ρ vs T for Fe-0.5 at.% Pd.

not happen in the FePd system with the Pd concentration less than 3 at.%. This is in good agreement with the constitutional phase diagram of the Fe-Pd system in Hansen and Anderko[4], Elliott[5] and Shunk[6]. Because the solubility

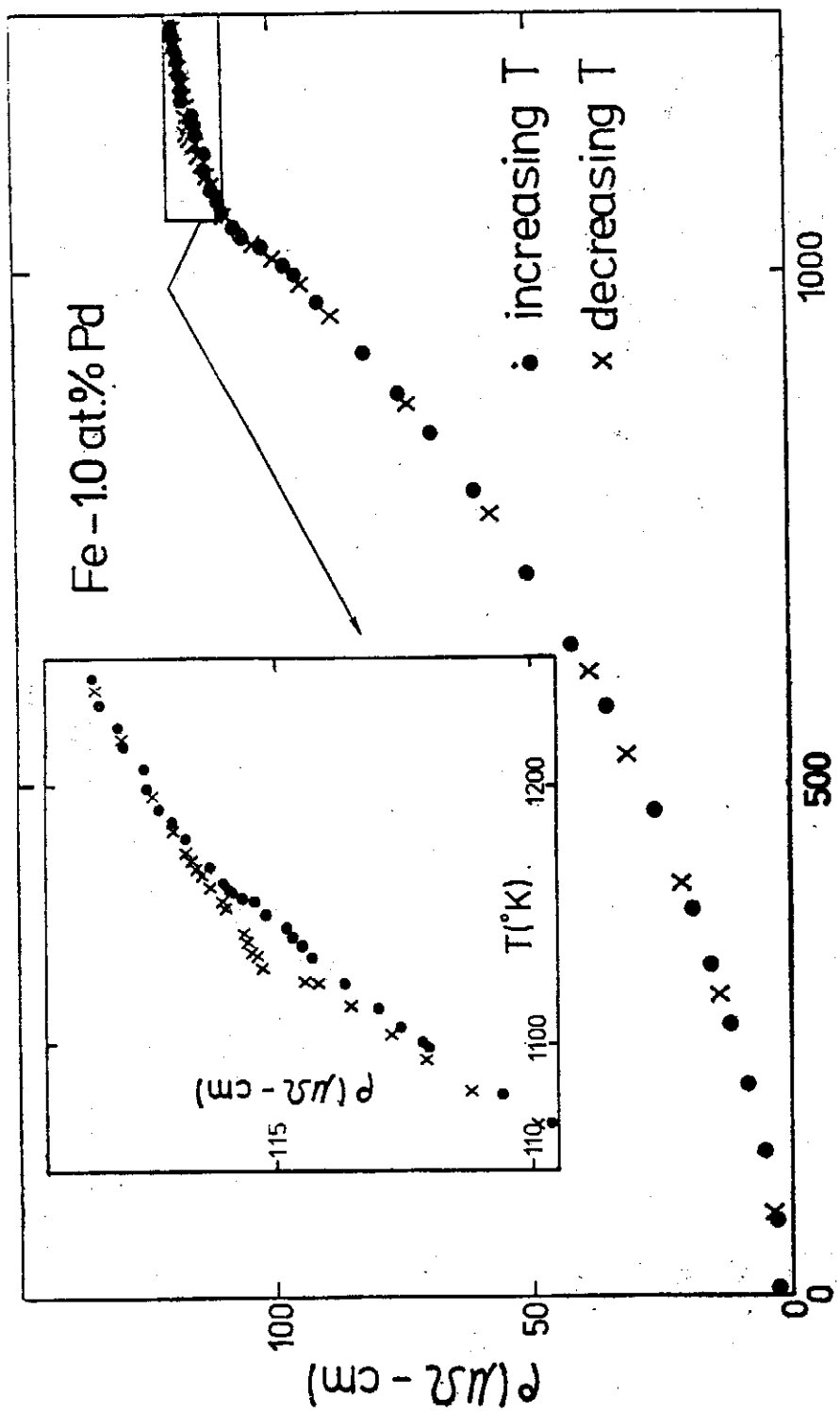

FIG. 2 (b) ρ vs T for Fe-1.0 at.% Pd.

of Pd in α-Fe was estimated from lattice-parameter data to be a few at.% Pd between 500 and 850°C[4]; and roughly speaking, it has been found to be less than 5 at.% Pd[5] or 7 at.% Pd[6]. This implies that in Fe-rich Fe-Pd system with higher

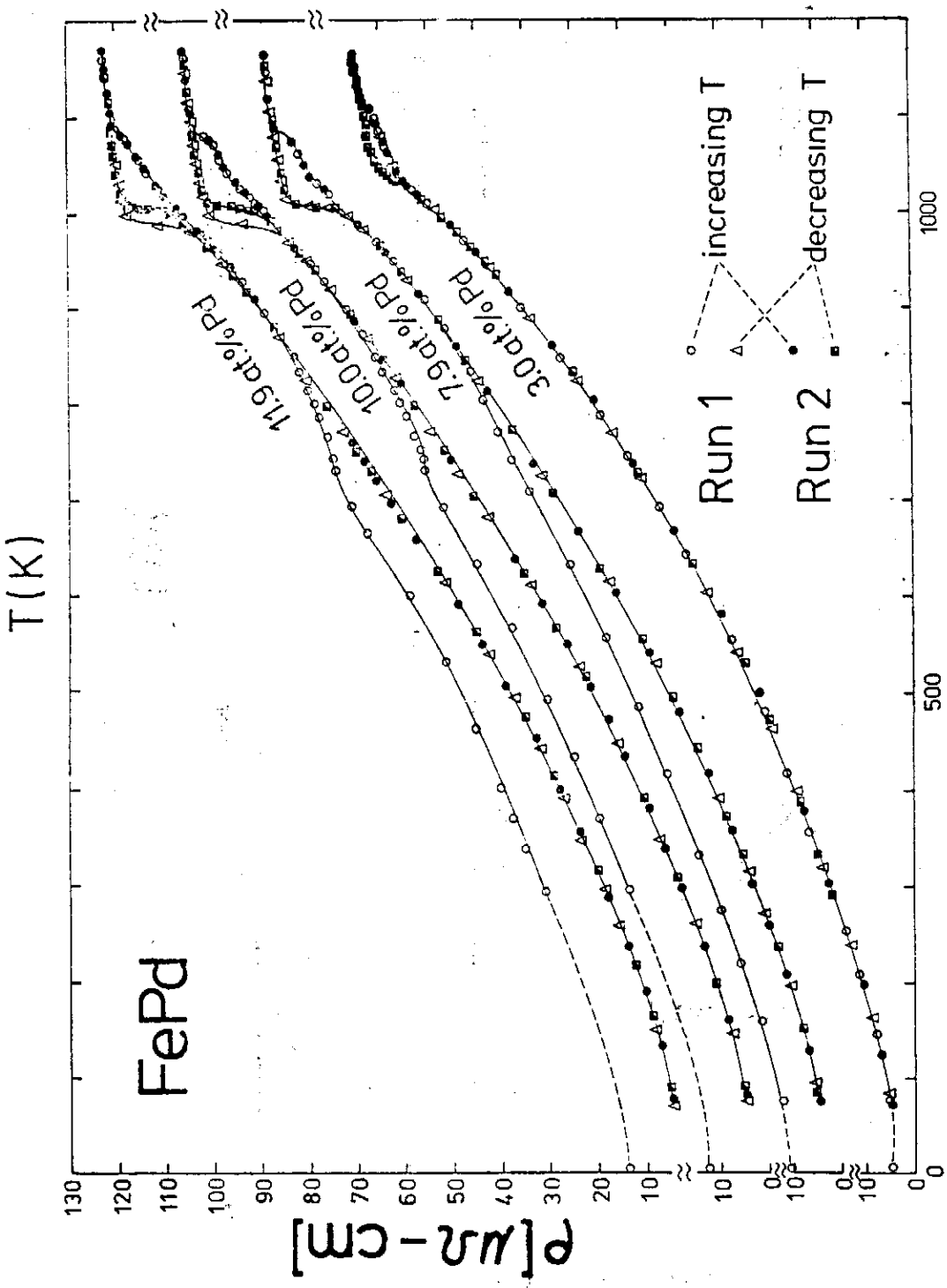

FIG. 2 (c) ρ vs T for Fe-Pd alloys containing 3.0, 7.9, 10.0 and 11.9 at% Pd.

Pd concentration, say 7.9 at.% Pd, palladium can be supersaturated or frozen in the system to form a metastable phase; and when the temperature is going up, palladium will gradually get enough energy to diffuse irreversibly to the atomi-

cally ordered stable state. According to the metallurgical phase diagram of the Fe-Pd system[4,5,6] in Fe-rich Fe-Pd samples with higher concentration of Pd, a number of pure Pd cluster may also be existed in the final stable state. This means that the value of the electrical resistivity of these alloys will be decreased when it is transformed from the atomically disordered metastable phase to the final stable state formed by the atomically ordered intermetallic compound of FePd as well as a few of Pd clusters.

In Fig. 2 (a) and (b), the dots represent the heating runs; crosses show the cooling runs. Besides the hystersis feature near the α-ν transition at high temperatures, the electrical resistivity data are completely matched between heating and cooling runs. We can clearly observe the change in the slope of the ρ vs. T curves due to the ferromagnetic-paramagnetic phase transition. The detailed temperature variation of the electrical resistivity in the neighborhood of the α-ν transition is shown in the insert figures of Fig. 2(a) and (b) for Fe-0.5 at.% Pd and Fe-1.0 at.% Pd, respectively. This two hysteresis features of the electrical resistivity are roughly extended about 26 K for Fe-0.5 at.% Pd and 34 K for Fe-1.0 at.% Pd. A drop in ρ going from ν phase to α phase is about 0.4% for Fe-0.5 at.% Pd and 0.7% for Fe-1.0 at.% Pd. Similar hysteresis feature of the electrical resistivity near the α-ν transition has also been observed in FeCo system by Seehra and Silinsky[7]. However, according to Arajs and Colvin[8], the electrical resistivity of high purity (99.99$^+$%) iron, which was zone-refined, increases by about 2% going from ν phase to α phase, and the hystersis feature is about 2 K near the α-ν transition temperature ($\sim$ 1183 K). Therefore, the behavior of the α-ν transition in Fe-based alloy system seems quite different from that in pure Fe.

Let us first consider the high temperature electrical resistivity. The electrical resistivity (ρ) can be expressed in terms of the electrical charge (e), an effective electron mass (m*), a relaxation time (τ) and the density of electron (n) as

$$\rho = m^*/ne^2\tau \propto 1/n\tau \qquad (1)$$

At high temperature, the relaxation time approximation holds good, because the change in electron energy at a collision is very much small than K_BT and collision are effectively elastic, where K_B is the Boltzmann constant. Under this situation, a classical approach can lead to a transition probability that is proportional to the mean square amplitude of the lattice vibrations ($\overline{x^2}$). Application of the theorem of equipartition of energy to the vibrating ions of mass (M) and frequency (f) then gives $4\pi^2f^2M\overline{x^2} = K_BT$. Therefore, if θ is a characteristic temperature defined by $hf = K_B\theta$, we have

$$\frac{1}{\tau} \sim \overline{x^2} = \frac{\hbar^2}{K_B} \frac{T}{M\theta^2} \qquad (2)$$

and therefore

$$\rho \propto \frac{T}{nM\theta^2} \qquad (3)$$

Eq. (3) can be used for a qualitative comparison of the different behavior of the electrical resistivity near the α-ν transition between pure Fe and Fe-based alloys. In pure iron system, the phonon spectrum should contain only the acoustical modes. A drop in ρ for very pure iron from α phase to ν phase as observed by Arajs and Colvin[8] indicates an jumped increase in θ as well as f. This means that the frequency of the vibrating Fe ions are increased by a jump from B.C.C. structure to F.C.C. structure. However, in iron-based alloys, because there are different kinds of atoms in the primitive cell, the phonon spectrum should contain both the acoustical and optical modes. Therefore, at the α-ν transition, the effect due to the optical modes can be larger than that due to the acoustical modes; and the result is a jumped drop in θ as well as in f from B.C.C. to F.C.C. iron. In other words, the electrical resistivity will show a jumped drop from ν phase to α phase, or a jumped increase from α phase to ν phase, for Fe-based alloys which contain the impurity above a critical concentration.

The difference in the electrical resistivity ($\Delta\rho$) going from B.C.C. to F.C.C. Fe at the α-ν transition is a negative value for pure Fe and is a positive values for Fe-based alloys. This suggests that $\Delta\rho$ should be a function of the impurities added to the iron-based system. Fig. 3 presents $\Delta\rho/\rho_{T\alpha}$ as a function of the Pd concentration, where $\rho_{T\alpha}$ is the electrical resistivity near T_α and T_α has been defined in a previous publication[1]. The solid curve in Fig 3 connects our experimental results with that due to Arajs and Colvin[8]. Two facts are obvious from this plot. First, the connecting from the positive values of $\Delta\rho/\rho_{T\alpha}$ for FePd system to the negative value of $\Delta\rho/\rho_{T\alpha}$ for pure Fe is a smooth curve and should be quite reasonable. Second, there exists a critical concentration (x_0) that the α-ν transition is not observable by the electrical resistivity measurement. According to Fig. 3, x_0 should be small than 0.5 at. % Pd in the Fe-rich Fe-Pd system.

For a quantitative analysis, the changes of n and M in Eq. (3), the previous thermal history of the sample, and the rate and direction of the temperature changes etc. must also be taken into account. Unfortunately, this is a very complicated problem and is difficult to analysis. Therefore, more experimental data are definitely necessary for doing any further quantitative analysis.

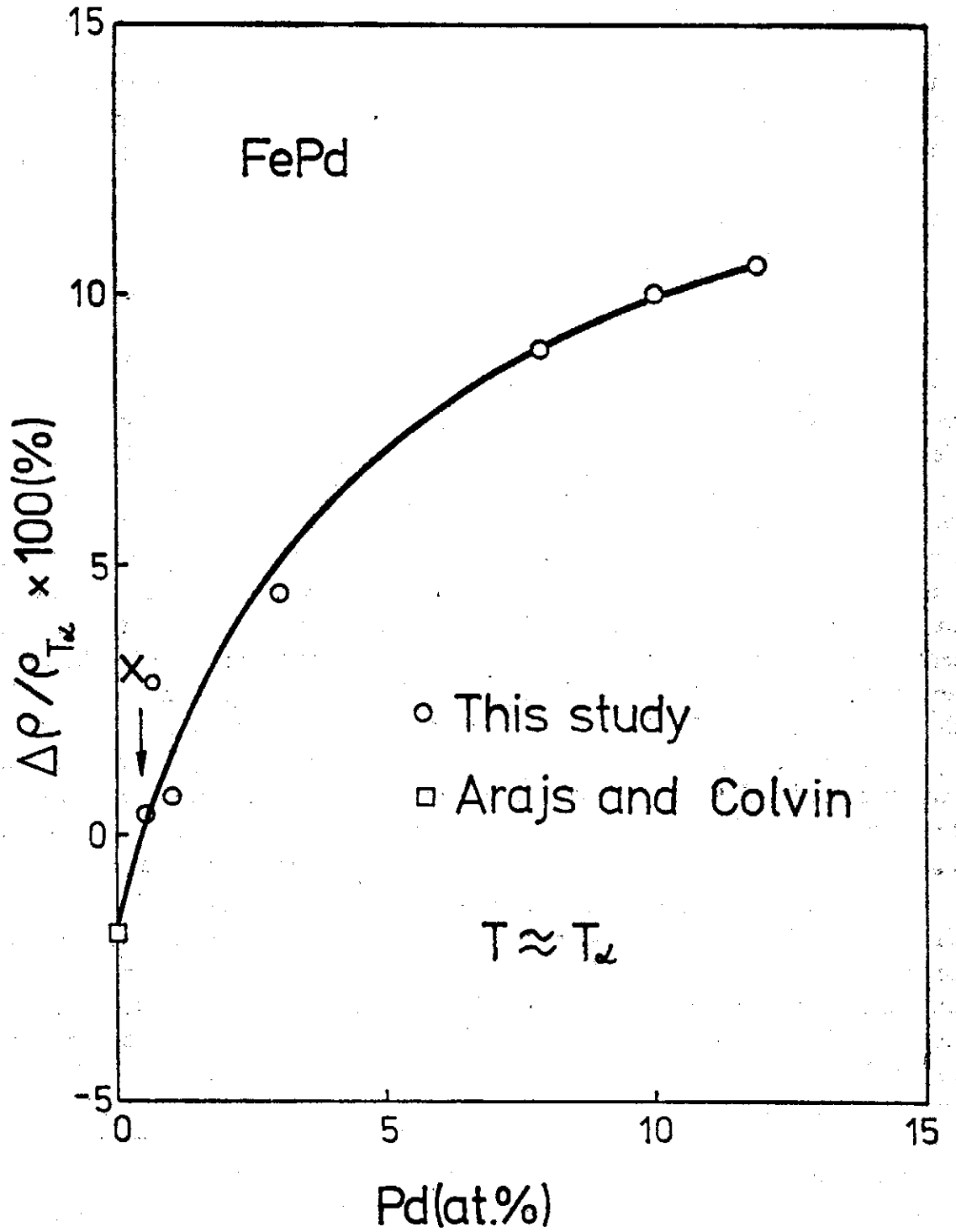

FIG. 3. Ratio of the difference in electrical resistivity of the FePd system near the α-ν transition as a function of the Pd concentration.

In Fig. 2(c), the circles and triangles present Run 1; the dots and squares present Run 2. For the Fe-3.0 at. % Pd sample, the highest temperature of Run 1 is not high enough to pass the α-ν transition, the electrical resistivity data are completely reproducible. Hawever, temperatures of Run 2 for the Fe-3.0 at. % Pd sample were going high enough to pass the α-ν transition; so that the hysteresis feature of the electrical resistivity near the α-ν transition were observed and as shown in Fig. 2(c). The detailed physical picture about the overlapping between magnetic and α-ν transition in Fe-3.0 at. % Pd and Fe-7.9 at. % Pd has been reported in the previous publication[1]. We have defined that T_α is the temperature below which the ν phase Fe is completely transformed to α phase Fe; and T_ν is the temperature above which α phase Fe is completely transformed to ν phase Fe. The electrical resistivity decrease from the ν phase to the α phase is roughly 4.5%, 9.0%, 10.0% and 10.5% for Fe-3.0 at. % Pd, Fe-7.9 at. % Pd, Fe-10.0 at. % Pd and Fe-11.9 at. % Pd, respectively. For the Fe-7.9 at. % Pd sample, we choose roughly the same rate of temperature changes ($\sim$ 0.5 K/min) between Run 1 and Run 2 in the neighborhood of the α-ν transition. It was observed that the hysteresis feature due to the α-ν transition as completely coincided between two runs. However, for the Fe-10.0 at.% Pd and Fe-11.9 at.% Pd samples, we let the rate of temperature changes in the heating runs of Run 1 and Run 2 to be the same, and choose the cooling rate of Run 1 ($\sim$ 1 K/min) to be approximately twice that of Run 2 ($\sim$ 0.5 K/min). The result is that the heating run part of the hysteresis feature for both Fe-10.0 at.% Pd and Fe-11.9 at.% Pd are completely coincided. But the cooling run parts of the hysteresis feature between two runs are not matched as shown in Fig. 2(c). This suggests that the value of T_α and T_ν can be slightly varied by the rate of temperature changes.

Fig. 4 shows the first temperature derivative of the electrical resistivity data of our Fe-Pd system with both increasing and decreasing temperatures between 400 and 1,200 K. The various type of points shown in Fig. 4 are associated with different heating or cooling runs as indicated in Fig. 4. Again, for clarity not all the data are presented. The slope changes associated with the shift of the electrical resistivity of these Fe-Pd samples containing 7.9, 10.0 and 11.9 at.% Pd are manifested roughly between 700 and 900 K as shown in Fig. 4 (b), (c) and (d). This has been explained by the transformation from the metastable phase to the stable state. The Curie temperature (T_c) is determined from these maxima in Fig. 4 with the characteristic of a gentle rise towards the maximum and a sharp drop just above the maximum. This is a typical $d\rho/dT$ variation near T_c for many ferromagnetic alloys. T_α and T_ν are determined from other maximum shown in Fig. 4 with the characteristic of a sharp increase just below the maximum and a sharp decrease just

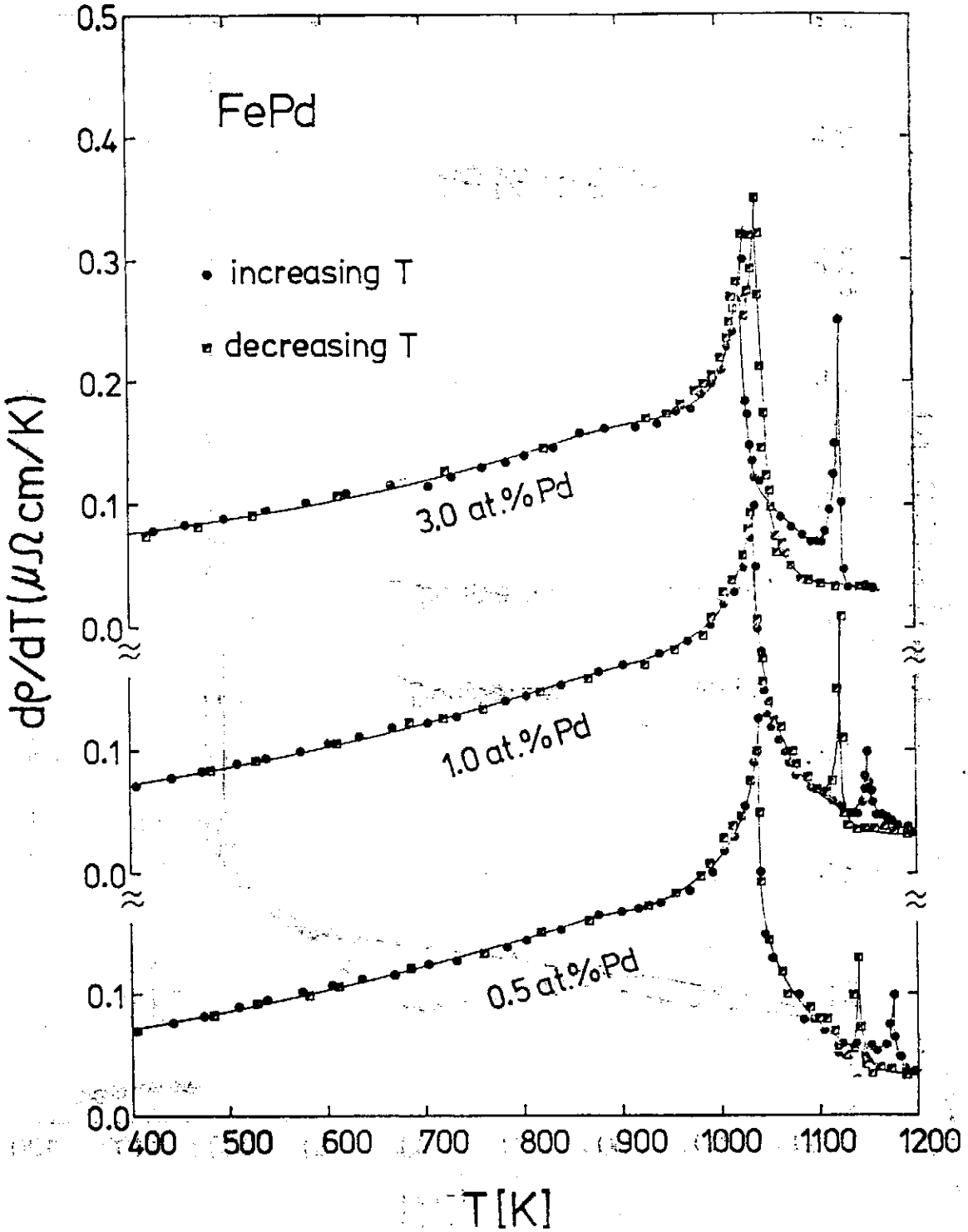

FIG. 4. First temperature derivative of the electrical resistivity of the FePd system as a function of temperatures between 400 and 1200 K.
(a) $d\rho/dT$ vs T for Fe-Pd alloys containing 0.5, 1.0 and 3.0 at.% Pd.

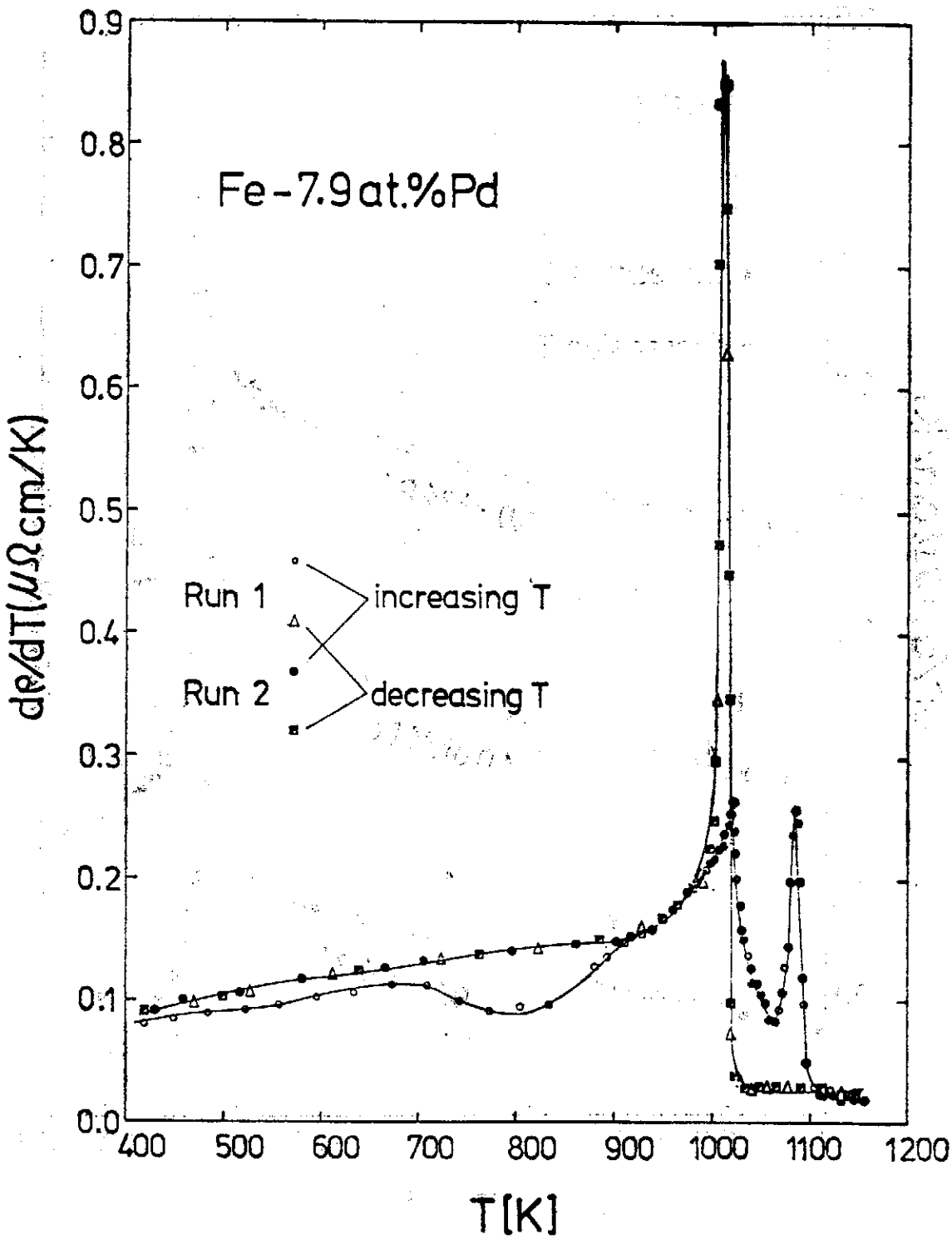

FIG 4. (b) $d\rho/dT$ vs T for Fe-7.9 at.% Pd.

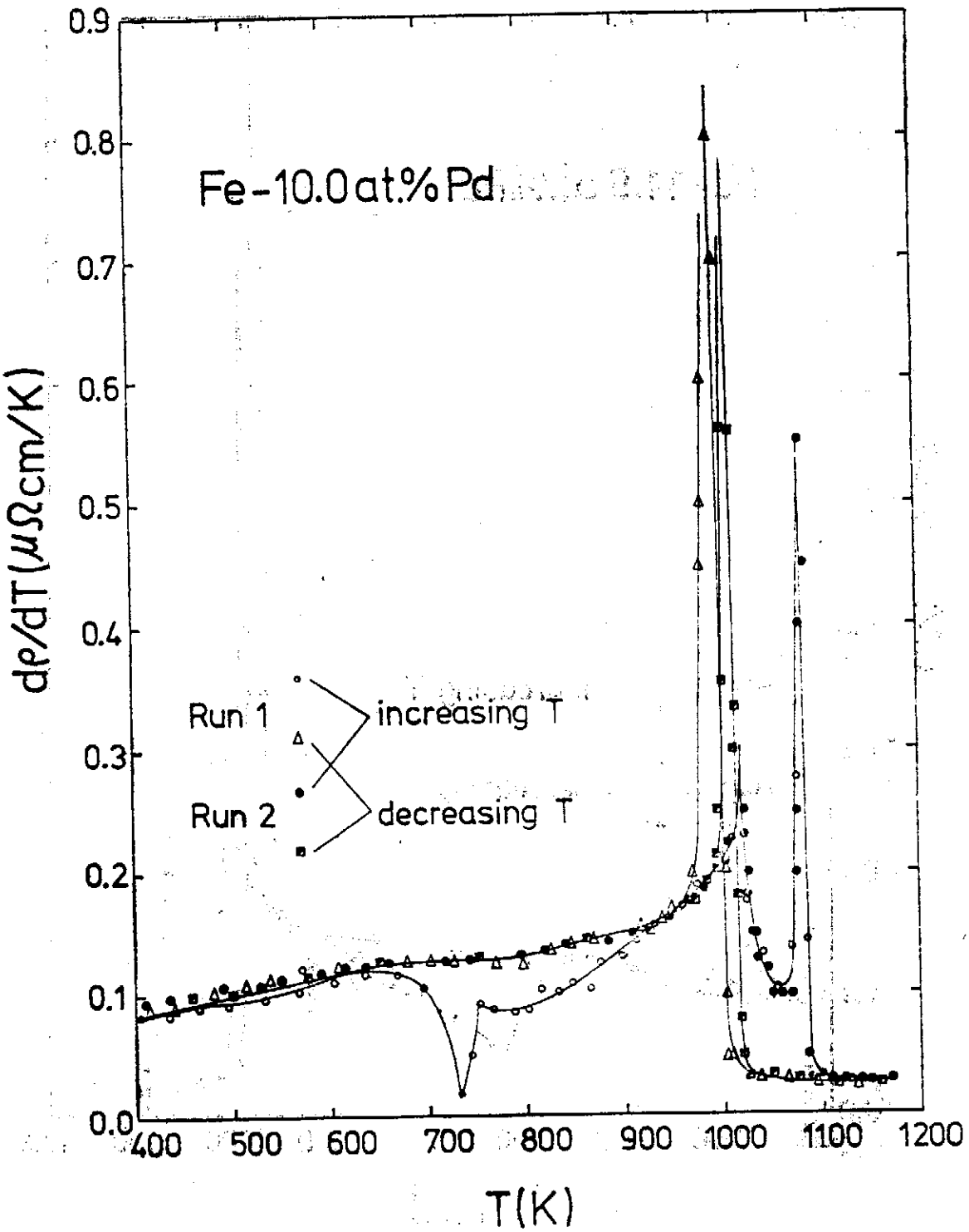

FIG. 4. (c) $d\rho/dT$ vs T for Fe-10.0 at.% Pd.

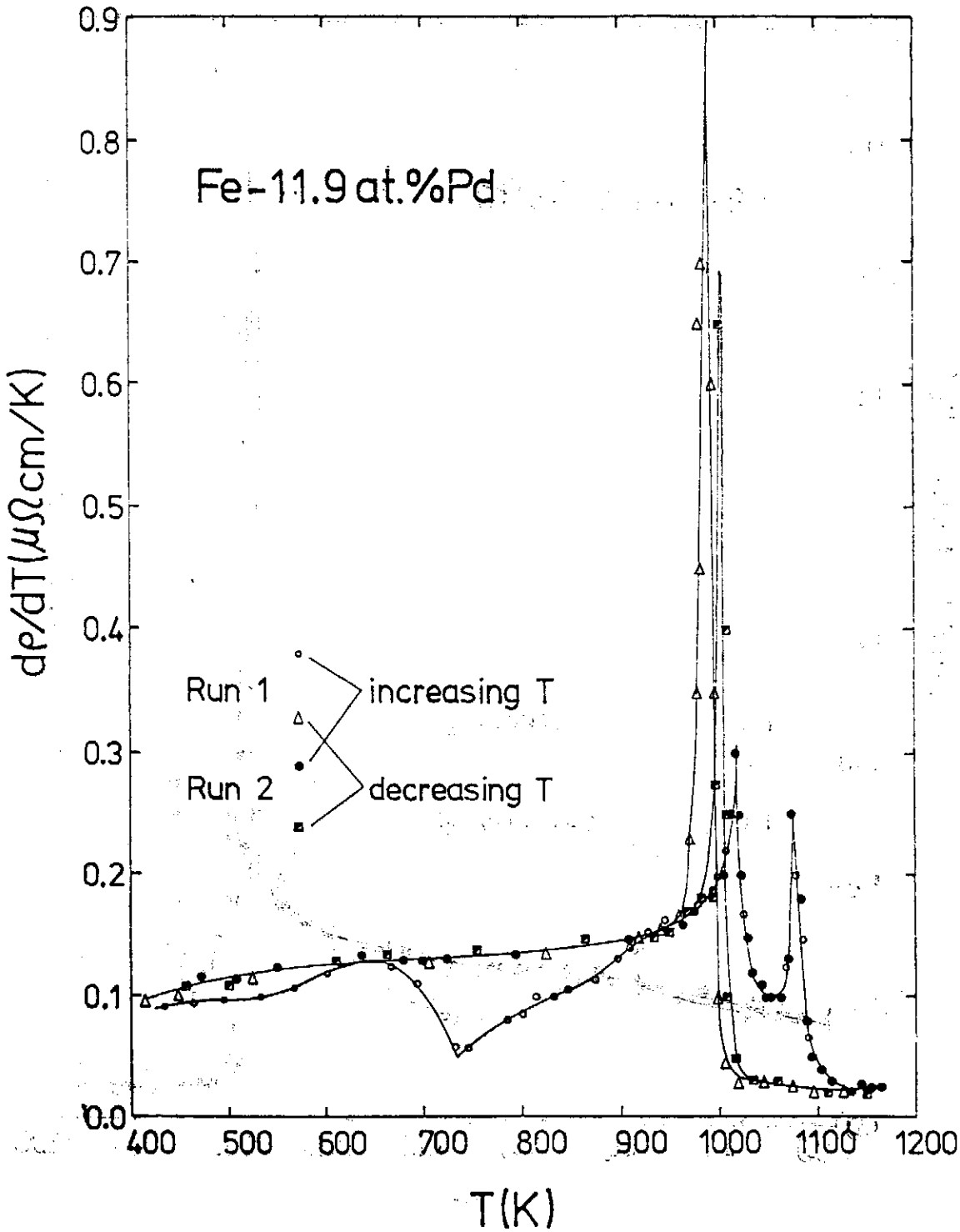

FIG. 4. (d) $d\rho/dT$ vs T for Fe-11.9 at.% Pd.

above the maximum. In table I all the T_c, T_a and T_v determined from Fig. 4 (a) to (d) are listed. The readings with an asterisk means obtained by the rate of temperature change roughly twice as that of the non-asterisk.

In the analysis of the experimental results near the ferromagnetic phase transition, it is convenient to fit the experimental electrical resistivity data to the following equations:

$$\frac{d\rho}{dT} = \frac{A^+}{\lambda^+}(\varepsilon^{-\lambda^+}-1)+B^+ \quad \text{for } T > T_c \tag{4}$$

$$\frac{d\rho}{dT} = \frac{A^-}{\lambda^-}(\varepsilon^{-\lambda^-}-1)+B^- \quad \text{for } T < T_c \tag{5}$$

where $\varepsilon = |T-T_c|/T_c$; A^+, A^-, B^+ and B^- are constants; and λ^+, λ^- are the critical exponents. In the limit $\lambda^+ \to 0$ and $\lambda^- \to 0$, these equations represent a logarithmic divergence. For pure iron, the presently available values of λ^+ and λ^- are not consistent yet. As an example, Nagy and Pál[9] reported that $\lambda^+ \approx 0.4 \pm 0.1$ for $10^{-3} \leq \varepsilon \leq 3.3\times10^{-3}$; but according to Kraftmakher et al[10, 11], $\lambda^+ \approx \lambda^- \approx 0 \pm 0.1$; and using an AC technique, Shacklette[12] reported that $\lambda^+ \approx \lambda^- \approx -0.120 \pm 0.01$.

As to the binary iron alloy systems, the value of λ^+ in Fe-rich FeV system[13], for $3.7\times10^{-3} \leq \varepsilon \leq 1.4\times10^{-2}$, has been determined as a function of V concentration. However, the value of λ^+ in Pd-rich Pd-Fe system[14] is quite insensitive to the iron concentration. It is reported that the critical behavior of Pd-rich Pd-Fe system scales with T_c. Basing on the above situation, it is difficult to propose a model which would clarify the critical behavior in binary iron alloy systems.

The study of the critical exponents λ^* requires very accurate electrical resistivity measurements, because small deviation will make strongly influence the determined values of critical exponents. Even our data are not accuracy enough to analyze both λ^- and λ^+, for comparison purpose, we have done our best to computer the $d^2\rho/dT^2$ values from our heating run data to analyze λ^+. The results are shown in Fig. 5 as log-log plots of $-d^2\rho/dT^2$ vs. ε for $3.7\times10^{-3} \leq \varepsilon \leq 1.4\times10^{-2}$. This $d^2\rho/dT^2$ computer generate data shown in Fig. 5 show approximately straight lines. The slope of these straight lines should be equal to $-(\lambda^+ + 1)$ and gives the value of λ^+. We list these values of λ^+ found from Fig. 5 in table I. The values of λ^+ are fluctuated roughly between $+0.3\pm0.2$ and -0.2 ± 0.2. This suggests that there seems to be very little dependence of the critical exponent λ^+ on the Pd concentration in Fe-rich Fe-Pd system, even λ^+ is still a function of the Pd concentration. Further studies about the critical behavior in pure Fe and binary Fe alloys using more

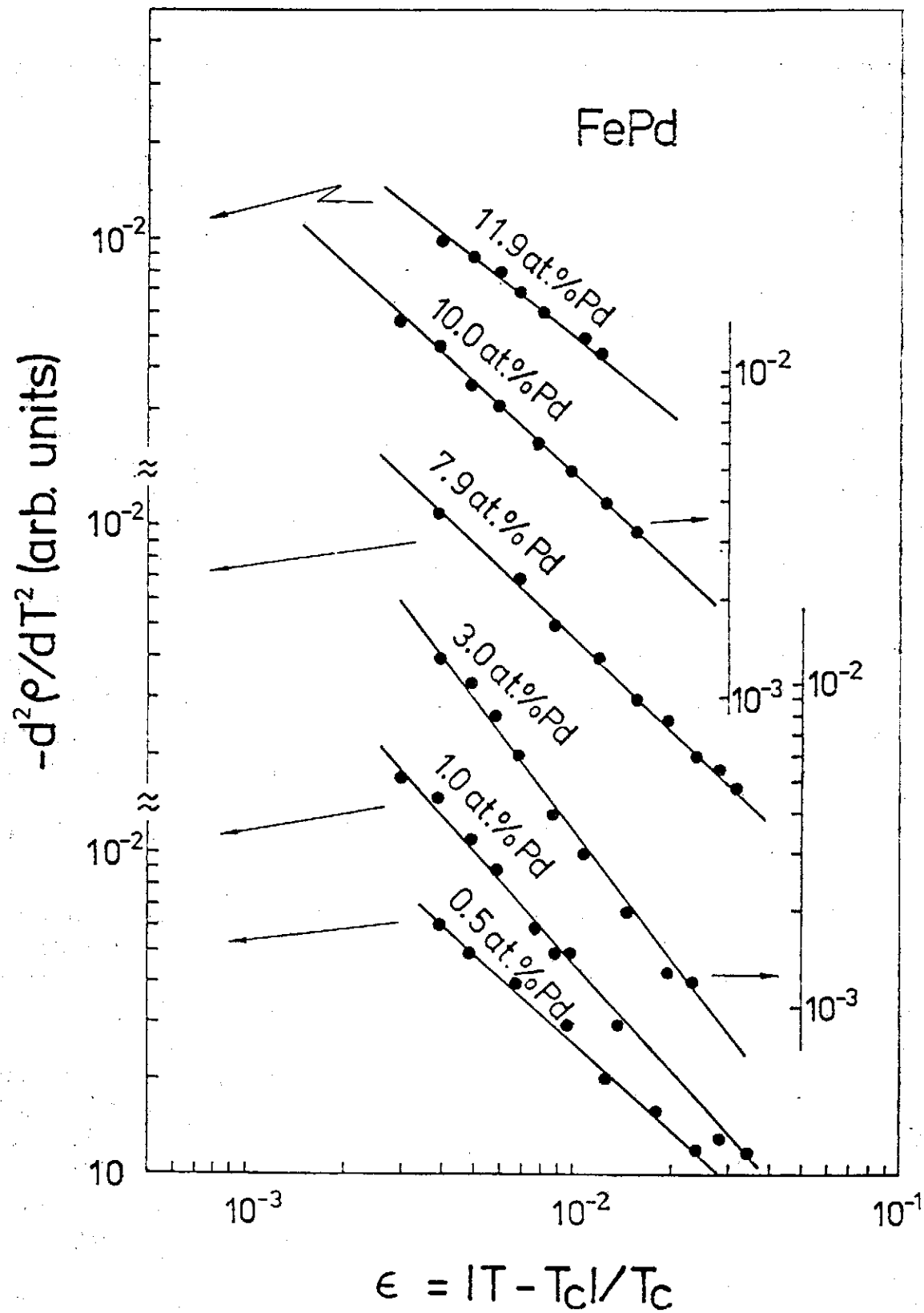

FIG. 5. Second temperature derivative of the electrical resistivity of the FePd system as a function of reduced temperature interval above T_c.

accurate experimental techniques such as the Direct Current Comparator method[15] etc. are definitely necessary.

TABLE I: T_c, T_α, T_γ and λ^+ of the Fe-Pd alloys

at.% Pd	T_c(K)	T_α(K)	T_γ(K)	λ^+
0.5	1040±1	1140±1	1174±1	−0.1±0.2
1.0	1036±1	1125±1	1151±1	+0.1±0.2
3.0	1028±1	1042±1	1123±1	+0.3±0.2
7.9	1022±1	1012±1	1085±1	−0.1±0.2
10.0	1020±1	1006±1 *991±1	1081±1	−0.1±0.2
11.9	1018±1	1004±1 *990±1	1075±1	−0.2±0.2

* Obtained with twice the rate of temperature change of the non-asterisk reading.

Acknowledgement: One of us (Y.D.Y.) is grateful to the National Science Council, R.O.C. for the financial support of this work.

REFERENCES

(1) Y. D. Yao and S. Arajs, Phys. Stat. Sol. (a) **55,** K201 (1979).
(2) S. Arajs, Phys. Stat. Sol. **15,** 501 (1966).
(3) H. S. Chen and Y. Waseda, Phys. Stat. Sol. (a) **51,** 593 (1979).
(4) M. Hansen and K. Anderko, *Constitution of Binary Alloys,* 2nd. edition, (McGraw-Hill, New York, 1958) p. 696
(5) R. P. Elliott, *Constitution of Binary Alloys, First Supplement,* (McGraw-Hill, New York 1965) p. 427
(6) F. A. Shunk, *Constitution of Binary Alloys, Second Supplement,* (McGraw-Hill, New York 1969) p. 340
(7) M. S. Seehra and P. Silinsky, Phys. Rev. **B13,** 5183 (1976).
(8) S. Arajs and R. V. Colvin, Phys. Stat. Sol. **6,** 797 (1964).
(9) I. Nagy and L. Pal, J. Physique Cl, Suppl. 2-3, **32,** 531 (1971).
(10) Ya. A. Kraftmakher and T. Yu Romashina, Soviet Phys. Solid State **9,** 1459 (1967).
(11) Ya. A. Kraftmakher and T. Yu. Pinegina, Soviet Phys. Solid State **16,** 78 (1974).
(12) L. W. Shacklette, Phys. Rev. **9,** 3789 (1974).
(13) W. Teoh, S. Arajs, D. Abukay and E. E. Anderson, J. Magnetism Magnetic Mat. **3,** 260 (1976).
(14) M. P. Kawatra, S. Skalski, J. A. Mydosh and J. I. Budnick, J. App. Phys. **40,** 1202 (1969).
(15) N. L. Klusters and M. P. MacMartin, Trans. IEEE **IM-19,** 219 (1970).

ELECTRICAL RESISTIVITY OF AMORPHOUS $Fe_{80}B_{20-x-y}Si_xC_y$ ALLOYS

Y. D. YAO (姚 永 德)
Institute of Physics, Academia Sinica
Nankang, Taipei, 115, R.O.C.

S. ARAJS
Department of Physics, Clarkson College of Technology
Potsdam, N.Y. 13676, U.S.A.

and

S. T. LIN
Department of Physics, Cheng Kung University
Tainan, Taiwan, 700, R.O.C.

Abstract

Electrical resistivity (ρ) of metallic glasses $Fe_{80}B_{20}$, $Fe_{80}B_{18}Si_2$ and $Fe_{80}B_{13}Si_4C_3$ has been measured as a function of temperature (T) between 15 and 300 K. The temperature dependence of the resistivity is linear for $120 \leq T \leq 300$ K and quadratic for $20 \leq T \leq 100$ K. This is explained by an extension of the theory of resistivity for liquid transition metals.

INTRODUCTION

In recent years amorphous ferromagnetic alloys have been a subject of considerable interest. These metallic glasses are typical examples of relatively high electrical resistivity metallic systems which can be considered as a category between crystalline metallic and semiconducting types of conductivity. A number of mechanisms have been used to explain the behaviors of these systems. Examples are break-down of the Boltzman equation[1], electron localization[2], multiple-scattering effects[3], the diffraction model[4], Debye-Waller factor calculation[5, 6] and modified relaxation time technique[7]. The temperature dependence of the resistivity in metallic glasses has been studied in a variety of systems, such as $Fe_xNi_{80-x}P_{14}B_6$[8], $Fe_{40}Ni_{40}P_{14}B_6$[9] Ni-P[10, 11], (Fe, Co or Ni)$_{1-x}Au_x$[12], Nb-Ni[13] and Fe-B[14] etc.. It is of great interest to see if these properties are also found in other systems of amorphous materials. The present paper deals with this subject in the Fe-B-Si-C system. Our experimental results are briefly described below. This is just a beginning of our systematic investigations about the temperature dependence of the resistivity in metallic glasses.

EXPERIMENTAL CONSIDERATION

The glassy metallic alloys used in this study were prepared by the technique of solidifying a stream of molten metal against the outside of a rapidly rotating

copper drum[15]. The resistivities of three Fe-B-Si-C alloys (i.e. $Fe_{80}B_{20}$, $Fe_{80}B_{18}Si_2$ and $Fe_{80}B_{13}Si_4C_3$) were measured between 15 and 300 K using the conventional four-point probe technique. The samples were roughly in a form of ribbon 1-2 mm wide, 20-40 μm thick and 1-2 cm in length. Four copper electrodes were lightly spot welded to each sample, the two central electrodes being used as potential leads and the other two as current leads.

Temperatures between 15 and 300 K were achieved in a Displex closed-cycle refrigeration system (model CS-202, Air Products and Chemicals). The temperature was controlled by a proportional plus rate cryogenic temperature controller (model 3610, Air Products and Chemicals). The short term stability of this temperature controller is within ± 0.01 K and long term stability is within ± 0.1K. Two temperature sensors were placed beneath and above the sample and the average of the readings was assumed to be the temperature of the sample. A d.c. current was maintained constant to about one part in 10^5 and the voltage was measured with an accuracy to a few nanovolts. A GE adhesive (No. 7031) or the equivalent was used between the sample and a large copper base of good conductivity to ensure electrical insulation and good thermal conduction.

RESULTS AND DISCUSSION

Figure 1 shows the electrical resistivity of the three amorphous samples

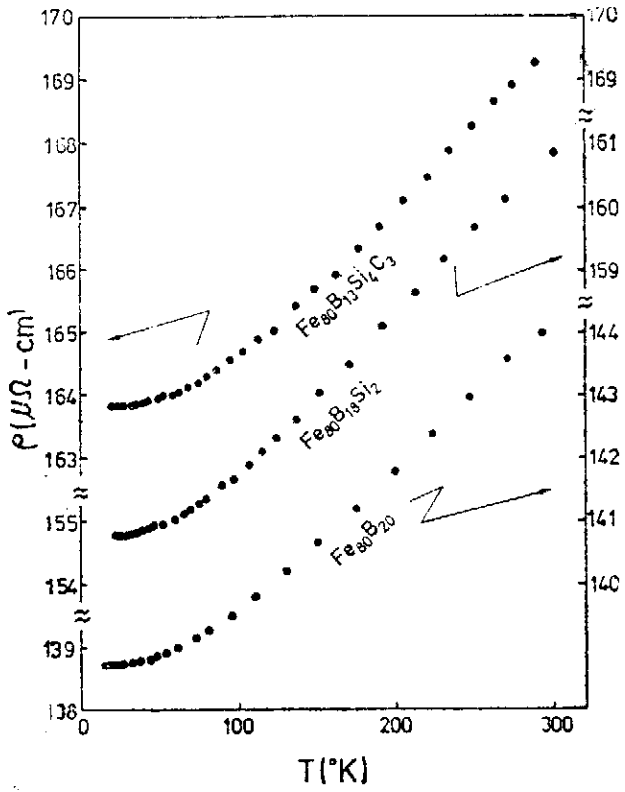

FIG. 1. Electrical resistivity of $Fe_{80}B_{20}$, $Fe_{80}B_{18}Si_2$ and $Fe_{80}B_{13}Si_4C_3$ between 15 and 300 K.

($Fe_{80}B_{20}$, $Fe_{80}B_{18}Si_2$ and $Fe_{80}B_{13}Si_4C_3$) between 15 and 300 K. The value of the electrical resistivity is found to be increased when silicon and/or carbon atoms are substituted for some boron atoms in the $Fe_{80}B_{20}$ system. Unfortunately, owing to the limitation of our closed cycle refrigeration system, our measurements do not extend to low enough temperatures to observe the resistivity minimum. According to Rayne and Levy[9], the temperature to occur resistivity minimum is about 14 K. No electrical resistivity minimum was observed above 15 K in our three samples, we conclude that electrical resistivity minimum should be below 15 K for $Fe_{80}B_{20}$, $Fe_{80}B_{18}Si_2$ and $Fe_{80}B_{13}Si_4C_3$ systems, if it is existed.

The normalized electrical resistivity ρ/ρ_{300}, where ρ_{300} is the value of ρ at 300 K, as a function of T is shown in Fig. 2. The temperature dependence of electrical resistivity has a linear T dependence between 120 and 300 K. The temperature coefficient of electrical resistivity $\alpha=\rho^{-1}(d\rho/dT)$ as a function of the concentration of Si and C is presented in Fig. 3. It can be seen that α is positive and approximately independent on the concentration of Si and C. The bars in Fig. 3 represent the experimental error limitation. At temperatures roughly between 20 and 100 K the electrical resistivity shows an approximately quadratic temperature dependence, as can be seen from Fig. 4.

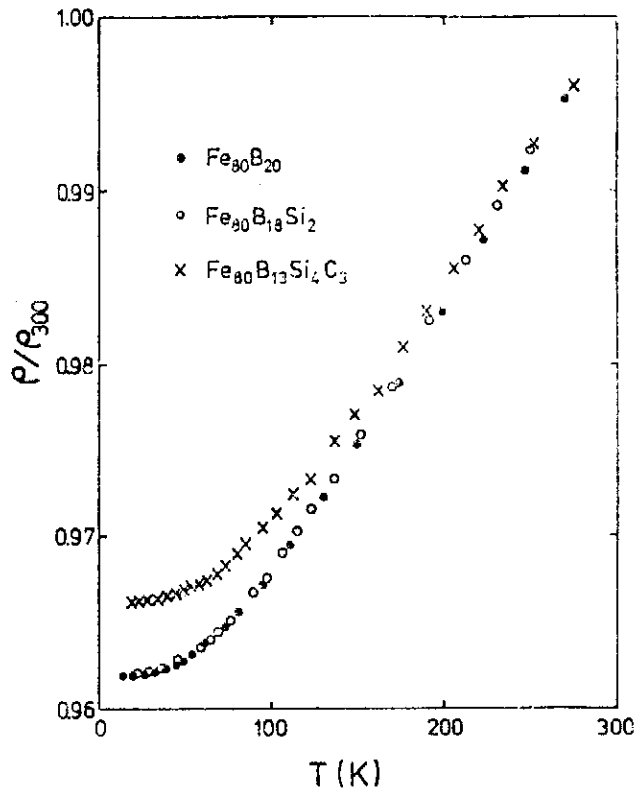

FIG. 2. Normalized electrical resistivity of $Fe_{80}B_{20}$, $Fe_{80}B_{18}Si_2$ and $Fe_{80}B_{13}Si_4C_3$ as a function of temperature.

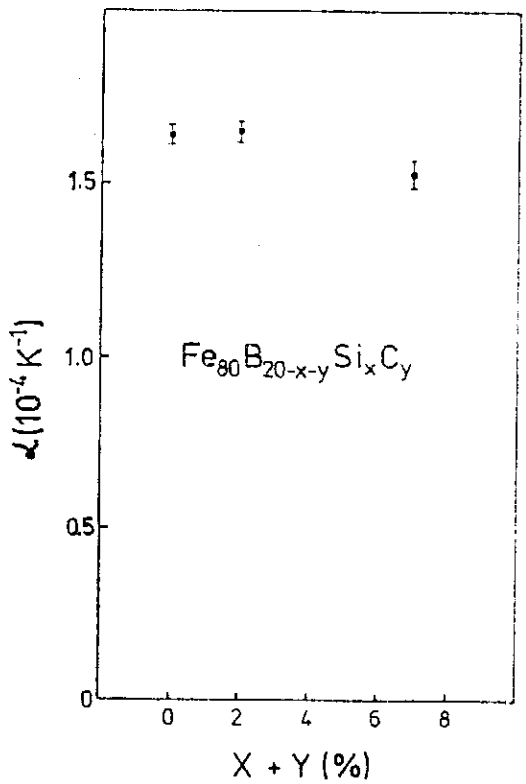

FIG. 3. Temperature coefficient of electrical resistivity in the linear T region ($120 \leq T \leq 300$ K)

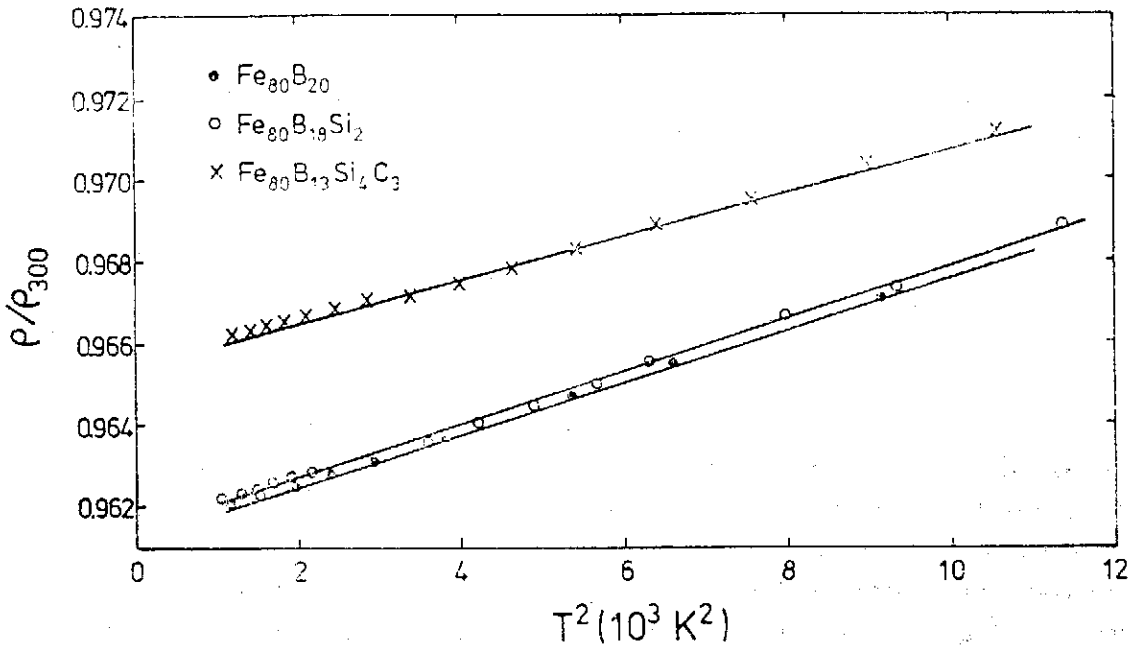

FIG. 4. Normalized electrical resistivity Versus T^2 between 20 and 100 K.

The T and T^2 dependence of electrical resistivity we have reported in Fe-B-Si-C system is in qualitative agreement with predictions of recent theoretical models based on extensions of the theory of resistivity for liquid metals[4,6]. Following the same argument for the Fe-B system[14], and letting Z be the number of electrons per atom contributing to conduction. The value of Z for the $Fe_{80}B_{20-x-y}Si_xC_y$ system is $Ze = 0.8\,Z_{Fe} + Z_B(20\text{-}x\text{-}y)/100 + Z_{Si}(x/100) + Z_C(y/100)$. Since Si and C are poor conductors, at temperatures below room temperature; and based on the increasing of the electrical resistivity by substituting Si and C for B in the $Fe_{80}B_{20}$ system, we conclude that $0 \leq Z_{Si}, Z_C \leq 1$. Finally, it is concluded that $Ze \leq 1$ with likely values of $Z_{Fe} \leq 1$ and $0 \leq Z_B$, Z_{Si} and $Z_C \leq 1$.

In summary, our experimental data further support the conclusion made from the Fe-B system[14]. Further systematic investigations on a variety of glassy systems are now in progress in our laboratories and will be reported later.

Acknowledgements: We thank Dr. Ho, Miss Shyong, Mr. Ueng and Mr. Young for experimental assistance.

REFERENCES

(1) P. B. Allen, Phys. Rev. Lett. **37,** 1638 (1976).
(2) K. L. Chopra, A. P. Thakoor, S. K. Barthwal and P. Nath, Phys. Stat. Sol. **A40,** 247 (1977).
(3) R. Harris, M. Shalmon and M. Zuckermann, J. Phys. F. **7,** L259 (1977).

(4) P. J. Cote and L. V. Meisel, Phys. Rev. Lett. **39,** 102 (1977); **40,** 1586 (1978) and Phys. Rev. **B20,** 3030 (1979).
L. V. Meisel and P. J. Cote, Phys. Rev. **B17,** 4652, (1978).
(5) D. Markowitz, Phys. Rev. **B15,** 3617 (1977).
(6) S. R. Nagel, Phys. Rev. **B16,** 1694 (1977).
(7) J. Krempasky, J. Vajda, A. Zentko and P. Duhaj, Phys. Stat. Sol. **A52,** 387 (1979).
(8) E. Babic, Z. Marohnic and J. Ivkov, Solid St. Comm. **27,** 441 (1978).
(9) J. A. Rayne and R. A. Levy, Amorphous Magnetism, Vol. 2, Ed. R. A. Levy and R. Hasegawa, Plenum Press, N.Y. 1977 (p. 319).
(10) L. V. Meisel and P. J. Cote, Phys. Rev. **B15,** 2970 (1977).
(11) A. Berrada, M. F. Lapierre, B. Loegel, P. Panissod and C. Robert, J. Phys. **F8,** 845 (1978).
(12) G. Bergmann and P. Marquardt Phys. Rev. **B17,** 1355 (1978).
(13) S. R. Nagel, J. Vassiliou, P. M. Horn and B. C. Giessen, Phys. Rev. **B17,** 462 (1978).
(14) A. Mogro-Campero and J. L. Walter, Phys. Rev. **B20,** 5030 (1979).
(15) H. H. Lieberman and C. D. Graham Jr., IEEE Tran. Magn. MAG-12, 921 (1976).

ON THE CONCEPT OF NEGATIVE CORRELATION ENERGY AND PROCESS OF DEFECT FORMATION IN CHALCOGENIDE GLASSES

CHUN CHIANG (蔣 听 儻)

Institute of Physics Academia Sinica
Nankang, Taepei, Taiwan, Republic of China

Abstract

The concept of negative correlation energy is criticized and a process of defect formation is proposed to explain the fact that no EPR signals are observed in chalcogenide glasses.

Recently, intensive research has been carried out in amorphous thin film. Considerable progress in controlling the conductivity of tetrahedrally bonded amorphous thin film has been made, however, so far it is not yet possible to controll the conductivity of chalcogenide amorphous this film. Other differences of properties between these two types of amorphous thin films are: EPR signals are observed in a-Si but not in chalcogenide glass, d.c. conductivity at low temperature varies according to $T^{1/4}$ for a-Si and a-Ge film but varies according to $e^{-E/KT}$ for chalcogenide glasses.

Anderson[1] has proposed that the effective interaction between a pair of electrons in the same site can be attractive because of coupling to atomic motion, therefore can explain the fact that no EPR signals are observed in chalcogenide glasses. This attraction is the effective negative correlation energy resulting from the polaron energy gained by the contraction of a bond more than compensates for the electron repulsion. Street and Mott[2] further apply this idea to point defects, they also assume that local lattice distortion occurs when the electron occupation of the dangling bond changes and that it is sufficiently strong for the reaction

$$2D^0 \rightarrow D^+ + D^- \qquad (1)$$

to be exothermic. The lattice distortion they proposed is that D^+ can attract and distort the neighoring lone pair to form a bond, a large electronic energy is released thus eq. (1) is exothermic, and the states exist an effective electron-electron correlation energy. Kastner et al[3] and Fritzshe[4] further propose the valence alternation pair to account for the states in eq. (1). They find that the lowest energy defect states are C_3^+ and C_1^-, and C_3^0 is unstable because

$$2C_3^0 \rightarrow C_3^+ + C_1^- \qquad (2)$$

is exothermic with an energy gain of negative effective correlation energy. The reaction for the first electron lifted from C_1^- to conduction band is

$$C_1^- \rightarrow C_3^0 + e \qquad (3)$$

and for the second electron lifted to the conduction band is

$$C_3^0 \rightarrow C_3^+ + e \qquad (4)$$

and they assert that reaction(4) takes less energy than reaction(3), namely, it takes less energy to excite the second electron than the first electron to the conduction band, and this is the negative effective correlation energy. With this kind of negative effective correlation energy, Okamoto and Hamakawa[5], Adler and Yoffa[7] and Shimizu[6] made some quantitative calculation.

However, this kind of negative effective correlation is misleading and not very fruitful, the reasons for objection are:

(1) for the same atom, it always takes more energy to excite the second electron than the first electron.

(2) If after exciting the first electron, the atom interact with the environment to raise the energy of the second electron, then it may be possible to excite the second electron with less energy. But, if the atom is interacting with the environment to raise the energy of the second electron, it should also interact with the environment to raise the energy of the first electron, therefore, there is still no reason for the second electron to be excited to the conduction band with less energy than the first electron.

For example, eq. (3) and eq. (4) should really be written as

$$C_1^- \rightarrow C_1^0 + e \qquad (5)$$

$$C_1^0 + \text{energy} \rightarrow C_3^0 \qquad (6)$$

$$C_3^0 \rightarrow C_3^+ + e \qquad (4)$$

Then it can be seen that it takes less energy to excite electron in eq. (4) than in eq. (5), the reason is that energy has been supplied in eq. (6), since the energy is supplied by the interacting neighbor, this neighbor should also supply the energy to C_1^- in eq. (5) to raise the energy of the first electron, thus it should take less energy to excit the eletron. Thus the concept of negative effective correlation energy could not be true.

(3) It could be true that D^+ state and D^- state prevailes in the film, however, the D^- state is the result of electrons in the system to move from other high energy places to this low energy defect locations, not the result of so called negative effective correlation energy at this defect location. Realization of this point is very important to understand the electron process in chalcogenide glasses.

To propose a new mechanism without using negative correlation energy, we assume that in the chalcogenide glasses, there are defects of dangling bonds. The formation of these is due to the fact that the atomic configuration is either to loose or to tight (stress) for the formation of regular bond in amorphous film. Thus there is a distribution of energy of dangling bonds. Also, due to irregular configuration, there are interactions between two lone pair or between lone pair and dangling bonds, thus, there are defects such as:

$$\text{Bonds with large stress} \rightarrow \text{dangling bonds} \tag{7}$$

$$C_2\text{: (lone pair)} + C_2\text{: (lone pair)} \rightarrow C_2^{+} - C_2^{+} + 2e \tag{8}$$

$$C_2\text{: (lone pair)} + \dot{C}_1\text{: (dangling bond)} \rightarrow C_2^{+} - \ddot{C}_1 + e \tag{9}$$

Thus, in the chalcogenide glasses, there are C_1^0 (dangling bonds), C_2^0, C_3^+ and free electrons. These free electrons should move to lowest energy states available, which are the dangling bonds, thus

$$C_1^0 + e \rightarrow C_1^- \tag{10}$$

Thus, there are defects such as C_1^- and C_3^+. This explains the formation of defects and the reason for not being able to observe the EPR signals without using the concept of negative effective correlation energy. The explaination of other experimental facts will be reported soon.

REFERENCES

(1) Anderson, P. W. Phys. Rev. Lett. **34,** 953 (1975).
(2) Street, R. A. and Mott, N. F., Phys. Rev. Lett. **35,** 1293 (1975).
(3) Kastner, M. Adler, D. and Fritzsche, H., Phys. Rev. Lett. **37,** 1504 (1976).
(4) Fritzsche, H., Chinese J. Phys. **15,** 74
(5) Okamoto, H. and Hamakawa, Y., Solid State Communications, **24,** 23 (1977).
(6) Shimizu, T., Jap. J. Appl. Phys. **17,** 463 (1978).
(7) Adler, D. and Yoffa, E. J. Phys. Rev. Lett. **36,** 1197 (1976).

A SIMPLE METHOD TO STUDY THE IONIC CONDITION OF MUSCLE

WEI KUNG WANG (王 唯 工)

Biophysics Laboratory, Institute of Physics, Academia Sinica
Taipei, Taiwan, Rep. of Chmia

Abstract

We have suggested that the isolated muscle cell can not be in a steady inoic state due to the active transport. A simple method was deviced to study the ionic condition in muscle.

The denervated muscles as well as the normal muscles extract was separated from the debris by centrifuging the homogenate. The debris was heated in oven at 80°C to get the dry weight and the supernatant was diluted appropriately to measure the $[Na^+]$ and $[K^+]$ concentrations with the flamephotometer. We could get the total weight of extar- and intracellular solutions by substracting the dry weight from the total muscle weight. We could then calculate the $[K^+]$ and $[Na^+]$ in muscle (including intracellular and extracellular). Therefore, no matter how the extracellular/intracellular ratio varies, we can express the relation between $[Na^+]$ and $[K^+]$ as following:

$$[Na^+] - I_{Na} = \frac{(E_{Na} - I_{Na})}{(E_K - I_K)} ([K^+] - I_K)$$

If we plot $[Na^+]$ against $[K^+]$, we can get a straight line.

In our result we found that the K^+ and Na^+ in normal muscle were near the line. However, the K^+ and Na^+ in the denervated muscle were not around the line. It implied that apart from the atrophy as would be seen easily, the ionic condition in the denervated muscle cell had also change.

INTRODUCTION

To study the ionic condition inside cells is not easy. There are some development on ion-sensitive microelectrode[1], however, it can only be applied to those large cells that can be penetrated safely by the microelectrode.

Recently, we have suggested that isolated muscle cell can not be in a steady ionic state due to the active transport[2,3]. Therefore, a simple method was developed to study the ionic condition of muscle. Applying this method we compare the inoic condition of normal muscle and denervated muscle.

MATERIAL AND METHOD

Siate nerves on one leg of a Sprauge Dawley rat was scissored near the knee. After about 20 days muscle atrophy could be clearly seen by checking the paralyzed legs which are smaller in size. The other leg which was not touched was used as control.

The denervated muscles as well as the normal muscles were dissected and homogenized by glass homogenizer in ten volumn double distilled water. The muscle extract was separated from the debris by centrifuging the homogenate at 1200xg for 30 minutes. Sometimes it was necessary to centrifuge for several times to get clear supernatant. The debris was heated in oven at 80°C to get the dry weight and the supernatant was diluted appropriately to measure the $[Na^+]$ and $[K^+]$ concentration with the flame photometer from Evans Electroselenium LTD England.

THEORY

If we assume that the dry weight of the debris was the weight of solid structure in the normal cell, we could get the total weight of the extra — and intra cellular solutions by substracting the dry weight from the total muscle weight. The density of the intra- and extracellular solution are approximate by 1 that is the density of water. We may then calculate the $[K^+]$ = the average K^+ concentration of the intra and extra cellular solution. $[Na^+]$ = the average Na^+ concentration of the intra and extracellular solution by the following equation

$$[Na^+] = \frac{X_{Na^+}}{\Delta\omega} \times \omega$$

$$[K^+] = \frac{X_{K^+}}{\Delta\omega} \times \omega$$

X_{K^+}: K^+ measured
X_{Na^+}: Na^+ measured
ω: total muscle weight
$\Delta\omega = \omega -$ dry weight

It is known that $[Na^+]$ and $[K^+]$ in the intracellular solution are about 16mM and 150mM respectively, in extracellular solution they are about 150mM and 6.5mM.

No matter what is the ratio of intracellular solution/extracellular solution varis, we may express the relation of $[K^+]$ and $[Na^+]$ as following

$$\text{suppose } X = \frac{\text{Extracellular solution}}{\text{intracellular solution} + \text{extracellular solution}}$$

$$[K^+] = E_k\, X + (1-x)\, I_k \qquad (1)$$

E_k : K^+ concentration in extracellular solution
I_k : K^+ concentration in intracellular solution

$$[Na^+] = E_{Na}\, X + (1-x)\, I_{Na} \qquad (2)$$

E_{Na} : Na^+ concentration in extracellular solution
I_{Na} : Na^+ concentration in intracellular solution

Using equation (1) and (2) we will have

$$[Na^+]-I_{Na}=\frac{(E_{Na}-I_{Na})}{(E_K-I_K)}([K^+]-I_K) \qquad (3)$$

No matter how X varies, the plot of $[Na^+]$ and $[K^+]$ will be near the line according to equ 3.

RESULT AND DISCUSSION

The results were summerized in Fig. 1. It turn out that the $[K^+]$ and $[Na^+]$ in normal muscle were near the line. However, the $[K^+]$ and $[Na^+]$ in the denervated muscle were not around the line.

If the effect of atrophy will change the size of the muscle and thus reduce

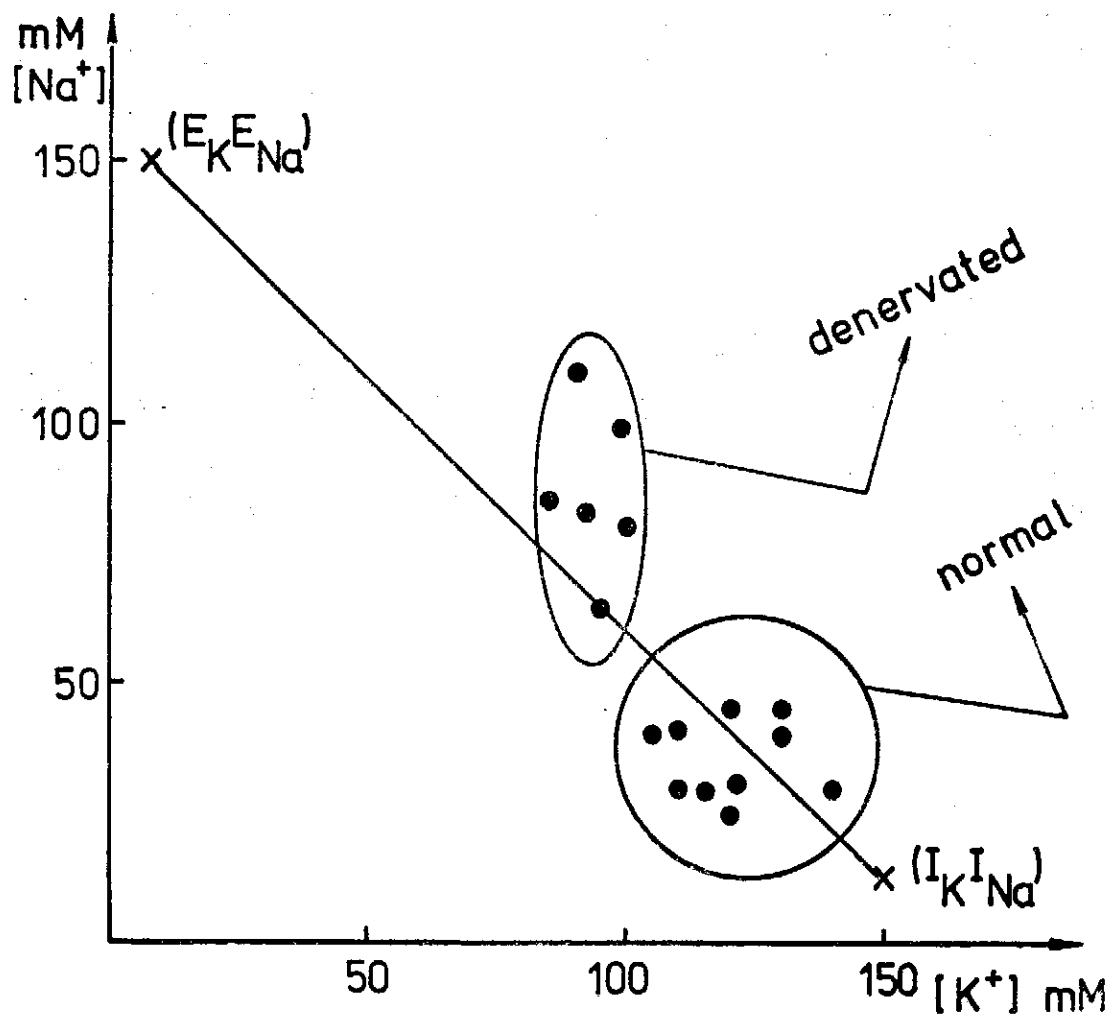

the volumn of intracellular solution compare to extracellular solution. In other word increase the X in the equ. (1) and equ. (2). In this case the $[K^+]$ and $[Na^+]$ will shift along the line to the upper left. According to our results, the $[K^+]$ and $[Na^+]$ does move toward upper left, at the same time, it also move away from the line toward the right side of the line.

From these data, it can be deduced that in normal muscle the $X \simeq \frac{1}{6}$, for denervated muscle X increase to $\frac{2}{5}$. For normal muscle, most data are on the left side of the line, these results may be due to that when we use $\Delta\omega t = \omega t -$ dry weight, the $\Delta\omega t$ may also contain some soluble protein which should be included in the dry weight, the $\Delta\omega t$ are over estimated, and therefore, the $[K^+]$ and $[Na^+]$ are some what below the real value. While for denervated muscle the data are mostly at the right side of the line. If we assume the E_K, E_{Na} are the same for denervated muscle (because extracellular solution should not be changed by a local events), and plot another line which pass the (E_K E_{Na}) and the average value of $[K^+]$ and $[Na^+]$ of the denervated muscle, we will see that either I_{Na} or I_K of denervated muscle may have significantly increased from the normal muscle. In other words, the ionic condition of denervated muscle is not in an ionic steady state.

REFERENCES

(1) R. C. Thomas, Intracellular sodium activity and the sodium in snail neuroues. J. Physiol. 220, 55-71, 1972.

(2) Wei-Kung Wang and Yuh-Ying L. Wang, Membrane potential, active transport and maxwell demon. Annual Report of the Institute of Physics, Academia Sinica 6, 77-86, 1976.

(3) Yuh-Ying L. Wang, and Wei-Kung Wang, Membrane potential and active transport—An information theory approach. Biological Chemistry and Physics Vol. 11, No. 1, 77-82, 1979.

INHIBITION OF CATECHOLAMINE BIOSYNTHESIS BY α-METHYL-TYROSINE, 3-IODOTYROSINE AND DIETHYLDITHIOCARBAMIC ACID IN RAT BRAIN

WEI KUNG WANG (王 唯 工) and YI CHIANG (蔣 宜)

Biophysics Laboratory, Institute of Physics, Academia Sinica
Taipei, Taiwan, Rep. of China

Abstract

α-methyl-tyrosine, 3-iodotyrosine and Diethyldithiocarbamic acid were incubate with crude synaptosomal preparation. Labelled CO_2 from L(1 - ^{14}C)tyrosine were measured by a respirometer to indicate the rate of catecholamine synthesis. It was found that all three drugs inhibit dopamine formation in Corpus striatum as well as Norepinephine formation in Hypothalamus. However there was a definite amount of $^{14}CO_2$ release, which might be from denatured tyrosine, could not be inhibited.

INTRODUCTION

Presynaptic regulation on catecholamine biosynthesis may happen in several different sites these include regulating the activity of Tyrosine Hydroxylase (T.H.), regulating the activity of the Dopamine-β-Hydroxylase (DβH), regulating through the pre-synaptic autoreceptors and etc..

Recently we developed a instrument to study the rate of dopamine formation in synaptosome[1]. In this report, we will check the system by inhibiting the dopamine formation by Tyrosine Hydroxylase inhibitor. And Dopamine-β-Hydroxylase inhibitor for two purpose.

1. To understand inhibitory effects of this inhibitors in synaptosomal preaparation and compare to those pre-synaptic autoreceptor stimulating drugs.[2]

2. To understand the method and instrument more clearly for both theory and application.

MATERIAL AND METHOD

Male Sprauge-Dawley Rat (Weight 180g-230g) raised in our laboratory was sacrificed by decapitation. Brain was removed and dissected on ice. Corpora Striatum (containing caudate nucleus and a portion of putaman) and Hypothalamus was removed and homogenized in 10 volumns of ice-cold 0.32M sucrose by teflon pestle tissue homogenizer (Arthus H. Thomas Co. Phailadelphia). The homogenate was centrifuge (O°C-4°C) at 1000 × g 15 minutes to sediment nuclei and debris. Several 50 μℓ aliquots of supernatant (equivalent to 5 mg wet

weight tissue) containing synaptosomes and other cellular components were added to test tubes each containing 150$\mu\ell$ physiological medium which containing 125 mM NaCl 1.48 mM $CaCl_2$ 4.8 mM KCl 2.5 mM $MgS0_4$ 22 mM NaH_2PO_4, 10mM $NaHCO_3$ and 16mM glucose (chemicals are all from Sigma) and gave a final PH=6.6 when equilibrated with 95% 0_2-5% CO_2. Tyrosine concentration was about 50μM (Specific activity 50m Ci/m mole from New England Nuclear Corp.) α-methyl-tyrosin, 3-iodo-tyrosine and Diethyl dithiocorbamic acid were added to the incubation medium with 10$\mu\ell$ 0.1 N phosphorous buffer PH=6.6 as correct the control tube was also added with 10$\mu\ell$ of the same buffer. Liberated $^{14}CO_2$ from (1-^{14}C) tyrosine were measured for every 10 minutes by a respirometer.

RESULT

All the results were shown clearly by figures and may be summerized as following. The inhibition of α-methly-tyrosine and 3-Iodo-tyrosine on $^{14}CO_2$

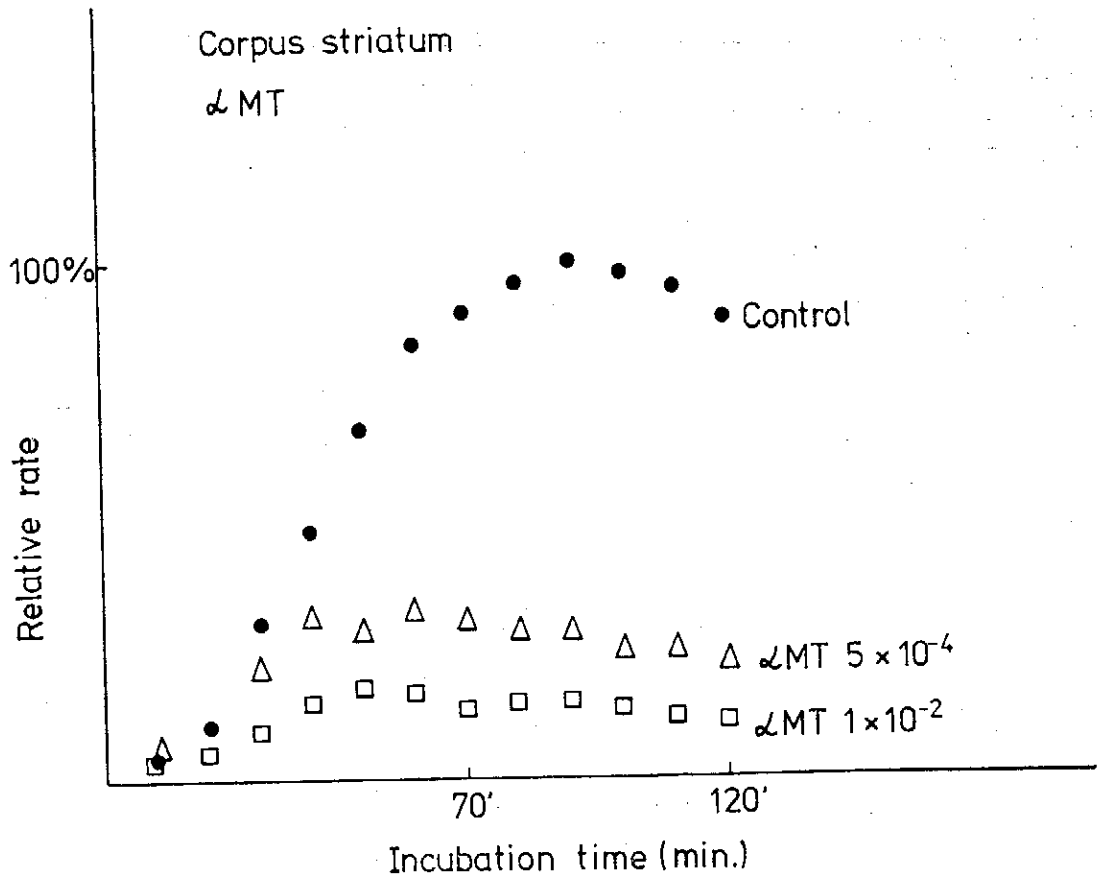

FIG. 1. Inhibition of α-methyl-tyrosine (αMT) on the dopamine formation as a function of incubation time. Values on the right of the data are the concentration of αMT.

release from ($1\text{-}_{14}C$) tyrosine are about the same that is more than 90% in Corpus Striatum and about 50% in Hypothalamus preparation for high dose. The 3-I-tyrosine are more effective in inhibiting the $^{14}CO_2$ release at the same dose. For 3-I-tyrosine at 5×10^{-4}M the inhibition were almost complete while the α-methyl-tyrosine needed about 10^{-2}M to be as effective.

The DDC was found to be as effective in inhibiting $^{14}CO_2$ release as the α-methyl-tyrosine. Both in Corpus Striatum and Hypothalaum.

DISCUSSION

Before further discussion of the result, we shall first explain briefly the theory on which we could distinguish some different mechanisms on the modification of $^{14}CO_2$ liberation rate. When we use a labelled precursor to study the formation of certain compound in a separated compartment, for example, in a

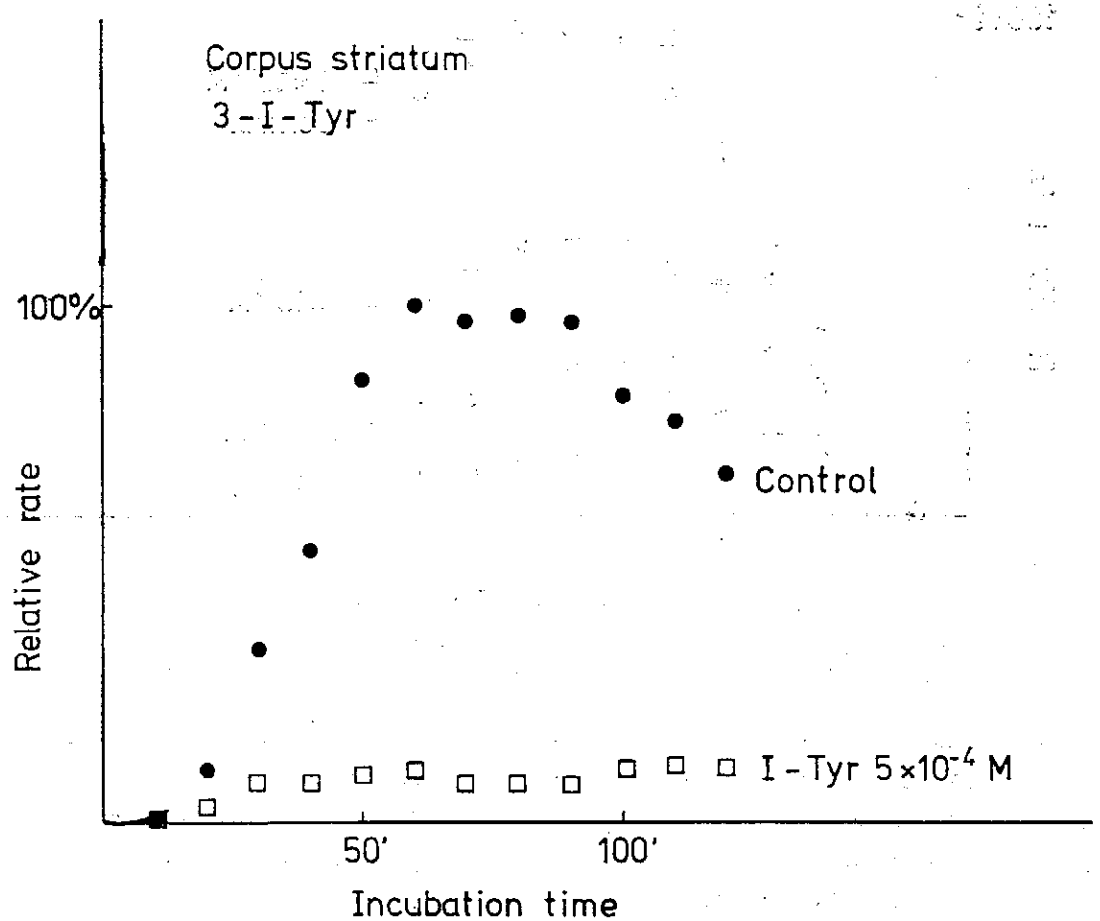

FIG. 2. Inhibition of 3-I-tyrosine on the dopamine formation as a function of incubation time: Values on the right of the data are the concentration of 3-I-tyr.

cell or a synaptosome, the most difficult point is how to determine the concentration of the endogenous precursor. If we measured the formation of the labelled product after a specific reaction time, the change of specific activity due to the dilution of the endogenous precusor will greatly affect the final result.

Here we will derive a mathematical model to simulate the production pattern of our labelled compound from the preparation and try to explain the advantage of our approach.

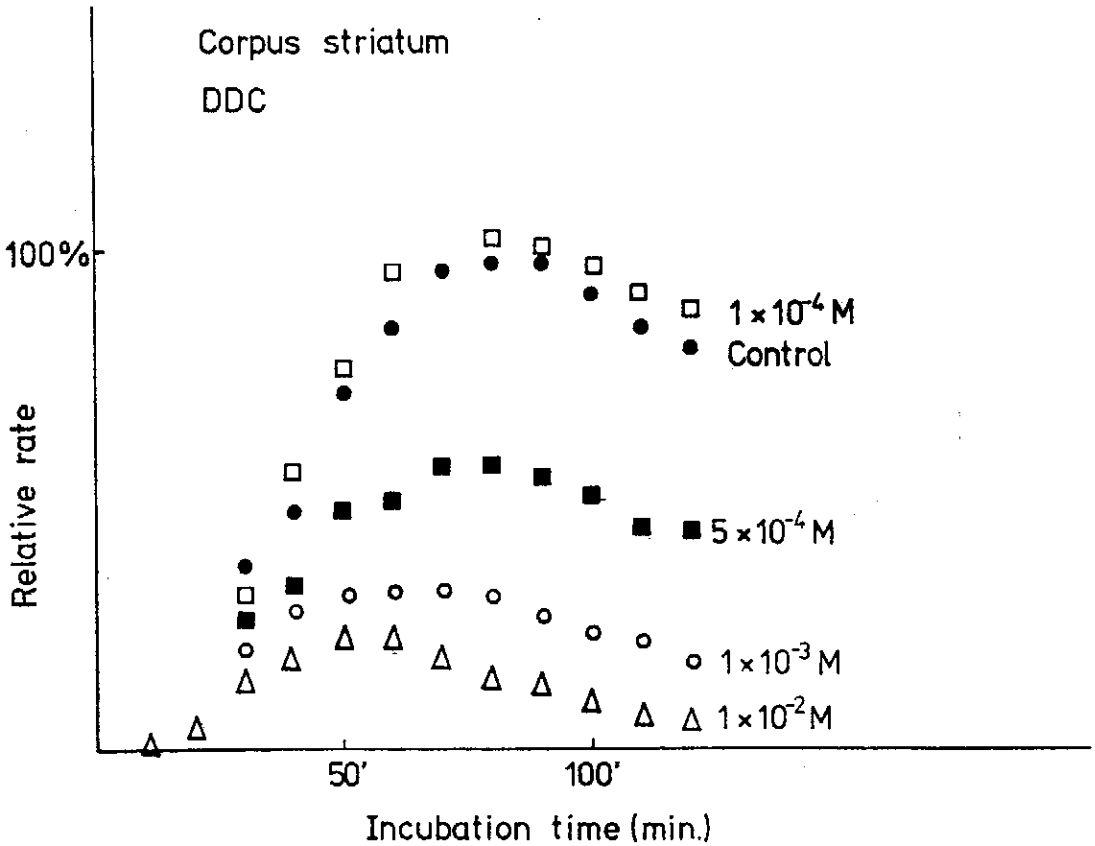

FIG. 3. Inhibition of DDC on the dopamine formation as a function of incubation time. Values on the right of the data are the concentration of DDC.

This mathematical model was first derived for glucose metabolism. Here a simplified version will be given. In a metabolic pathway, if we look at a specific intermediate α with endogenous pool size P_1, the flux rate into P_1 is V_α, and the flux rate out of P_1 is V_β. In a steady state $V_\alpha = V_\beta = V$. Suppose the flux into P_1 contains isotope ^{14}C of specific activity S_α, the specific activity in the P_1 is zero at $t=0$. When the intermediate α is converted at rate V and flow into the pool P_1, the rate of change of specific activity S in P_1 is

$$\frac{dS}{dt} = \frac{V(S_\infty - S)}{P_1} \quad (1)$$

This equation has a solution

$$S = S_\infty (1 - e^{-\frac{V}{P_1} t}) \quad (2)$$

For more than two intermediates, the specific activity of the product will be $S \simeq S_\infty (1 - e^{-\frac{V}{P_1} t})$, where P_1 is the largest pool in the series of reactions.

According to equ. (2), the amount of $^{14}CO_2$ produced from the following reactions

$$(1-{}^{14}C) \text{ tyrosine} \rightarrow (1-{}^{14}C) \text{ dopa} \rightarrow \text{dopamine} + {}^{14}CO_2$$

inside the synaptosome will follow a exponentially increasing curve and reach steady state with time constant P/V, where V is metabolic rate of this series of reaction, while P is the pool size of tyrosine inside the synaptosome.

The drugs we studied will directly effect the T.H. or DβH in an enzyme preparation. Here we took advantage of our method to study the time course of this inhibition in synaptosomal preparation.

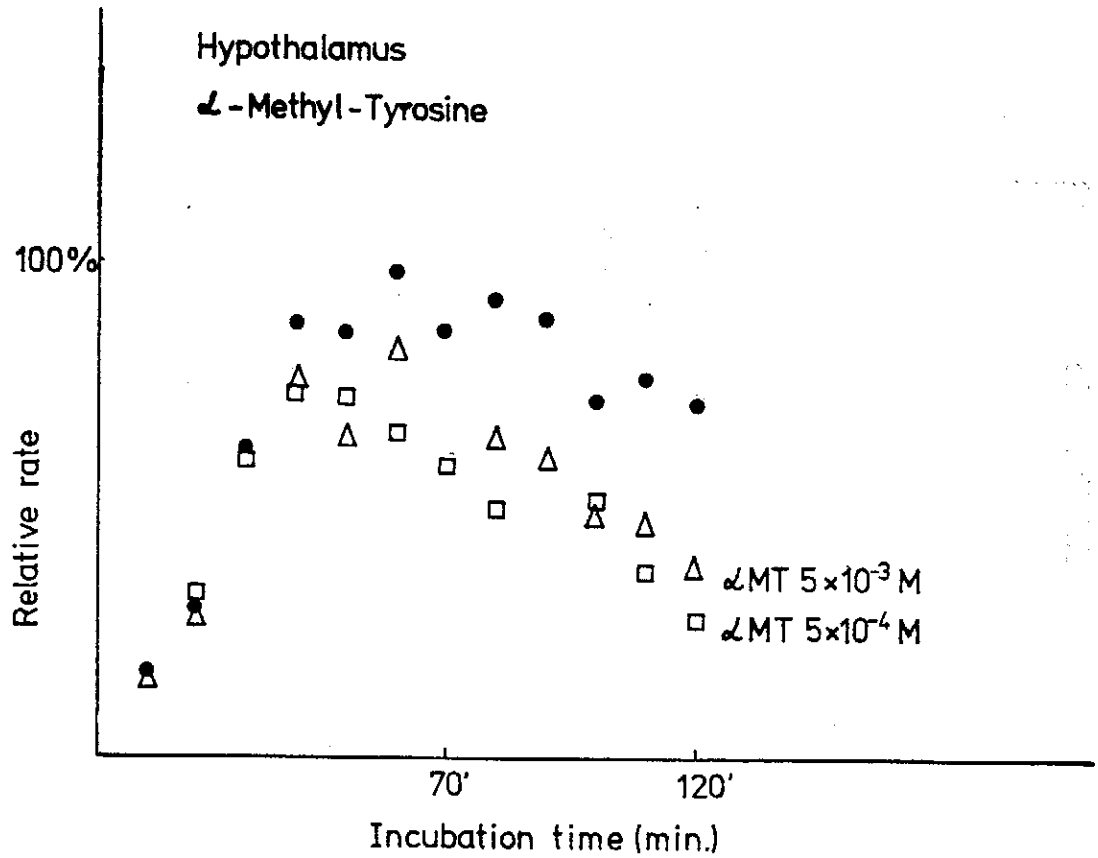

FIG. 4. Inhibition of α-methyl-tyrosine on the $^{14}CO_2$ release from hypothalamic preparation as a function time. Values on the right of the data are the concentraton of αMT.

From these results, it is clear that the drugs could effect the catecholamine synthesis inside the synaptosome, fastly, the inhibition of labelled CO_2 release happened as soon as the incubation started.

The amount of inhibition also justified the statement that "In Corpus Striatum, the $^{14}CO_2$ release we studied are almost totally from the (1 - ^{14}C) Dopa → Dopamine + $^{14}CO_2$" we also found that when labelled tyrosine were used for several months, the $^{14}CO_2$ release that could not be inhibited by all these drugs would slowly increase from a few percents upto 10 percents different or even more.

For Hypothalamic preparation, the inhibition was about 50% of the $^{14}CO_2$ release when (1 - ^{14}C)tyrosine are reasonably fresh*. However, the absolute magnitute of the $^{14}CO_2$ that can not be inhibited by these drug were about the same as the preparation from corpus striatum. Suggesting that there is a different way for these ^{14}C which are originally from (1 - ^{14}C)tyrosine to be converted to $^{14}CO_2$.

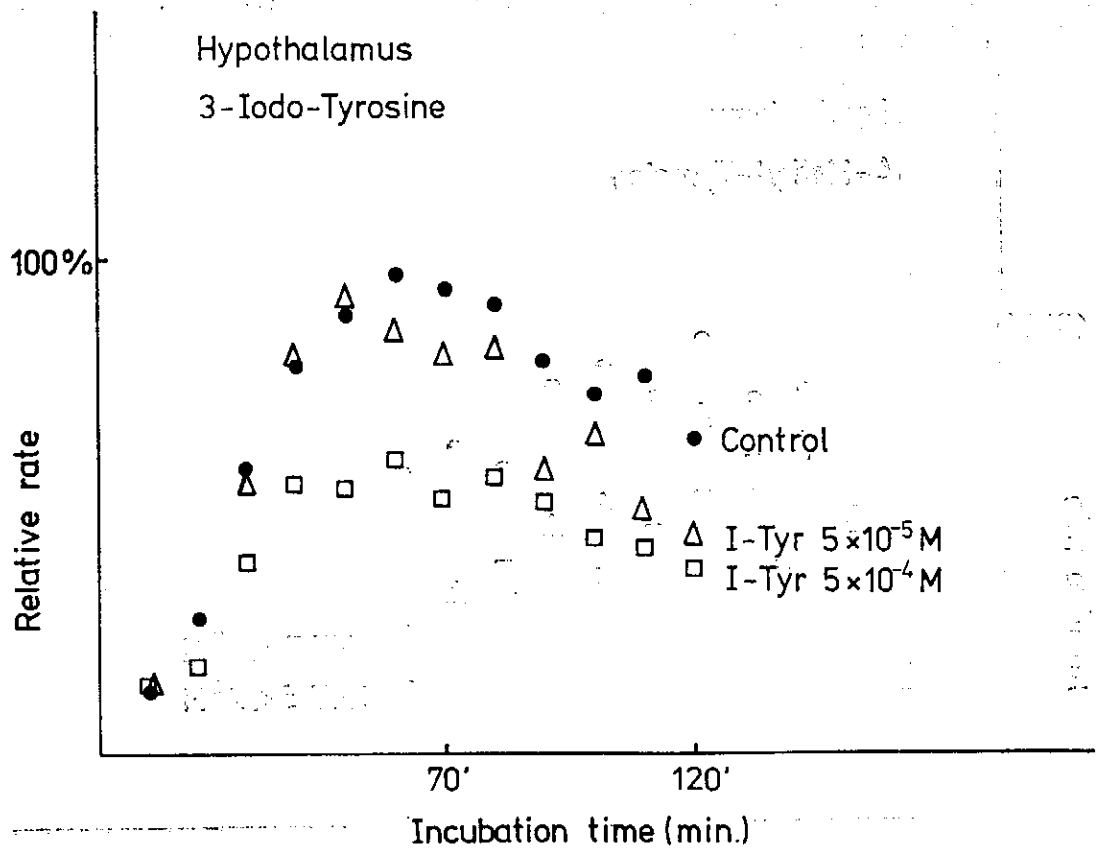

FIG. 5. Inhibition of 3-I-tyrosine on the $^{14}CO_2$ release from hypothalamic preparation as a function of incubation time. Values on the right of the data are the concentration of 3-I-tyr.

* We could not get very fresh (1 - ^{14}C)tyrosine, because it took about a month to get the tyrosine we ordered.

The most interesting results are that the DDC inhibit the $^{14}CO_2$ release from (1 - ^{14}C)tyrosine in Corpus Striatum preparation as effective as that of α-methyl-tyrosine.

DDC will inhibit $^{14}CO_2$ release from (1 - ^{14}C)tyrosine in Hypothalamic preparation, because it inhibits DβH, and the neurotransmitter in Hypothalamic area are mainly N.E.

These facts suggested that the inhibition of DDC is not limited to D-β-H.

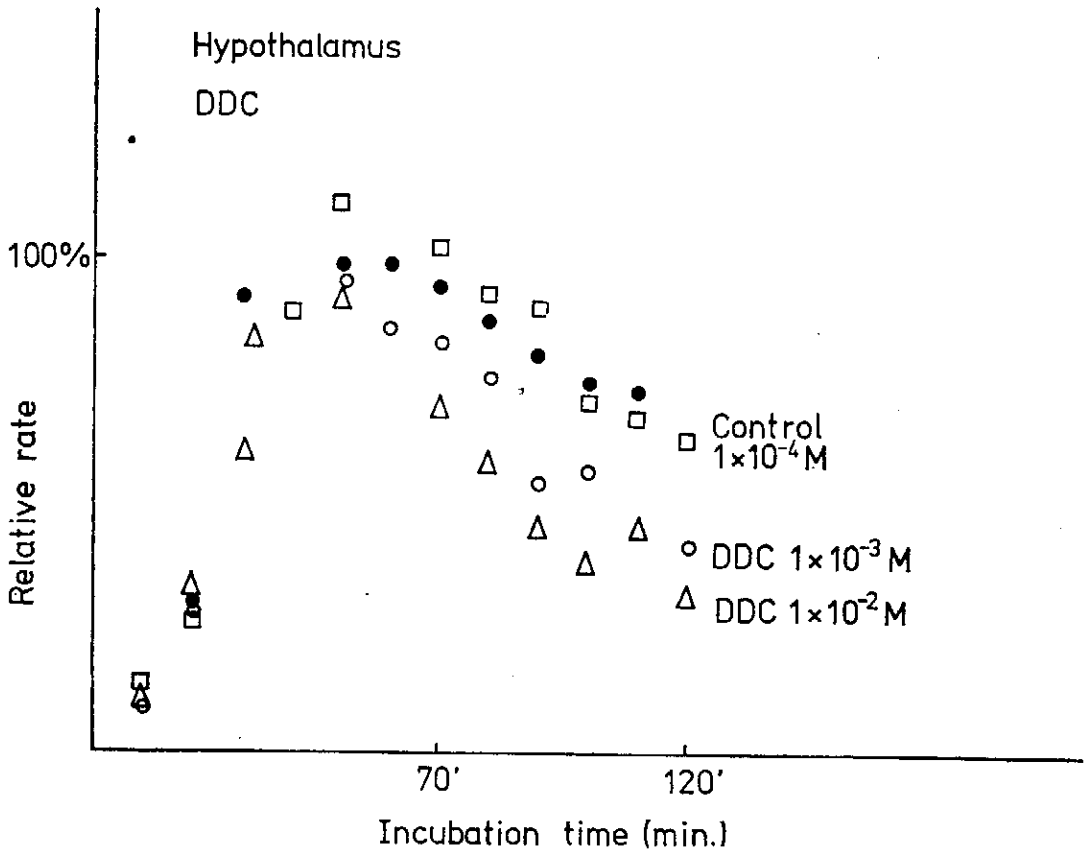

FIG. 6. Inhibition of DDC of the $^{14}CO_2$ release from hypothalamic preparation, as a function of incubation time. Values on the right of the data are the concentration of DDC.

REFERENCES

(1) Wang W. K. and Y. Chiang (1977) A Method to Study the Rate of Intrasynaptosomal Catecholamine Biosynthesis. Bull. Inst. Zool. Academia Sinica 16: 131-135.

(2) Wang W. K., T. Y. Hai and Y. Chiang (1980) Different Inhibitory Effects of Dopa, Dopamine and Apomorphine on Dopamine Biosynthesis, Bull. Inst. Zool Academia Sinica 19(1) 33-37.

FURTHER STUDIES ON THE INTERFERENCE EFFECT OF CATAMARAN PLANING HULLS

CHUN-TSUNG WANG (汪 群 從)

INTRODUCTION

By assuming that the effective width of a catamaran planing surface is the total width of the two surfaces or the width of the individual surface, Wang at al[1] obtained two sets of equations for lift of such a surface. Comparing the experimental data with the calculated results, it was found that the drag-lift ratio of the experimental data were larger than those calculated by assuming that the effective width is the total width of the two surfaces. The deviation may be mainly due to the neglecting of the interaction effect of the two surfaces. Savitsky and Dingee[2] studied the interference effects between two flat surfaces planing parallel to each other. They found that the lift generated by an individual surface when the two surfaces were placed closely together was always larger than when the surfaces were widely separated. The difference may be attributed to the interference phenomena. Adapting Savitsky's planing equations[3], Liu and Wang[4] tried to introduce an interference factor to study the interference effect of planing hulls.

The present study intends to study interference effect from planing equations developed by Savitsky[3] and Shuford[5]. Also preliminary analysis on how the interference effect may be incorporated to study catamaran planing hull performance is introduced. It is also found that the interference factor A does not seem to depend on speed coefficient when planing hulls are lightly loaded.

INTERFERENCE EFFECT

The equations developed by Savitsky[3] have been widely used to predict the resistance and running trim of a V-shaped planing surface. The equations to compute lift and center of pressure for flat planing surface with width b are:

$$\Delta = \frac{1}{2}\rho\, v^2 b^2 [0.012\,\lambda^{0.5} + \frac{0.0055\,\lambda^{2.5}}{C_v^{\,2}}]\,\tau^{1.1} \qquad (1)$$

and

$$\frac{LCG}{\lambda b} \cong 0.75 - [2.39 + 5.21\,\frac{C_v^{\,2}}{\lambda^2}]^{-1} \qquad (2)$$

where

λ = mean wetted length-beam ratio, $\ell m/b$; $\lambda \leq 4$

C_v = speed coefficient, $v/\sqrt{gb}$, $0.6 \leq C_v \leq 13.0$

τ = trim angle; $2° \leq \tau \leq 15°$

v = planing speed

LCG = the longitudinal distance of center of gravity from transom

For a flat catamaran planing hull with zero separation, i.e. being equivalent to a flat planing hull of width 2b, the lift, Δ_1, and center of pressure, LCG_1, attributed to half of the surface with width b are

$$\Delta_1 = \frac{1}{4}\rho\, v^2(2b)^2 \left[0.012\left(\frac{\ell m}{2b}\right)^{0.5} + \frac{0.0055\left(\frac{\ell m}{2b}\right)^{2.5}}{\frac{v^2}{g\cdot 2b}}\right] \tau^{1.1} \qquad (3)$$

and

$$\frac{LCG_1}{\ell m} \cong 0.75 - \left[2.39 + 5.21\,\frac{v^2\cdot 2b}{g\cdot \ell m^2}\right]^{-1} \qquad (4)$$

At large planing speed, i.e. when $C_v \to \infty$, the dynamic component of the lift is predominant. Eqs. (1) and (3) together give the ratio of the lift Δ_1 for one flat plate running parallel to another flat plate with zero separation to the lift Δ of one flat plate planning alone at the same speed, trim and mean whetted length, i.e.

$$\frac{\Delta_1}{\Delta} = \sqrt{2} \text{ when } \frac{d}{b} = 0.0 \text{ and } C_v \to \infty \qquad (5)$$

were d is the distance between the two catamaran surfaces. Eqs. (2) and (4) together give

$$LCG_1 = LCG \qquad (6)$$

In other words, when $C_v \to \infty$, eg. (5) holds when speed, trim, mean wetted length and LCG remain the same for the two cases compared. When C_v becomes finite, the mean wetted length could no longer be the same if LCG's are kept the same.

Liu and Wang[4] earlier adapted Savitsky's equations and pointed out that Δ_1/Δ approaches $\sqrt{2}$ when C_v becomes large. Now it is evident that this could only be true if trim and mean wetted length are also kept the same as implied by eq. (5). Not to mention the possibility that Savitsky's equations (1) and (3) might not be applicable at such high speeds.

When the separation distance between the two surfaces of a catamaran planing hull becomes large, it is obvious that each surface is planing without any interference from the other surface. And the lift Δ_1 and center of pres-

sure attributed to half of the planing surface with width b are the same as those obtained from a flat planing surface with width b planing alone, i.e.

$$\frac{\Delta_1}{\Delta} = 1.0 \qquad \text{when } \frac{d}{b} \to \infty \text{ at all speeds} \tag{7}$$

$$LCG_1 = LCG$$

Experimental data collected by Savitsky and Dingee[2] gave Δ_1/Δ at different separation distance when trim, speed, and depth of immersion at transom, h, were kept the same. At $C_v = 7.5$, $\bar{\lambda}_1 = 2.6$ and $\bar{\tau} = 10°$, test results show that

$$\frac{\Delta_1}{\Delta} \cong 1.45 \quad \text{what } \frac{d}{b} = 0.0 \qquad = 1.0 \quad \geq 4.0 \tag{8}$$

where $\lambda_1 = h/b \cdot \sin\tau = \dfrac{\ell m}{b} - \delta\lambda$

$\delta\lambda = 0.6$ when $(d/b) = 0.0$ and $\delta\lambda = 0.3$ when $(d/b) \geq 4.0$

$-$: stands for mean testing value

Whereas Eqs. (1) and (3) together give

$$\frac{\Delta_1}{\Delta} = 1.448 \quad \text{when } \frac{d}{b} = 0.0 \qquad = 1.0 \quad \geq 4.0 \tag{9}$$

when speed, trim and depth of immersion at transom are kept the same. Analytical results as given in eq. (9) confirm with the experimental observation of eq. (8), suggesting that Savitsky's equations may be used to study catamaran interference effects.

When the mean wetted length-beam ratio becomes large, the equations developed by Shuford[5] may be more applicable in studying planing hull performance. When $\dfrac{d}{b} \to \infty$, the equations for lift and center of pressure for flat planing surface with width b are

$$\frac{\Delta}{\frac{1}{2}\rho v^2 b^2} = \frac{\pi}{4} \sin 2\tau \cdot \cos\tau \cdot \left[\frac{\lambda}{1+\lambda} + \frac{1.33}{\pi} \sin 2\tau \cdot \lambda + 0.4 \sec\tau \cdot \frac{\lambda^2}{C_v^2}\right] \tag{10}$$

and

$$\frac{LCG}{\ell m} \cong \frac{\dfrac{0.875}{1+\lambda} + \dfrac{1.33}{2\pi} \sin 2\tau + \dfrac{0.4}{3} \sec\tau \cdot \dfrac{\lambda}{C_v^2}}{\dfrac{1}{1+\lambda} + \dfrac{1.33}{\pi} \sin 2\tau + 0.4 \sec\tau \cdot \dfrac{\lambda}{C_v^2}} \tag{11}$$

These empirical equations are applicable for $2° \leq \tau \leq 30°$, $1 \leq \lambda \leq 7.$, and $0.5 \leq C_v^2 \leq 50$. When $\frac{d}{b} \to 0$, the equations become

$$\frac{2\,\Delta_1}{\frac{1}{2}\rho v^2 (2b)^2} = \frac{\pi}{4} \sin 2\tau \cdot \cos\tau \cdot \left[\frac{\frac{\ell m}{2b}}{1+\frac{\ell m}{2b}} + \frac{1.33}{\pi} \sin 2\tau \cdot \frac{\ell m}{2b} + 0.4 \sec\tau \frac{\left(\frac{\ell m}{2b}\right)^2}{\frac{v^2}{g \cdot 2b}} \right] \quad (12)$$

and

$$\frac{LCG_1}{LCG} = \frac{\frac{0.875}{1+(\ell m/2b)} + \frac{1.33}{2\pi} \sin 2\tau + \frac{0.4}{3} \sec\tau \cdot \frac{g\ell m}{v^2}}{\frac{1}{1+(\ell m/2b)} + \frac{1.33}{\pi} \sin 2\tau + 0.4 \sec\tau \cdot \frac{g\ell m}{v^2}} \quad (13)$$

Eqs. (10) and (12) together give

$$\begin{aligned} \frac{\Delta_1}{\Delta} &= 1.444 && \text{when } \frac{d}{b} = 0 \\ &= 1.0 && \geq 4.0 \end{aligned} \quad (14)$$

for the test conditions outlined in eq. (8), which confirm with test results obtained in[2]. At zero separation distance, Δ_1/Δ in general does not approach $\sqrt{2}$ as suggested by eq. (5), instead, eqs. (10) and (12) show that Δ_1/Δ is a function of λ and τ when C_v becomes large. Also eqs. (11) and (13) show that LCG are not the same, differeent from that suggested in eq. (6)

Rewriting eq. (12) gives

$$\frac{\Delta_1}{\frac{1}{2}\rho v^2 b^2} = \frac{\pi}{4} \sin 2\tau \cdot \cos\tau \cdot \left[\frac{\lambda}{1+0.5\lambda} + \frac{1.33}{\pi} \sin 2\tau \cdot \lambda + 0.4 \sec\tau \cdot \frac{\lambda^2}{C_v^2} \right] \quad (12)'$$

when compared with eq. (10), it is seen that when separation distance decreases from infinity to zero, the change in lift from the interference effect is mainly due to the linear term appeared as the first term in the r.h.s. of eqs. (10) and (12)′. Whereas the cross-flow term and the static term remain the same when trim, mean wetted length-beam ratio and speed are kept the same.

From the above analysis, it is shown that planing equations developed by Savitsky, eqs. (1)-(4), and Shuford, eqs. (10)-(13), could both be used to study interference effect of planing hulls within their range of applicability. However any implication, e.g. eqs. (5) and (6), drawn from empirical equations should be trusted only when they can be experimentally verified.

INTERFERENCE FACTOR

For catamaran planing hulls of zero deadrise angle, the mean wetted length-beam ratio may become quite large. Consequently the equations developed by Shuford[5] may be more applicable in computing the lift for flat

planing surfaces. At $\frac{d}{b} = 0.0$ and ∞. Shuford's equations have been found to give analytical results comparable to those collected experimentally as shown in eq. (14). At moderate separtion distance, Δ_1/Δ varies between the two limiting values as $\frac{d}{b}$ increases from zero to infinity[2] A resonable way to take the interference effect into consideration is to use the following synthetic equation to relate τ and ℓm when b, v and Δ_1 are given, i.e.

$$\frac{A^*\Delta_1}{\frac{1}{2}\rho v^2(Ab)^2} = \frac{\pi}{4}\sin 2\tau \cdot \cos\tau \cdot \lambda^* \left[\frac{1}{1+\lambda^*} + \frac{1.33}{\pi}\sin 2\tau + 0.4\sec\tau\frac{\lambda^*}{C_v^*}\right] \qquad (15)$$

where A* and A are the interference factors, $\lambda^* = \frac{\ell m}{Ab}$, $C_v^* = \frac{v}{\sqrt{gAb}}$. At zero separation, $A^* = A = 2.0$ and eq. (15) reduced to eq. (12). At infinite separation, $A^* = A = 1.0$ and eq. (15) reduced to eq. (10). For the present study, it is assumed that

$$A^* = A = f_n\left(\frac{d}{b}\right) \qquad (16)$$

whether this is the case or whether A depends on hull loading, $A_p/\nabla^{3/2}$, where A_p is the projected catamaran hull bottom area, and ∇ is the hull displacement, will be investigated in a separate study.

Eqs. (15) and (10) give

$$\frac{\Delta_1}{\Delta} = \frac{(\lambda_1+\delta\lambda)\left[\left(1+\frac{\lambda_1+\delta\lambda}{A}\right)^{-1} + \frac{1.33}{\pi}\sin 2\tau + 0.4\sec\tau\frac{\lambda_1+\delta\lambda}{C_v^2}\right]}{(\lambda_1+0.3)\left[(1+\lambda_1+0.3)^{-1} + \frac{1.33}{\pi}\sin 2\tau + 0.4\sec\tau\cdot\frac{\lambda_1+0.3}{C_v^2}\right]} \qquad (17)$$

when v, τ and h are kept the same for the two cases compared. Based on experimentally collected Δ_1/Δ, λ_1, $\lambda_1+\delta\lambda$ values at $C_v = 7.5$ given in[2], eq. (17) can be used to compute A at various $\frac{d}{b}$ ratios, Fig. 1 shows that the interference factor A decreases from 2.0 to 1.0 as the separation distance increases from zero to infinity.

CATAMARAN PLANING HULLS

For catamaran planing hulls with zero deadrise angle at a given separation distance d, the equation for the center of pressure remains to be investigated. In the present study, it is assumed that as the two surfaces of a catamaran planing hull move from infinite separation to some finite separation

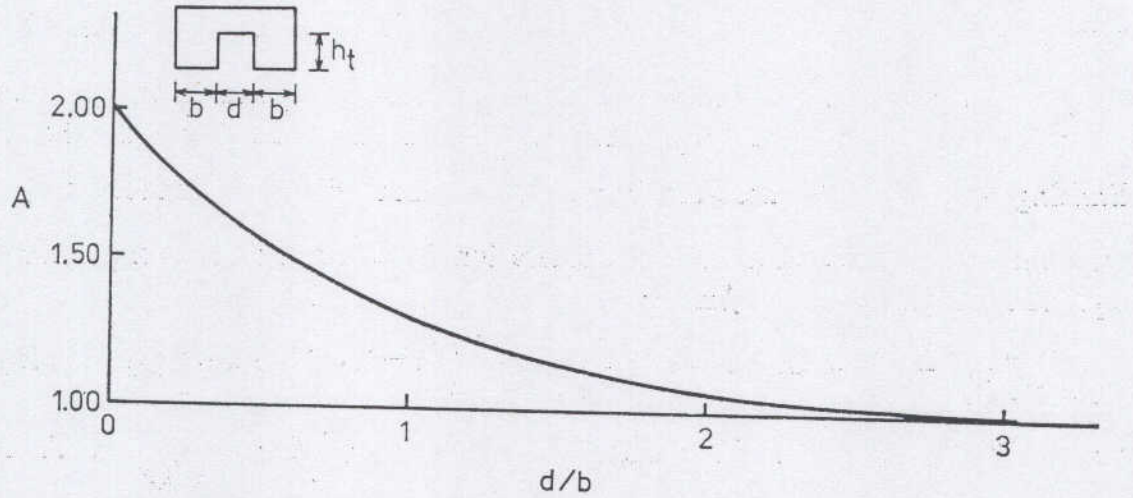

FIG. 1. Interference Factor between Two Planing Surfaces.

distance d, the extra loading due to interference effect acts at 0.5 ℓm from the transom. And the equation to compute the center of pressure is

$$\frac{LCG}{\ell m} = \frac{\frac{0.375}{1+\lambda} + \frac{0.5}{1+\lambda^*} + \frac{1.33}{\pi}\sin 2\tau + \frac{0.4}{3}\sec\tau\frac{\lambda^*}{C_v^{*2}}}{\frac{1}{1+\lambda^*} + \frac{1.33}{\pi}\sin 2\tau + 0.4\sec\tau\frac{\lambda^*}{C_v^{*2}}} \tag{18}$$

For lightly loaded catamaran planing hulls, where the inner top surface is not wetted, the total wetted surface, S, is assumed to include the wetted parts of the two bottom surfaces and the two outer reattached surfaces, if any. It can be expressed as

$$S \cong \ell m \cdot 2b + 2h_t \cdot \ell \tag{19}$$

where

h_t = height at transom
ℓ = reattached length, $\ell m - 3v^2 \sin\tau/g \geq 0$

The drag-lift ratio can be approximated as

$$\frac{D}{2\Delta_1} = \tan\tau + \frac{1}{2\Delta_1} \cdot \frac{\rho}{2}\frac{V_m^2 C_f}{\cos\tau} \cdot S \tag{20}$$

where[1]

V_m = the average bottom relative velocity
C_f = the skin friction coefficient

Eqs. (15), (16), (18), (19) and (20) could be used to predict drag-lift ratio for catamaran planing hull of different separation ratios and speed coefficients. Figs. 2 and 3 show the test results collected at the Ship Model Basin, National Taiwan University[1] as well as the computed results obtained from

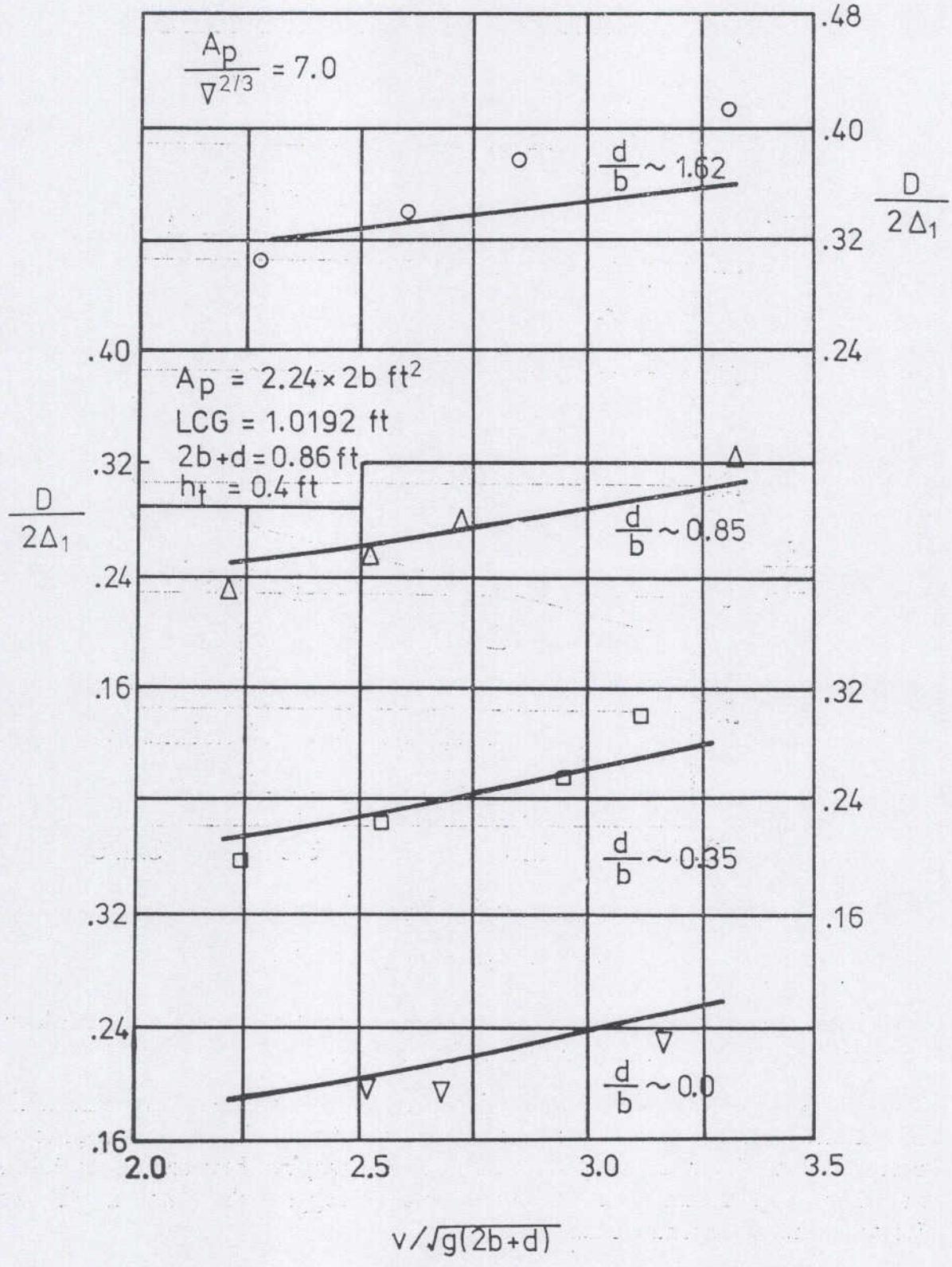

FIG. 2. Comparisons of Drag-Lift Ratios.

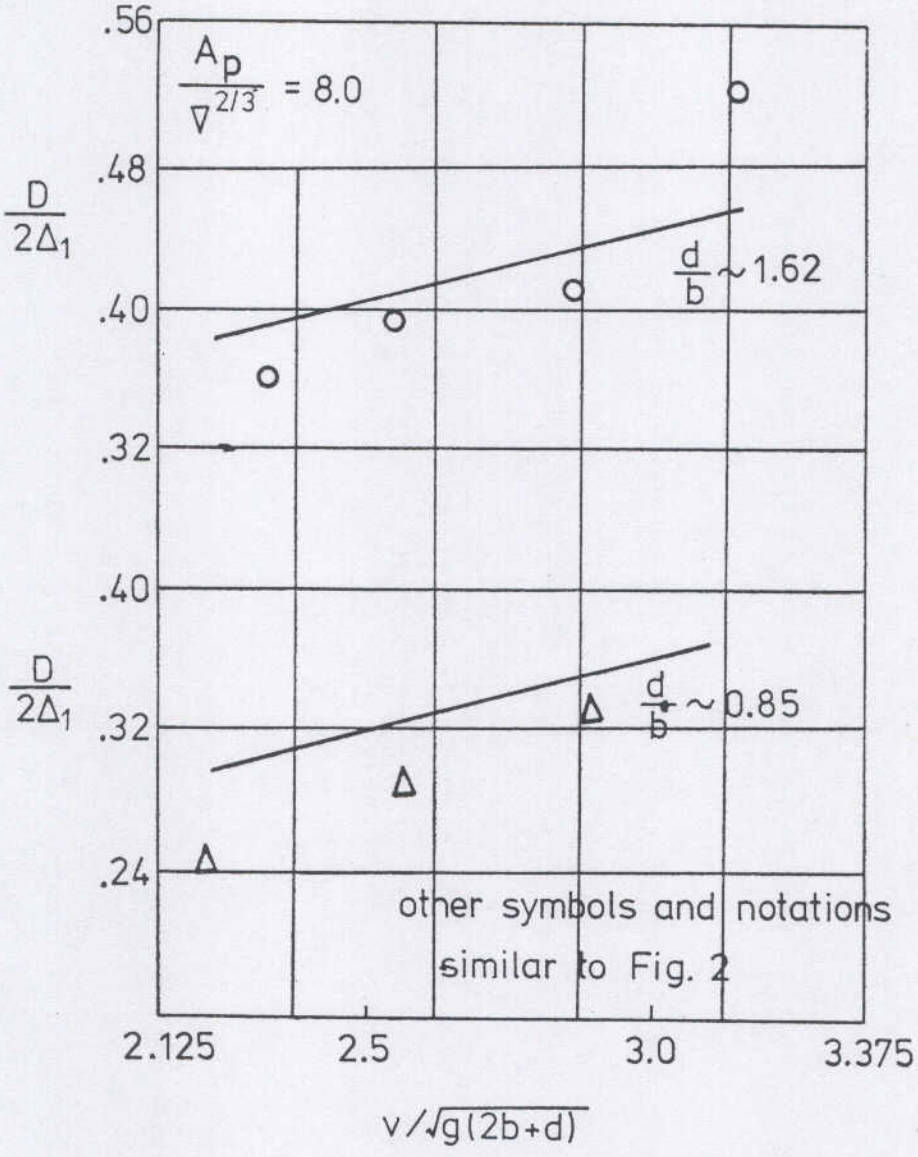

FIG. 3. Comparisons of Drag-Lift Ratios.

the above analysis (solid curves). Although data scattering is observed, in general test results confirm with analytical results.

It is also to be noted that the interference factor A was experimentally determined from test data obtained at $C_v = 7.5$[3]. When it was applied to compute drag-lift ratio at speed coefficient C_v varying between 3.0 to 6.5 as shown in Figs. 2 and 3, no evidence tends to suggest that the interference factor A should depend on C_v.

Acknowledgment: Supports from National Science Council are appreciated.

REFERENCES

(1) Wang, C. T., Liu, C. Y., and Guo, C. L., Effect of the Separation Ratio on the Still Water Resistance of Catamaran Planing Hull, Inst. Naval Arch., National Taiwan Univ., NTU-INA-34, May, 1975.

(2) Savitsky, D., and Dingee, D. A., Some Interference Effects between two Flat Surfaces Planing Parallel to each Other at High Speed, J. Aeronautical Sci., 419, June, 1954.

(3) Savitsky, D., Hydrodynamic Design of Planing Hulls, Marine Technology, 1, 71, 1964.

(4) Liu, C. Y., and Wang, C. T., Interference Effect of Catamaran Planing Hulls, J. Hydronautics, 12, 31, 1979.

(5) Brow, P. W., An Experimental and Theoretical Study of Planing Surfaces with Trim Flaps, AD 722 393, Stevens Inst. Tech., Apr. 1971.

PREDICTIONS OF TEMTERATURE DISTRIBUTIONS RESULTING FROM THE SURFACE DISCHARGE OF HEATED WATER INTO LARGE BODIES OF WATER

by

ROBERT R. HWANG* (黃 榮 璧) and SHAIN-WAY JANG**

Abstract

In this study, a far field model has been developed for predicting the transient distribution of excess temperatures resulting from heated water discharges into large bodies of water. The model calculates three-dimensional excess temperature by superimposing the temperature distributions obtained from a number of discrete, vertically-distributed line sources which may be subject to the far field processes of ambient advection, diffusion and surface heat transfer. Ambient currents considered can vary in the vertical direction and with time. The method has been verified and the result shows that the comparison with the analytical solution is strike.

1. INTRODUCTION

Beyond the near field, the processes of surface heat exchange, ambient and buoyant advection and ambient turbulent diffusion must be considered. Loosely speaking these processes may be associated with the oth, 1st and 2nd moments of the excess temperature distribution in a receiving water body: the total excess heat contained within the body (oth moment) depends ultimately on the rate of surface heat exchange, the location of the heat (1st moment) depends on ambient advection, and spreading of the heat (2nd moment) is largely depend on buoyant advection and on diffusion properties.

In contrast to the near field, the processes—and ambient advection in particular—must be treated as time-varying. That is the time scale over which temperatures must be studied. Because ambient currents may vary considerably, the process of ambient advection is probably the most important for far field process.

Several types of far field models have been developed recently to predict concentrations or temperatures in a large body of water. Quasi-analytical (or superposition) models of continuous sources can be constructed by superposition of analytical solutions for discrete sources. Simple models of this kind are presented by Abraham and Van Dam (1970), Koh and Chang (1973), Van Dam (1974), Christodoulou et al (1974), and Adams et al (1975). In each case the near field was considered as a point source. For the study of Koh

* Research Fellow of Institute of Physics, Academia Sinica, R.O.C..

** Research Assistant.

and Chang, a mathematical formulation for a time-varying current was suggested but calculations were performed for a steady current only. The second type of models is simulation techniques suggested by Ahn and Smith (1972). The model tracks idealized particles in ways which simulate advection and diffusion from a source. The third type is the numerical models. Most numerical models assumed a two-dimensional velocity field and solve for vertically-integrated concentration using dispersion coefficients in finite difference schemes or finite element methods. Three-dimensional aspects are possible by coupling two or more two-dimensional layers through kinematic and dynamic interfacial boundary conditions. These numerical models are studies of Leendertse and Liu (1970, 1973), Tsai and Change (1973), Boericks and Hall (1974), and Leimkuhler (1974).

Each type of models introduced above has advantages and disadvantages. The choice of a far field model depends largely on the receiving water body of interest. For the objectives of the present study, a model of the first category—superposition models, is chosen for development in this study. It is felt that for analysis of a discharge into a large open body of water, analytical superposition models can provide realistic three-dimensional temperature prediction under a variety of transient current conditions. This type of model can easily include near field source conditions, is inexpensive to run and uses the type of field data most easily obtained-namely time series data from moored current meters and diffusion experiments. This information can then be used to help focus future efforts in the areas of discharge structure design, field measurement and further mathematical modeling.

2. MODEL ASSUMPTIONS

Although the basic assumptions of a superposition model are quite general and do not imply any inherent limitations on the source characteristics, the structure of the ambient current, the representation of the diffusion or heat loss processes, or the topography of the receiving water body, the following additional assumptions are made to insure that the representations and parameterizations utilized in the model are consistent with the present theoretical and empirical knowledge of the physical processes involved and that the resulting computations are within the range of practical feasibility.

1. The velocity field in the receiving water is unperturbed by the presence of the discharge. Furthermore, it is considered to be two-dimensional, horizontally uniform, and vertically sheared:

$$\begin{aligned} u &= \bar{u}(t) + u''(z, t) \\ v &= \bar{v}(t) + v''(z, t) \end{aligned} \tag{1}$$

where $\bar{u}(t)$ and $\bar{v}(t)$ are depth-averaged velocities and z is a vertical coordinate. Because there is no horizontal variation of velocity, the assumed velocity field may, in principle, be ascertained from a time series of currents measured over a vertical profile at one station. However, the presence of a simply shoreline may be represented approximately by the use of one or more image sources if necessary.

2. The ambient water temperature is known so that the actual water temperatures can be determined from excess temperature calculations.

3. Diffusion is horizontally homogeneous but may be anisotropic with respect to the axes (x, y, z).

4. Surface heat exchange can be expressed as a linear function of the difference between surface water temperature and a reference temperature. No heat transfer takes place through the water bottom.

3. ANALYSIS OF DISCRETE INJECTION

Before treating the case of a continuous solution, it is necessary to find the excess temperature at time T due to the release at time τ and horizontal location (x_0, y_0) of a discrete source with excess temperature distribution per unit depth, $m_z(z)$. For convenience $m_z(z)$ is chosen to have unit strength per unit depth when averaged over the depth of injection, h_T,

$$\int_0^{h_T} m_z(z)dz = h_T \tag{2}$$

The governing equation and the boundary and initial conditions used to describe the temperature distribution within the patch are

$$\frac{\partial c}{\partial t} + u(z, t)\frac{\partial c}{\partial x} + v(z, t)\frac{\partial c}{\partial y} = E_x(z, t-\tau)\frac{\partial^2 c}{\partial x^2} + E_y(z, t-\tau)\frac{\partial^2 c}{\partial y^2} + \frac{\partial}{\partial z}\left(E_z(z)\frac{\partial c}{\partial z}\right) - K_d(t, t-\tau)(c - c_{ref}) \tag{3}$$

$$E_z\frac{\partial c}{\partial z} = 0 \quad \text{at } z=0, H \tag{4}$$

$$c = c_a \qquad x \text{ or } y = \pm\infty \tag{5}$$

$$c = c(x-x_0, y-y_0, z) \qquad t=\tau \tag{6}$$

where the above formulation c represents temperature, c_a is the ambient temperature, c_{ref} is a reference temperature, E_x, E_y and E_z are turbulent relative diffusion coefficients and K_d is a first order decay coefficient which can be used to represent surface heat exchange.

An expression for excess temperature $\Delta c = c - c_a$, is developed by writing a similar equation with boundary and initial conditions for the ambient temperature and subtracting it from equation (3) yielding

$$\frac{\partial \Delta c}{\partial t} + u\frac{\partial \Delta c}{\partial x} + v\frac{\partial \Delta c}{\partial y} = E_x\frac{\partial^2 \Delta c}{\partial x^2} + E_y\frac{\partial^2 \Delta c}{\partial x^2} + \frac{\partial}{\partial z}\left(E_z\frac{\partial \Delta c}{\partial z}\right) - K_d \Delta c \qquad (7)$$

$$E_z\frac{\partial \Delta c}{\partial z} = 0 \text{ at } z = 0,\ H \qquad (8)$$

$$\Delta c = 0 \qquad x \text{ or } y = \pm\infty \qquad (9)$$

$$\Delta c = \Delta c(x - x_0,\ y - y_0,\ z) \qquad t = \tau \qquad (10)$$

The decay coefficient K_d is related to a kinematic surface heat exchange coefficient, $K/(\rho c_p)$, and the excess temperature profile by

$$K_d = K\ \Delta c\,|_{z=0}/(\rho c_p \int_0^H \Delta c dz) \qquad (11)$$

Statistics of the temperature distribution from this discrete injection may be obtained by the method of moments following Aris (1956), and Koh and Change (1973). Each term of equations (7) and (8) is multiplied by $x^k y^\ell$, and integrated over the domain $-\infty < x,\ y < \infty$ to obtain equations for the moments $C_{k,\ell}(z,\ t,\ \tau)$. Thus

$$\frac{\partial C_{k,\ell}}{\partial t} - kuC_{k-1,\ell} - \ell v C_{k,\ell-1} = k(k-1)E_x C_{k-2,\ell} + \ell(\ell+1)E_y C_{k,\ell-2} + \frac{\partial}{\partial z}\left(E_z\frac{\partial C_{k,\ell}}{\partial z}\right) - K_d C_{k,\ell} \qquad (12)$$

$$E_z\frac{\partial C_{k,\ell}}{\partial z} = 0 \text{ at } z = 0,\ H \qquad (13)$$

where

$$C_{k,\ell} = \int_{-\infty}^{\infty}\int_{-\infty}^{\infty} \Delta c x^k y^\ell\ dxdy \qquad (14)$$

The moment equations (12) can be integrated numerically beginning with the lower moments from $t = \tau$ to T. Initial conditions are specified according to the initial distribution of the source and include

$$C_{00}(z,\ t = \tau) = m_z(z) \qquad (15)$$

$$C_{10}(z,\ t = \tau) = x_0 \qquad (16)$$

$$C_{01}(z,\ t = \tau) = y_0 \qquad (17)$$

Higher moments are chosen to approximate the initial patch distribution.

Familiar statistics describing the distribution of excess temperature within the patch can be derived from the moments $C_{k,\ell}$. For example the statistics corresponding to the lower moments are

$$
\begin{aligned}
x_c &= C_{10}/C_{00} \\
y_c &= C_{01}/C_{00} \\
\sigma_x^2 &= C_{20}/C_{00} - (C_{10}/C_{00})^2 \\
\sigma_y^2 &= C_{02}/C_{00} - (C_{01}/C_{00})^2 \\
\sigma_{xy}^2 &= C_{11}/C_{00} - C_{10}\ C_{01}/C_{00}^2
\end{aligned}
\tag{18}
$$

where x_c and y_c are the coordinates of the center of mass of the distribution and σ_x^2, σ_y^2 and σ_{xy}^2 are the variances and the covariance of the distribution about its center of mass. A large number of moments would be necessary to completely describe a single patch. However, the lower moments provide the most information, and when a number of individual source solutions are superimposed to form a continuous solution, it is reasoned that the lower moments for each patch are sufficient to approximate the continuous plume. For instance, each patch could be replaced by a Gaussian patch with the same oth, 1st and 2nd moments. The peak concentration of this Gassian patch would be

$$C_{max} = C_{00}/(2\pi\sqrt{\sigma_x^2\sigma_y^2 - \sigma_{xy}^4}) \tag{19}$$

and the excess temperature distributions at time T after a release of source at time τ would be

$$
\begin{aligned}
C_i\ (w, y, z, T, \tau) = C_{max}\ \exp -\Bigg\{ \frac{\sigma_x^2\sigma_y^2}{\sigma_x^2\sigma_y^2 - \sigma_{xy}^4} \Bigg[\frac{(x-x_c)^2}{2\sigma_x^2} + \frac{(y-y_c)^2}{2\sigma_y^2} - \\
\frac{\sigma_{xy}^2 (x-x_c)\ (y-y_c)}{\sigma_x^2\sigma_y^2} \Bigg] \Bigg\}
\end{aligned}
\tag{20}
$$

Based on the linearity to equation (7), the temperature resulting from a source with excess temperature per unit depth of $\Delta M m_z(z)$ can be found by multiplying the equation for a unit injection (Equation (20)) by ΔM.

4. ANALYSIS OF A CONTINUOUS RELEASE

The far field source which is used in the present analysis is shown in Fig. 1 and is characterized by dimensions x_0, y_0, h_T and B, and angle θ, and the excess temperature distribution ΔC_s from the near field calculation. The excess temperature from the near field is expressed as

$$\Delta C_s = \frac{\Delta C_0}{D}\ T_y(\tilde{\tilde{y}}) T_z(z) \tag{21}$$

where D is the near field dilution and ΔC_0 is the initial temperature rise between plant intake and discharge. T_y and T_z are lateral and vertical distribution functions satisfying the relationships

$$
\begin{aligned}
\int_{-B/2}^{B/2} T_y(\tilde{\tilde{y}}) d\tilde{\tilde{y}} &= B \\
\int_0^{h_T} T_z(z) dz &= h_T
\end{aligned}
\tag{22}
$$

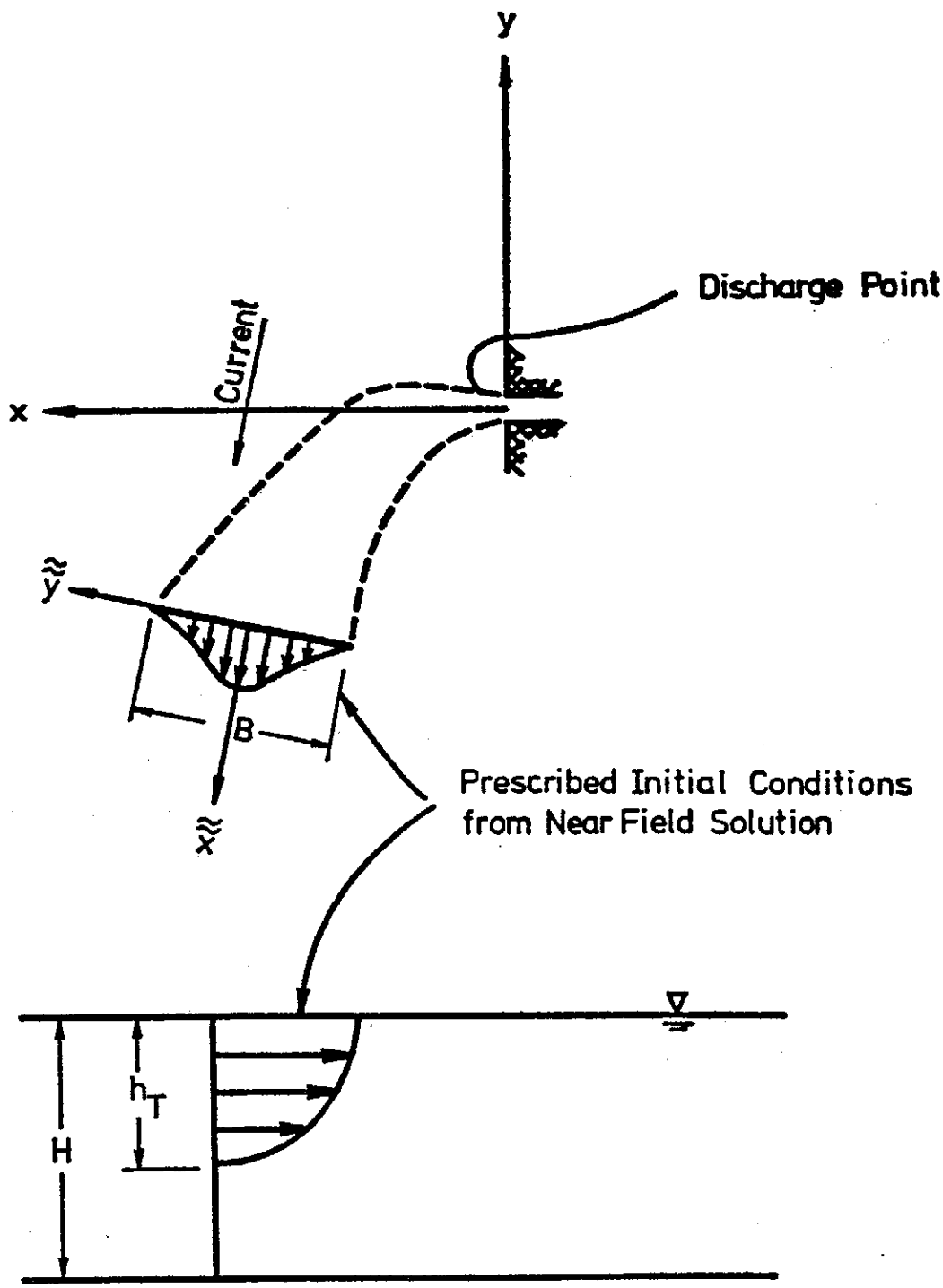

FIG. 1. Far Field Structure.

A continuous solution is approximated by superimposing the distrubtision from vertically-distributed discrete injections using NT time steps and NI(k) laterally distributed sources at each time step. Thus

$$C(x, y, z, T) = \sum_{k=1}^{NT} \sum_{n=1}^{NI(k)} \frac{m'(\tau)B(\tau)}{NI(k)} C_i(x, y, z, T, \tau)\Delta\tau(k) \qquad (23)$$

The strength of each discrete source, $\Delta M = m'm_z B(\tau)\Delta\tau/NI(k)$ is chosen to conserve heat and to provide a distribution of excess temperature at the source which is consistent with equation (21). Thus

$$\Delta M = \frac{Q_0 \Delta C_0 T_y(y) T_z(z) \Delta\tau \tilde{\tilde{\Delta y}}}{B\ h_T} \qquad (24)$$

The distribution of discrete source along the far field source and hence the initial conditions for x_c, y_c, σ_x^2 and σ_y^2 are chosen to provide a smooth temperature distribution at all points in the far field and to provide a reasonable approximation to the desired temperature distribution near the far field source. For small diffusion times, $t-\tau$, small values of $\Delta\tau$ are used and more than one source may be used at each time ($NI(k)>1$), while at larger diffusion times the time step increases and a single source is sufficient at each time step.

5. COMPUTATIONAL PROCEDURES

For the calculations of excess temperatures, equations (12) with the appropriate boundary and initial conditions are used to calculate $C_{k,\ell}$ and the excess temperature is obtained in relating to the moments from Eq. (20). The system equations for solving various order moments $C_{k,\ell}$, for example, the oth, 1st, and 2nd moments are

$$\frac{\partial C_{00}}{\partial t} = \frac{\partial}{\partial z}\left(E_z \frac{\partial C_{00}}{\partial z}\right) - K_d\ C_{00} \qquad (25)$$

$$\frac{\partial C_{10}}{\partial t} - u\ C_{00} = \frac{\partial}{\partial z}\left(E_z \frac{\partial C_{10}}{\partial z}\right) - K_d\ C_{10} \qquad (26)$$

$$\frac{\partial C_{01}}{\partial t} - v\ C_{00} = \frac{\partial}{\partial z}\left(E_z \frac{\partial C_{01}}{\partial z}\right) - K_d\ C_{01} \qquad (27)$$

$$\frac{\partial C_{20}}{\partial t} - 2u\ C_{10} = 2E_z\ C_{00} + \frac{\partial}{\partial z}\left(E_z \frac{\partial C_{20}}{\partial z}\right) - K_d\ C_{20} \qquad (28)$$

$$\frac{\partial C_{02}}{\partial t} - 2v\ C_{01} = 2E_y\ C_{00} + \frac{\partial}{\partial z}\left(E_z \frac{\partial C_{02}}{\partial z}\right) - K_d\ C_{02} \qquad (29)$$

$$\frac{\partial C_{11}}{\partial t} - u\ C_{01} - v\ C_{10} = \frac{\partial}{\partial z}\left(E_z \frac{\partial C_{11}}{\partial z}\right) - K_d\ C_{11} \qquad (30)$$

Equations (25)-(30) are weakly coupled and can be integrated numerically in the order of moments. In the numerical integration for $C_{k,\ell}$, a central difference in space and a Crank-Nicolson difference scheme in time are employed

whereby difference equations are expressed using variables averaged over the present and subsequent time steps. Uniform vertical grid spacing is used and variables are defined at grid points except for vertical diffusion which is defined for the interval between points.

The system equations (25)-(30) have the similar forms which the lefth-and side indicates the terms of local change advection while the righthand side contains the terms of diffusion and dissination. Since the advection terms and the diffusive terms in horizontal directions in each equation contain the lower moments which have been obtained from the previous equation, the approximation for these terms are then calculated directly from the present time step. The dinite-difference forms for terms at each grid point z and time step t are indicated below where $z=(j-1)\,\Delta z$, and $t=\tau+(n-1)\,\Delta\tau$, and the moment subscripts have been dropped for convenience.

$$\frac{\partial c}{\partial t} = (C_j^{n+1}-C_j^n)/\Delta\tau \tag{31}$$

$$\frac{\partial}{\partial z}\left(E_z \frac{\partial c}{\partial z}\right) = [E_{zj}\,(C_{j+1}^{n+1}+C_{j+1}^n-C_j^{n+1}-C_j^n) - E_{zj-1}\,(C_j^{n+1}+C_j^n-C_{j-1}^{n+1}-C_{j-1}^n)\,]/(2\Delta z^2) \tag{32}$$

$$K_d\ C = K_d^n(C_j^{n+1}+C_j^n)/2 \tag{33}$$

The diffusive terms at the surface and the bottom are written as

$$\begin{aligned}\frac{\partial}{\partial z}\left(E_z \frac{\partial c}{\partial z}\right)_{surf} &= E_{z1}(C_2^{n+1}+C_2^n-C_1^{n+1}-C_1^n)/\Delta z^2 \\ \frac{\partial}{\partial z}\left(E_z \frac{\partial c}{\partial z}\right)_{botton} &= E_{zNz}(C_{Nz-1}^{n+1}+C_{Nz-1}^n-C_{Nz}^{n+1}-C_{Nz}^n)/\Delta z^2\end{aligned} \tag{34}$$

After writing in the finite-difference form, the system of simultaneous difference equations for equations (25)-(30) has a tridiagonal coefficient matrix and is solved by Gaussian elimination. The distribution of discrete sources along the far field source is chosen to provide a smooth temperature distribution at all points in the far field and to provide a reasonable approximation to the desired temperature distribution near the far field source. Hence, the number of discrete sources used in describing the temperature distribution near the source is selected as NI where NI is an integer, and $NI \geq 1$. The error associated with the speading of the field width may increase with increasing NI, but in general the fit to the desired far fild source temperature distribution improves with increasing NI.

6. MODEL VERIFICATION

In order to verify the numerical scheme described previously, the numerical

model was used to compute the steady state two-dimensional excess temperature distribution downstream from a passive source of width B emitting a conservating substance of constant strength in a steady current with velocity of U in the x direction. A 4/3 diffusion law of the form

$$E_{x,y} = A\ \sigma_{x,y}^{4/3} \tag{35}$$

was assumed.

Calculations are compared with an analytical solution derived by Brooks (1960). Brooks computed a far field width L and centerline excess temperature C_{max} as a function of x using the equation

$$U\frac{\partial \Delta c}{\partial x} = E_y(x)\frac{\partial^2 \Delta c}{\partial y^2} \tag{36}$$

with boundacy conditions at $x=0$ of

$$\begin{aligned} \Delta c &= 1 \quad |y| \leq \frac{B}{2} \\ \Delta c &= 0 \quad |y| > \frac{B}{2} \end{aligned} \tag{37}$$

For the 4/3 diffusion law, his results are

$$\frac{L}{B} = \left(1 + \frac{9E_{y0}x}{UB^2}\right)^{3/2} \tag{38}$$

and

$$\frac{\Delta c_{max}}{\Delta c_0} = \mathrm{erf}\left\{\frac{3}{2}\left[\left(1 + \frac{8E_{y0}x}{B^2}\right)^3 - 1\right]^{-1}\right\} \tag{39}$$

where

Δc_0 = initial excess temperature

$L = 2\sqrt{3}\ \sigma_D$ ($L = B$ at $x = 0$)

$$\sigma_D^2(x) = \int_{-\infty}^{\infty} y^2 c(x, y)\, dy \Big/ \int_{-\infty}^{\infty} c(x, y)\, dy$$

and E_{y0} is the coefficient in his 4/3 power law,

$$E_y = E_{y0}\left(\frac{L(x)}{B}\right)^{4/3}$$

Relevant parameters used in the superposition calculation of the present model included $U = 15$ cm/sec, $B = 36{,}000$ cm, $A = 0.0517$ cm$^{2/3}$/sec, $NI = 5$, and $m = 1$. A comparison of dimensionless centerline temperature decay and lateral spreading is shown in Fig. 2. As expected the comparison is quite good. At the origin and at large x, the variances of the analytical and predicted solutions match exactly while for intermediate distances the analytical distribution is slightly wider.

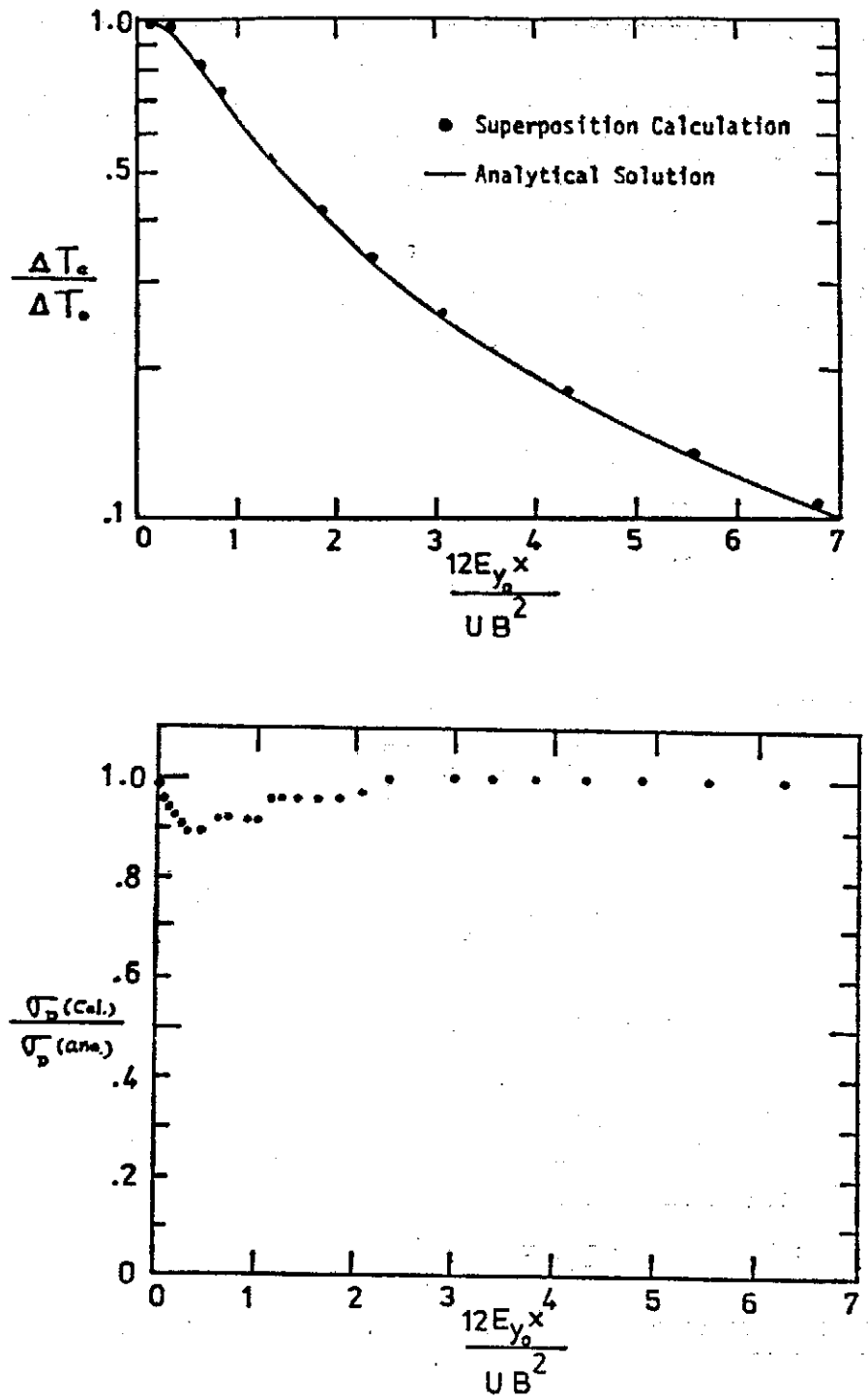

FIG. 2. Comparison of Analytical and Superposition Calculation for centerline Temperature Decay and Lateral Spreading.

7. APPLICATIONS

The model presented in this study has been applied to a site of power station to estimate the far field temperature distributions resulting from the surface discharge of heated water into the coastal sea. A combination of net alongshore current and tidal current are employed for the advection of the induced temperature calculations. The net alongshore current is considered to be wind driven and the tidal current is represented in both of the onshore-offshore component and the alongshore component. Far field source parameters were determined from the analysis of the near field calculations. Some of the computational results are shown in Fig. 3 and Fig. 4.

8. CONCLUSIONS

A far field model for calculating excess water temperatures resulting from the discharge of heated water in large bodies of water has been presented. In this model, three-dimensional excess temperatures were calculated for ambient currents which can be varied in the vertical direction and with time. Surface heat loss and turbulent diffusion in all dimensions could be included. The presence and dynamic effect of the near field can be handled explicitly by representing the location, size and dilution achieved in the near field as a known function of time.

REFERENCES

(1) Abraham, G. and G. C. Van Dam, "On the Predictability of Waste Concentrations", FAO Technical Conference on Marine Pollution, Rome, Italy, 1970.

(2) Adams, E. E. and D.R.F. Harleman, "Temperature Predictions for Offshore Power Plants", Proc. of ASCE Symposium on Modeling Techniques for Waterways and Coastal Engineering, San Francisco, 1975.

(3) Boericke, R. R. and D. W. Hall, "Hydraulic and Thermal Dispersion in an Irregular Estuary" ASCE, 100 HY1, 1974.

(4) Koh, R.C.Y. and C. Chang, "Mathematical Models for the Prediction of Temperature Distributions Resulting from the Discharge of Heated Water in Large Bodies of Water", EPA Water Pollution Control Series 16130 DWO, 1970.

(5) Leederse, J. J. and S. K. Liu, "A Water Quality Simulation Model for Well-Mixed Estuaries and Coastal Seas", The Rand Corp., Memo RM-6230-RC, 1970.

(6) Leedertse, J. J., and S. K. Liu et al, "A Three-Dimensional Model for Estuaries and Coastal Seas", The Rand Corp., R-1417-OWRR, 1973.

(7) Tsai, Y. J., and Y. C. Chang, "Two-Dimensional Transient Hydrothermal Mathematical Model", 1st World Congress on Water Resources, Chicago, Illinois, 1973.

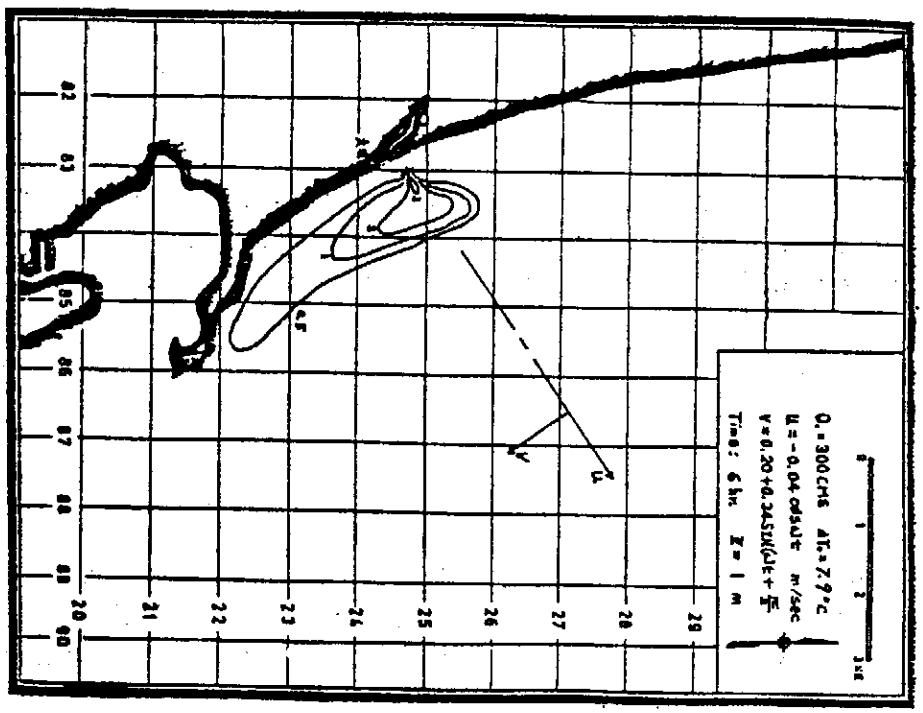

(a)

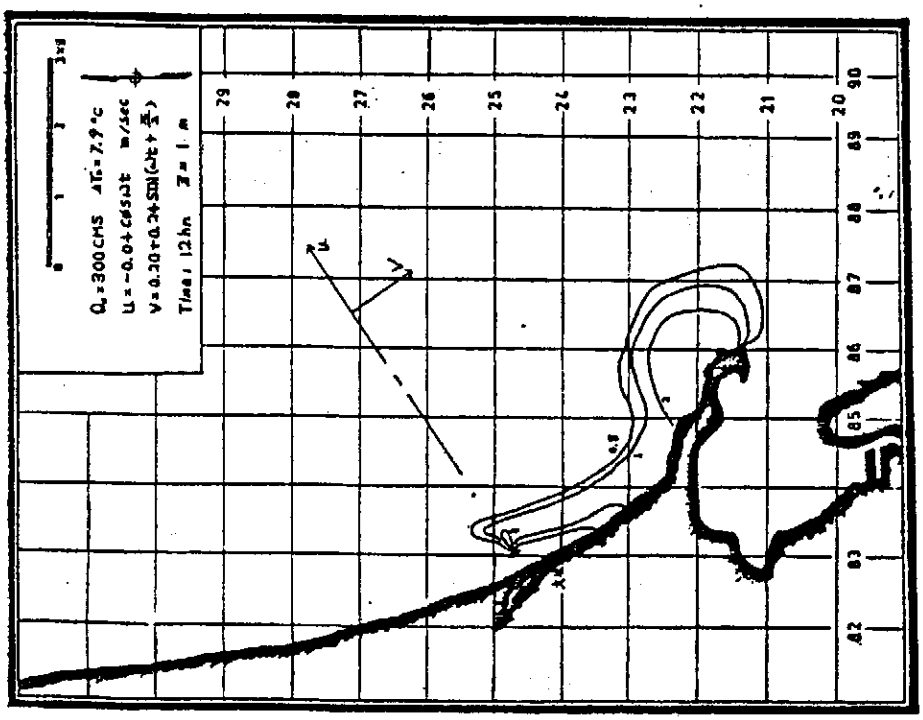

(b)

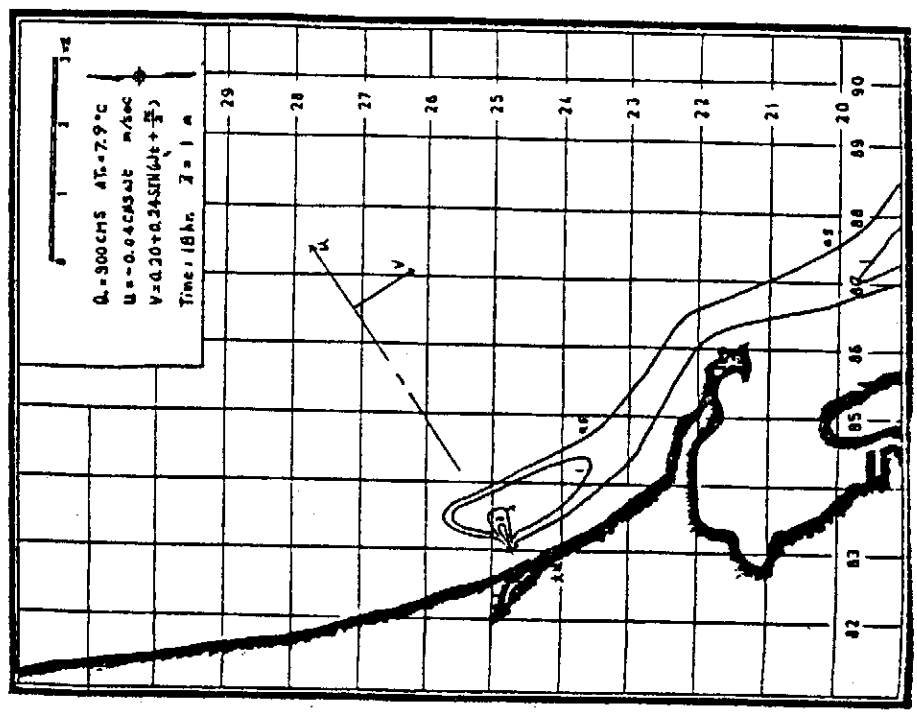

(c)

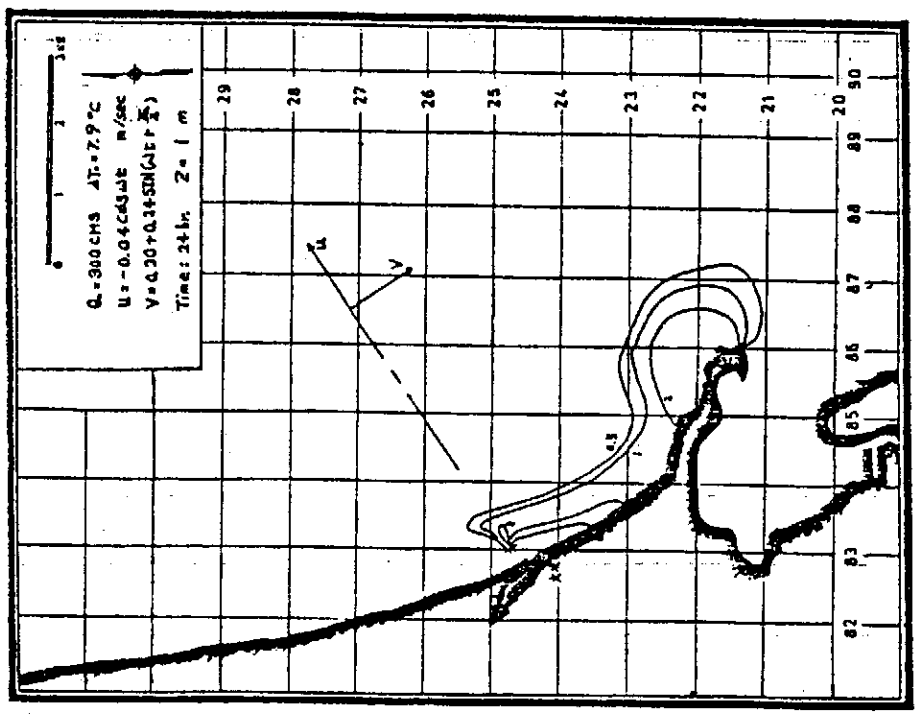

(d)

FIG. 3. Excess Temperature Calculations using Tidal and Net Longshore Currents at. Z=1 m.

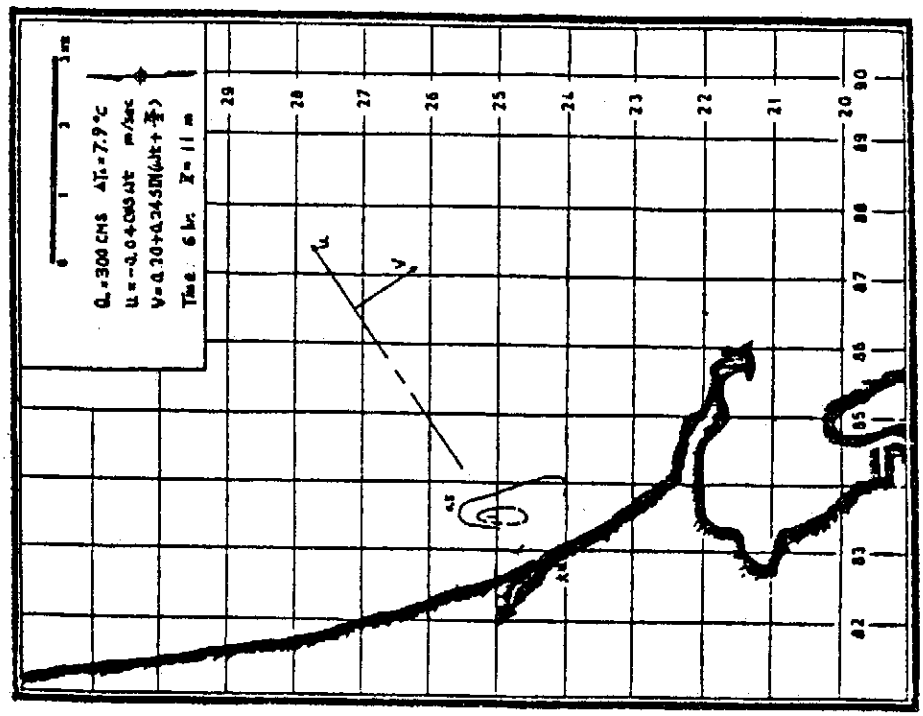

(a)

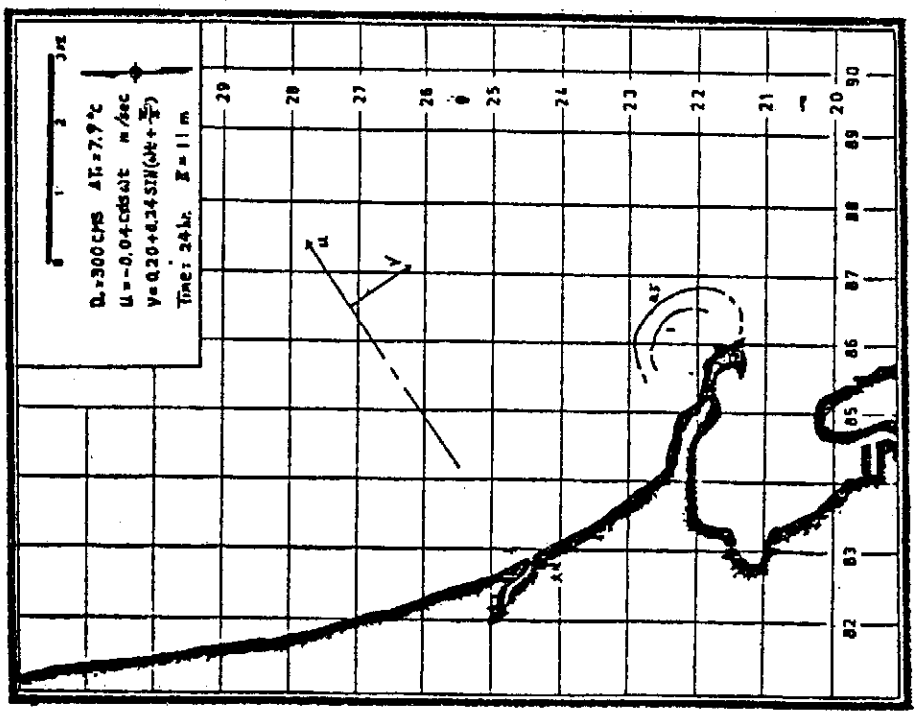

(b)

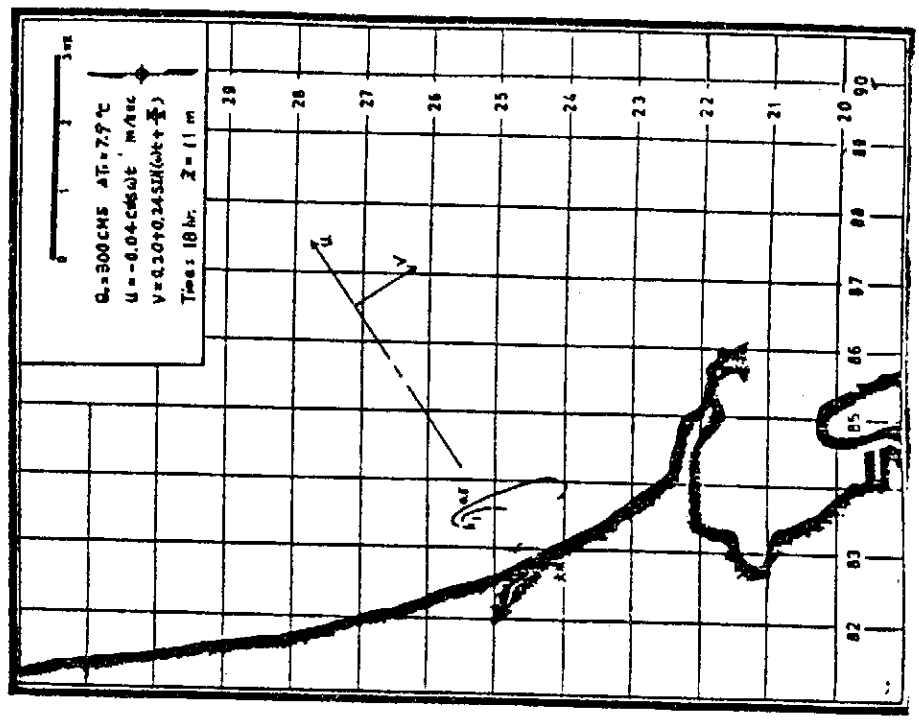

(c)

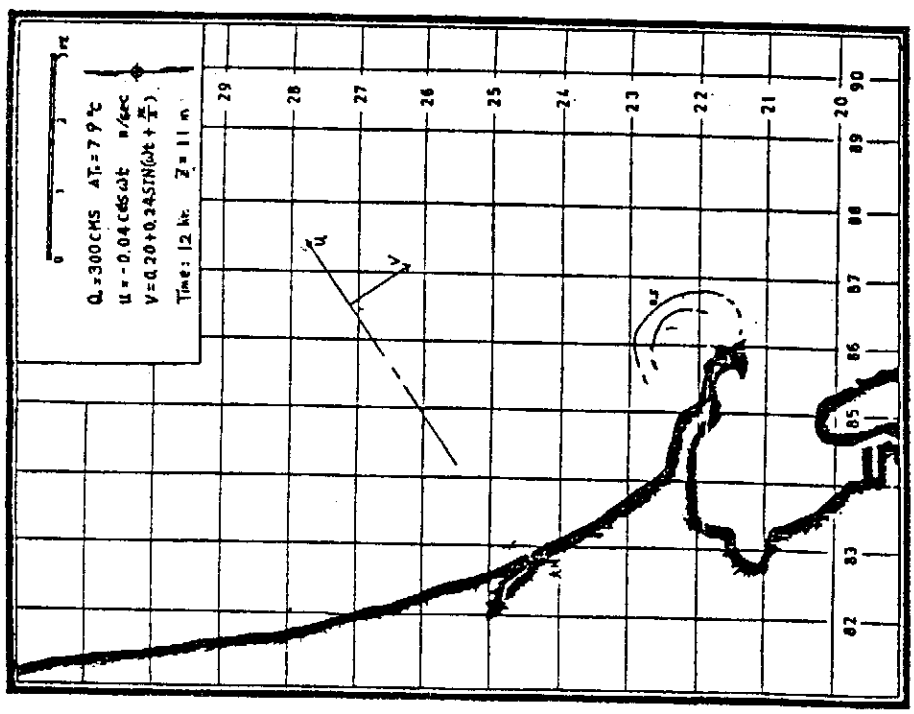

(d)

FIG. 4. Excess Temperature Calculations using Tidal and Net Longshore Currents at Z=11 m.

THE BUOYANT RISE OF PLUMES IN A STRATIFIED ENVIRONMENT*

ROBERT R. HWANG (黃榮燮)

Institute of Physics, Academia Sinica
Nankang, Taipei, Taiwan, R.O.C.

Abstract

A laboratory technique is developed for studying the rise of plane buoyant plumes issued vertically in a calm density-stratified environment. This study is to obtain such a jet-rise formula from correlating a substantial series of experimental data of experimental series of experimental data of laboratory study according to simple theoretical considerations such as dimensional analysis. The height of rise was obtained in terms of the initial momentum and buoyancy of plume and the stratification of the surrounding

A numerical technique for integrating the full Navier-Stokes and diffusion equations through an initial value problem has been used to investigate the time development of a line buoyant sturce issuing in the density-stratiffied environment. The basic physical features and some structures of the interactions of the motion at the intermediate mixing region are obtained. Results show that the stratification tends to inhibit the flow development of the buoyant source and to encourage the formation of a recirculatory vortex on the lower region near the source and the upper region.

1. INTRODUCTION

The rise of forced plumes in a possibly stratified environment is a particularly complex phenomenon. Buoyancy and initial momentum of the plume will cause the rise of the buoyant plume vertically and the density gradient of the stratified environment will influence the establishment of the flow field. In a stably stratified environment, the plume first behaves like a buoyant jet and mixes with heavy bottom ambient producing a neutrally buoyant cloud. The density deficit (or the temperature difference) of the buoyant plume will reduce continuously and becomes zero at a certain height (point of neutral buoyancy). The buoyancy force, from here-on, will be negative and the flow will be decelerated, turned down and spreaded sideway after reaching a maximum height.

Most of the plume-rise formulae appearing in the literature[1, 2, 3] are for plumes in a cross wind. They are not very universal, that is they often fit well only the data from they were correlated but not other data obtained under similar circumstances. Using the integral method and assuming a constant entrainment coefficient, Fan and Brooks[4] obtained a formula of rise of the waste-water plume discharged vertically into a linearly stratified environment. In replacement of the Gaussian profiles adopted in neutral environments, Morton et al[5] recommended top-hat profiles of vertical velocity and buoyancy in

* This paper also presented on 5th International Clean Air Congress, Buenos Aires, 20-26 October, 1980.

a stably stratified environment and obtained a scale diagram for maximum ascent heights of forced plumes to permit choice of the range of source conditions for a specified height of ascent and ambient stratification. These results of determining the rise of buoyant plumes in stratified environments have untill recently been no sufficiently well documented experimental evidence with which the theoretical predictions could be compared.

Previous research on buoyant discharge may conclude that it has concentrated mainly on the near field using the integral method with Gaussian diffusion model and empirical entrainment coefficients; and on the far field, the buoyancy effect is generally neglected and the pollutant becomes passive, advected by the ambient current and spreading under the action of ambient turbulent dispersion. Large scale interaction between the effluent and the receiving environment has to a large extent not been addressed, nor has the dynamics of the intermediate stage of pollutant spreading and flow variation. The intermediate stage is in most cases the principal stage of the development of the fate of the pollutant. Its study will provide a clearer understanding for the ceiling effect of a forced plume discharge into a stratified environment.

In this study, the rise of plane buoyant plumes discharged vertically into linearly stratified environments are investigated both experimentally and numerically. By using the dimensional analysis, the maximum height of rise of buoyant plume is related functionally to the discharge configurations and the stratifications of environments from correlating a substantial series of experimental data. A rise-formula was obtained in terms of the initial densimetric Froude number of discharged sources and the stratification parameter of the surroundinding environment. In numerical study, the dynamics of establishment of flow for a line buoyancy source discharged vertically into a linear stratified are investigated from the integration of the full Navier-Stokes and diffusion equations numerically through an initial value problem.

2. EXPERIMENTAL STUDY AND RESULTS

2.1. Dimensional Analysis

The discharge of a buoyant plume vertically into a calm environment subjects the mechanical effects of the jet momentum and buoyancy. Near the source, differences in velocity and volume flux between the effluent and the ambient fluid produce mixing due to the instability of the interface and due to the turbulent energy contained in the jet. Buoyancy causes rise of the plume. In a stably stratified environment, the density stratification can prevent the rise of plumes by inducing rapid mixing with the heavy bottom fluid,

thus producing a neutrally buoyant cloud. Therefore, the functional relationship which exists between the mximum height of rise of the plane buoyant plume and other variables involved, may be written in the form

$$Y_m = \phi_1(\mu_0,\ m_0,\ \beta_0,\ G) \tag{2-1}$$

in which, $\mu_0 = U_0 b_0$, $m_0 = U_0^2 b_0$, and $\beta_0 = [\ (\rho_1 - \rho_0)/\rho_1]\ g U_0 b_0$ are the initial fluxes of specific volume, momentum and buoyancy respectively; $G = (g/\rho_1)\ (-d\rho_a/dy)$, the parameter described the stratification of the environment.

By dimensional analysis, the functional relationship can be written as

$$\phi_2(Y_m \beta_0^{-1/3} G^{1/2},\ m_0^{-1} \beta_0^{1/3} \mu_0,\ m_0^2 \beta_0^{-2} G) = 0 \tag{2-2}$$

The first term indicates the normalized length scale of the height of rise; the second term is the ration of buoyancy to inertial forces at the source and can be simplified to a form of $F_0^{-2/3}$; while the last term in sq. (2-2) can be formed as $F_0^2\ S^{-1}$, in which $F_0 = U_0/\sqrt{(\Delta\rho/\rho_1)\, g b_0}$ and $S = (\Delta\rho/b_0)/(-d\rho_a/dy)$ are termed as densimetric Froude number and the stratification parameter respectivelly. Eq. (2-2) can then be rewritten as

$$\zeta_m = \phi_3(F_0^{-2/3},\ F_0^2\ S^{-1}) \tag{2-3a}$$

or

$$F_0^{-2} \zeta_m = \phi_4(F_0^{-8/3},\ S^{-1}) \tag{2-3b}$$

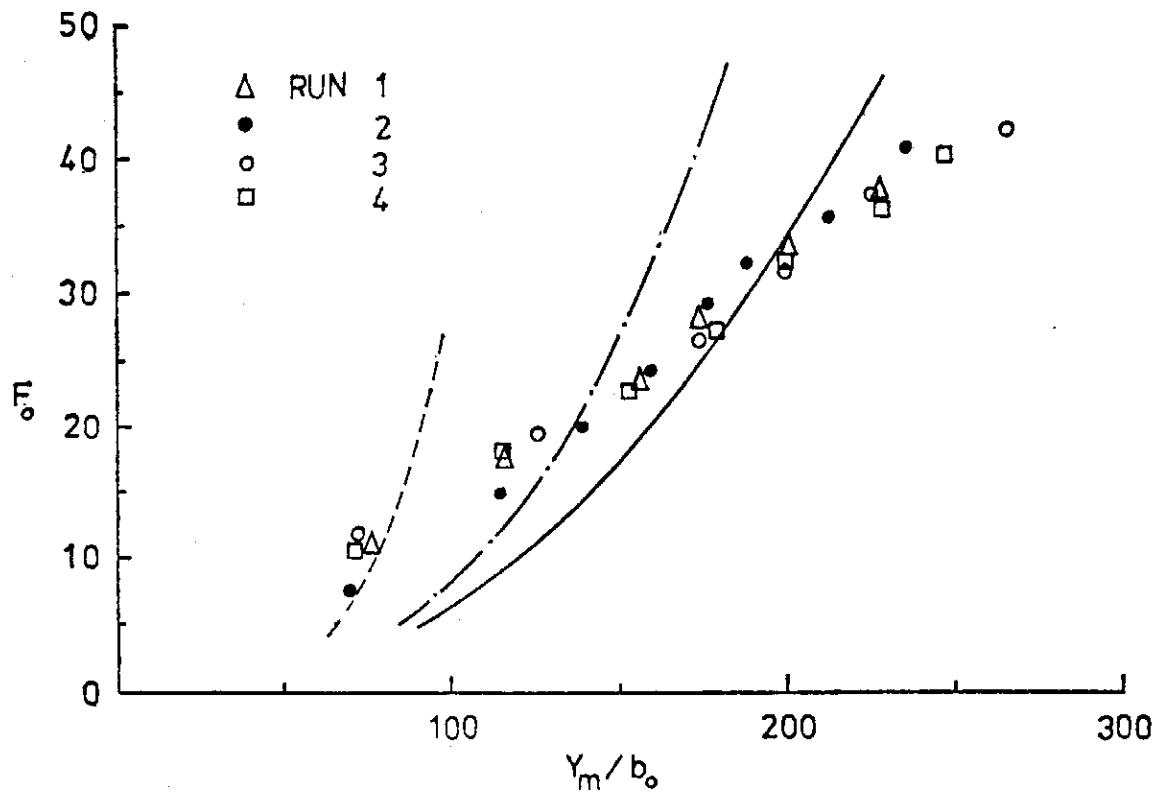

FIG. 1. Comparison of experimental and theoretical results on rise of vertical buoyant jets. Experimental results: △—S=310, ●—S=320. o—S=330, □—S=300: theoretical results: Brooks et al[4]…Briggs[1] Hwang et al for S=320.

in which $\zeta_m = F_0^{-1/3} S^{-1/2} Y_m/b_0$. The program of study was therefore designed to determine the functional relationship which exists between ζ_m and the other variables involved experimentally.

2.2 Experimental Procedure

The laboratory experiments were performed in a plexiglas test tank 178 cm long, 85 cm deep and 20 cm wide, filled with a linearly density-stratified salt solution. The equipment and the procedure used for filling a stratified salt solution can be referred from Hwang[6]. The flow was made visible by a suspension of small Pliolite S-5 beads which were illuminated by sheath light from both of the upper and the lower light boxes. A photographic technique given in Hwang[7] is used to trace the development of the flow field. Fig. 2. shows a photographic flow development with its corresponding density profile of the environment from the experiments.

A substantial number of experiments on plane buoyant plumes covered a wide range of flow configurations and ambient stratification were performed in the laboratory study. The experimental data were plotted in a full-logarithmic coordinates according to the dimensional analysis of Eq. (2-3) presents the plot of the ceiling height of rise against the variables involved. It is seen that the relationship can be represented approximately by a line and the ceiling height of rise can be described by

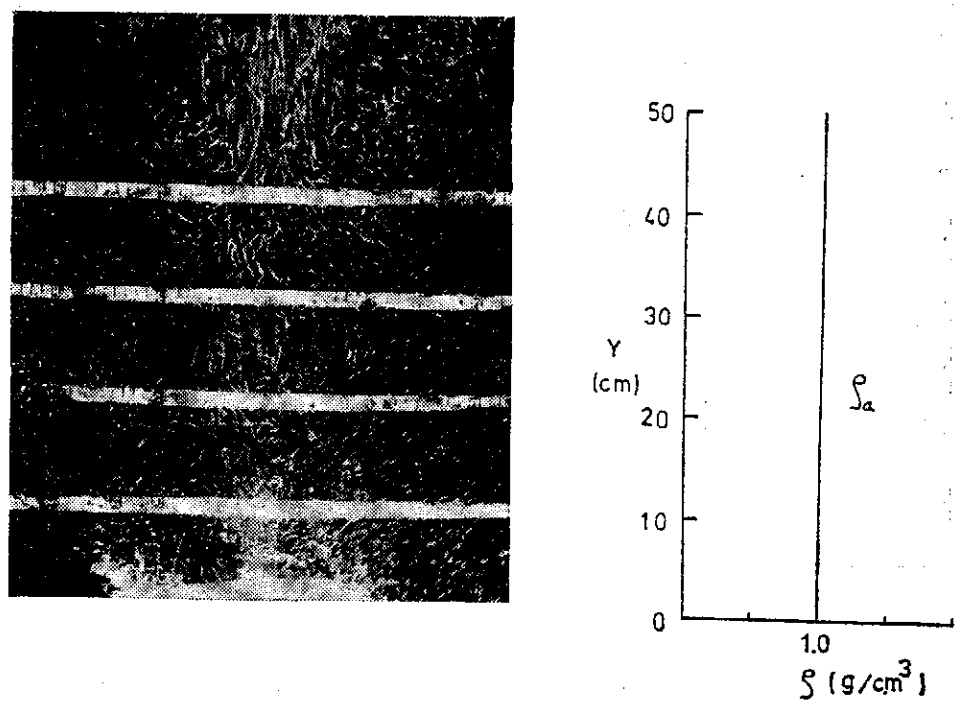

(a) $F_o = 10.$, $G = 0$, $S = \infty$

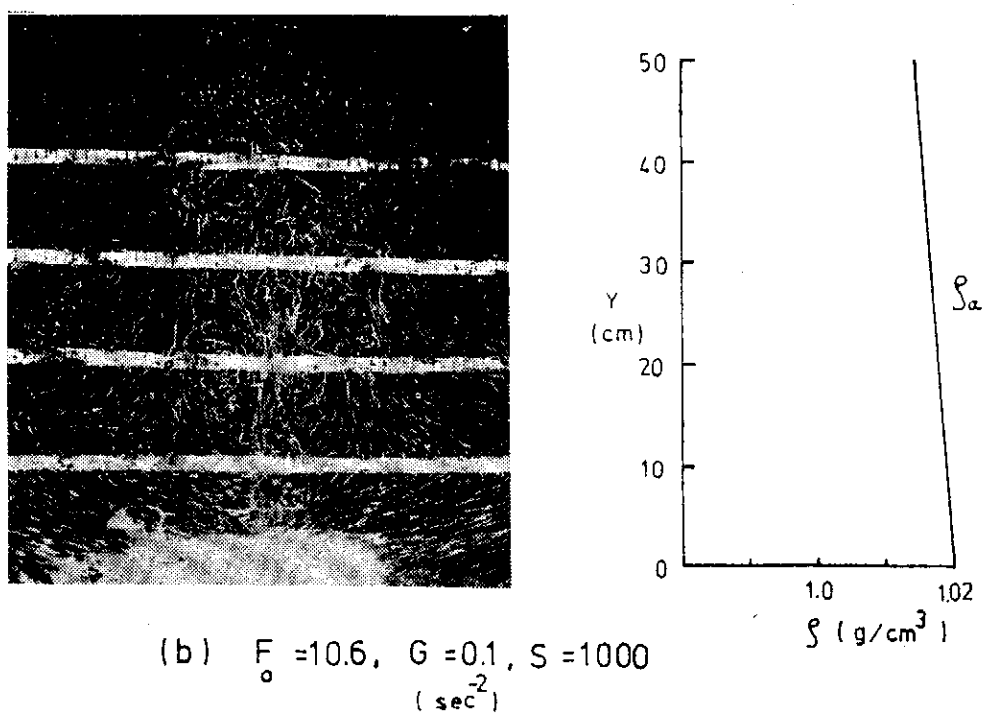

FIG. 2. Laboratory experiments of vertical buoyant jets into the correspondint environments

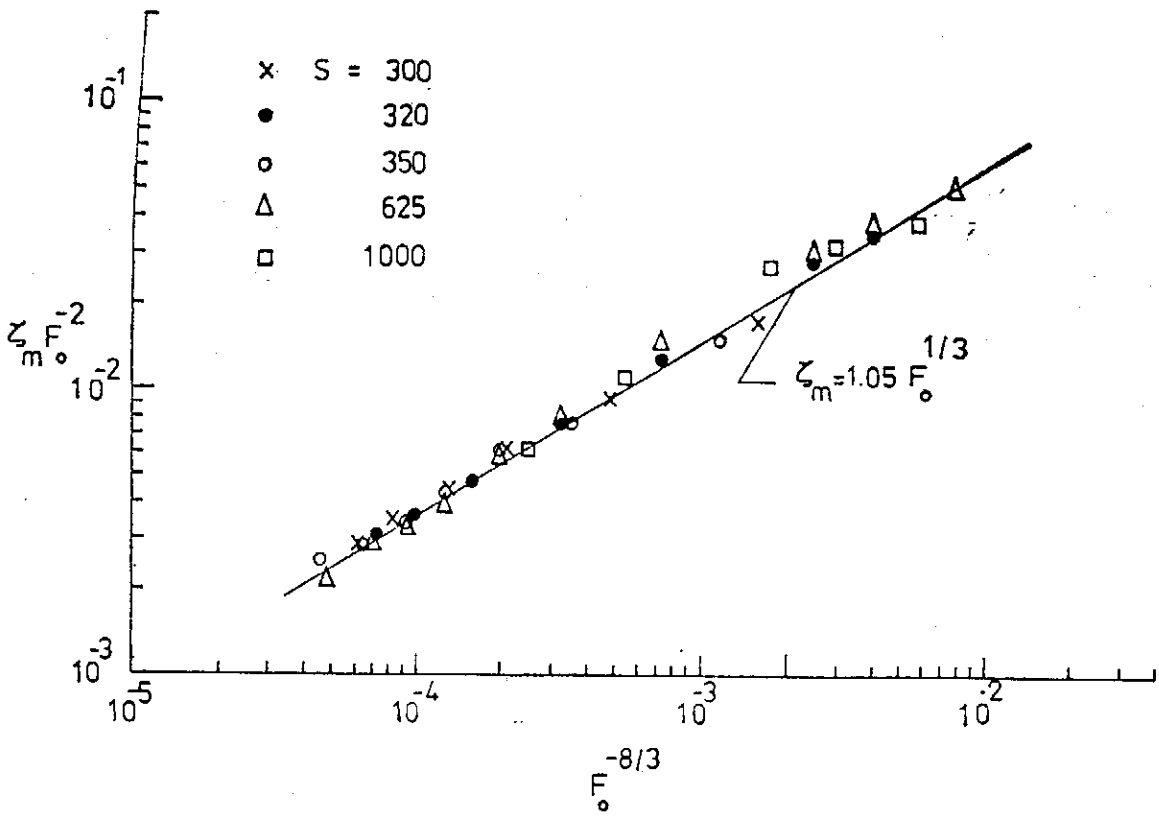

FIG. 3. The maximum height of rise of vertical buoyant jets in linearly density-stratified environments.

$$\zeta_m = 1.05\ F_0^{-1/3} \tag{2-4}$$

or in a simple form as

$$Y_m/b_0 = 1.05\ F_0^{2/3}\ S^{1/2} \tag{2-5}$$

The result, therefore, suggests that the maximum rise of plane buoyant plume is proportional to $F_0^{2/3}$ and $S^{1/2}$.

3. NUMERICAL STUDY

3.1 Formulation

In order to investigated the intermediate stage connecting the near and far fields for a line buoyant source discharged vertically into a stably stratified environment by following the behavior of the inflow throughout its history, the full Navier-Stokes equations, incorporating viscosity and diffusivity, will be solved numerically by a finite-difference scheme. The governing equations for an incompressible, viscous diffusive stably stratified Boussinesq fluid, two-dimensional flow in demsionless form are

$$\frac{\partial \gamma}{\partial t} + \frac{\partial}{\partial x}(u\gamma) + \frac{\partial}{\partial y}(v\gamma) = S_c^{-1}\ Re^{-1}\left(\frac{\partial^2 \gamma}{\partial x^2} + \frac{\partial^2 \gamma}{\partial y^2}\right) \tag{3-1}$$

$$\frac{\partial \zeta}{\partial t} + \frac{\partial}{\partial x}(u\zeta) + \frac{\partial}{\partial y}(v\zeta) = -F^{-2}\frac{\partial \gamma}{\partial x} + Re^{-1}\left(\frac{\partial^2 \zeta}{\partial x^2} + \frac{\partial^2 \zeta}{\partial y^2}\right) \tag{3-2}$$

$$\frac{\partial^2 \psi}{\partial x^2} + \frac{\partial^2 \psi}{\partial y^2} = \zeta \tag{3-3}$$

where $\zeta = \frac{\partial u}{\partial y} - \frac{\partial v}{\partial x}$, $u = \frac{\partial \psi}{\partial y}$, $v = -\frac{\partial \psi}{\partial x}$, $\gamma = (\rho_1 - \rho)/(\rho_1 - \rho_s)$, $t = t^*Q/d^2$

$Re = Q/\nu$ is the Reynolds number, $F = Q/(Nd^2)$ is the densimetric Froude number and $S_c = \nu/D$ is the Schmidt number, with ν, D and N denoting the kinematic viscosity, diffusivity and Vaisala frequency. Q is half of the discharge per unit width of the line source.

The flow field for the line buoyant source discharged vertically into a stratified environment is taken to be symmetric with respect to the effluent axis. A flow region as shown in figure 4 is then considered. The system of equations (3-1) through (3-3) are to be solved subject to the following boundary and initial conditions. These boundary and initial conditions are summarized as follows:

(1) $\psi = 1 - \frac{d}{h_e}x$, $\gamma = \gamma_e$, $\zeta = 0$; for $y = 0$, $0 \leq x \leq \frac{h_e}{d}$

(2) $\psi = y$, $\zeta = 0$; for $x \to \infty$, $0 < y < 1$

(3) $\psi = 1$, $\gamma = 1$, $\zeta = 0$; for $x > 0$, $y = 1$

(4) $\psi=1,\ \partial\gamma/\partial x=0,\ \zeta=0;$ for $x=0,\ 0<y<1$

(5) $\psi=0,\ \gamma=0,\ \zeta=0;$ for $x>0,\ y=0$

(6) $\psi=y+\frac{2}{\pi}\sum_{n=1}^{\infty}\frac{1}{n}\exp(-n\pi x)\sin n\pi y,\ \zeta=0,\ \gamma=y,$ for $t=0,\ x>0.$

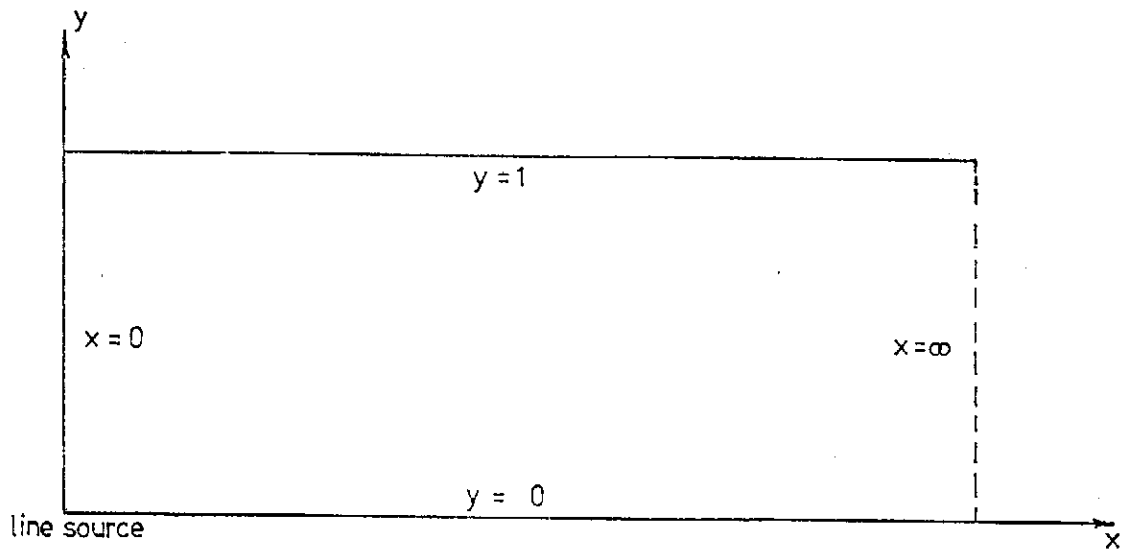

FIG. 4. Flow region for line source issued vertically of the study.

3.2 Numerical procedure

The present problem involves a boundary at infinity. In order to keep the finite-difference grid mesh fine in the vinicity of the source, where the gradients gradients are largest, and at the same time having larger grid points far away from the source, a stretched coordinate system in rendering the computational region finite similar to that described in Pao et al[6] is used. The transformation for such a system is given as

$$\bar{x}=1-\exp(-ax),\ \bar{y}=y \tag{3-4}$$

where a is a scale factor. On substituting the transformation relation (3-4) into the governing equations (3-1)-(3-3), we obtain

$$\frac{\partial\gamma}{\partial t}+a(1-\bar{x})\frac{\partial}{\partial\bar{x}}(u\gamma)+a(1-\bar{x})\frac{\partial}{\partial\bar{y}}(v\gamma)=S_c^{-1}Re^{-1}[a^2(1-\bar{x})^2\frac{\partial^2\gamma}{\partial\bar{x}^2}-a^2(1-\bar{x})\frac{\partial\gamma}{\partial\bar{x}}+\frac{\partial^2\gamma}{\partial\bar{y}^2}] \tag{3-5}$$

$$\frac{\partial\zeta}{\partial t}+a(1-\bar{x})\frac{\partial}{\partial\bar{x}}(u\zeta)+a(1-\bar{x})\frac{\partial}{\partial\bar{y}}(v_1\zeta)=-F^{-2}a(1-\bar{x})\frac{\partial\gamma}{\partial\bar{x}}+Re^{-1}[a^2(1-\bar{x})^2\frac{\partial^2\zeta}{\partial\bar{x}^2}-a^2(1-\bar{x})\frac{\partial\zeta}{\partial\bar{x}}+\frac{\partial^2\zeta}{\partial\bar{y}^2}] \tag{3-6}$$

$$a^2(1-\bar{x})^2\frac{\partial\psi}{\partial\bar{x}^2}-a^2(1-\bar{x})\frac{\partial\psi}{\partial\bar{x}}+\frac{\partial^2\psi}{\partial\bar{y}^2}=\zeta \tag{3-7}$$

where $v_1 = -\partial\psi/\partial\bar{x}$

The solution of Eqs. (3-5)-(3-7) subject to the appropriate boundary and initial conditions is accomplished by writing these equations in a finite-difference form, and solving them on a digital computer, according to the following algorithm. (1) At $t=0$ the initial conditions prevail. (ii) The u and v_1 velocity fields at $t=0$ are computed from the relationship of u and v_1 with ψ. (iii) Eq. (3-5), subject to the appropriate boundary conditions, is used to make a time step in the density field γ. (iv) Eq. (3-6) is used to make a time step in the vorticity field ζ. (v) With the new result for the vorticity field, a new value for the ψ field is computed by over-relaxing Eq. (3-7), subject to the appropriate boundary conditions. (vi) The velocity fields u and v_1 are then update from this new field by performing the step (iii)-(vi) are repeated so that the time development of flow field can be studied.

For finite differencing, a central difference in space and forward difference in time are used, except in the case of the nonlinear terms, for which three-point non-central differencing method similar to that described in Torrance & Rockett[9] is adopted. By choosing the scale factor properly, Δx can be made equal to 0.1 near the origin, while Δx invariably becomes very large as Δx approaches infinity. In most runs, the time increment Δt was set 1.0×10^{-3} and $\Delta\bar{y}$ was chosen to be 0.025, which corresponds to 40 equal grid spacings in the vertical direction.

3.3 Numerical results

The establishment of flow for a line buoyant source discharged vertically into a stratified environment of finite depth was computed numerically in the variations of the discharge condition and the ambient stratification. Fig. 5 shows the flow field of $F=0.11$ $Re=200$, $Sc=5$ and $\gamma_j=1.0$ (or corresponding to $Fo=4.001$ at $t=0.2$. The stratification of the ambient prevents the effluent from inducing a vortex in the lower region. The formation of the vortex may be explained that the first term on the right-hand side of Eq. (3-6. (3-6) represents the vorticity generation by buoyancy forces; this term can be written as $-F^{-2}\partial\gamma/\partial x$. It is seen that near the exit of the line source, heavier fluid lies to the right of lighter fluid, $\partial\gamma/\partial x$ is negative and positive vorticity (clockwise rotation) will be generated due to the tendendcy of the lighter fluid to rise and the heavier fluid to fall. The vorticity which is produced at the lower region near the exit is positive.

As the stratification of the ambient environment is increased, the retardation of the flow development from the source efflux becomes serious. The phenomena of ceiling effect due to the ambient stratification can be seen from

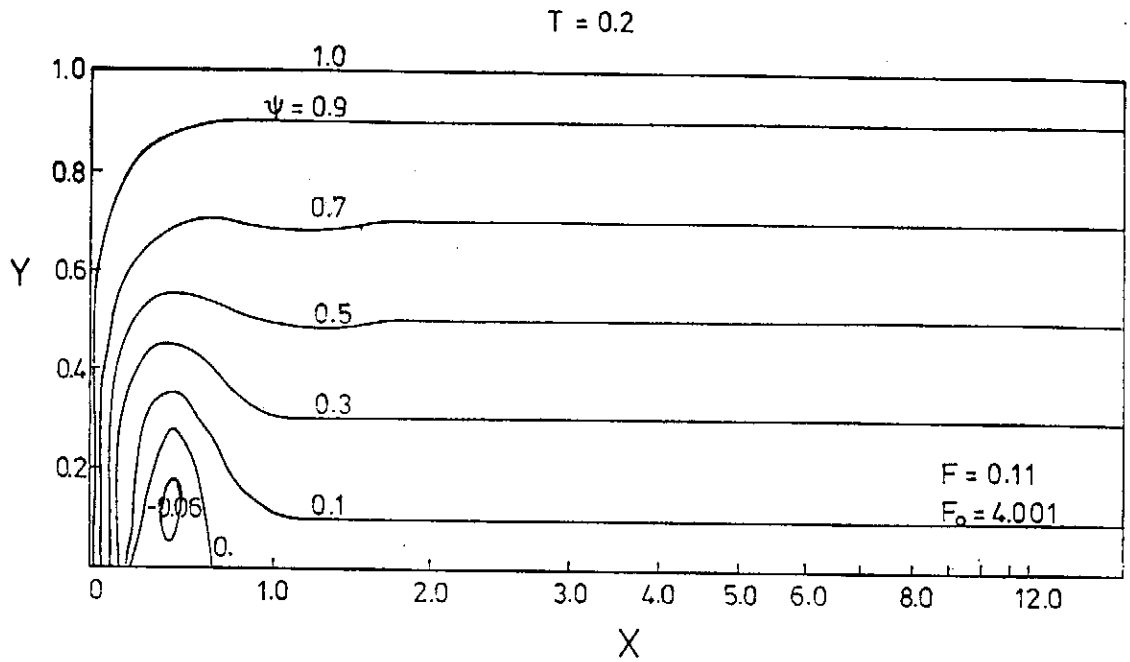

FIG. 5. Streamline pattern for F=0.11, Re=200, Sc=5 and Fo=4.001 at t=0.2.

Fig. 6. Fig. 6 shows the flow development of $F=4.45\times10^{-2}$,Re=200, $S_c=5$ and Fo=4.0 at t=0.2. It is seen that the retardation of the flow development from the ambient stratification is to form an anti-clockwise vortex in the upper region. The vortex region will grow in sense of time. Figure 7 shows the

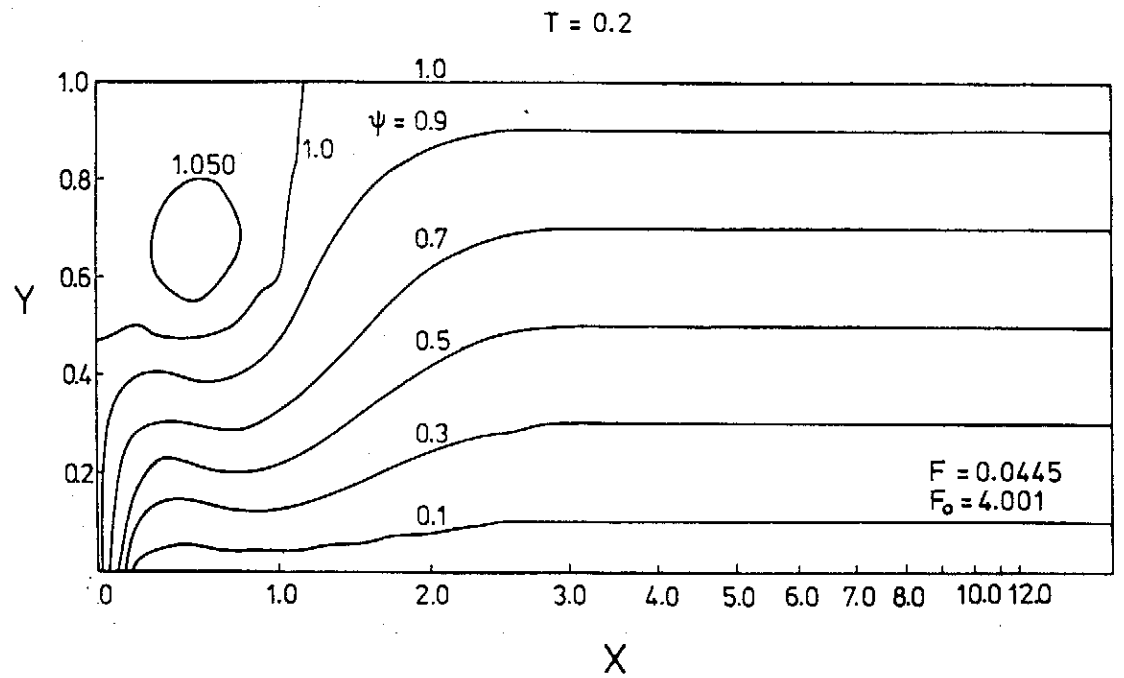

FIG. 6. Streamline Pattern for $F=4.45\times10^{-2}$ Re=200, Sc=5 and Fo=4.001 at t=0.2.

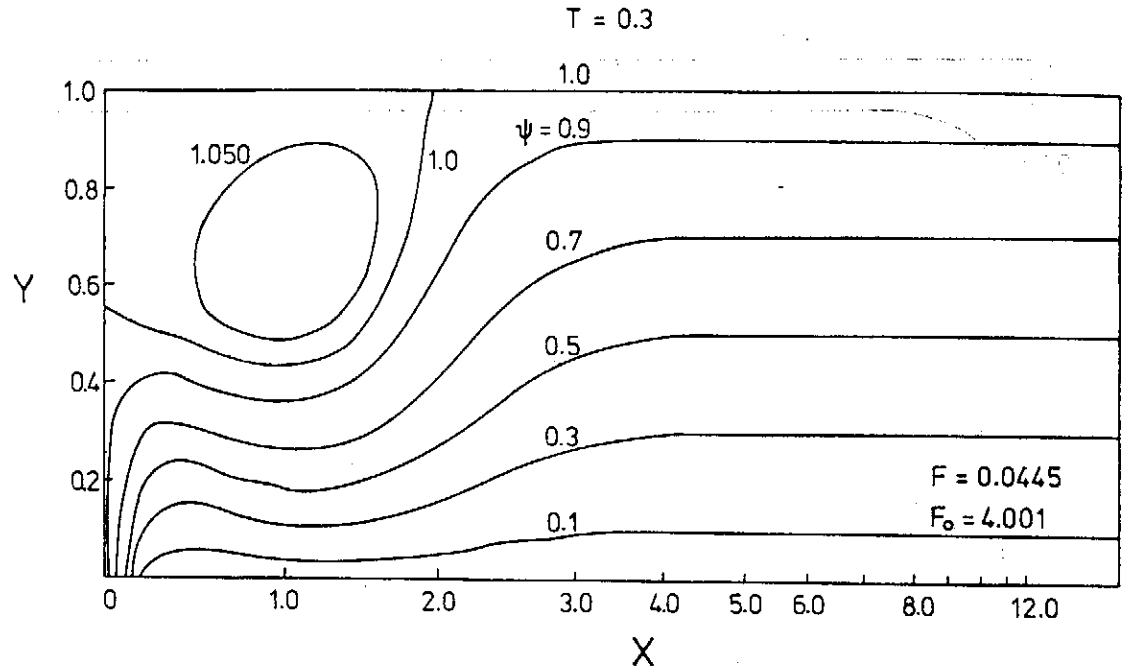

FIG. 7. Same flow conditions as Fig. 6 except at t=0.3

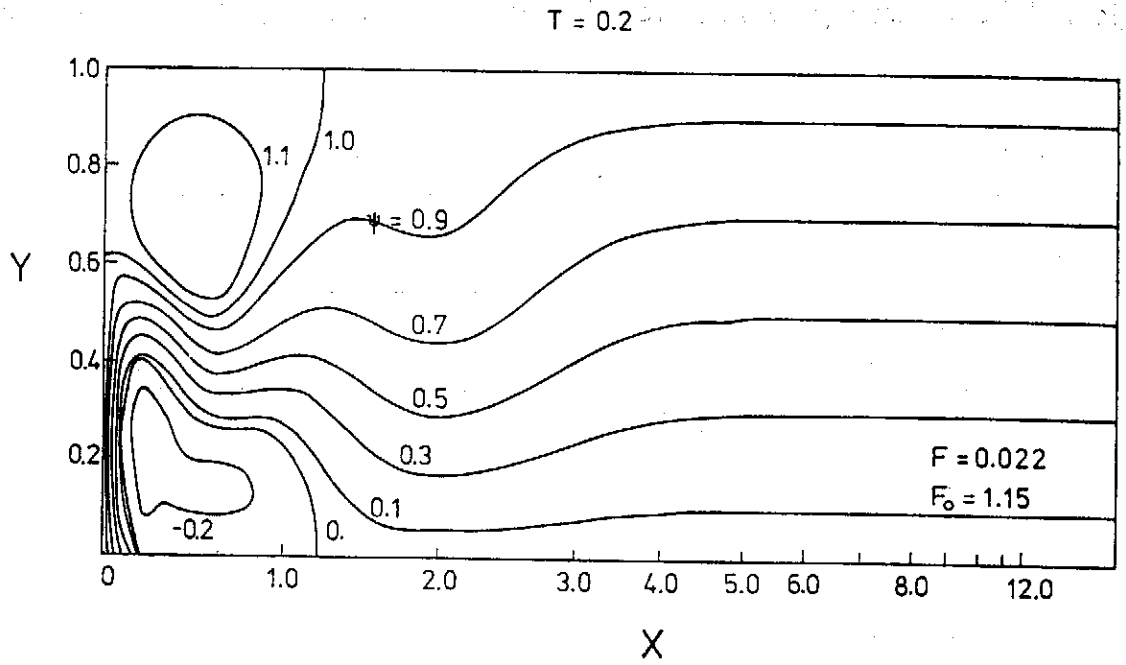

FIG. 8. Streamline pattern for F=0.022, Re=200, Sc=5 and Fo=1.15 at t=0.2

time development of the flow field at $t=0.3$. When the density of the exit source decreases and the stratification of the ambient environment increases, the interaction between the effluent and the receiving environment becones very complicated. Vortexes are formed in both of the lower and upper regions. The dynamics of the establishment for such case can be seen in figure 8. This figure shows the flow development of $F=0.022$ and $Fo=1.15$ at $t=0.2$. It is also noted that a wave-like flow pattern was formed in this time stage. It is properly due to the propagation of the disturbances in the stratified environments in which internal wave are generated. This may explain the flow establishment at this intermediate region in some extent.

4. CONCLUDING REMARKS

A laboratory technique is developed for studying the rise of plane buoyant plumes discharged vertically in the density-stratified environments. The maximum height of rise is related functionally to the discharge configuration of efflux and the stratification of surrounding environments on the basis of dimensional analysis. Although some theoretical computations are available in predicting the ceiling height of buoyant plumes discharged in the stratified environments, those models were obtained underlying that the velocity profiles as well as density profiles are assumed to be similar at all cross sections normal to the jet trajectory throughout the flow field. It is seen that the density deficit of a buoyant plume issuing into a stably stratified environment reduced continuously and becomes zero at the point of neutral buoyancy. Beyond it, the flow decelerates and spreads sideways, and the flow is no more similar. Therefore, the functional result relating the maximum height of rise to the discharge configuration and the ambient stratification obtained in this study provides a powerful result.

The detailed structure of flow field for a line buoyant source discharged in a stratified fluid at the intermediate region is not clear at the present. In this study, a laminar model from the numerical integration of the full Navier-Stokes and diffusion equations through an initial value provides a mean in investigating the time development of flow feld to account for the motions in both the buoyant efflux and the surrounding environment of density stratification in some extent. The results obtained from this numerical study are very encouraging for the precusor to study the detailed structure and the basic physical features of the intermediate mixing region.

REFERENCES

(1) Briggs, G. A. (1969) Plume rise, U.S. Atomic Energy Commission, Div. Technical Information.
(2) Csanady, G. T. (1973) Effect of plume rise on ground pollution, Atmospheric Environment 7, 1-16.
(3) Moore, D. J. (1974) A comparison of the trajectories of rising buoyant plume with theoretical/empirical models, Atmospheric Environment 8, 441-457.
(4) Fan, L. N. & Brooks, N. H. (1975) Fluid mechanics of waste-water disposal in the ocean, Ann. Rev. of Fluid Mech., 7, 187-211.
(5) Morton, B. R. & Middleton, J. (1973) Scale diagrams for forced plumes, J. Fluid Mech. 58, 165-176.
(6) Hwang, R. R. (1979) Rise of buoyant jets in density-stratified environments—a laboratory study, Proc. of the NSC, Vol. 3, 242-247.
(7) Hwang, R. R. et al (1978) Laboratory study of the effects on typhoons encountering the mountains of Taiwan islands, Studies & Essays in Commemoration of the Golden Jubilee of Academia Sinica, R.O.C., 171-190.
(8) Pao, H. P. & Kao, T. W. (1974) Dynamics of establishment of selective withdrawal of a stratified fluid from a line sink, J. Fluid Mech., 65, 657-688.
(9) Torrance, K. E. & Rockett, J. A. (1969) Numerical study of natural convection in an enclosure with localized heating from below, J. Fluid Mech., 36, 33-54.

A NEW TIME INTEGRATION SCHEME FOR PRIMITIVE EQUATION MODEL OVER EAST ASIA AREA

LAI-CHEN CHIEN (簡 來 成)

Institute of Physics, Academia Sidica, Taipei, Taiwan

Abstract

A four-level primitive equation model in pressure coordinate incorporation an efficiency computational scheme, hopscotch method, has been developed for numerical weather prediction in Mei-Yu season over the East Asia. The forecast equations are carried out by making use of this scheme. The method applies explicit and implicit finite difference schemes at alternate mesh points to integrate the forecast equations. Each time step the prognostic equations are calculated in two sweeps of the mesh. In the first and subsequent odd-numbered time steps, the grid points with i+j odd (i is the row number, j the column number) are calculated based on current values of the neighboring points. For the second sweep at the same time level, the computation is carried out at the points with i+j even, using the advanced values of neighboring points calculated in the first sweep. The first sweep is explicit, while the second is fully implicit with no simultaneous algebraic solution. The forecasts have been made for real data using time step up to 30 minutes. For comparion, the twenty-four hour predicted geopotential field pattern agrees with that of four-level baroclinic quasi-geostraphic model. The hopscotch method enables primitive equation model to use the integration time steps similar to those of quasi-geostraphic model.

1. INTRODUCTION

Numerical models based on the baroclinic primitive equation model established for several years are the powerful implements to study large-scale weather forecasts. Although the primitive equation models are simpler and involve fewer approximations than filtered equation model, the presence of gravity wave requires a much smaller time step during numerical integration. Investigators use a wide variety of time integration schemes for their numerical experiments. Smagorinsky, Manabe and Holloway (1965) studied the general circulation model by centered difference method. Kasahara and Washington (1967) developed NCAR global circulation model using the modified version of Lax-Wendroff scheme. Young (1968), Lilly (1965) and Kurihara (1965) performed different computational methods and investigated a number of time integration schemes. The accumulation of experimental evidence did not succeed in reducing the number of integration considered by atomospheric scientists.

The finite difference methods developed by Shuman (1962) and later used at National Meteorological Center in the operational primitive equation forecast model developed by Shuman and Hovermale (1968) were explicit method.

The explicit schemes require small time step to avoid computational instability. It is expensive in terms of computer time. As a consequence, there has been considerable effort to circumvent the stability requirement. Shuman (1971) suggested a modification of the leap-forg time-differencing system for his model which could reduce the number of calculation for a given forecast by up to a factor of two.

Marchuk (1966) introduced a finite differencing scheme which treated the gravity waves implicitly, and developed a number of practical problem permitting a much larger time step. Kurihara (1965) and Holton (1967) applied the implicit method to linear wave equations. Robert (1969) performed nonlinear barotropic integration with a spectral model based on primitive equation by implicit method using a time step of the order of 10 minutes. Kwizak and Robert (1971) successfully applied a semi-implicit differencing method to a barotropic 500 mb forecast which allowed a computational saving of factors up to three over conventional explicit method. Shortly afterwards, the same method was applied to three-dimensional baroclinic models. Gerrity, McPherson and Scolnik (1973) developed the semi-implicit differencing equations using Shuman's semi-momentum differencing technique for National Meteorological Center six-layer primitive equations model. Robert, Henderson and Turnbull (1972) Bourke (1974), Gauntlett, Leslie, McGregor and Hincksman (1976), Campana (1979) have reported similar experimental success of semi-implicit concepts to integrate the models using a larger time step.

Recently, the split explit schemes is developed (Gadd, 1978; Madala, 1979) and is used operationally for 10-level model at Meteorological office with computing time required one-third of semi-implicit scheme. The author (Chien and Wang, 1979) adopted a newly developed numerical scheme, hopscotch method, to integrate the quasi-geostraphic equations for numerical weather prediction with satisfactory results. Twenty-four hour integration from real data with time steps of 30 and 60 minutes shows no difference for 3 significant figures. The new numerical scheme is tried to adopted to integrate the primitive equation over the East Asia Aera to obtain the accurate results by increasing time step. The forecasts have been made for real data in Mei-Yu season using time step up to thirty minutes. For comparison, the twenty-four hour predicted geopotential field pattern agrees with that of four-level baroclinic quasi-geostraphic model (Chien and Wang 1979).

For the sake of economy and ease of experimentation, the oragraphy, friction and diabatic effect have not been employed. The model is flexible so that it will be relatively easy to perform numerical experiments with integration schemes.

2. DESCRIPTION OF THE MODEL

The limited area model described here is an adoption to a Lambert conformal projection of the domain over the East Asia. For simplicity, we consider the rectangular grid and arrange all variables in the equation on the same grid points (Okamura, 1975). The model is a four-level primitive equation model, Fig. 1. The predicting wind velocities geopotential and temperature are at 300 mb, 700 mb and 900 mb. The equations governing large-scale atmospheric phenomena are expressed using Cartesian coordinates and pressure vertical coordinate. Using the notation defined in Table 1, we can write the differential equations in of (x, y, p) coordinate as follows.

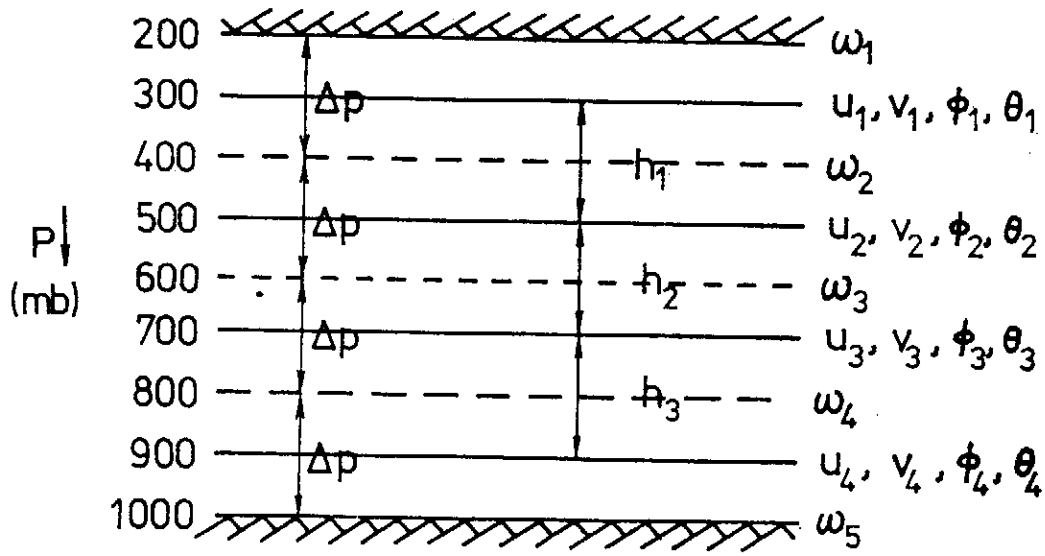

FIG. 1. Schematic diagram for the vertical structure of four-level model.

TABLE 1

x, y	Cartesian coordinates in East and North directions
p	vertical pressure coordinate
t	time
$\frac{\partial}{\partial t}$	partial derivative with respect to time
u	component of the horizontal wind in the x direction
v	compon en t of the horizontal wind in the y direction
ω	component of vertical p-velocity
ϕ	geopotential
R	the gas constat for pure dry air
T	temperature
θ	potential temperature
f	coriolis parameter
ψ	stream function
χ	velocity potential

The equations governing the horizontal velocity are

$$\frac{\partial u}{\partial t} + u\frac{\partial u}{\partial x} + v\frac{\partial u}{\partial y} + \omega\frac{\partial u}{\partial p} - fv + \frac{\partial \phi}{\partial x} = 0, \tag{1}$$

$$\frac{\partial v}{\partial t} + u\frac{\partial v}{\partial x} + v\frac{\partial v}{\partial y} + \omega\frac{\partial v}{\partial p} + fu + \frac{\partial \phi}{\partial y} = 0. \tag{2}$$

The quasi-static appromimation between gravity and the static air pressure, the hydrostatic equation, is

$$\frac{\partial \phi}{\partial p} = -\frac{RT}{p}. \tag{3}$$

Continuity equation for quasi-static atmosphere is

$$\frac{\partial u}{\partial x} + \frac{\partial v}{\partial y} + \frac{\partial \omega}{\partial p} = 0. \tag{4}$$

The thermodynamic energy equation is

$$\frac{\partial \theta}{\partial t} + u\frac{\partial \theta}{\partial x} + v\frac{\partial \theta}{\partial y} + \omega\frac{\partial \theta}{\partial p} = 0, \tag{5}$$

where θ is potential temperature, defined by

$$\theta = T(P_{1000}/P)^{R/C_p}/P. \tag{6}$$

u, v, ω, ϕ and θ, the five dependent variables as the velocities in x-direction and y-direction, the vertical p-velocity, the geopotential and the potential temperature can be solved by the above equations.

How to formulate the lateral boundary conditions is one of the most serious problem in limited area numerical weather prediction. Although it is well known, the problem has not been resolved. In the past, most of the investigators (Bushby and Timpson, 1967, Shuman, 1962) treated a rather simple way. They assummed that all variables were held constant at their initial values on the boundary during the forecast. The tests showed a great deal of noise being generated at the lateral boundaries. Some attempts were made to find boundary conditions closer to the physical problems (Williamson and Browning, 1974; Gauntett, Leslie, McGregor and Hincksman 1978).

To reduce the amplitude of all computational modes and other short-wave disturbance but leave the main solution unaltered, Perkey and Kreitzberg (1976) constructed the numerical boundary conditions of "sponge damping" with weighting tendencies. The variable $A_{i,j}^{n+1}$, at time n+1 on the grid point (i, j), is computed from the previous time step quantity and its tendency,

$$A_{i,j}^{n+1} = A_{i,j}^{n} + \omega_{i,j}\left(\frac{\partial A_{i,j}}{\partial t}\right)^{n}\Delta t \tag{7}$$

where n is the time step index, Δt the time step increment, $\omega_{i,j}$ the weighting coefficent. In this study, we take $\omega_{i,j}=0.5$.

3. FINITE DIFFERENCE EQUATIONS

The numerical experiment in this study try to incorporate the new numerical scheme in four-level primitive equation model. As presented by shuman and Hovermal (1968), Millers (1969) Gerrity, McPherson and Scolink (1973), the government equations were transformed into difference equations containing a great deal of horizontal averaging. The variables u, v, ω, θ and ϕ were defined at the grid points with averages. And differencing was defined between the neighbor grid points, e.g.,

$$\bar{u}^{x}_{i,j}=(u_{i+1,j}+u_{i-1,j})/2\,, \tag{8}$$

$$(u_{i,j})_x=\frac{1}{2\Delta x}(u_{i+1,j}-u_{i-1,j})\,. \tag{9}$$

In this system, equation (1) was written as (Shuman and Hovermal, 1968)

$$\bar{u}^{t}_{t}=-\overline{\bar{m}^{xy}[\bar{u}^{xy}\bar{u}^{y}_{x}+\bar{v}^{xy}\bar{u}^{x}_{y}+\bar{\phi}^{y}_{x}]-\bar{\omega}^{pp}\bar{u}^{xy}+f^{xy}\bar{v}^{xy}}^{\,xy}\,. \tag{10}$$

The excess averaging on the terms might upset the balance in the forecast equations. Gerrity and McPherson (1971) have successfully used unaveraged velocity components in Corilis terms to preserve a reasonable geostraphic balance. And it was attemped in a semi-implicit model (Campana, 1974). The finite difference scheme used in this study is the semi-momentum introduced by Shuman (1962). Equaton (1) is written as

$$\bar{u}^{t}_{t}=-\bar{m}^{xy}[\bar{u}^{xy}\bar{u}^{y}_{x}+\bar{v}^{xy}\bar{u}^{x}_{y}+\bar{\phi}^{y}_{x}]-\bar{\omega}^{pp}\bar{u}^{xy}_{p}+f^{xy}\bar{v}^{xy}\,. \tag{11}$$

Equation (2) and (4) are transformed in the similar fasions,

$$\bar{v}^{t}_{t}=-\bar{m}^{xy}[\bar{u}^{xy}\bar{v}^{y}_{x}+\bar{v}^{xy}\bar{v}^{x}_{y}+\bar{\phi}^{x}_{y}]-\bar{\omega}^{pp}\bar{v}^{xy}_{p}-f^{xy}\bar{u}^{xy}\,, \tag{12}$$

$$\bar{\theta}^{t}_{t}=-\bar{m}^{xy}[\bar{u}^{xy}\bar{\theta}^{y}_{x}+\bar{v}^{xy}\bar{\theta}^{x}_{y}]-\bar{\omega}^{pp}\bar{\theta}^{xy}_{p}\,. \tag{13}$$

The average and difference of $u_{i,j}$ is obtained by the values the neighboring points;

$$\bar{u}^{xy}_{i,j}=\frac{1}{4}[u_{i+1,j}+u_{i-1,j}+u_{i,j+1}+u_{i,j-1}]\,, \tag{14}$$

$$[\bar{u}^{y}_{i,j}]_x=\frac{1}{4\Delta x}[u_{i+1,j+1}+u_{i+1,j-1}-u_{i-1,j+1}-u_{i-1\ j-1}]\,, \tag{15}$$

$$[u_{i,j}]_p=\frac{1}{2\Delta p}[(u_{i,j})_{k+1}-(u_{i,j})_{k-1}]\,, \tag{16}$$

where the subscript k is the index for the vertical level.

For time difference, $\partial u_{i,j}/\partial t$ is

$$(u_{i,j})_t = \frac{1}{\Delta t}\left(u^{n+\frac{1}{2}}_{i,j} - u^{n-\frac{1}{2}}_{i,j}\right). \tag{17}$$

And the term $\bar{u}^t_t$ is

$$(\bar{u}^t_{i,j})_t = \frac{1}{2\Delta t}\left(u^{n+1}_{i,j} - u^{n-1}_{i,j}\right), \tag{18}$$

where the superscript n is the index for time step index.

The time derivative is a simple centered-difference approximation of second order accuracy.

In this study, a newly developed numerical scheme, hopscotch method, is adopted to integrate the prognositc equations. The method computes each time step in two sweeps of the mesh. In the first and subsequent odd number time steps, the grid points with i+j equal to odd are calculated based on the current values of the neighboring points. For equation (11), the new values of $u^{n+1}_{i,j}$ are given by

$$\begin{aligned} u^{n+1}_{i,j} = u^{n-1}_{i,j} - 2\Delta t \{ & \bar{m}^{xy}_{ij}\,[(u^n_{i+1,j}+u^n_{i-1,j}+u^n_{i,j+1}+u^n_{i,j-1})\,(u^n_{i+1,j+1} \\ & + u^n_{i+1,j-1} - u^n_{i-1,j+1} - u^n_{i-1,j-1})/16\Delta x + (v^n_{i+1,j}+v^n_{i,j+1}+v^n_{i,j+1}+v^n_{i,j-1}) \\ & \times (u^n_{i+1,j+1}+u^n_{i-1,j+1}-u^n_{i+1,j-1}-u^n_{i-1,j-1})/16\Delta y \\ & + (\phi^n_{i+1,j+1}+\phi^n_{i+1,j-1}-\phi^n_{i-1,j+1}-\phi^n_{i-1,j-1})/4\Delta x] \\ & + \frac{1}{8\Delta p}(\omega^n_{i,j,k+1}+\omega^n_{i,j,k-1}-2\omega^n_{i,j,k})\,[(\bar{u}^{xy}_{i,j})^n_{k+1} - (\bar{u}^{xy}_{i,j})^n_{k-1}] \\ & - \frac{1}{4} f^{xy}_{ij}[v^n_{i+1,j}+v^n_{i-1,j}+v^n_{i,j+1}+v^n_{i,j-1}] \} \qquad \text{for } i+j=\text{odd} \end{aligned} \tag{19a}$$

Equation (12) and (13) may be written in the similar forms.

The first sweep consists of center-time-center-space differencing to forecast the new values of $u^{n+1}_{i,j}$, $v^{n+1}_{i,j}$ and $\theta^{n+1}_{i,j}$ at odd points.

The second sweep at the same time level, the same calculation is used at nodes points with i+j even by now using the known advanced values of neighboring points calculated in the first sweep:

$$\begin{aligned} u^{n+1}_{i,j} = u^{n-1}_{i,j} - 2\Delta t \{ & \bar{m}^{xy}_{i,j}\,[(u^{n+1}_{i+1,j}+u^{n+1}_{i-1,j}+u^{n+1}_{i,j+1}+u^{n+1}_{i,j-1})\,(u^{n+1}_{i+1,j+1} \\ & + u^{n+1}_{i+1,j-1} - u^{n+1}_{i-1,j+1}) - u^{n+1}_{i-1,j-1})\,/16\Delta x + (v^{n+1}_{i+1,j}+v^{n+1}_{i-1,j}+v^{n+1}_{i,j+1}+v^{n+1}_{i,j-1}) \\ & \times (u^{n+1}_{i+1,j+1}+u^{n+1}_{i-1,j+1}-u^{n+1}_{i+1,j-1}-u^{n+1}_{i-1,j-1})/16\Delta y \\ & + (\phi^n_{i+1,j+1}+\psi^n_{i+1,j-1}-\phi^n_{i-1,j+1}-\psi^n_{i-1,j-1})\,/4\Delta x] \\ & + \frac{1}{8\Delta p}(\omega_{i,j,k+1}+\omega_{i,j,k-1}-2\omega_{i,j,k})\,[(\bar{u}^{xy}_{ij})^{n+1}_{k+1} - (\bar{u}^{xy}_{ij})^{n+1}_{k-1}] \end{aligned}$$

$$- \frac{1}{4} \bar{f}^{xy} \left[v^{n+1}_{i+1,j} + v^{n+1}_{i-1,j} + v^{n+1}_{i,j+1} + v^{n+1}_{i,j-1} \right] \Big\}$$

$$\text{for } i+j = \text{even} \tag{19b}$$

This second sweep is fully implicit in the sense that $(n+1)$ values are required at points $(i \pm 1, j)$ and $(i, j \pm 1)$, but this implicitness involves no simultaneous algebraic solutions, since the neighboring advanced values are already computed from the first sweep.

The vertical p-velocity is obtained by the equation of continuity (6) with difference equation

$$\bar{\omega}^{p}_{p} = -\bar{m}^{xy}(\bar{u}^{y}_{x} + \bar{v}^{x}_{y}) \tag{20}$$

with the boundary condition at 200 mb with $\omega = 0$.

For each time step, the hydrostatic equation with no averaging was used (Shuman and Hovermal, 1968, p. 531 Eq. (5-3)), to obtain the geopotential field. The geopotential for the four levels was calculated from the potential temperature and the thickness of the level. The hydrostatic equation (3) is integrated downward to obtain the height field, while the heights of the upper level, 200 mb, is held fixed (Rosenthal, 1964; Millers, 1969).

4. INITIALIZATION OF DATA

Despite considerable inprovement in observational netwerks and analysis procedures, the initial fields provided for starting up primitive equation models are not fully satisfactory. The initial wind and mass field are not completely balanced. They will cause amplification of the gravitational and inertial oscillations in subsequent numerical integrations. To reduce these waves, great care must be taken to bring the initial fields to a stable of better balance before beginning the forecast.

Numerous authors have investigated the initialization problem and proposed methods of obtaining an initially balanced state by removing high frequency oscillations for the primitive equation models (Krishnamurti and Baumhefner, 1966; Shuman and Hovermale, 1968, Daley, 1978). The most common method of obtaining the initial fields is by solution of the balance equations (Haltiner and Williams, 1975). The basic equations in our initialization process are balance, omega, continuity and hydrostatic equations. The geopotential data, were smooth once in horizontal by nine-point smoothing operator and once in the vertical, over three points, with top and bottom levels being omitted from vertical smoothing.

The balance equation,

$$f\nabla^2\psi - f_y u + 2(\psi_{xx}\ \psi_{yy} - \psi_{xy}^2) = \nabla^2\phi\,, \tag{21}$$

was solved for the stream function, using the method described by Shuman (1957) and Wang (1975), by relaxation method. The temperatures were obtained by solving hydrostatic equation. And the vertical motion was prepared by solving omega equation described by the previous study (Chien and Wang, 1979). The equation of continuity

$$\nabla^2\,\chi = -\ \frac{\partial\omega}{\partial p} \tag{22}$$

was solved for velocity potential, with χ set equal to zero on the boundary. The total wind was obtained by adding the divergent and the rotational components

$$u = -\ \frac{\partial\psi}{\partial y} + \frac{\partial\chi}{\partial x} \tag{23a}$$

and

$$v = \frac{\partial\psi}{\partial x} + \frac{\partial\chi}{\partial y} \tag{23b}$$

The above processes were repeated unitl the vertical velocities at the two consecutive cycles of computation approach the balance criterion Max $|\ \omega_{ijk}^{n+1} - \omega_{ijk}^{n+1}\ | \leq 10^{-5}$ mb/sec. This completes the initialization process. The converging vertical p-velocity, and velocity fields are the initial balanced data for numerical integrations.

5. RESULTS OF EXPERIMENTAL INTEGRATIONS

The numerical technique described in the preceeding sections has been applied to th meteorogical charts for and integrated to twenty four hours in order to obtain some estimate of the characteristics of this technique as compared with other methods.

To compare the hopscotch forecast in primitive equation model with that that produced by the baroclini-geostraphic model (Chien and Wang, 1979), we use the same initial condition. The computation domain covers from 10N to 55N and from 85 E to 150 E with grid size 240 Km. The initial data used in this experiment were June 10, 1975. The data were analyzed for the diagnostic study of the atmospheric structure for Mei-Yu system in the vicinity of Taiwan (Chen and Tsay, 1977), and were not specifically prepared for testing the model of numerical weather prediction. Geopotential height analyses at the grid point were performed on isobaric surfaces. We read the analysed data from tape and smoothed horizonatally using a nine-point smoothing operator and vertically over three points. Initialization process described in section

4 is performed to obtain the balanced wind, temperature, geopotential and vertical velocity for numerical integrations. Fig. 2(a) through 2(d) show the balanced geopotential heigh and temperature fields other initialization at 300 mb, 500 mb, 700 mb and 900 mb.

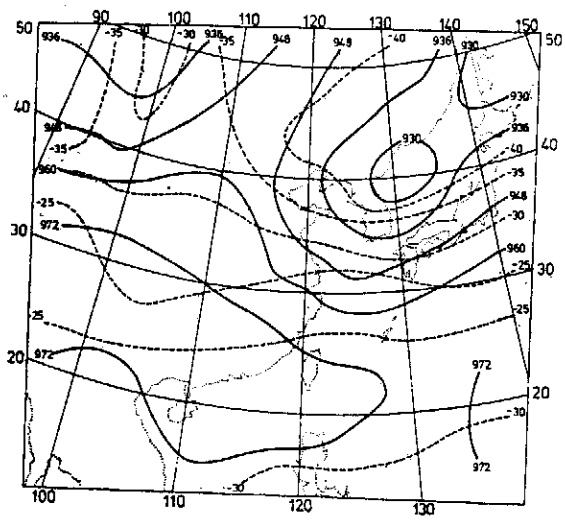

FIG. 2(a) Initial analysis geopotialheight (solid line) and temperature (dash line) on 300 mb at 0000Z 10 Jane, 1975.

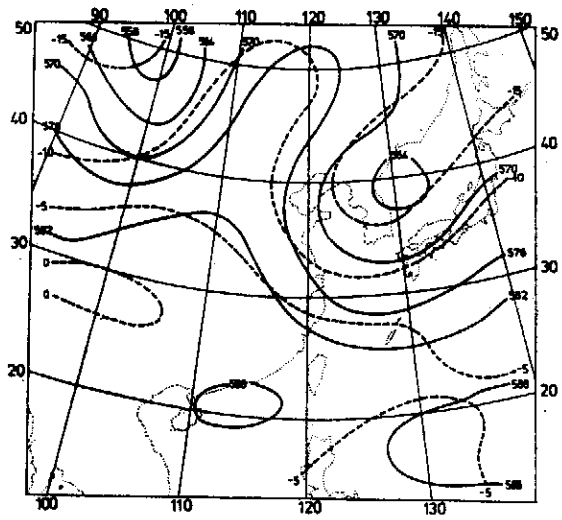

FIG. 2(b) Initial analysis geopotial height (solid line) and temperature (dash line) on 500mb at 0000Z 10 June, 1975.

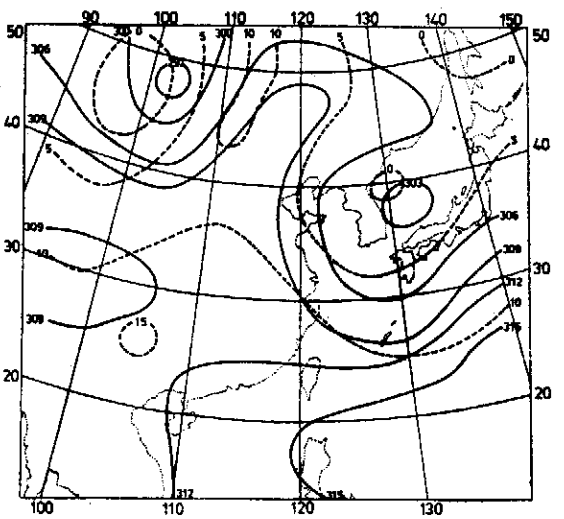

FIG. 2(c) Initial analysis geopotential height (solid line) and temperature (dash line) on 700 mb at 0000Z 10 June, 1975.

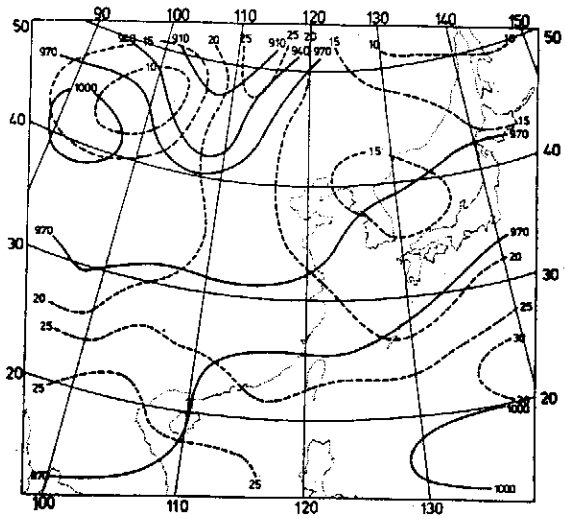

FIG. 2(d) Initial analysis geopotential height (solid line) and temperature (dash line) on goo mb at 0000Z 10 June, 1975.

A twenty-four hour forecast was produced with the method described in this study with time increment ten minutes, larger than experimented by Shiau and Wang (1976) using explicit method with six minutes, Fig. 3(a) through 3(d) show the geopotential and temperature fields predicted after 24 hours. They are similar to those forecasted by baroclinic quasigeostraphic model, although we used the different boundary conditions. The former applied the sponge damping, and the latter free slip boundary conditions.

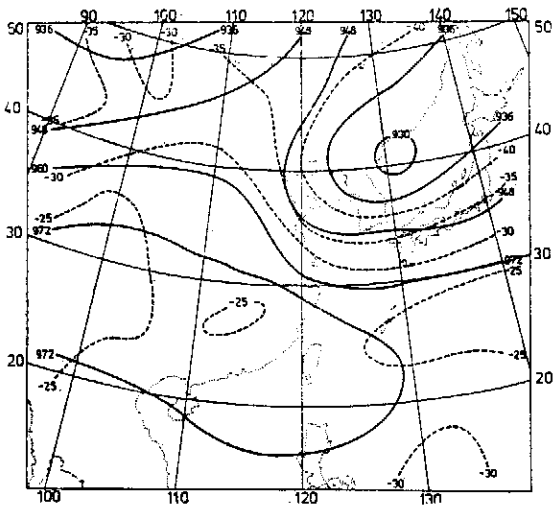

FIG. 3(a) 24-hour Primitive equation model prognsis geopotential height (solid line) and temperature (dash line) on 300 mb.

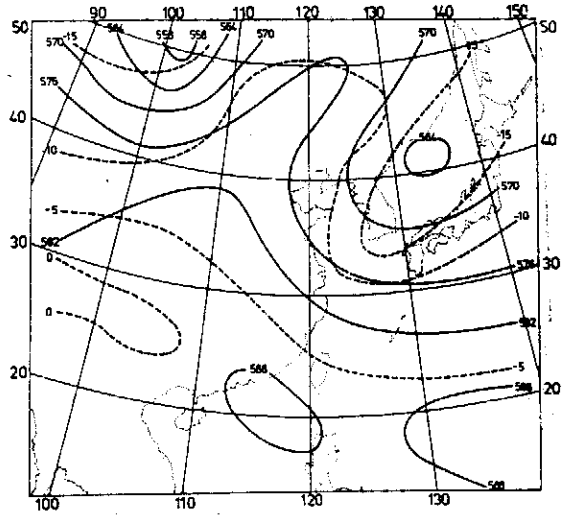

FIG. 3(b) 24-hour Primitive equation model prognosis geopotential neight (solid line) and temperature (dash line) on 500 mb.

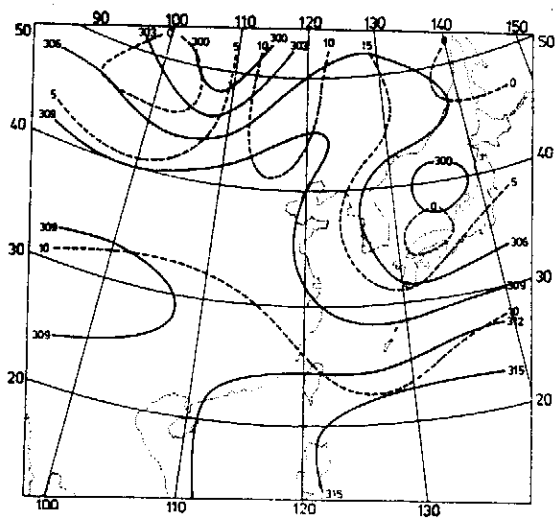

FIG. 3(c) 24-hour primitive equation model prognosiss geopotential neight (solid line) and temperature (dash line) on 700 mb.

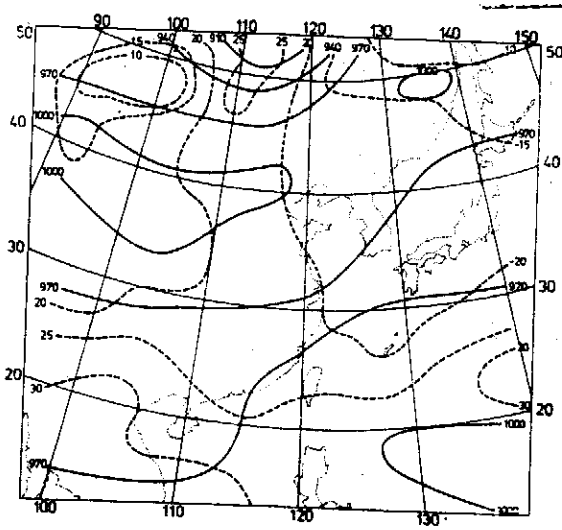

FIG. 3(d) 24-hour primitive equation model prognosis geopotential neight (solid line) and temperature (dash line) on 900 mb.

We adoped the hopscotch numerical integration scheme with the same initial and boundary conditions except the integration time steps are increased by double. The predicted geopotential and temperature fields shows no difference for 3 significant figures compared with $\Delta t = 10$ minutes.

Further, the numerical experiment was performed with larger time increment $\Delta t = 30$ minutes. The predicted fields agree with those of $\Delta t = 10$ minutes.

6. CONCLUSIONS AND RECOMMENDATIONS

The major objective of this study has been to apply the newly developed numerical scheme, hopscotch method, to four-level prinitive equation model. The development reported here in is part of a continuing international trend towards the application of the limited area primitive equations models for routine operational forecasting purposes, e.g. Okamura (1975), Burridge (1975), and Campana (1979). An algorithm to incorporate the hopscotch time integration scheme has been presented and it is found to be meteorologically equivalent to four level baroclinic quasi-geostraphic model using the explicit and hopscotch time integration to 24 hours over the East Asia Area during the Mei-Yu season. The main advantage of the operational forecasting of the scheme is a substantial economy in computation by permitting the longer time step and is a modest improvement in the accuracy of the forecasts. Another advantages of the model are its unconditional stable and its simplicit, involving no simultaneous algebraic solution in prognostic equations, and no poisson equation solution in diagnostic equation.

Although we have incorporated the new numerical scheme to the primitive equation model with priliminary satisfactory results, we are not complete our study. Additional developments of the model should include diabatic, surface friction and orography effects. The features recently, developed in computational mechanics should also be added to the model to promote a longer, more stable forecast by controlling the nonmeteorological noise that develops during the integrations. And the comparison between the semi-implicit, split ' explit scheme and the numerical method proposed in this study should be excuted using the same grid spacing and initial conditions so that we can compare the computational economy and efficiency.

REFERENCES

Bourke, W. (1974). A multi-level spectral model, I. Formulation and hemispheric integrations, Month. Weath. Rev., Vol. 102, pp. 687-701.

Benwell, G.R.R. and F. H. Bushby, (1970). A case study of frontal behaviour using a 10-level primitive equation model. Quart. J. R. Met. Soc., Vol. 96, pp. 287-296.

Brown, J. A. Jr and K. A. Campana (1978). An economic time-differencing system for numerical weather prediction, Month. Weath. Rev., Vol. 106, pp. 1125-1136.

Burridge, D. M. (1975). A split semi-implicit reformulation of the Bushby-Timpson 10-level model, Quart. J. R. Met. Soc., Vol. 101, pp. 777-792.

Bushby, F. H. ant Timpson, M. S. (1967). A 10-level atmospheric model and frontal rain, Quart. J. R. Met. Soc., Vol. 93, pp. 1-17.

Campana, K. (1974). Status reporton a semi-implicit version of the shuman-Hovermale model, NOAA Tech. Memo. NWS NMC-54, 22pp.

Campana, K. A. (1979). Higer order finite-difference experiments with a semi-implicit model at the National Meteorological Center, Month. Weath. Rev., Vol. 107, pp. 363-376.

Chen, T. J. G. and C.Y. Tsay (1977). A detailed analysis of a case of Mei-Yu system in the vicinity of Taiwan, Tech. Rept. No. Mei-Yu-001, Dept. Atmo. Sci., National Taiwan University.

Chien, L. C. and C. T. Wang (1979). Hopscotch integration scheme for numerical weathe prediction in Mei-Yu season, Proc. Natl. Sci. Coun. ROC. Vol. 3, pp. 356-363.

Daley, R. (1978). Variational non-linear normal mode initialization, Tellus, Vol. 30, pp. 208-218.

Gadd, A. J. (1978). A split explicit integration scheme for numerical weather prediction, Quart. J. R. Met. Soc., Vol. 104, pp. 569-582.

Gauntett, D. J., L. M. Leslie, J. L. McGregor, and D. R. Hincksman (1978). A limited area nested numerical weather prediction model: Formulation and preliminary results, Quart. J. R. Met. Soc., Vol. 104, pp. 103-117.

Gerrity, J. P. Jr. and R. D. McPherson (1971). On an efficient scheme for the numerical integration of a primitive equation barotropic model, J. App. Met., Vol. 10, pp. 353-363.

Gerrity, J. P. Jr., R. D. McPherson and S. Scolnik (1973). A semi-implicit version of the Shuman-Hovermale model, NOAA Tech. Memo. NWS NMC-53, 44pp.

Haltiner, C. J. and R. T. Williams (1975). Some recent advances in numerical weather prediction, Month. Weath. Rev., Vol. 103, pp. 571-604.

Holton, J. A. (1967). A stable finite difference scheme for linearized vorticity and divergence equation system, J. Appl. Met., Vol. 6, pp. 519-522.

Kasahara, A. and Washington, W. M. (1967). NCAR global general circulation model of the atmosphere, Mon. Weath. Rev., Vol. 95, pp. 389-402.

Kurihara, Y. (1965). On the use of implicit and iterative method for the time integration of the wave equation, Month. Weath. Rev., Vol. 93, pp. 33-46.

Krishnamurti, T. N. and D. Baumhefer (1966). Structure of a tropical disturbance based on solutions of a multi-level baroclinic model, J. App. Met., Vol. 5, pp. 396-406.

Kwizak, M. and A. J. Robert (1971). A semi-implicit scheme for grid point atmospheric model of the primitive equations, Month. Weath. Rev. Vol. 99, pp. 32-36.

Lilly, D. K. (1965). On the computational stability of time-dependent non-linear geo-physical fluid dynamics problems, Month. Weath. Rev., Vol. 93, pp. 11-26.

Madala, R. V. (1979). Split explicit integration method for tropical cyclones, AMS 12th technical conference on hurricanes and tropical meteorology, New Orlean, Louisiana, April 24-27, 1979.

Marchuk, G. I. (1966). A new approach to numerical solution of differential equations of atmospheric processes, WMO, Tech. Note, No. 66, pp. 286-294.

Millers, B. I. (1969). Experiments in forecasting hurricane development with real data, ERLTM-NHRL. 85, 28pp.

Okamura, Y. (1975). Computational design of a limited-area prediction model, J. Met. Soc. Japan, Vol. 55, pp. 175-188.

Perkey, D. J. and C. W. Kreitzberg (1976). A time-dependent lateral boundary scheme for limited-area primitive equation models, Month. Weath. Rev., Vol. 105, pp. 744-755.

Robert, A. J. (1969). Integration of a spectral model of the atmosphere by implicit method, Proc. WMO/IUGG Symposium on Numerical Weather Prediction, Tokyo, November 26-December 4, 1968, Japan Met. Agency, Tokyo.

Robert, A., Handerson, J. and Turnbull, C. (1972). An implicit time integration scheme for baroclinic models of the atmosphere, Month. Weath. Rev., Vol. 100, 329-335.

Rosenthal, S. L. (1964). Some attempts to simulate the development of tropical cyclones by numerical methods Month. Weath. Rev. Vol. 92, pp. 1-21.

Smagorinsky, J., Manabe, S. and Holloway, J. L. Jr. (1965). Numerical results from a nine-level general circulation model of the atmosphere, Month. Weath. Rev., Vol. 95, pp. 727-768.

Shiau, C. J. and C. T. Wang, (1976). On the preliminary study of limited-area primitive equation model, Ann. Rept. Inst. Phys. Acad. Sin. 1976. 231—262.

Shuman, F. G. (1957). Numerical methods in weather prediction, Month. Weath. Rev., Vol. 85, pp. 329-332, pp. 357-361.

Shuman, F. G. (1962). Numerical experiments with the primitive equations, Proc. Inter. Symp. Numerical Weather Prediction, Tokyo, November 7-13, 1960, Japan Meteorological Agency, Tokyo, pp. 85-117.

Shuman, F. G. and J. B. Hovermale (1968). An operational six-layer primitive equation model, J. Appl. Met., Vol. 7, pp. 525-547.

Shuman, F. G. (1971). Resuscitation of an integration procedure. NMC Office Note 54, 55 pp.

Wang, C. T. (1975). Numerical study of a simplified balanced model. Atm. Sci., Vol. 2, pp. 51-58.

Williamson, D. L. and G. L. Browning, (1974). Formulation of the lateral boundary cenditions for NCAR limited-area model, J. Appl. Met., Vol. 13, pp. 8-16.

Young, J. A. (1968). Comparative properties of some time differencing schemes for linear and non-linear oscillations, Month. Weath. Rev., Vol. 96, pp. 357-364.

客觀分析程式之驗證

劉　玉　龍

中　央　氣　象　局

曾　忠　一

中央研究院物理研究所

國立臺灣大學大氣科學系

摘　　要

客觀分析之結果對於大氣狀況的掌握及數值天氣預報的準確性，具有很重要的影響力。本研究採用 1975 年 6 月 10日 格林尼治零時的 (0000 GMT) 個案資料，來驗證 Barnes, Cressman，及 Inman 客觀分析程式，而以主觀分析之結果，作爲比較的標準。

爲了更確定主觀分析的可信性，本研究進一步的作靜水檢定，靜力穩定度檢定及橢圓型條件的檢定，並計算渦度場及輻散場，與天氣系統比較，用以確定分析場在垂直方向及水平方向的一致性，完成主觀分析精度之評估。三種客觀分析的分析場，除了與主觀分析場比較外，亦分別進行上述的檢定。

關於大氣的垂直速度在大氣現象中，如雲量之預報及研究，是很重要的參數，但由於在大幅度運動中其數值很小，不易由儀器直接測得，必須由其他氣象變數間接計算得到，而此計算結果對氣象變數的變化非常敏感，因此可利用各客觀分析的垂直速度計算結果與實際天氣系統或衛星雲圖相比較，則可瞭解各客觀分析程式的分析能力。

本研究選用運動學法，準地轉垂直速度方程式及線性平衡方程式等三種垂直速度計算法，計算主觀分析及三種客觀分析的垂直速度，並與 NOAA-4 紅外光衛星照片及雲量觀測資料比較。

壹、導　　言

近年來數值預報作業已進入自動化程序，各測站所傳送進來的氣象電碼，直接輸入電腦中解譯成氣象資料予以貯存，可隨時讀出使用。由於測站的分佈極不規則，對於大氣的分析工作，極不方便；另一方面，人爲的天氣圖分析，在時效上無法作實際的應用。爲了解決這些問題，於是便產生了客觀的分析的觀念。客觀分析是把分佈不規則測站上的氣象變數資料，利用內插法轉換到排列規則的網格點上，所

得到的網格點值，可作爲例行天氣預報的初始值，或供繪圖機繪製實際天氣圖，分析大氣現象。

Bergthorssen 和 Döös (1955) 首先建立了客觀分析的基本概念，他們把網格點周圍測站上的氣象變數資料作加權平均而求得該變數在網格點上之值。在進行客觀分析時，由於測站密度極不均勻，某些地區測站的分佈非常稀疏，嚴重影響分析的結果，因此在客觀分析中使用初次估計值，可減少許多在資料缺乏地區進行分析工作時所發生的困難。Bushby 和 Huckle (1956) 利用預報值作爲初次估計值。Shuman (1957) 使用濾波器，減少分析場中的短波。Cressman (1959) 設計一種權重，考慮測站與網格點間之距離對分析值的影響，以提高分析結果的可靠性，此種權重已爲美國氣象中心 (NMC) 使用於例行的天氣分析 (McDonell, 1962). Inman (1970) 考慮到測站上風對權重的影響，將 Cressman 的權重加以修改，加重上風處與下風處的權重。Barnes (1973) 利用指數權重來分析中幅度的大氣現象，並指出這種權重的優點。McFarland (1975) 綜合 Inman 和 Barnes 權重的優點，設計一種非均質非等向性的權重，來分析暴風環境。曾氏 (1976，1977) 利用變分最佳化原理，進行東亞天氣資料之高度場、溫度場和風場的分析，結果與主觀分析場甚爲接近。胡氏 (1977) 從事高空天氣圖客觀分析之研究，在分析高度場時，加入地轉平衡的假設，其結果顯示出高度場之客觀分析能够相當準確地定出高低壓中心位置，等高線的梯度與實際觀測風速也能密切配合；溫度場的客觀分析，能正確定出冷暖區的位置，等溫線的型態大致與主觀分析相同。

客觀分析的結果，對於大氣狀況的掌握及天氣預報的準確性，具有很大的影響力，因此對於各客觀分析程式的優點及可信度應充分了解，以作爲選用的依據，並期能作進一步的修正和改進。Peterson (1973) 比較 NMC 300 mb 高度分析程式及最佳內插法 ("Optimal" objective analysis) 的權重係數。Stuart (1974) 就北美地區，根據三種主觀分析及兩種客觀分析，分別計算垂直速度，發現具有相似的數值和型態。Schlatter et al (1976) 就北半球地區，比較多元性統計分析程式 (multi-variate statistical analyses), NMC 的 Cressman 分析程式及主觀分析程式的結果。Otto-Bliesner, Baumhefner, Schlatter 和 Bleck (1977) 選用逐次校正客觀分析 (Successive-correction objective analysis)，多元統計分析 (global statistical multivariate analysis)，等熵分析 (isentropic analysis) 和主觀分析等四種分析程

式，比較其分析場與觀測資料的配合程度及天氣系統定位的準確性，研究結果發現客觀分析較主觀分析爲佳，客觀分析之誤差在觀測誤差之內，而主觀分析則否，此外在選用的三種客觀分析中，400 mb 以下各層之分析場，以逐次校正法及等熵分析程式較佳。

本研究選用 Barnes, Cressman 和 Inman 客觀分析程式，作爲驗證的對象，並引用梅雨報告 (Chen and Tsay, 1977) 的主觀分析，評估其精度，而作爲比較的標準。各客觀分析程式所得的分析場亦分別進行靜水檢定、靜力穩定度檢定、橢圓型條件的檢定，以及比較其觀測風渦度場與地轉渦度場，來驗證其分析場的合理程度。另一方面在大氣運動的診斷和預報研究，以及雲量的判斷，垂直速度是很重要的參數，由於垂直速度在大氣大幅度的運動中數值很小，不易直接由現有的觀測儀器觀測得到，而必須由其他氣象變數如高度、溫度等資料計算求得。由於垂直速度的計算結果，對於氣象變數之變化非常敏感，因此將各客觀分析程式所得之資料，計算出垂直速度，再將計算結果與實際天氣系統或衛星雲圖比較，以了解各客觀分析程式的分析能力。

垂直速度計算部份，本研究選用運動學法，準地轉垂直速度方程式及線性平衡方程式組等三種計算法，分別計算出主觀分析及各客觀分析的垂直速度場，再與 NOAA-4 紅外光衛星照片及雲量的觀測資料比較，以確定其符合的程度。

貳、客觀分析法

各測站上的高度、溫度和風等資料，經各種檢定改正錯誤及補充漏失的資料後，即可進行客觀分析的工作，將測站上的天氣資料，內插到網格點上。對於各氣象變數的分析，除高度場的分析稍有不同外，其他變數的基本分析法大致相同。本研究所選用的 Barnes, Cressman 和 Inman 等三種客觀分析程式，其基本架構相同，係 Cressman (1959) 所提出的逐次校正法，而三種分析程式之主要差別在於使用的權重有所不同。分析方法分別在下面討論。

一、基本分析法

設 Z_k 爲測站 k 上某氣象變數的觀測值，$Z_s^{\mu-1}$ 是測站 k 第 $\mu-1$ 次 的分析值。$D_k^{\mu-1}$ 爲測站 k 上觀測值與第 $\mu-1$ 次分析值的差值，即：

$$D_k^{\mu-1} = Z_k - Z_s^{\mu-1}$$

對某一網格點 (i，j)， 其校正值 C_{ij}^{μ} 可由影響半徑R範圍內的 $D_k^{\mu-1}$ 值加權平均求得：

$$C_{ij}^{\mu} = \frac{\sum_{k=1}^{N} W_k D_k^{\mu-1}}{\sum_{k=1}^{N} W_k}$$

上式中，N爲測站數，W_k 爲測站 k 的權重函數。將第 $\mu-1$ 次的分析值加上校正值，即得到新的分析值。依此網路點上的分析值，利用線性內插法（圖 1），求得測站上的分析值 Z_s：

$$Z_s = Z_1 + (Z_4 - Z_1)\frac{\Delta y}{d} + (Z_2 - Z_1)\frac{\Delta x}{d} - (Z_2 - Z_3 + Z_4 - Z_1)\frac{\Delta x \Delta y}{d^2}$$

式中：1，2，3，4 分別代表四網格點，k 代表測站，d 爲網格長度。將測站上的觀測值與分析值比較，若兩者差值的絕對值大於某最大容許差異值 ε ，即 $|D_k^{\mu}| > \varepsilon^{\mu}$ 時，則可判斷此測站的資料有錯，在進行下一次掃描時，錯誤的資料捨棄不用。按照上述方法，掃描三至四次，即可得到分析的結果。

二、高度場分析

高度場的分析法與上節所述之方法相仿，而高度的校正值爲風觀測值與高度觀測值的函數。由於大幅度大氣運動保持準地轉平衡，因此觀測風代表高度場的傾斜率。假設測站爲等間距分佈，則此測站所能測得的最短波長爲測站間距的兩倍。根據取樣定理 (Stephens, 1971)，假如在測站上同時測得某一變數的梯度，則可縮短這些測站所能測得的最短波長，亦即可定義幅度 (definable scale) 減小，因此更能代表實際的天氣資料。雖然測站的分佈，實際上極不均勻，但原理仍是一樣，同時使用高度與風的觀測值，會使資料更再代表性，尤其在資料缺乏的地區爲然。

在分析高度時，有三種情形：(1)測站上只有高度記錄，(2)測站上只有風的記錄，(3)測站上兼有高度與風的記錄。在本研究中只論及(1)和(3)。

當測站只有高度記錄時，可直接求高度觀測值與分析值之差值 D_k：

$$D_k = Z_k - Z_s$$

式中 Z_k 和 Z_s 分別爲測站之高度觀測值與分析值，求得 D_k 後，再依照第一節所述之分析法進行分析。

若測站兼有高度和風的記錄，則

$$D_k = Z_k + \left(\frac{\partial Z}{\partial x}\Delta x + \frac{\partial Z}{\partial y}\Delta y\right) - Z_{ij}$$

式中 Z_{ij} 爲網格點之分析值，$\frac{\partial Z}{\partial x}$、$\frac{\partial Z}{\partial y}$ 分別爲 x 和 y 方向的高度梯度，可利用地轉風的關係式由觀測風求得：

$$\frac{\partial Z}{\partial x} = \frac{1.08f}{m\,\sigma\,g}v$$

$$\frac{\partial Z}{\partial y} = -\frac{1.08f}{m\,\sigma\,g}u$$

上二式中 f 爲科氏參數，σ 爲地圖投影變形因子，m爲地圖比例尺，g 爲重力加速度。u，v 各爲觀測風在 x 及 y 方向上之分量，常數 1.08 是地轉風對觀測風之平均比例。

根據上述的方法，即可求得網格點上的分析值，重覆掃描三至四次，逐次縮小影響半徑，以使較短波重現在分析場上。

三、權重函數

(1) Cressman (1959) 之權重函數

Cressman (1959) 使用的權重函數較簡單，與測站至某一網格點間之距離有關，即：

$$W_k = \frac{R^2 - d_k^2}{R^2 + d_k^2} \quad d_k < R$$

$$= 0 \qquad d_k \geq R$$

式中R爲影響半徑，d_k 爲測站與網格點間之距離，W_k 只取正值，因此當測站位於影響半徑之外時，即 $d_k \geq R$，則

$$W_k = 0$$

(2) Inman (1970) 之權重函數

Inman 之權重函數考慮風對權重的影響，修改 Cressman 的權重，加重上風處與下風處之權重，即：

$$W_k = \frac{R^{*2} - d_k^2}{R^{*2} + d_k^2}$$

$$R^{*2}=R^2(1+\beta\ \cos^2\ \theta)$$

θ 是風向與網格點至測站方向角間的夾角（圖 2），β 值可由下式推定：

$$\beta=\frac{b\ c}{c^*}$$

式中 c 爲風速。c* 爲最大風速，b 是常數，一般均定爲 1。

(3) Barnes (1973) 之權重函數

Barnes 使用的指數權重卽：

$$W_k=\frac{1}{4\pi K}\exp\ (-\frac{d_k^2}{4K})$$

式中K爲濾波參數，在進行分析時，K值的選定必須適當，K值若取太大，則會發生修勻過度的現象；反之若取太小，則可能電子計算機會發生溢位的情形。在本研究中，4K 值定爲 $0.8cm^2$ ，若以地球上的距離來表示，則 4K等於 $18,000km^2$ ，卽假設測站資料影響的幅度爲 135 km。

Barnes 並指出此種權重函數具有下列優點：

(a) 濾波參數 4K可以事先決定，因此反應函數亦可以事先知道。

(b) 由於指數權重函數隨測站與網格點的距離增加而趨近於零，因此測站上的資料可以影響到各處的網格點。

(c) 指數權重具有濾波效果，可以濾去雜波，而不需再使用濾波器。

(d) 使用指數權重，只需掃描一次卽可，可以節省許多時間。

四、初始估計值

初始估計值卽 $Z_{ij}^{(0)}$ 和 $Z_s^{(0)}$，在進行分析之初，無分析值可用，因此必須引用初始估計值，此估計值可用氣候值，十二小時前的分析值或預報值。Cressman (1959) 進行高度分析時，850 mb 定壓面之分析，以 500 mb 之高度減去 500-850 mb 厚度作爲初始值；500 mb 定壓面之分析，則以十二小時前之預報值爲初始值；300 mb 定壓面之分析，以 850 mb 及 500 mb 高度外插所得之高度值作爲初始值。McDonell (1962) 曾比較各種客觀分析的初始估計值。初始估計值的選定非常重要，尤其是資料缺乏的區域，若初始估計值選擇不當，則分析場不一定會收斂。曾氏 (1976) 在東亞地區天氣資料變分客觀分析之研究中顯示風場的初始估計值定爲

零時，所得的結果非常不好，若改用地轉風時，則分析之結果較好。

基於方便起見，本研究中，溫度和高度的初始估計值定爲零，風的初始估計值定爲地轉風。

叁、分析場的檢定法

測站的氣象觀測資料，在觀測、編碼、傳送、譯碼等一系列的過程中，其中部份資料，可能由於觀測偏差，編譯電碼不愼或通訊線路不穩定而產生錯誤。以中央氣象局臺北氣象測站至東京點間的通訊線路爲例，日本氣象廳將氣象資料由自動編輯切換系統 (Automatic data editing and switching system)，經通訊衛星線路傳送至臺北，此線路通訊信號之傳送，相當穩定，少有干擾發生，但仍有10%至15%之高空測站資料錯誤或漏失（胡，1977），因此對氣象資料的輸入，應先加以檢定，以濾除可能的錯誤資料，並提高各測站資料的可信度。

本研究所用之資料，在分析前並未進行檢定工作，而只作人爲的除錯和訂正。對於分析結果，爲了確定其垂直和水平方向的內部一致性，所以將分析場進行靜水檢定，靜力穩定度檢定及橢圓型條件的檢定，而所得之檢定結果亦可反映出各氣象資料垂直和水平方向之一致性。

一、靜水檢定 (hydrostatic check)

假設大氣滿足靜水平衡，在 i 及i+1層定壓面上，應滿足下列關係式 (Inman, 1968)：

$$\Delta H_i = H_{i+1} - H_i$$

$$= -\frac{R}{2g}(T_i + T_{i+1} + 546.3)\ \ln\frac{p_i}{p_{i+1}}$$

其中 g 爲重力加速度，R爲氣體常數， p_i, T_i 分別爲 i 層的氣壓值和溫度值 (°C)，ΔH_i 爲靜水平衡的厚度理論值。設 δ 爲實際厚度值與理論厚度值的差值，即

$$\delta_i = h_{i+1} - h_i - \Delta H_i$$

h_i 及 h_{i+1} 分別爲第 i 及 i+1 層之高度觀測值。若 δ_i 的絕對值小於最大容許差異 Δ_i，即 $|\delta_i| < \Delta_i$，則第 i 層滿足靜水平衡。各定壓層厚度的最大容許差異如表一。當 $|\delta_i| > \Delta_i$ 時，則第 i 層不滿足靜水平衡。因爲大幅度大氣運動都應滿足靜

表一　進行靜水檢定時，各層的最大容許差異

(a)　　Δ（單位：m）

層　次	850 mb 700 mb	700 mq 500 mb	500 mb 400 mb	400 mb 300 mb	300 mb 250 mb	250 mb 200 mb	200 mb 150 mb	150 mb 100 mb
Δ　值	30	35	30	30	30	30	50	50

(a) 主觀分析

(b)

層　次	850 mb 700 mb	700 mb 500 mb	500 mb 300 mb	300 mb 200 mb	200 mb 100 mb
Δ　值	30	35	50	50	80

(b) 客觀分析

水平衡，如果不滿足靜水平衡的區域太大，則表示主觀分析場或客觀分析場不太合理。

二、靜力穩定度檢定 (static stability check)

當氣溫之遞減率大於乾絕熱遞減率時，則大氣呈不穩定狀態，而產生對流作用。大氣各層之靜力穩定度 σ，可由下式求得：

$$\sigma = -\frac{\alpha}{\theta}\frac{\partial\theta}{\partial p}$$

式中 α 爲大氣的比容，θ 爲各定壓面之位溫，即

$$\theta = T\left(\frac{1000}{p}\right)^{R/c_p}$$

此處T爲觀測溫度，c_p 爲定壓比熱，R爲氣體常數。當上層的位溫小於下層的位溫時，大氣呈不穩定狀態。除了近地層之外，大氣應當都是處於靜力穩定狀態。因此不論主觀分析場或客觀分析場中，若靜力不穩定的地區出現太多時，可以判斷主觀分析或客觀分析場在垂直方向不能維持內部一致。

三、橢圓型條件 (ellipticity condition)

利用原始方程式進行短期的天氣預報時，質量場和風場的初始平衡非常重要。在進行初值化時，一般都用平衡方程式由高度場求得旋轉風，由連續方程式求得

風。非線性平衡方程式的形式如下 (Haltiner, 1971)：

$$\nabla \cdot f\nabla\psi + 2(\psi_{xx}\psi_{yy} - \psi_{xy}^2) = \nabla^2\varphi$$

上式中流線函數 ψ 是未知數，這是 Monge-Ampere 型偏微分方程式，由於邊界條件是 Dirichlet 型的，因此平衡方程式必須爲橢圓型的才有解。上式的橢圓型條件爲 (Haltiner, 1971)：

$$\nabla^2\varphi - \frac{g}{f}\nabla\varphi \cdot \nabla f + \frac{f^2}{2} > 0$$

在求流線函數時，高度場必須滿足上列橢圓型條件，才能得到解，因此橢圓型條件可說是高度場的一種約束條件。若高度場不能滿足橢圓型條件，則高度場必須加以修改，才能求出流線函數。非橢圓型資料大部份出現在資料缺乏的地區以及强烈的反氣旋地區。

肆、垂直速度計算法

垂直速度的計算，最常用的方法有三種：(1)運動學法，利用連續方程式，由水平風的觀測值求得。此法的計算最簡單，靜水平衡是唯一的假設，但如果風的觀測值不準確或水平輻散的計算有誤差時，則由底層的垂直速度求上層的垂直速度時，所作的垂直積分，必產生誤差的累積，若未加以適當的校正，則必然得到不合理的數值。(2)絕熱法，利用熱力學方程式，由風和溫度的觀測值求得，計算也很簡單，唯一的假設是絕熱過程，而當非絕熱效應具有影響時，則所得的垂直速度，誤差會很大。此外當大氣的溫度遞減率接近乾絕熱遞減率時，所得的垂直速度亦不準確。(3)動力學法，利用準地轉方程組或平衡方程組的垂直速度方程式，由等壓面的高度值求得。此法的優點在於只利用等壓面上的高度值，而高度值是氣象變數中較準確的觀測值，其缺點在於計算極爲繁雜，必須解橢圓型偏微分方程式，且要考慮摩擦及加熱效應的影響。

Miller 和 Panofsky (1957) 指出垂直速度的計算，運動學法較其他方法爲佳。Danard (1964) 發現若不考慮潛熱的釋出，在 600 mb 以下各層，由準地轉方程組所得到的垂直速度只有運動學法之結果的四分之一。Wilson (1976) 比較絕熱法與運動學法計算所得的垂直速度，他以絕熱法求得之 100 mb 處的垂直速度，作爲頂層邊界條件來修正運動學法之結果，經此修正後，與實際天氣特性最爲配合。

Vincent, Bossingham 和 Edmon (1976) 就運動學法與準地轉垂直速度方程式所計算之垂直速度作比較，發現運動學法所求得的結果較佳，用準地轉垂直速度方程式所得之垂直速度場與天氣系統不完全吻合，而且顯示出垂直運動相當微弱，其最大值僅爲運動學法之五分之一。美國國家氣象中心，已經用運動學法代替垂直速度方程式，以計算垂直速度。

本研究中，選用運動學法、準地轉垂直速度方程式及線性平衡方程式等三種計算法，分述如下。

一、運 動 學 法

運動學法是利用連續方程式，在兩等壓面之間積分求得垂直速度，其唯一的假設爲靜水平衡。在等壓座標上，連續方程式可寫爲：

$$\frac{\partial u}{\partial x}+\frac{\partial v}{\partial y}+\frac{\partial \omega}{\partial p}=0 \tag{1}$$

式中 u，v 分別爲風速在 x 及 y 方向上的分量，ω 爲垂直速度，定義爲 $\omega=dp/dt$，由(1)式就某一大氣層 Δp，予以積分，即：

$$\omega_p=\omega_{p+\Delta p}+\int_p^{p+\Delta p}\left(\frac{\partial u}{\partial x}+\frac{\partial v}{\partial y}\right)dp \tag{2}$$

令 D_k 爲大氣層 Δp 之平均輻散，可由 u，v 的觀測值求得：

$$D_k=\int_p^{p+\Delta p}\left(\frac{\partial u}{\partial x}+\frac{\partial v}{\partial y}\right)dp \tag{3}$$

(2)式可改寫爲：

$$\omega_k=\omega_{k-1}+D_k \tag{4}$$

式中 ω_k，ω_{k-1} 分別爲大氣層 Δp 上界面與下界面之垂直速度，見圖 3。令 ω_0 代表大氣柱底部的垂直速度，此爲一特定值，則(4)式可改爲：

$$\omega_k=\omega_0+\sum_{i=1}^{k} D_i \tag{5}$$

由(5)式可求得任何較高層的垂直速度。

運動學法的計算，係由下往上垂直積分，故不需四周邊界條件，其網格垂直結構如圖 4，但由於積分時，誤差會發生累積，使得頂層所得的垂直速度會有不合理的現象，因此需要頂層邊界條件，作爲修正之用。

由(5)式可求得各層的垂直速度，底層的垂直速度，係採用梅雨報告 850 mb 之垂直速度計算結果（圖9）；頂層邊界條件係假設 10 mb 層之垂直速度爲零，即 $\omega_T=0$。利用此上下邊界條件來修正計算所得之垂直速度。因 ω 值是在兩定壓層之中間層計算，所以計算出結果後，再內插至各定壓層上。

二、準地轉垂直速度方程式

準地轉垂直速度方程式由熱力學方程式及渦度方程式消去 $\partial\zeta/\partial t$ 項而導出，本研究不考慮非絕熱加熱及摩擦的效應。準地轉垂直速度方程式的形式如下式（Haltiner 1971）：

$$\sigma_s\nabla\omega+f^2\frac{\partial^2\omega}{\partial p^2}=\frac{\partial}{\partial p}J(\varphi,\ f+\zeta)-\frac{1}{f}\nabla^2J\left(\varphi,\ \frac{\partial\varphi}{\partial p}\right) \qquad (6)$$

式中各符號的定義如下：

$$\sigma_s=\overline{\frac{1}{\rho}\frac{\partial\ln\theta}{\partial p}}\text{，各層平均靜力穩定度} \qquad (7)$$

f_0 ：平均科氏參數

φ ：重力位

ζ ：地轉渦度

θ ：位溫

ρ ：空氣密度

$$\nabla=\frac{\partial}{\partial x}\mathbf{i}+\frac{\partial}{\partial y}\mathbf{j}$$

$$J(a,\ b)\equiv\frac{\partial a}{\partial x}\frac{\partial b}{\partial y}-\frac{\partial b}{\partial x}\frac{\partial a}{\partial y}$$

(6)式中，左側項爲 ω 作一三維之 Laplacian，相當於 ω 乘上一個負值係數，右側第一項是絕對渦度平流的垂直變化；右側第二項爲溫度平流的 Laplacian。ω 方程式右側分爲兩項，由於此兩項並非獨立的，因此有可能導致錯誤的結果（Trenberth, 1978）。靜力穩定度 σ_s 爲氣壓的函數，在 x, y 方向上爲一常數。準地轉 ω 方程式中，若 σ_s 爲正值，是爲橢圓型偏微分方程式，可用緩和法求解。利用此方程式求垂直速度，需要四週及上下邊界條件。

本研究中，準地轉 ω 方程式之網格垂直結構如圖 5，以運動學法之計算結果作爲四周及上下邊界條件。先利用觀測高度及科氏參數 f 求得渦度；求出各層之靜力穩定度；而後解準地轉 ω 方程式，求得兩定壓層之間的垂直速度，再內插到各定壓層上。

三、線性平衡方程式組

線性平衡方程式組係由渦度方程式，熱力學方程式及輻散方程式所導出，本研究中不考慮摩擦效應及加熱效應。線性平衡方程式組的形式如下 (Haltiner, 1971):

$$\nabla^2\frac{\partial\psi}{\partial t}+J(\psi,\ \zeta+f)+\nabla\chi\cdot\nabla f=f\frac{\partial\omega}{\partial p} \tag{8}$$

$$\nabla\cdot(f\nabla\psi)=\nabla^2\varphi \tag{9}$$

$$\nabla^2\chi+\frac{\partial\omega}{\partial p}=0 \tag{10}$$

$$\nabla^2(\sigma\omega)+f^2\frac{\partial^2\omega}{\partial p^2}=f\frac{\partial}{\partial p}[J(\psi,\ \zeta+f)+\nabla\cdot\nabla\chi]$$

$$-\nabla^2\left[J\left(\psi,\ \frac{\partial\psi}{\partial p}\right)+\nabla\chi\cdot\nabla\frac{\partial\psi}{\partial p}\right]-\nabla f\cdot\nabla\frac{\partial^2\psi}{\partial p\partial t} \tag{11}$$

上述各式中：

f ：科氏參數

ψ ：流線函數

σ ：靜力穩定度

$\zeta=\nabla^2\varphi$ 渦度

χ ：速度勢函數

線性平衡系較準地轉 ω 方程式更複雜，必須解三個橢圓型方程式。網格垂直結構與準地轉 ω 方程式同，另外上下四週的邊界條件亦採用運動學法之結果。

伍、資料來源及天氣狀況

一、資 料 來 源

本研究個案資料係 1975 年 6 月 10 日格林尼治零時高空資料，計有 220 個測站的觀測資料，範圍約在 10°N 至 60°N，70°E 至 160°E 之間，此區域包括中國、蒙古、日本、韓國、中南半島及西太平洋區。

所蒐集的高空資料包括高度，溫度、露點溫度、風向及風速等觀測值，其垂直層次計有六層，即 850 mb、700 mb、500 mb、300 mb、200 mb 及 100 mb 等定壓層，其中露點溫度只有 850 mb 、700 mb 及 500 mb 三層資料。另外還有 1000 mb 的高度場。

資料在傳遞之間，可能由於編譯電碼不慎或通訊線路不穩定而造成資訊的錯誤，因此在分析前，先經除錯，並在可能的情況下，予以更正。

所使用的網路系統爲 20×19，中心點在 30°N、120°E ，網格點間之距離對應於地球表面時，約爲 240 公里。

二、天 氣 狀 況

圖 8 爲海平面氣壓場，圖中虛線代表鋒面。蒙古高氣壓盤踞於蒙古及華北附近，另一高壓脊由鄂霍次克海向西南延伸進入中國東部；在此兩高壓系統之間有一鋒系存在。副熱帶太平洋高壓向西南延伸，進入西南太平洋，在鄂霍次克高壓脊和太平洋高壓脊之間，有一半滯留鋒，由日本東南方，向西南延伸，經過臺灣而進入華南，此一鋒系即爲梅雨鋒。

850 mb 之環流系統，其大致情形與地面系統相仿。在緯度之槽線，其位置與地面鋒系相一致，另外對應於梅雨鋒的槽線，其位置稍向梅雨鋒之西北方偏離。沿此槽線，中國東南部及東海地區之氣壓梯度甚微弱。到 700 mb 時，日本海上方有一封閉低壓環流，對應於梅雨鋒之槽線，由此低壓中心，向西南延伸，經臺灣北部附近，達於中國西南。此槽線隔開了中緯的高壓系統及太平洋高壓脊。此時太平洋高壓涵蓋華南及南中國海；另外，在中緯區之槽線，其位置偏向 850 mb 槽線之西側。

在 500 mb 上（圖 11a），對應於梅雨鋒之槽線，由日本海上方的低壓中心向

西南延伸至臺灣附近；中緯槽則偏於 700 mb 槽線位置之西側。中國東北有一封閉高壓系統；另外在南中國海亦有一封閉高壓系統，此高壓系統與太平洋高壓脊之間的槽區，位於臺灣及菲律賓之東方。

300 mb 以上，日本海上之低壓槽，漸呈寬廣，槽線由此向西南延伸，到達臺灣北部附近；太平洋高氣壓漸東退，中國西南則出現高壓系統；中緯槽度漸弱，100 mb 至時已告消失。

此一時間，一連續的雲帶，涵蓋日本東南方，琉球、臺灣及華南一帶。根據 NOAA—4 衛星雲圖（圖 6）顯示，以臺灣北部一帶雲層最厚：另外綏遠、陝西一帶亦爲雲帶所覆蓋。

陸、主觀分析精度之評估

本研究驗證客觀分析時，選用 Chen and Tsay (1977) 之梅雨報的主觀分析場，作爲比較之標準。在該報告中，使用 158 站測站資料，這些測站卽本研究所選用測站的主要部份。此 158 站的觀測資料，先經主觀除錯及訂正，而後在定壓層上進行主觀分析，並利用剖面圖協助分析。另外用等風速線及等風向線來輔助資料缺乏區域的分析，最後利用修勻法將分析場予以修勻而濾除場中雜波。經此處理後所得之高度場、風速場及溫度場，大致滿足地轉風、梯度風和溫度風的平衡。

由於主觀分析場在本研究中作爲比較之標準，因此，對於主觀分析的精度，應有相當的瞭解，以免比較之工作失去意義。首先就主觀分析場，進行靜水檢定，靜力穩定度檢定和橢圓型條件之檢定。靜水檢定及靜力穩定度檢定計分爲850–700 mb、700–500 mb、500–300 mb、300–250 mb、250–200 mb、200–150 mb、150–100 mb 等八層。結果計有 14%未通過靜水檢定，1%未通過靜力穩定度檢定。各層未通過靜水穩定及靜力穩定度檢定的網格點數如表(二)所示，由表中的結果可以看出，除 300–250 mb 及 250–200 mb 層之外，其他各層未通過檢定的網格點數，所佔的比例極少，尤其是靜力穩定度檢定，除上述二個層次外，其他各層均全數通過檢定，而且這些未通過檢定的網格點，大部份均分佈於分析場的周圍，此係受資料不足所影響。在 300–250 mb 及 250–200 mb 二層中，分別有 140 及 118 個網格點未通過靜水檢定；12 及 4 個網格點未通過靜力穩定度檢定。此二層未通過靜水

表二　未通過檢定之網格點數和百分比

(a) 主觀分析

主觀分析	850 mb 700 mb	700 mb 500 mb	500 mb 400 mb	400 mb 300 mb	300 mb 250 mb	250 mb 200 mb	200 mb 150 mb	150 mb 100 mb
靜水檢定	26 6.8%	10 2.6%	40 10.5%	12 3.2%	140 36.8%	118 31.1%	50 13.2%	30 7.9
靜力穩定度檢定	0	0	0	0	12 3.2%	4 1.1%	0	0

(b) 客觀分析

客觀分析		850 mb 700 mb	700 mb 500 mb	500 mb 300 mb	300 mb 200 mb	200 mb 100 mb
Barnes	A	17 4.5%	7 1.8%	4 1.1%	17 4.5%	45 11.8%
	B	0	0	0	0	0
Cressman	A	27 7.1%	7 1.8%	9 2.4%	14 3.7%	36 9.5%
	B	0	0	0	0	0
Inman	A	19 5.0%	12 3.2%	7 1.8%	14 3.7%	37 9.7%
	B	0	0	0	0	0

註：A：靜水檢定　　B：靜力穩定度檢定

檢定格網格點，其分佈的型態，大致相似，根據檢定的原理，可推斷 250 mb 之主觀分析場，不甚理想。

圖 21(a) 至 21(d) 爲橢圓型條件檢定之結果，圖中的陰影區爲非橢圓型條件區域。在 850 mb、700 mb、500 mb 各層，非橢圓型條件區域大部份集中於菲律賓附近的海面上，850 mb 的圖略而未予標示。300 mb、100 mb 各層，雖然非橢圓型條件區域漸漸擴大，但仍以低緯地區較爲密集。因此可知非橢圓型條件區出現的頻率，以低緯地區之洋面上爲最高，此係因爲洋面上測站密度非常稀疏所致。就垂直方向而言，非橢圓型條件區出現的頻率隨高度增加而增高。根據此檢定，可知中緯地區的主觀分析場相當合理，而低緯地區雖然相當數量的網格點無法滿足橢圓

型條件，但由於該地區的測站資料密度極稀，因此不能滿足橢圓型條件而完全否定此些網格點值的可信性。

就整個天氣系統而言，有兩條主要槽線，一條是由日本附近向西南延伸，經臺灣而進入華南，此槽線對應於地面系統的梅雨鋒；另一條則是居於蒙古高壓與鄂霍次克高壓間的中緯槽。低緯地區則爲高壓所涵蓋。

圖 17(a) 至 17(d) 爲觀測風渦度場與水平輻散場，圖中實線代表渦度場，虛線則爲輻散場，單位爲 10^{-5} sec^{-1}，等值線間隔爲二單位，在 850 mb 層上，氣旋型渦度場位於日本九州南方，中心最大值 4.1×10^{-5} sec^{-1}，其軸線向西南延伸，經臺灣北部，沿長江流域南側到達四川，此軸線大致位於 850 mb 槽線的南側。水平輻合區的位置大致與此相同，但其中心最大值位於長江中游，-5.6×10^{-6} sec^{-1}。另一氣旋形渦度場位於蒙古，其中心最大值爲 5.3×10^{-5} sec^{-1}，大致位於中緯槽之上，在此區域亦有一水平輻合區，其數值較小。在中國北部及西北，爲反氣旋型渦度場，數值較小；另一反氣旋型渦度場位於西南太平洋。此兩渦度場均伴有水平輻散場，且與脊線的位置相配合。

500 mb 層上，在日本附近的氣旋型渦度場，位置較 850 mb 之位置北偏，最大值爲 6.2×10^{-5} sec^{-1}，此渦度場大約位於 500 mb 槽線之南側。在蒙古有一氣旋型渦度場及水平輻合場其最大值分別爲 7.1×10^{-5} sec^{-1} 和 -3.6×10^{-6} sec^{-1}，其位置與中緯槽的位置一致。中國東北有一反氣旋型渦場，最大值 -4.9×10^{-5} sec^{-1}，與一高壓脊的位置相配合。低緯地區幾爲反氣旋渦度場所涵蓋，此與低緯的高壓系統相符合。100 mb 之渦度場較接近 300 mb，但渦度值甚低，氣旋型渦度最大值爲 5.8×10^{-5} sec^{-1}，位於日本海，與高度場之槽線相配合。

除了觀測風渦度場外，還計算出地轉渦度場，根據零線的分析，發現各定壓層上，兩種渦度場氣旋型、反氣旋型渦度場的配置，非常相似，由此顯示出高度場與風場相當配合。

在理論上，高度場與風場可作相互的轉換，因此，根據風場所得的高度場，應與實際高度場相一致，本研究選用 500 mb 的觀測的渦度，求得流線函數

$$\nabla^2\psi=\zeta=\frac{\partial v}{\partial x}-\frac{\partial u}{\partial y}$$

然後再利用非線性平衡方程式以求得高度場

$$\nabla^2\varphi = \nabla \cdot (f\nabla\psi) + 2(\psi_{xx}\psi_{yy} - \psi_{xy}^2)$$

計算時以高度觀測值作爲邊界條件。

經此運算後所得的結果如圖 10，其高低壓中心强度稍弱於主觀分析 500 mb 高度場，但兩者在型態上極爲相似。根據此一比較結果，可以論定主觀分析的 500 mb 高度場和風場在水平方向上可保持內部的一致性。

柒、主觀分析場之垂直運動結構

主觀分析利用運動學法求得各定壓層垂直速度場，分別如圖 9 (850 mb) 及圖 14 (a) (500 mb)。850 mb 之垂直速度場，其上升氣流區涵蓋日本、琉球、臺灣及長江流域以南的地區，大致偏於梅雨槽之南側，在臺灣南部及海南島附近各有一最大上升氣流中心，其速度各爲 -1.0 μb/sec 及 -1.6 μb/sec。在蒙古中部之上升氣流，位於中緯槽之東側，其最大上升速度爲 -1.7 μb/sec。雲貴高原一帶，上升氣流極爲旺盛，最大值達 -3 μb/sec。下降氣流區分佈於黃海、中國東北及菲律賓東方的太平洋洋面，其最大下降速度分別爲 1.2 μb/sec，1.7 μb/sec 及 1.1 μb/sec；另外在新疆省東部亦有旺盛的下降氣流，其下降速度爲 3 μb/sec，此與脊線的位置相配合。

700 mb 垂直速度場，在型態上大致與 850 mb 相似，但垂直速度較大。相對於梅雨鋒帶之上升氣流區，以琉球、臺灣及長江中游一帶較旺盛，最大上升速度 -5.2 μb/sec 位於長江中游。相對於中緯槽前方之上升氣流區，稍偏於 850 mb 之西側，最大上升速度爲 -2.5 μb/ses，位於綏遠省境。在中國東北南部，有一微弱的上升氣流區。在日本附近之梅雨槽的後方爲下降氣流區，其最大下降速度爲 2.9 μb/sec，在中緯槽後方甘肅、寧夏一帶，亦有旺盛下降氣流，最大值 2.8 μb/sec，在太平洋高壓脊區的下降氣流最大值爲 2.1 μb/sec。

垂直運動在 500 mb (圖 14) 上，更爲旺盛，各上升氣流區與下降氣流區的範圍，與 700 mb 之垂直速度場相似。由圖 14(a) 可知，上升氣流以琉球、臺灣及長江中游較爲旺盛，在琉球及長江中游之最大上升速度，分別爲 -5.1 μb/sec 及 -6.6 μb/sec。在綏遠省境有一上升氣流中心，其最大值爲 -4.5 μb/sec。山東半島有一下降氣流中心，其下降速度爲 4.9/μb sec；新疆省之下降氣流，最大值爲

4.6 μb/sec；位於西南太平洋的下降運動區，其下降速度稍强於 700 mb。

300 mb 的垂直速度有轉弱的趨勢，琉球附近之最大上升速度爲 −4.7 μb/sec，長江中游則爲 −4.3 μb/sec，稍弱於 500 mb。另外在蒙古，綏遠處之上升氣流亦較 500 mb 弱。日本北部轉變成下降氣流，各下降氣流區的變異不大，山東半島之最大下降氣流爲 5.0 μb/sec。200 mb 之垂直速度與 300 mb 大致相似，惟垂直速度稍弱。

在 100 mb 處，垂直速度更爲微弱。上升氣流仍以琉球附近較强，最大速度爲 −2.8 μb/sec；下降氣流則以山東半島附近較强，其最大值爲 3.5 μb/sec。

另外根據準地轉 ω 方程式及線性平衡方程式組求得的垂直速度場，圖 15(a)。由此結果可發現此二種方法所得之垂直速度較微弱，尤其是梅雨槽前之上升氣流區及長江中游一帶的上升氣流區，其最大值僅爲運動學法所得之垂直速度的 $^1/_5$，此係因本研究中準地轉 ω 方程式及線性平衡方程式組未考慮潛熱的釋出，而在梅雨鋒處，降水充沛，潛熱釋出的效應變得非常重要，因此這兩種方法均無法得到正確的垂直速度，不過其所得之垂直速度場的配置與運動學法之結果相差不大。

一般而言，上升運動分佈於槽線的東側或南側；下降運動則在脊線的東側或南側。換言之，上升運動在槽線的前方，而下降運動則在槽線的後方。綜觀三種計算法，其所得的垂直速度場，大致符合這個原理。

根據衛星照片（圖 6），可知在梅雨鋒帶，即日本、琉球及臺灣一帶，雲層甚厚，可推知此處有旺盛的上升氣流，由運動學法所得之垂直速度場，充分顯示出此一事實。又根據雲量觀測資料（圖 7），顯示在日本、琉球、臺灣、長江以南的區域以及綏遠、陝西一帶，均爲密雲；屬於上升氣流；山東、河北、遼寧一帶及蒙古，雲層（十分量）均在 1 以下，爲下降氣流，與計算結果相符。

捌、客觀分析場與主觀分析場之比較

Barnes, Cressman 及 Inman 三客觀分析程式之各層分析場，分別經靜水檢定及靜力穩定度檢定，其各層未通過檢定的網格點數如表二，其所佔的比例甚小，而且大部份都分佈於分析場的周圍。又橢圓型條件的檢定結果如圖 21 至 24。由圖中顯示，低層之分析場大部份符合橢圓型條件，而不符合橢圓型條件之區域，多集中於低緯區之洋面上；較高層之分析，非橢圓型條件之區域，隨高度增加而擴大。

圖 18，19，20 分別爲 Barnes, Cressman 及 Inman 客觀分析程式的渦度場與輻散場。三種客觀分析程式所得之結果，彼此非常相似，而且與主觀分析之渦度場與輻散場亦很相似。850 mb 層在日本南方，琉球、臺灣北部附近及長江中游一帶爲氣旋型渦度，最大中心在球琉附近，而此一區域亦爲水平輻合區。另外在蒙古，亦屬於氣旋型渦度，而水平輻合較弱。反氣旋渦度及水平輻散，涵蓋華北及中國東北一帶。就整個系統而言，與槽脊線的位置相當配合。700 mb 之型態與 850 mb 大致相同。

在 500 mb 層，日本附近的氣旋型渦度場較 700 mb 稍向北偏，而對應於中緯槽之氣旋型渦度場，其位置同於 700 mb；在低緯區及中國東北，則爲反氣旋渦度場及水平輻散區。300 mb 及 200 mb 之型態與 500 mb 相類似，惟强度漸次遞增。至 100 mb 時，强度變弱，最大氣旋渦度中心，三種客觀分析均位於韓國，偏於主觀分析之西側，主觀分析之最大氣旋渦度中心位於日本海。

綜觀整個系統，三種觀分析之渦度場與輻散場的配置大致能與槽脊線或高低壓系統的位置相配合。另外分別計算出三種客觀分析的地轉渦度場，在各定壓面上進行零線的分析，結果顯示，觀測風渦度場與地轉渦度場的型態非常相似，由此可推定客觀分析的高度場與風場相當配合。

圖 11 與圖 12 爲主觀分析及三種客觀分析在各定壓層上的高度場及溫度場。高度場的分析，500 mb 上等高線的間隔爲 60 m，溫度場的分析，以 3°C 爲間隔。850 mb 高度場，三種客觀分析之結果，不論在型態和强度方面，與主觀分析場的差異很小。位於蒙古的中緯槽及相對於梅雨鋒的槽線，其位置極爲吻合。但在低緯度分析場的邊區，則有所差異。在越南北部，三種客觀分析均有封閉低壓，但主觀分析則無；Cressman 及 Inman 客觀分析在雲貴高原另有一封閉低壓。另外在菲律賓東方之太平洋洋面上，Barnes 分析程式之結果高度較低。

700 mb 層，主觀分析場上有三個低壓系統，即位蒙古、日本海及西康省的低壓。位於日本海之低壓，其中心位置，三種客觀分析與主觀分析完全吻合，但 Barnes 客觀分析的中心强度較强。位於蒙古的低壓，Cressman 及 Inman 客觀分析程式所分析出的中心位置偏於主觀分析之中心位置的南方，而 Barnes 分析程式之結果則偏北，且中心高度值較高；位於西康省之低壓，三種客觀分析之中心位置均偏於主觀分析之西方，而且 Cressman 及 Inman 分析程式在四川附近分離出一封閉低

壓，此係受其中兩個測站觀測值偏低之影響，而 Barnes 分析程式，由於權重受各測站之影響，故未出現此一低壓。在菲律賓東方的太平洋洋面上，由於資料缺乏，因此三種客觀分析的結果均低於主觀分析。

500 mb 之分析場（圖 11），在型態上四種分析程式大致相仿。中緯槽的位置無所差異，但在强度上，三種客觀分析程式的結果均弱於主觀分析。對應於梅雨鋒之槽線，三客觀程式所定之位置均同於主觀分析，Cressman 及 Inman 分析場上，沿此槽線之氣壓梯度與主觀分析相接近，而 Barnes 分析場則較平緩。

在 300 mb 分析場中，中緯區氣壓系統的配置、梯度等，客觀分析場與主觀分析場相似，唯 Barnes 分析場之中緯槽的位置，略向西偏。

三種客觀分析程式之 200 mb 分析場，其對應於梅雨鋒之槽線的位置均與主觀分析相近，沿此槽線的氣壓梯度及等壓線的曲率，以 Cressman 與 Inman 之分析場較接近主觀分析場。位於華北之脊線，其位置亦以 Cressman 及 Inman 之分析結果較接近主觀分析，在西康之小高壓，三種客觀分析之結果均偏離主觀分析之位置甚多，根據鄰近的觀測資料來判斷，主觀分析所分析出來的小高壓，其本身有待商榷。

100 mb 之客觀分析場，曲線非常不平滑，雜波甚多，此完全是客觀分析受到本身權重的影響，對測站的資料，無法作彈性的選擇，加以資料不够充足，且分析場外無資料可供參考，協助分析，因此，各客觀分析本身，雖有濾波器，但仍有短波出現於分析場上。

根據各定壓層的主觀分析場與客觀分析場，比較其高度值的差異，如圖 22 至 24 所示，其分別爲 Barnes 客觀分析，Cressman 客觀分析及 Inman 客觀分析與主觀分析之差異，圖中實線卽爲主觀分析與客觀分析之高度的差值，以 30 m 爲間隔。因 850 mb 之差異均甚小，故圖例省略。在 700 mb 層，三種客觀分析和主觀分析之差異，主要在西太平洋，Barnes 分析程式與主觀分析之差異達 60 m。500 mb 層，Cressman 及 Inman 分析程式與主觀分析之差異仍不大，分佈於菲律賓東方之洋面上及蒙古一帶；而 Barnes 分析結果與主觀高度分析場的差異，除上述兩個外，尙有日本海及黃海等區域。300 mb 分析場上，Cressman 和 Inman 之高度場與主觀之分析高度，在日本南方及蒙古等區域，相差 30 m，而 Barnes 之分析，則相差 60 m；在日本北海道及庫頁島一帶，Inman 分析程式與主觀分析的差異最

大，達 90 m；而 Barnes 分析次之，有 60 m；Cressman；分析程式最少，有 30 m。在 100 mb 層，以中國東北處之差異最大，此外 Barnes 分析程式在蒙古一帶的差異高達 90 m，低緯區的差異，則大致相同。

圖 12 是 500 mb 上主觀分析程式與三種客觀分析程式的溫度場。在日本附近，主觀分析之溫度低於客觀分析。Cressman 和 Inman 分析程式的溫度場有短波出現。在低緯度，幾無溫度梯度可言。300 mb 之溫度場，最主要的差異在於蒙古地區的溫度梯度，主觀分析較平緩，而三種客觀分析的型態約略相同。至 200 mb 以上，溫度場極爲簡單，在型態上，四種分析程式大致相同。

圖 13 爲 500 mb 之風場，就整個分析場，可以看出，除低緯區以外，大致情形極爲相似，在低緯區，尤其是菲律賓東方之太平洋上，各分析程式的差異甚大。

除上述的比較外，本研究還計算各高度場，溫度場和風場的均方根誤差（RMSE），結果如表㈢，並將高度分析的均方根誤差與 Mc Donell (1962) 所作北半

表三　分析場的均方根誤差 (Root Mean Square Error)

Cressman 客觀分析	850 mb	700 mb	500 mb	300 mb	200 mb	100 mb
Z 高度 m	4.02	4.75	7.46	10.99	14.51	20.61
T 溫度 °C	0.60	0.54	0.57	0.55	0.59	0.93
T_d 露點溫度 °C	0.81	1.39	1.70	—	—	—
u 風速分量 m/s	1.40	1.69	1.60	1.88	1.99	1.43
v 風速分量 m/s	1.49	1.58	1.41	2.26	1.87	1.66

Inman 客觀分析	850 mb	700 mb	500 mb	300 mb	200 mb	100 mb
Z 高度 m	4.80	5.16	8.04	12.67	16.78	21.57
T 溫度 °C	0.70	0.63	0.66	0.66	0.71	1.00
T_d 露點溫度 °C	0.97	1.64	2.07	—	—	—
u 風速分量 m/s	1.67	1.93	1.85	2.04	2.45	1.54
v 風速分量 m/s	1.81	1.95	1.61	2.76	1.89	1.77

Barnes 客觀分析	850 mb	700 mb	500 mb	300 mb	200 mb	100 mb
Z 高度 m	5.24	6.08	9.48	15.13	20.04	24.65
T 溫度 °C	0.89	0.74	0.80	0.79	0.85	1.20
T_d 露點溫度 °C	11.21	2.10	2.58	—	—	—
u 風速分量 m/s	1.93	2.24	2.28	2.63	3.06	1.87
v 風速分量 m/s	2.24	2.36	2.06	3.28	2.69	2.12

主觀分析	850 mb	700 mb	500 mb	300 mb	200 mb	100 mb
Z 高度 m	9.1	7.9	15.9	24.2	36.2	44.9
T 溫度 °C	1.5	1.2	1.1	1.2	1.6	1.7
T_d 露點溫度 °C	1.6	2.5	2.7	—	—	—
u 風速分量 m/s	3.2	3.2	3.5	5.1	6.6	3.3
v 風速分量 m/s	3.8	2.9	3.1	5.8	4.5	3.1

球高度場客觀分析結果及胡（1977）之高空天氣圖客觀分析之研究結果作比較表四；溫度分析的均方根誤差與 Masuda 及 Arakawa（1960）所作東亞區溫度場客觀分析結果及胡（1977）之結果比較，發現高度分析之均方根誤差均小於兩者之結果，而且在觀測隨機誤差之內；溫度分析的均方根誤差與兩者之結果大約相近，且都在觀測誤差之內。

表四　高空天氣圖客觀分析（胡，1977）之高度場與溫度

	Z 高度 m		T 溫度 °C	
等壓面	By C. Y. Hu	By McDonell	By C. Y. Hu	By Masuda & Arakawa
850 mb	8.4	9.7	1.15	0.98
700 mb	8.5	8.5	0.68	0.96
500 mb	11.8	12.5	0.61	0.91
300 mb	22.1	19.8	0.75	1.16

玖、客觀分析場之垂直運動結構

圖 14 爲 500 mb 上三種客觀分析利用運動學法求得各層之垂直速度。在 700 mb 三種客觀分析之垂直速度，除中南半島北部外，其他地區大致相同，尤其是中緯區，幾無差異。上升氣流分佈於日本、琉球、臺灣及長江流域一帶，此與梅雨鋒相配合；在綏遠省之上升氣流則位於中緯槽之東側。三處最大上升氣流中心，分別在琉球附近，蒙古及雲貴高原。琉球附近之上升氣流，三種客觀之分析最大值均爲 -3.7 μb/sec，稍强於主觀分析，Cressman 和 Inman 分析程式之位置與主觀分析相近，而 Barnes 分析程式之位置則稍偏北。在蒙古之上升氣流，其最大值 Barnes 爲 -5.2 μb/sec，Cressman 和 Inman 分別爲 -4.2 及 -4.5 μb/sec，三者之位置相一致，但均偏離主觀分析之最大上升氣流中心甚遠，且上升速度，幾爲主觀分析之兩倍。在中國西南，其最大上升速度，Barnes, Cressman 和 Inman 依次爲 -6.1, -6.2 和 -6.9 μb/sec，另外在中國東北有一局部的上升氣流，三客觀分析種程式之範圍均小於主觀程式，但依雲量狀況（圖 7）來看則以 Barnes 之結果最爲配合。下降氣流較弱，分佈於黃海、中國東北、韓國、日本海，最大下降中心在山東半島，其最大值，Barnes 爲 2.0 μb/sec，Cressman 爲 3.1 μb/sec，Inman 爲 2.8 μb/sec；另一下降中心在長江口，其最大值，依次爲2.0, 2.8, 2.8 μb/sec。在新疆寧夏甘肅一帶，亦有旺盛下降氣流，其最大值 Barnes 爲 3.6 μb/sec，Cressman 和 Inman 同爲 3.9 μb/sec；在菲律賓東方之洋面上亦爲下降氣流。

500 mb 之垂直速度（圖 14）較 700 mb 旺盛，其型態與 700 mb 相似。在琉球附近有一最大上升中心，其速度分別爲 -6.5 μb/sec (Barnes)，-6.7 μb/sec (Cressman)，-6.8 μb/sec (Inman)。對應於中緯槽的上升氣流，其最大值依次爲 -8.1 μb/sec (Barnes)，-6.1 μb/sec (Cressman 和 Inman)。在山東半島及長江口各有一最大下降中心，三種客觀分析在山東半島之最大速度，分別爲 4.5 (Barnes)，6.8 μb/sec (Cressman) 和 6.3 μb/sec (Inman)。在長江和則依次爲 3.6, 4.8, 5.0 μb/sec 在蒙古中部，下降氣流亦相當强烈。在 500 mb 層上，除長江中游之上升氣流，主觀分析較强外，其餘各處的垂直速度，三客觀分析均强於主觀分析。

300 mb 之垂直速度，其型態與 500 mb 相似，但强度轉弱，在日本附近的上升氣流區，漸漸向南縮退，最大上升中心仍在琉球附近，Barnes 爲 -6.6 μb/sec，

Cressman 爲 −7.3 μb/sec，Inman 爲 −7.5 μb/sec。最大下降氣流中心仍位於山東半島長江口及蒙古中部，位置大致不變，强度稍弱。200 mb 之垂直速度較 300 mb 弱，但最大值之位置則大致不變。長江口以南的中國東南沿岸，三種客觀分析之結果均爲下降氣流，而主觀分析之結果則爲上升氣流；另外菲律賓附近之洋面上，主觀分析與客觀分析之結果亦不同，前者爲下降氣流，後者爲上升氣流。至 100 mb 時，垂直速度已甚微弱，而在中國東南沿海，主觀分析與客觀分析之結果亦不同。

圖 15 與圖 16 爲利用準地轉 ω 方程式及線性平衡方程式所得之垂直速度場，其型態與運動學法之結果大致相似，但在梅雨鋒處，上升氣流過於微弱，與實際天氣不符合；而對應於中緯槽之上升氣流，位置過於偏北。另外在中國東北，沒有局部的上升氣流出現，而且在低緯區的分析亦不理想。

綜觀上述之結果，客觀分析場所顯示出之上升氣流，分佈於日本、琉球、臺灣、長江流域一帶及綏遠省，另中國東北有局部微弱上升氣流；下降氣流分佈於黃海，中國東北及新疆寧夏一帶。根據衛星照片（圖 6），在日本、琉球、臺灣一帶，深厚的雲層，足以說明琉球一帶旺盛上升氣流的可信性，又由雲量狀況（圖 7），可確定垂直速度場與實際天氣相配合。

拾、結　　論

本研究以主觀客析場作爲比較之標準，因此對其精度，先進行評估。根據靜水檢定及靜力穩定度檢定之結果，顯示在垂直方向上，除 250 mb 定壓層外，其他各層分析場均滿足垂直一致性，而具有較高的可信度。利用 500 mb 之觀測風求得高度場，與高度分析場極爲相似，由此在推論在水平方向，主觀分析能充分滿足內部一致性。在橢圓型條件檢定中，低層之低緯區及較高層出現較密集的非橢圓型條件區，但此係受資料不足及分析時引用地轉假設之影響，因此不能因分析場不滿足橢圓型條件，即否定其可信性。

三種客觀分析經靜水檢定，靜力穩定度檢定及橢圓型條件檢定，結果顯示其分析場甚爲合理。在和主觀分析比較下，可發現各客觀分析對於高低壓系統或槽脊線的位置，大都能精確的定出。而客觀分析與主觀分析之差異大都出現於蒙古地區，日本海、庫頁島及菲律賓東方之太平洋上，查看此些區域，測站的密度非常稀疏，

嚴重地影響到客觀分析的作業，在觀測資訊稠密區，客觀分析與主觀分析場之差異甚小。

在分析場之中央部份，資訊充足，Barnes 分析程式之結果，如高低壓系統之位置，强度等，較接近主觀分析，但在資訊缺乏的地區或資料有錯時，則其分析結果易有雜波出現，Barnes 分析程式使用指數權重，一個測站的資料幾可影響所有的網格點，因此若資訊的準確性及測站的密度獲得改善，則 Barnes 客觀分析之結果甚佳，又其只要掃描一次，故可節省分析時間，其K值可事先給定，且具有濾波作用，故無須使用其他濾波器。Cresmsan 和 Inman 客觀分析程式，因所用之權重相差不大，所以其分析場極爲相似，由於此兩種分析程式，係採用逐次校正之原理，故對資料之除錯能力較 Barnes 分析程式爲佳。

主觀分析及三種客觀分析，分別利用運動學法，準地轉 ω 方程式及線性平衡方程式求得垂直速度場，由其所得之結果顯示，不論是主觀分析或客觀分析，由運動學法所得之垂直速度，最能與實際天氣系統或衛星雲圖相配合，而由準地轉 ω 方程式或線性平衡方程式求得之垂直速度，均弱於運動學法之結果，由於本研究中未考慮潛熱的釋出，因此在降水區其垂直速度的計算結果，更見微弱。

綜觀三客觀分析程式之分析場，可發現在分析場之中央部份，其資訊轉換之能力較佳，在低緯區及西太平洋區，由於資訊不足之影響，分析結果不佳，因此如何改進資訊不足之問題，有待更深入之研究。

致　　謝

本文在行政院國家科學委員會專案計畫 NSC-68M-02-08 (03) 補助下完成。中央研究院物理研究所簡中興先生協助程式上機工作，中央氣象局提供有關資料，對上述各單位及個人，作者深表謝意。

參 考 文 獻

胡仲英，1977：高空天氣圖客觀分析之研究，大氣科學，第四期，1～10。

曾忠一，1976：東亞地區天氣資料變分客觀分析之研究，中央研究院物理研究所集刊，第六卷，161～178。

曾忠一，1977：利用原始方程式進行變分客觀分析之研究，中央研究院物理研究所集刊，第七卷，77～92。

Barnes, S. L., 1973: Mesoscale objective map analysis using weighted time series observations. NOAA Tech. Memo ERL NSSL-62, 60pp.

Bergthorssen, P. and B. R. Doos, 1955: Numerical weather map analysis. Tellus, 2, 329-340.

Bushby, F. H. and V. M. Huckle, 1956: Objective analysis in numerical forecasting. Quart. J. Roy. Meteor. Soc. 82, 232-247.

Chen, T.-J. G. and C. Y. Tsay, 1977: A detailed analysis of a case of Mei-Yu system in the vicinity of Taiwan. Tech. Rept, No. Mei-Yu-001, Dept. of Atmospheric Sciences, National Taiwan University, Taipei, Taiwan, 249pp.

Cressman, G. R., 1959: An operational objective analysis scheme. Mon. Wea. Rev, 87, 367-374.

Danard, M. B. 1964: On the influence of released latent heat on cyclone development. J. Appl. Meteor. 3, 27-37.

Haltiner, G. J., 1971: Numerical Weather Prediction. Wiley, New York, 317 pp.

Inman, R. L. 1968: Objective dectection and correction of errors in radiosonde data. Tech. Memo. ERLTM-NSSL-40, 48 pp.

Inman, R. L. 1970: Papers on operational objective analysis schemes at NSSFC. NOAA Tech. Memo. ERL NSSL-51, 91 pp.

Masuda, Y., and A. Arakawa, 1960: On the objective analysis for surface and upper level maps. Proc. Symp. International Numerical Weather Prediction, Tokyo, 55-66.

McDonell, J. E., 1962: On the objective analysis scheme used at the National Meteorological Center. NMC TM No. 23, National Meteorological Center, Washington, D. C., 32 pp.

McFarland, M. J., 1975: Variational optimization analysis of temperature and moisture advection in a severe storm environment. WEAT Report No. 16, University of Oklahoma, Norman, Oklahoma 86 pp.

Miller, A. and H. A. Panofsky, 1957: Vertical motion and weather, January 1-31, 1953. Scientific Report No. 2 Contract AF19(604)-1025, Dept. of Meteorology, Pennsylvania State University.

Otto-Bliesner, B., D. P. Baumhefner, T. W. Schlatter and R. Bleck, 1977: A comparison of several meteorolgical analysis schemes over a data-rich region, Mon. Wea. Rev. 105, 1083-1091.

Peterson, D. P. 1973: A comparison of the performance of quasi-optimal and conventional objective analysis schemes. J. Appl. Meteor., 12, 1093-1101.

Schlatter, T. W., G. W. Branstator and L. G. Thiel, 1976: Testing a global multivariate statistical objective analysis scheme with observed data. Mon Wea. Rev., 104, 765-783.

Shuman, F. G. 1957: Numerical method in weather prediction: II. Smoothing and filtering. Mon. Wea. Rev., 85, 357-361.

Stephens, J. J., 1971: On the definable scale reduction by simultaneous observations. J. Appl. Meteor., 10, 23-25.

Stuart, D. W., 1974: A comparison of quasi-geostrophic vertical motion using various analysis. Mon. Wea. Rev., 102, 363-373.

Trenberth, K. E., 1978: On the interpretation of the diagnostic quasi-geostrophic omega equation. Mon. Wea. Rev., 106, 131-137.

Vincent, D. G., K. E. Bossingham and H. J. Edmon, 1976: Comparison of large scale vertical motions computed by the kinematic method and quasi-geostrophic omega equation. Preprints of Papers, Six Conference on Weather Forecating and Analysis, Albany N. Y. 357-364.

Wilson, G. S. 1976: Large scale vertical mothion calculation in the AVE IV experiment. Geophys. Res. Letters, 3, 735-738.

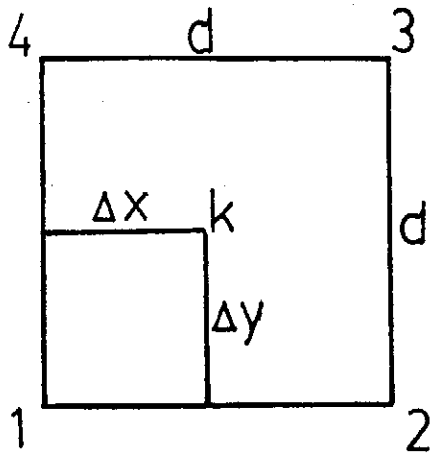

圖 1. 測站上分析值求法說明圖

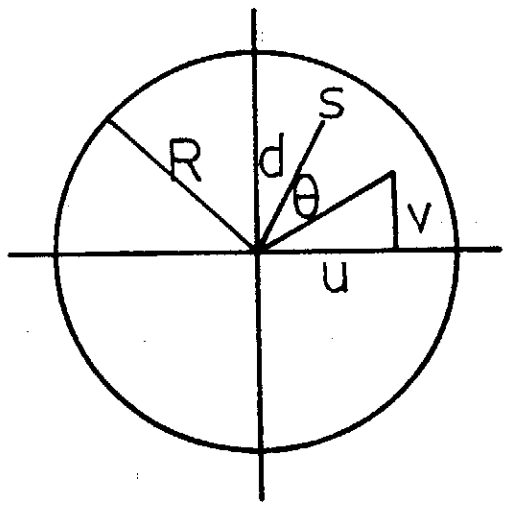

圖 2. Inman 權重的符號說明

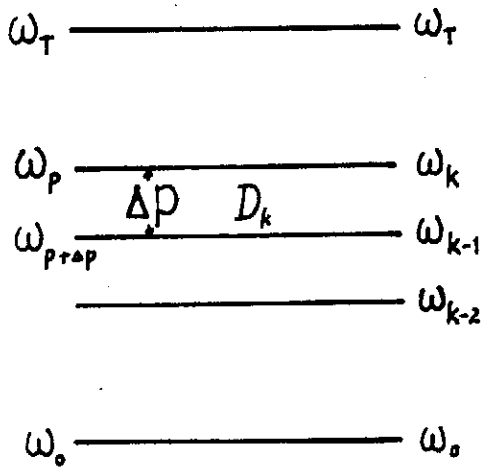

圖 3. 利用運動學法求垂直速度的說明圖 D_k 是氣層 Δp 的平均輻散，ω_0，ω_T 是大氣柱底部和頂部垂直速度的估計值。

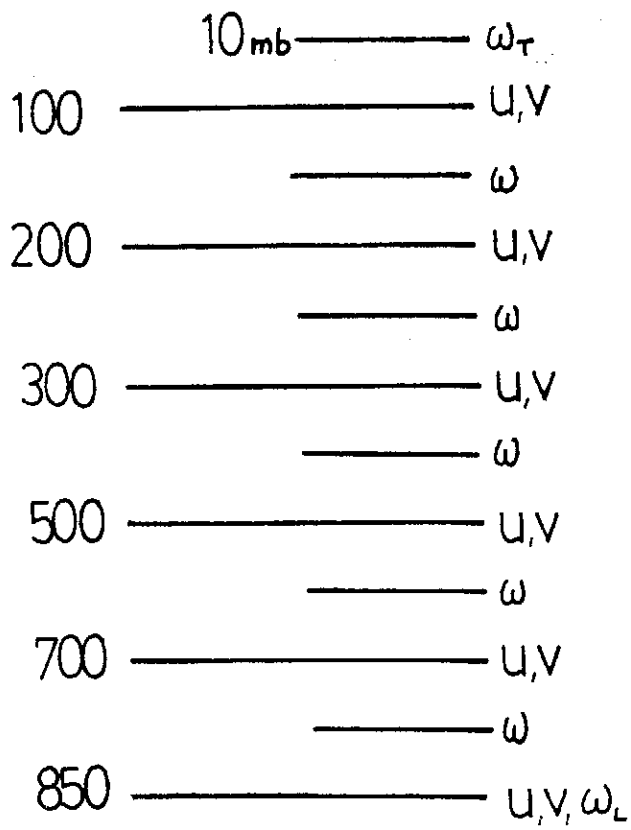

圖 4. 運動學法之網格系統的垂直結構。

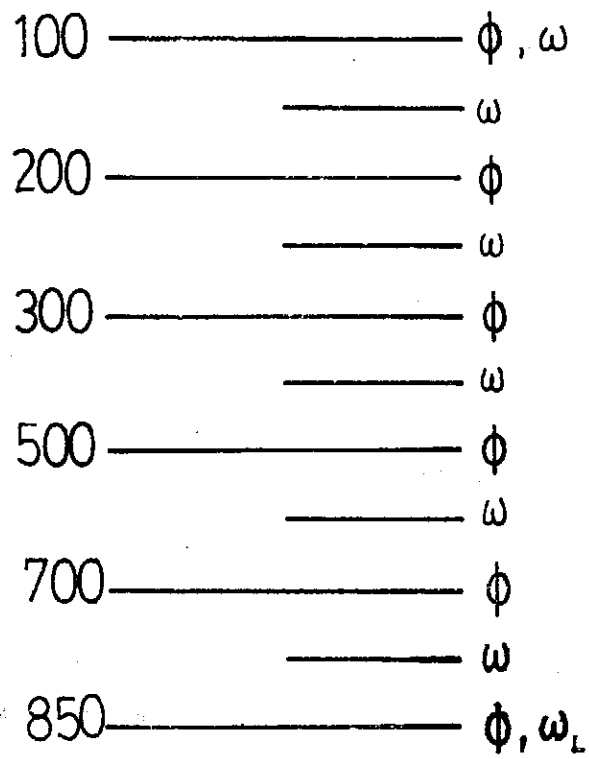

圖 5. 準地轉 ω 方程式和線性平衡方程式之網格系統的垂直結構。

圖 6. NOAA-4 紅外光衛星照片，白色虛線代表經緯度和海岸線，臺灣的位置用實線表示。

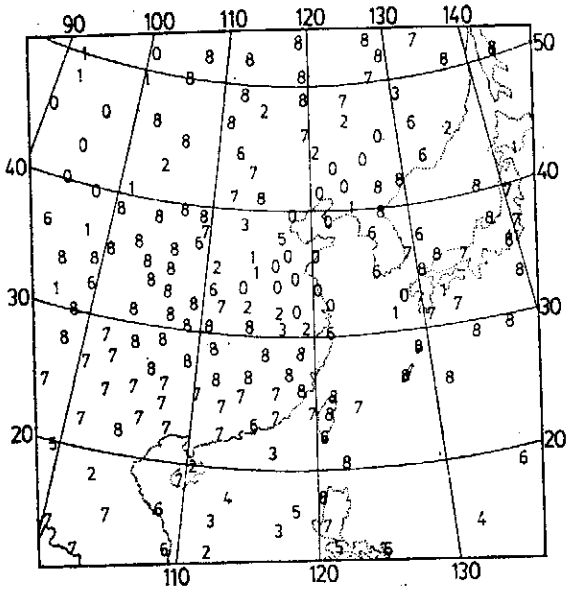

圖 7. 雲量（十分量）觀測記錄，數字標示點，即是測站的位置。

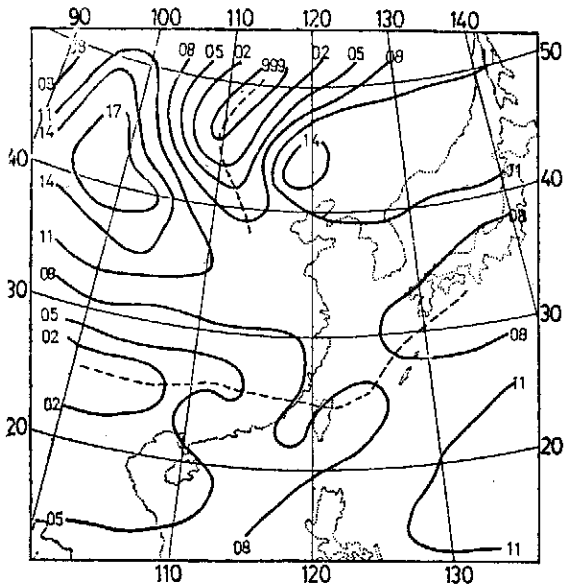

圖 8. 1975年 6 月10日 0000Z 主觀分析之海平面氣壓場，虛線代表鋒面。

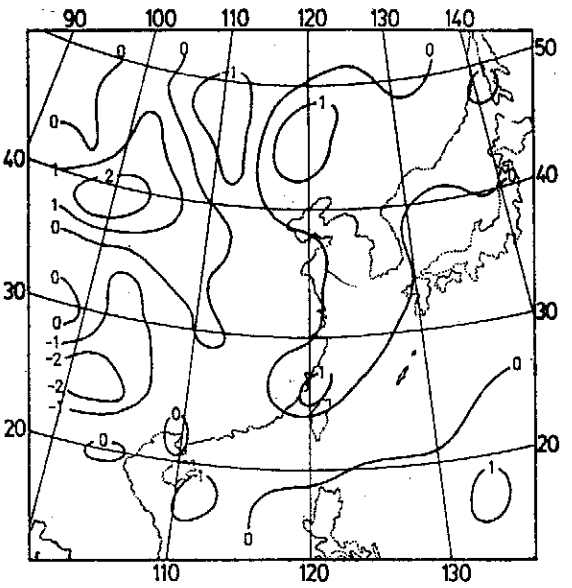

圖 9. 利用運動學法求得之主觀分析850mb 垂直速度場，單位：μb/sec
(Chen and Tsay, 1977)

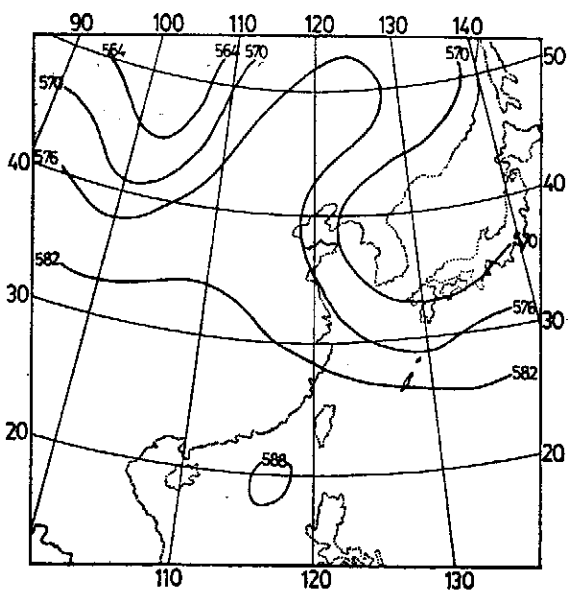

圖10. 利用 500mb 觀測風計算得到之高度場。

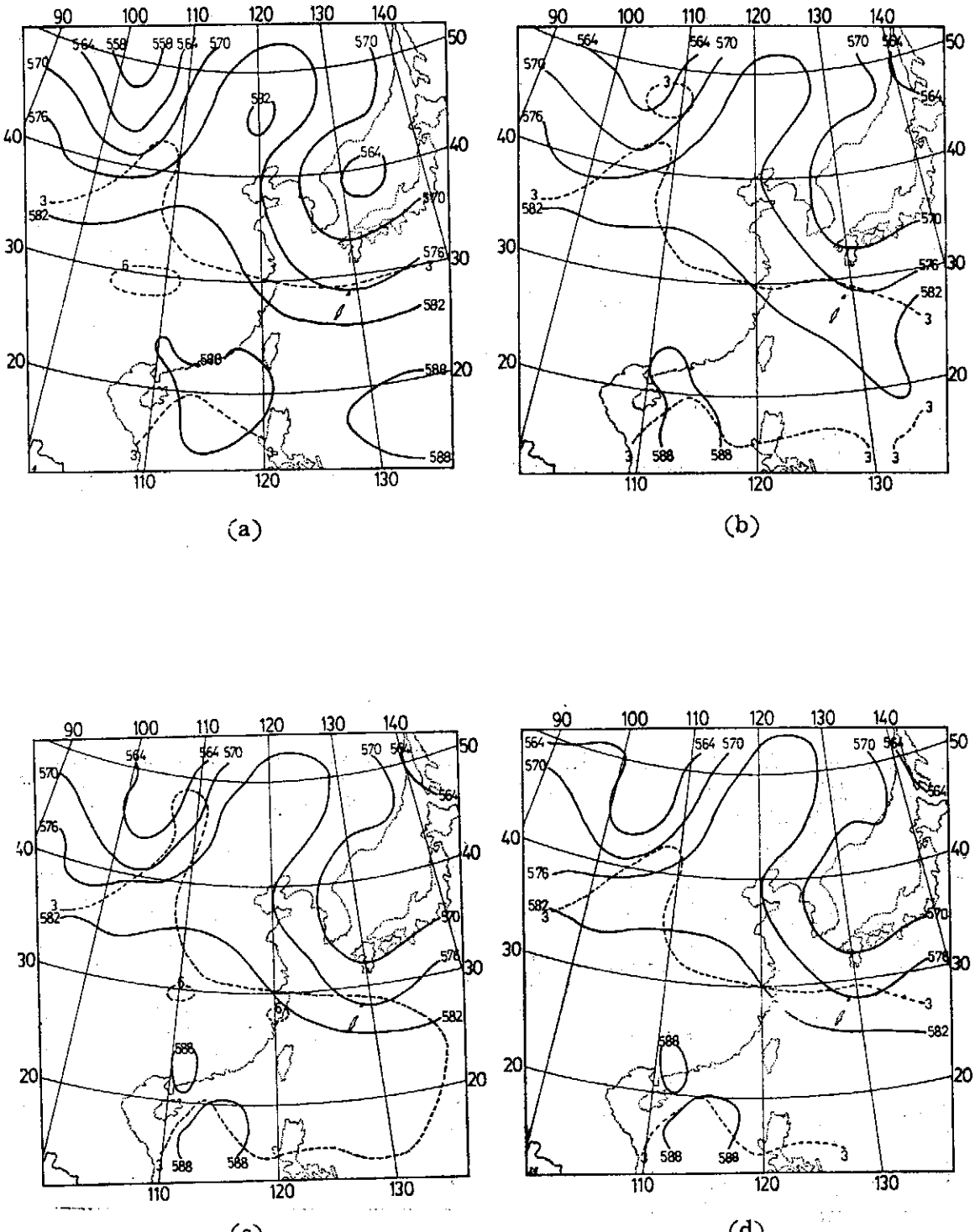

圖11. 500mb 高度場（實線，單位公尺）與混合比（虛線，單位 g/kg），(a) 主觀分析，(b) Barnes 客觀分析，(c) Cressman 客觀分析，(b) Inman 客觀分析。

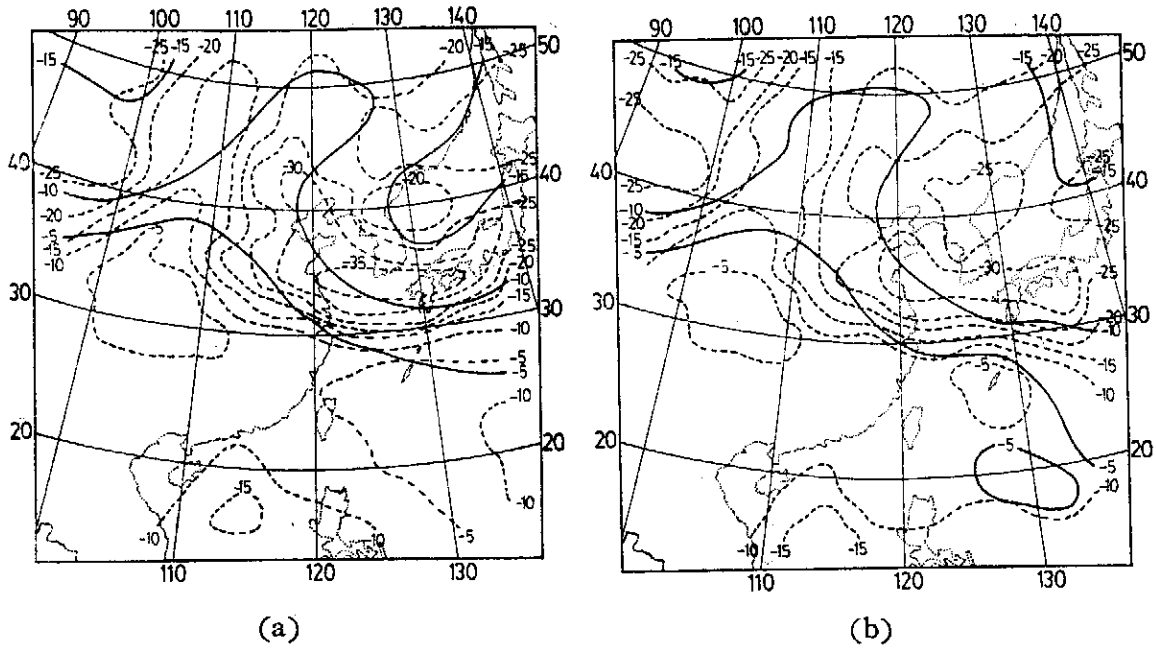

(a) (b)

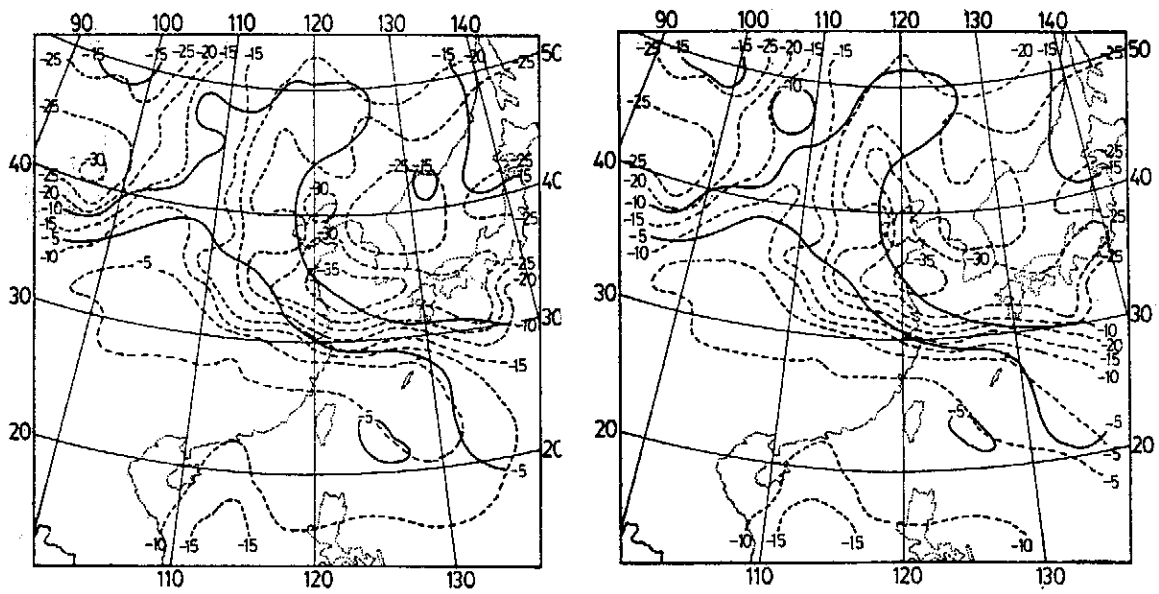

(c) (d)

圖12. 500mb 溫度場（實線，單位：°C）與露點溫度（虛線單位：°C）(a) 主觀分析 (b) Barnes 客觀分析 (c) Cressman 客觀分析 (d) Inman 客觀分析。

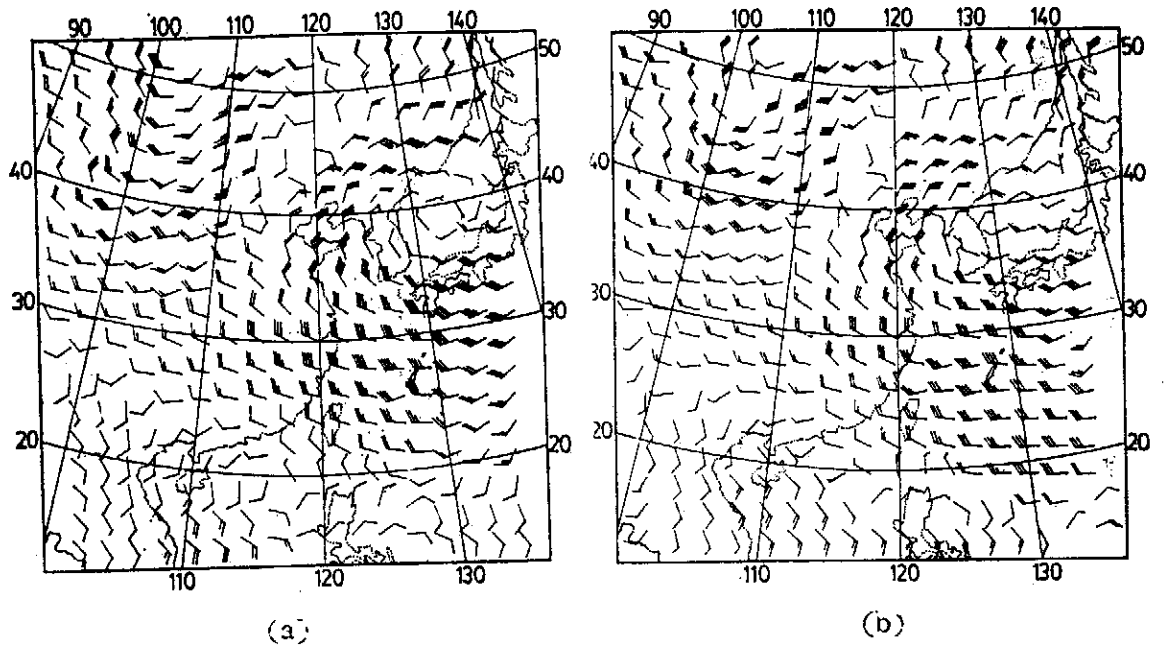

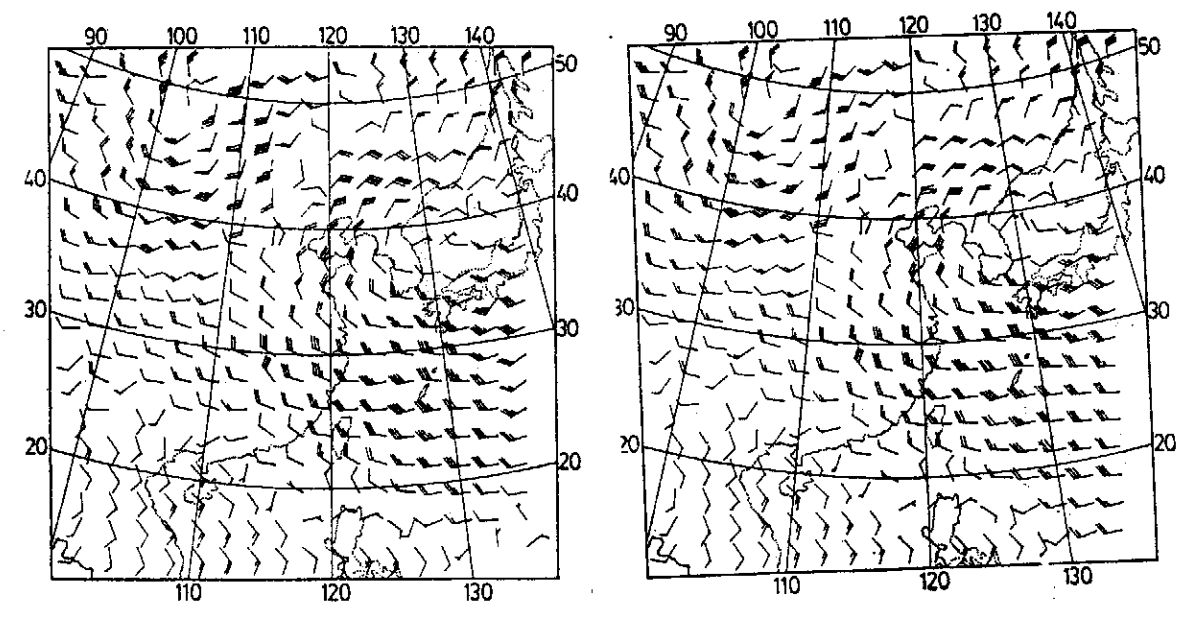

圖13. 500 mb 風場，(a) 主觀分析，(b) Barnes 客觀分析，(c) Cressman 客觀分析，(d) Inman 客觀分析。

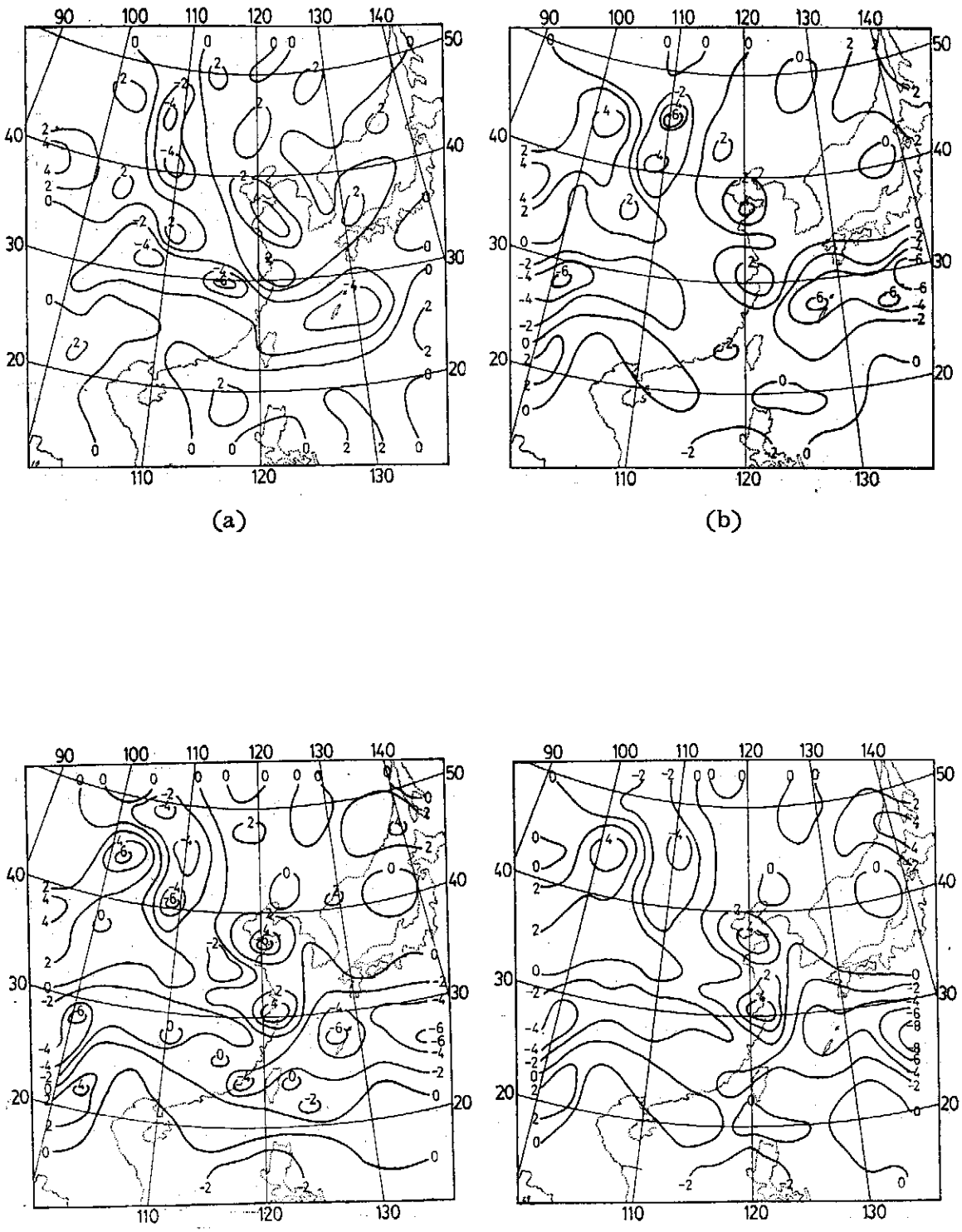

圖14. 利用運動學法求得的 500 mb 垂直速度，單位爲 μb/sec (a) 主觀分析，(b) Barnes 客觀分析，(c) Cressman 客觀分析，(d) Inman 客觀分析。

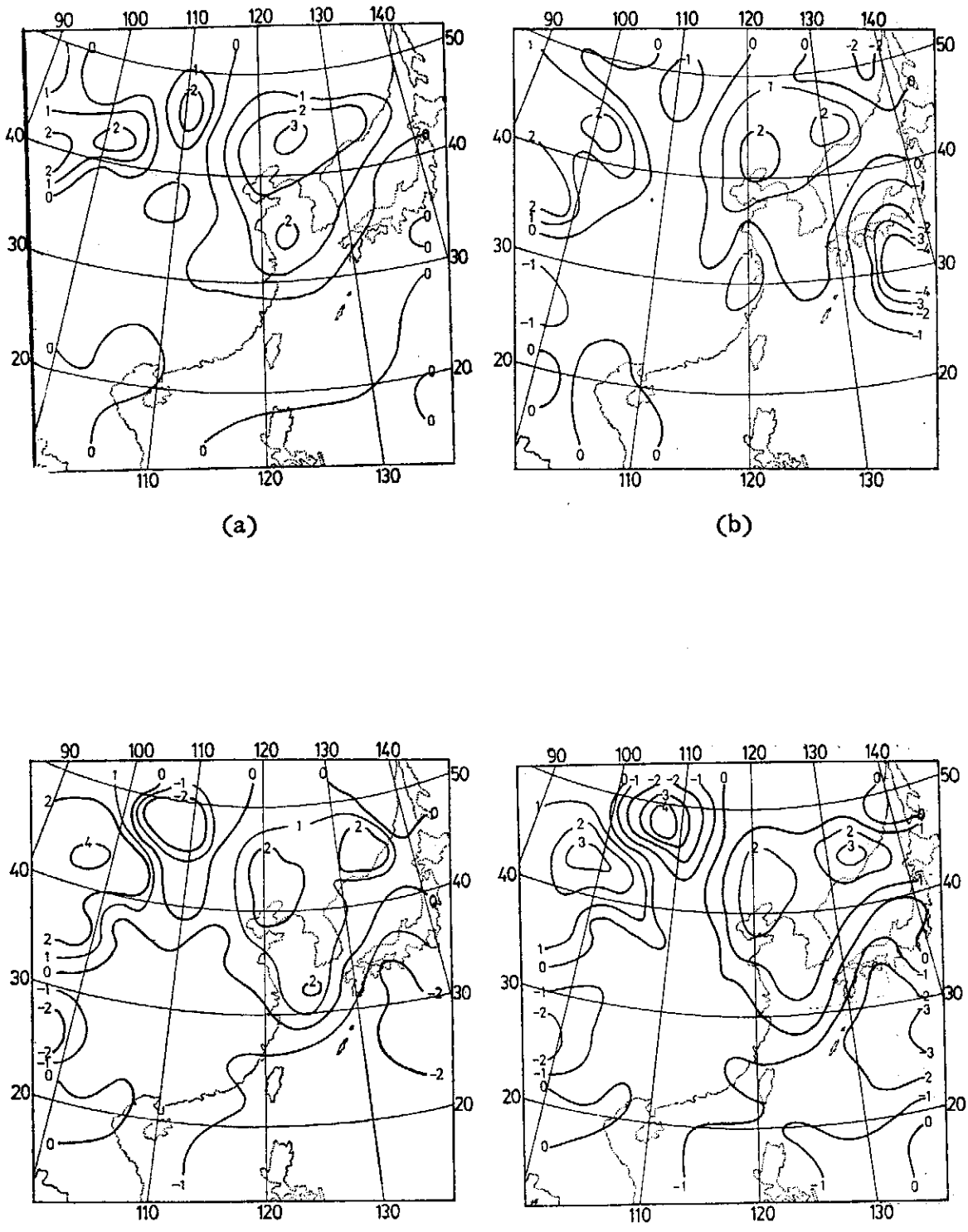

圖15. 利用準地轉 ω 方程式求得的 500 mb 垂直速度，單位爲 μb/sec (a) 主觀分析，(b) Barnes 客觀分析，(c) Cressman 客觀分析，(d) Inman 客觀分析。

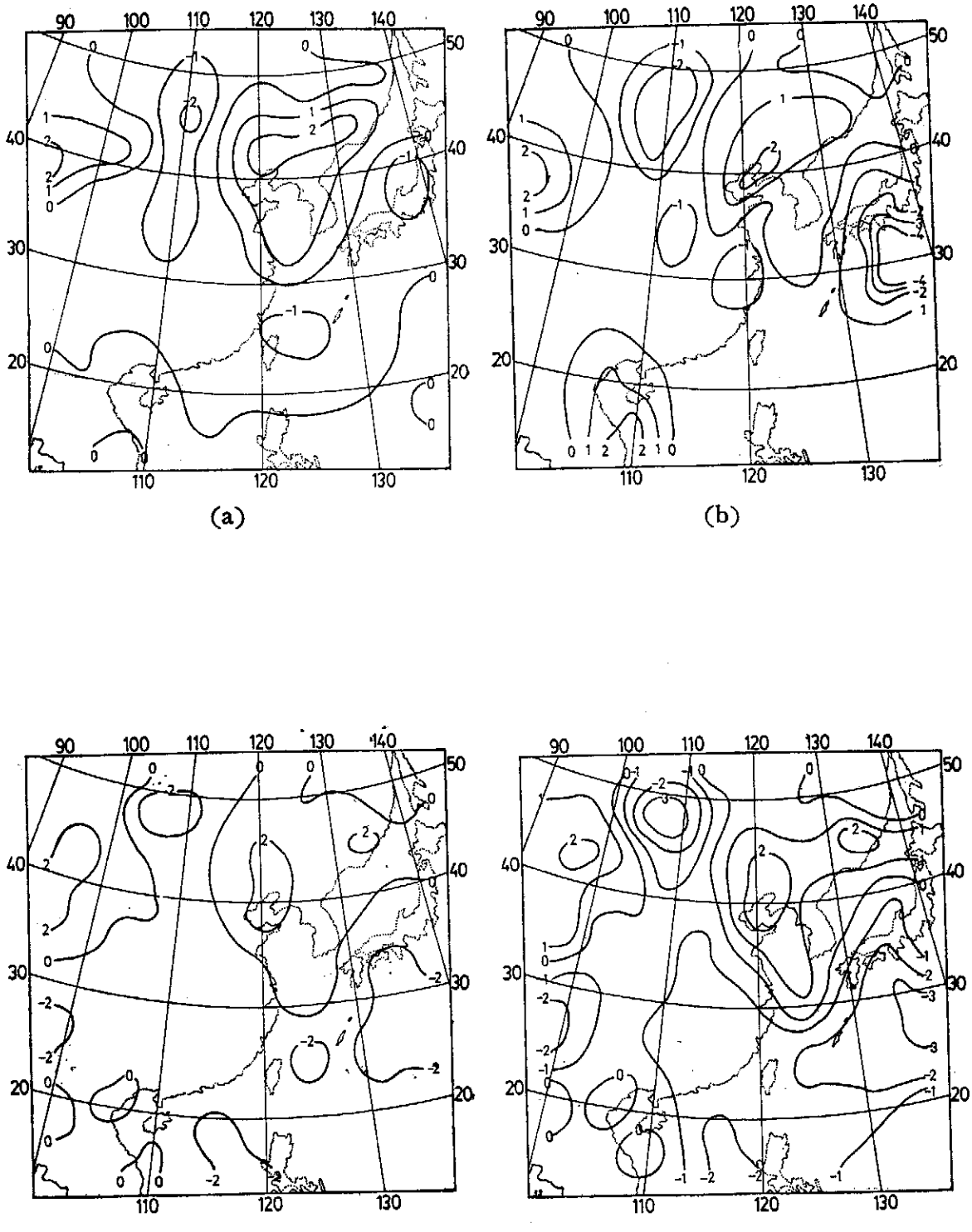

圖16. 利用線性平衡方程式求得 500 mb 垂直速度，單位爲 μb/sec，(a) 主觀分析，(b) Barnes 客觀分析，(c) Cressman 客觀分析，(d) Inman 客觀分析。

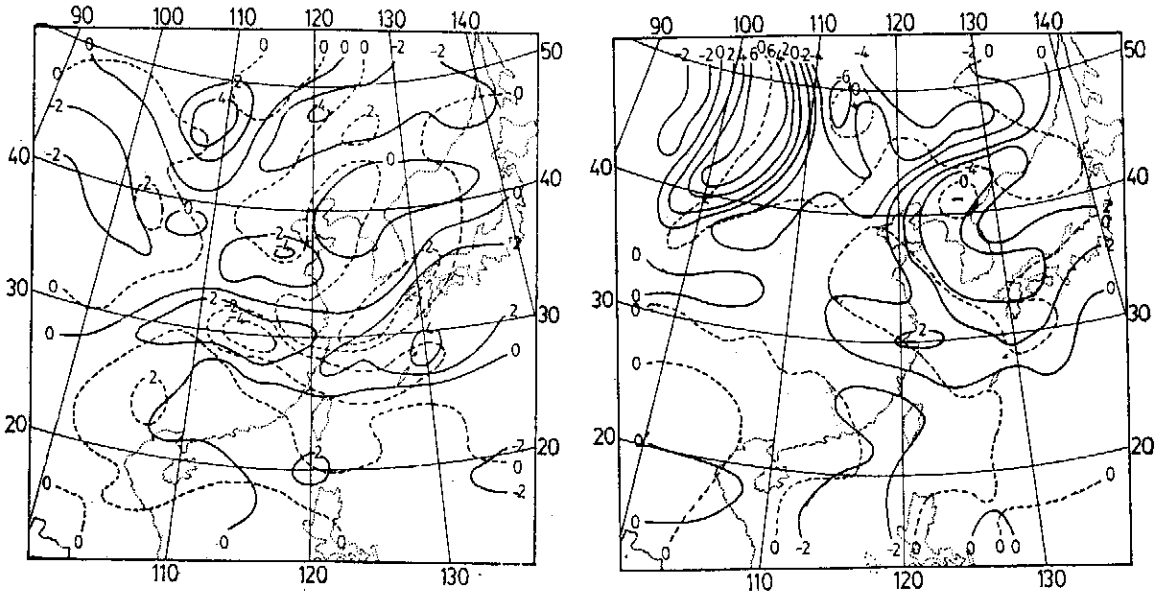

(a) (b)

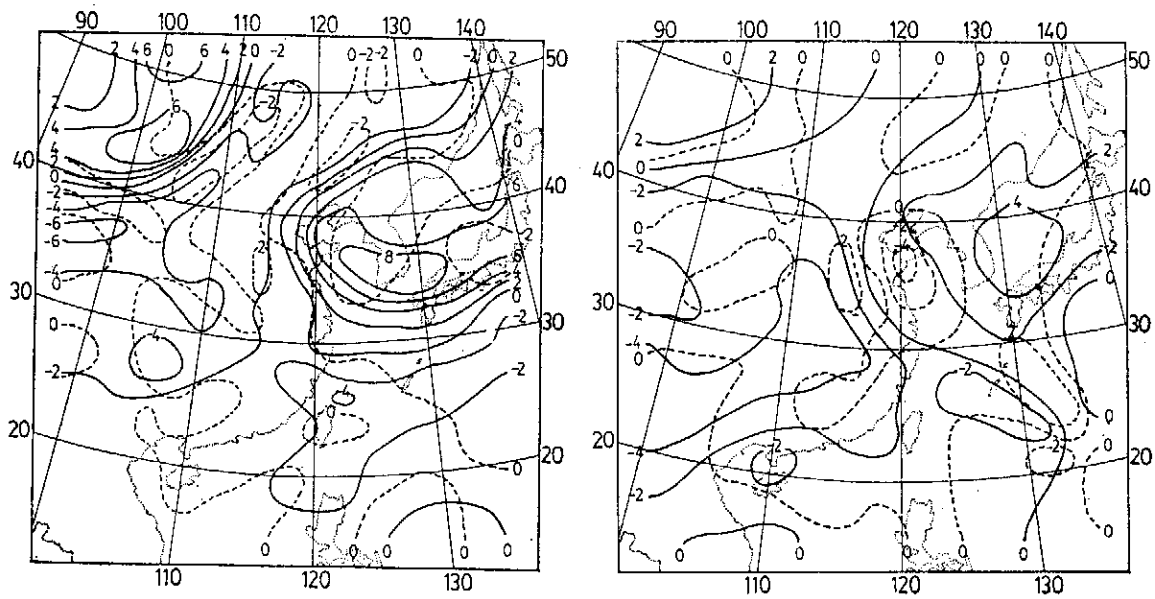

(c) (d)

圖17. 主觀分析的渦度場（實線，單位 10^{-5} sec^{-1}）與輻散場（虛線，單位 10^{-6} sec^{-1}）
(a) 850 mb (b) 500 mb (c) 300 mb (d) 100 mb

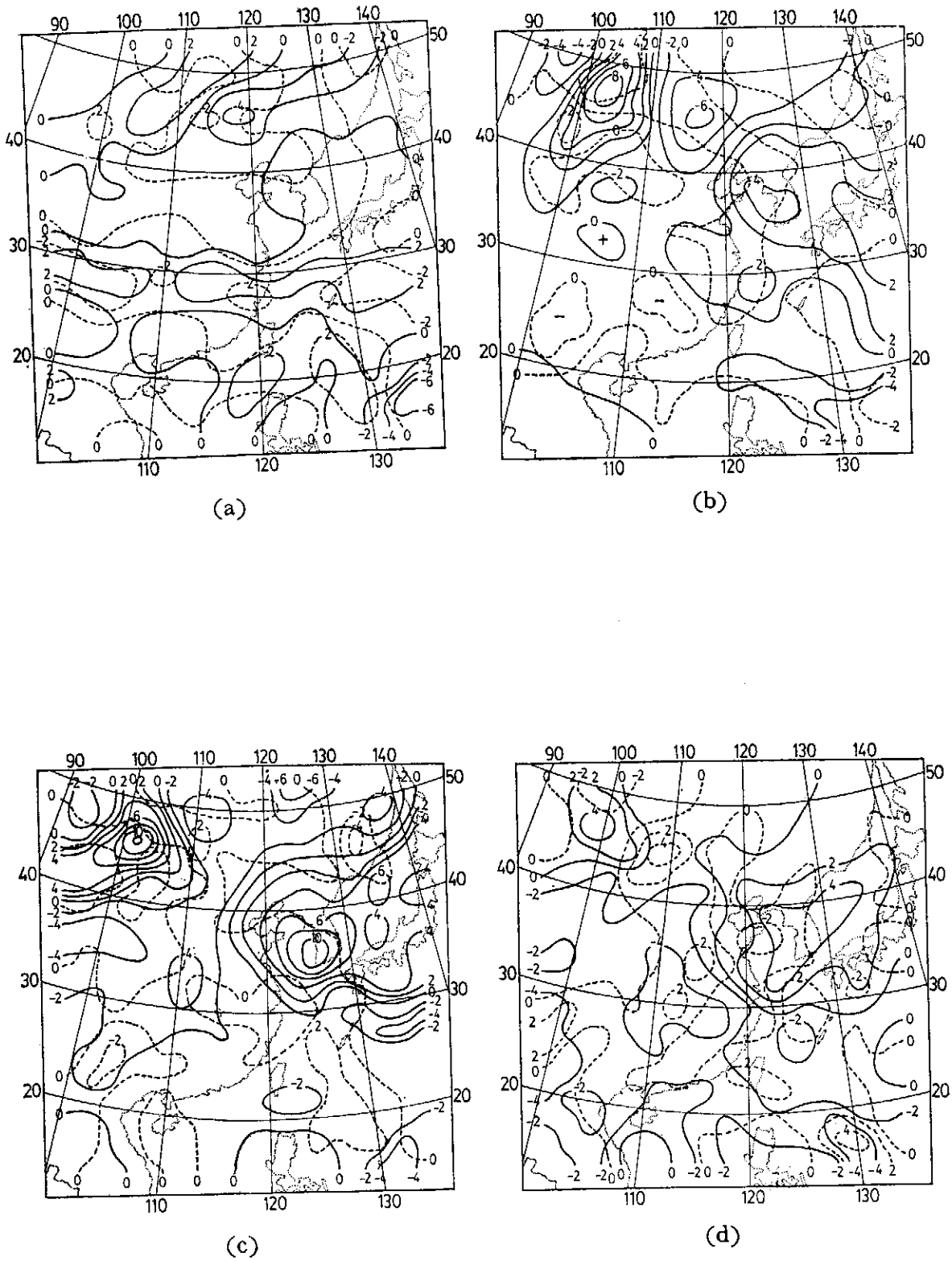

圖18. 同圖 17. 但爲 Barnes 客觀分析。

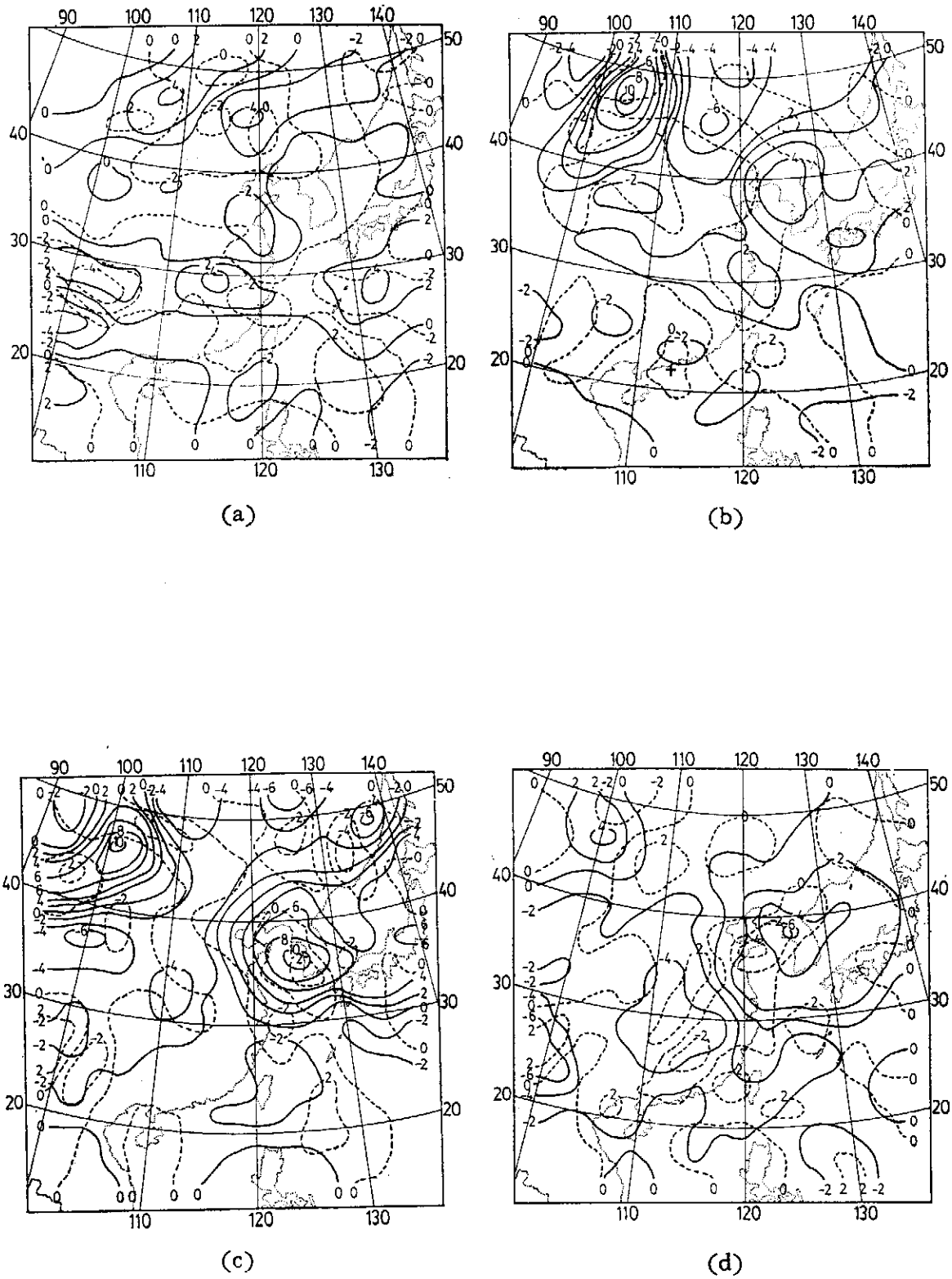

圖19. 同圖 17. 但爲 Cressman 客觀分析。

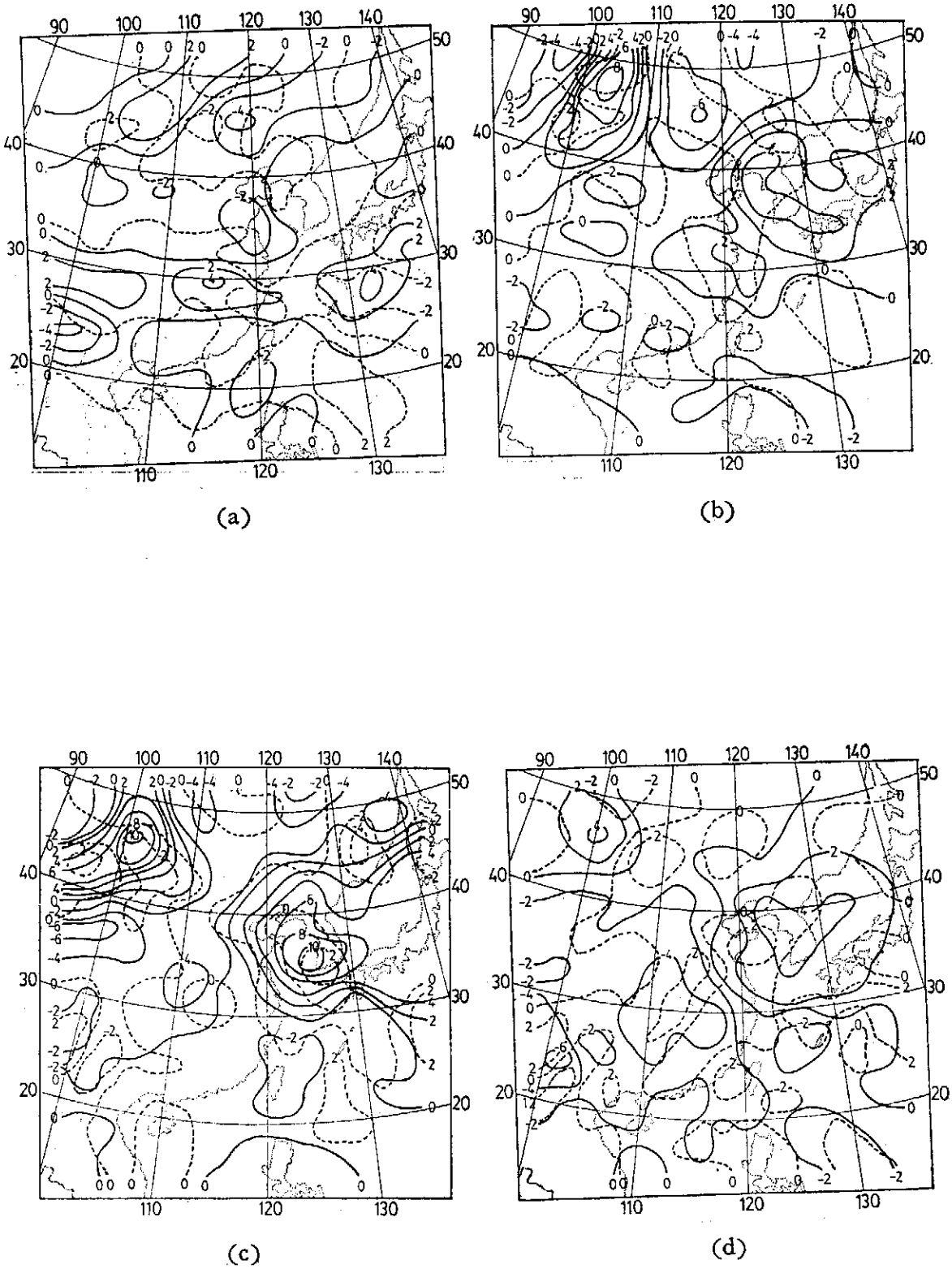

圖20. 同圖 17. 但爲 Inman 客觀分析。

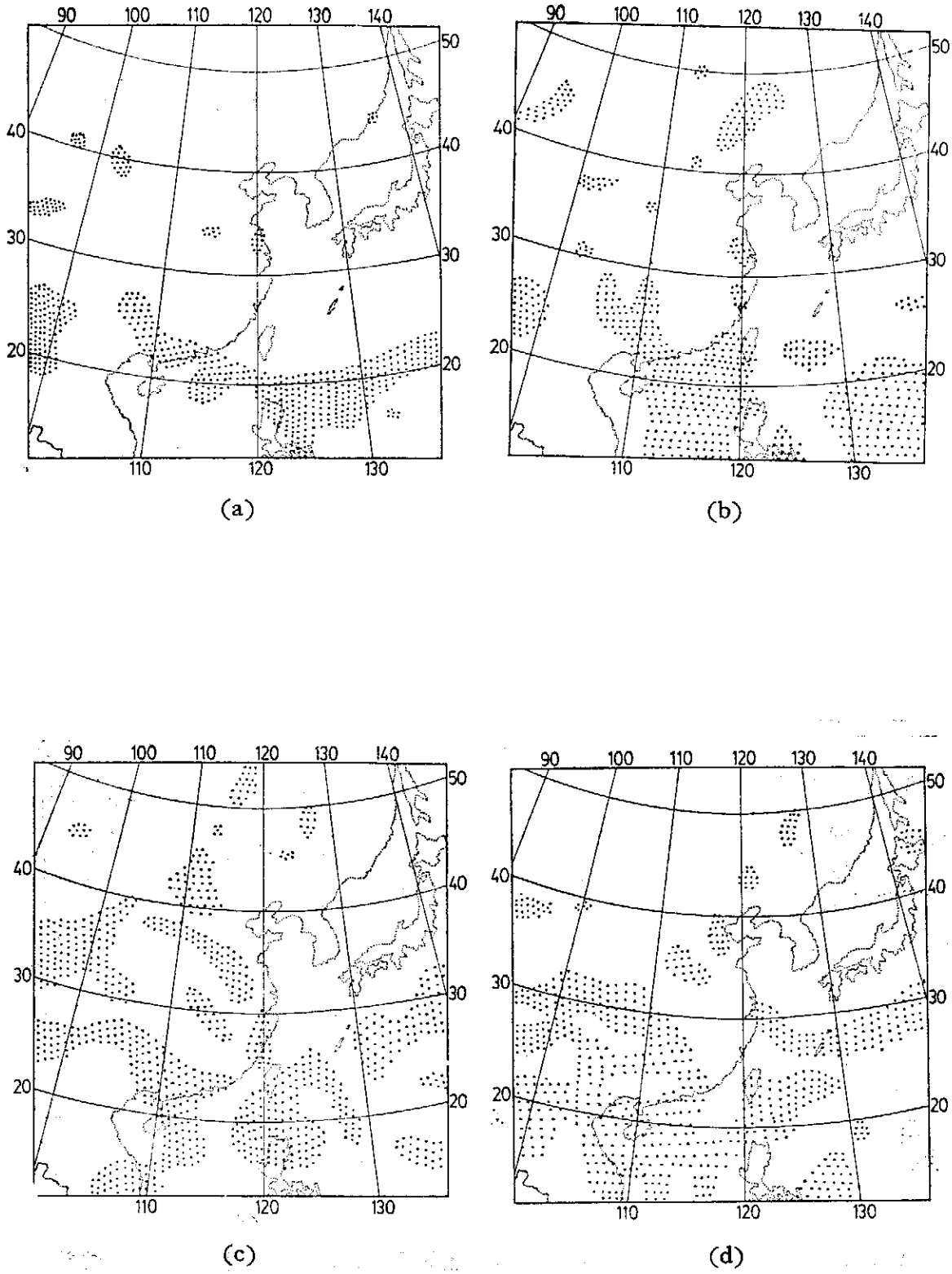

圖21. 主觀分析的橢圓型條件檢定 (a) 700mb (b) 500mb (c) 300mb (d) 100mb

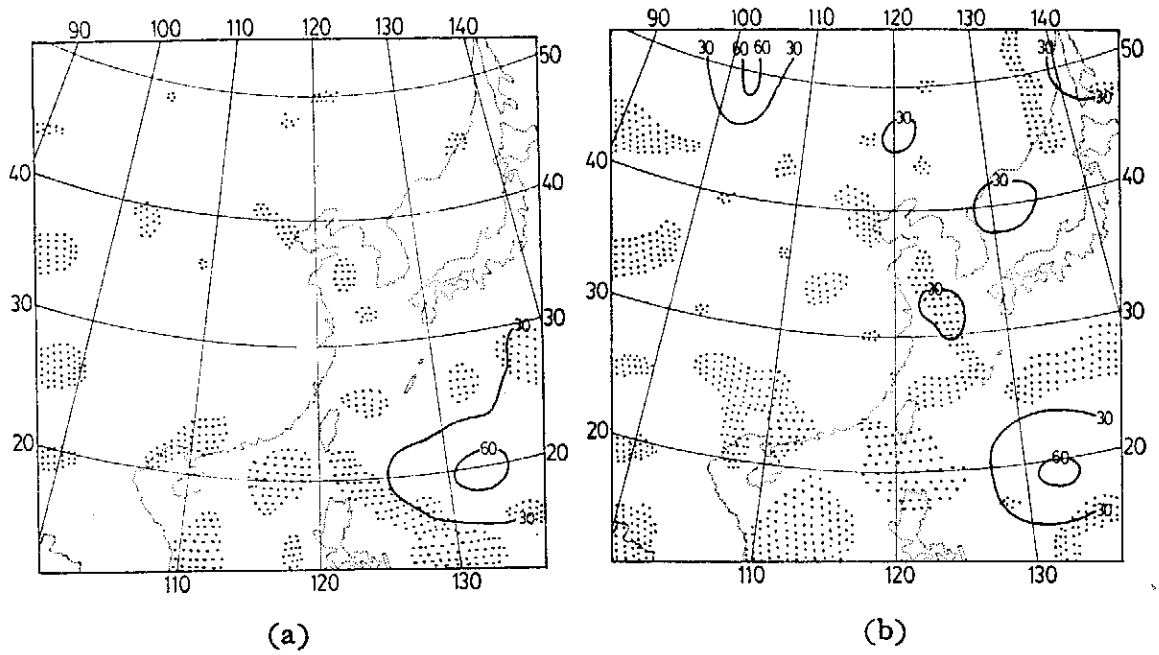

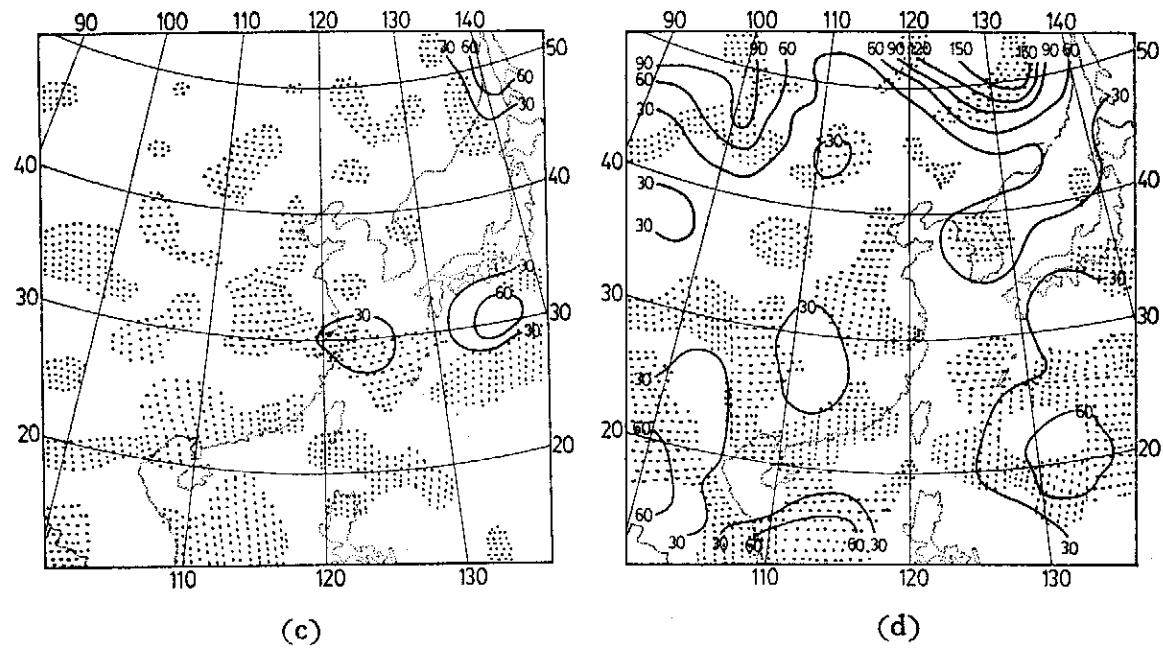

圖22. Barnes 客觀分析的橢圓型條件檢定。實線爲 Barnes 客觀分析和主觀分析之差異，單位爲 m (a) 700mb (b) 500mb (c) 300mb (d) 100mb

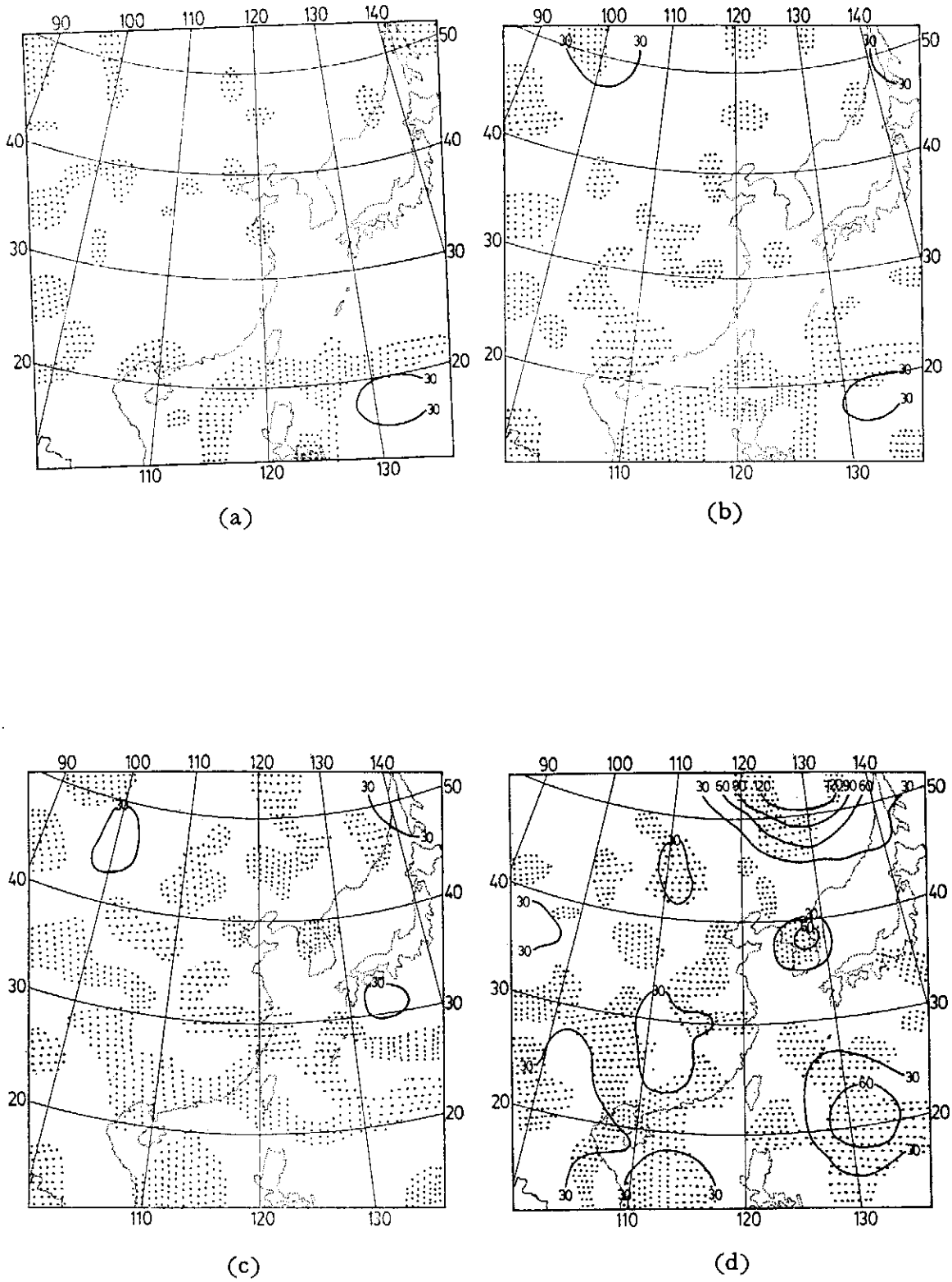

圖23. 同圖 22. 但爲 Cressman 客觀分析。

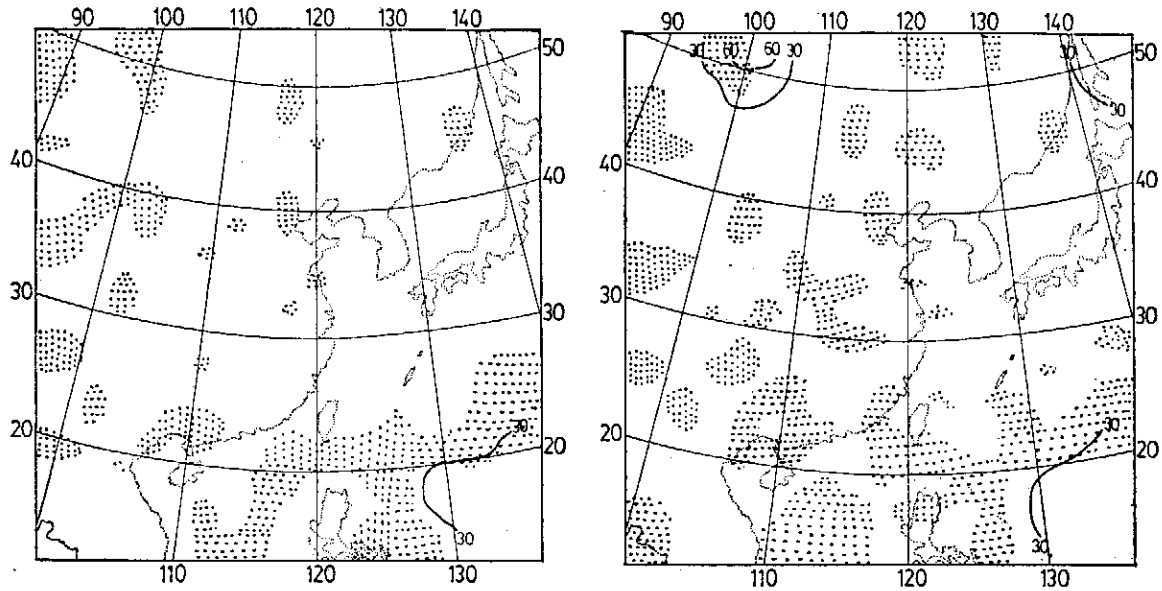

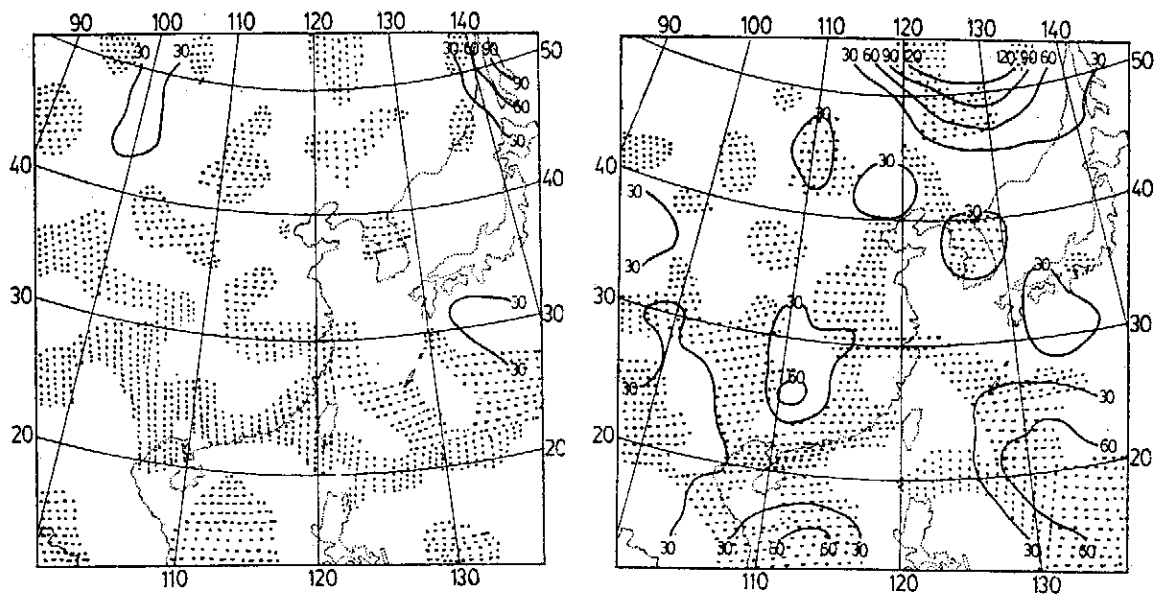

圖24. 同圖 22. 但爲 Inman 客觀分析。

台北市二氧化硫時序預報模式之研究

梁 文 傑

中央研究院物理研究所
國立臺灣大學機械研究所

蔡 豐 智

國立臺灣大學機械研究所

摘 要

本文是以臺北市二氧化硫的濃度變化爲對象來分析並建立小時濃度、日平均濃度的自廻歸積分、移動平均（ARIMA）模式，根據分析，此種模式可以有效地代表出二氧化硫濃度隨時間變化的情形而能用來作預報與控制的用途，對於週期性變化的情況也能有效地適用。

壹、導 論

在農業時代，因爲人口密度不高，都市人口集中的現象不嚴重，再加上排放污染物的量不多，所以污染問題不太受重視，但工業革命之後都市人口日見膨脹，工廠林立，大量排放各種廢氣廢水，於是水污染、空氣污染、熱污染及噪音等關乎人類生存環境品質的問題越發顯得重要。

空氣是人類和各種生物生存所必須而人類的活動在不知不覺中，改變了大氣的成份，於是二氧化硫（SO_2）、一氧化碳（CO）、氮氧化物（NO_x）、碳氫化合物（HC）、塵粒、黑煙等，成爲嚴重的空氣污染物，對人體健康、動植物的生長造成很大的危害，空氣污染史上曾發生幾次大災難，例如 1948 年美國賓州多羅那（Donova Pa）事件、1952 年倫敦大霧、1930 年比利時繆斯谷（Meuse Valley, Belgiun）等事件死了數千人[1]，而我國如民國 54 年高雄樹德女中師生 98 人，二氧化硫急性中毒等[2]等，說明了空氣污染防治的重要，而且事後的檢討顯示，上面各事件皆與二氧化硫含量過高有關，另據省環境衛生試驗所的調查，發現民國六十六年全省二十個縣市空氣污染損害作物 166.03 公頃中硫氧化物及硫化物佔了

32.03%，高居首位[3] 這乃是因二氧化硫的容許極限值 (Threshold limit value TLV) 只有 5 ppm[4] 容易造成傷害。

二氧化硫爲無色有窒息性的氣體，它會使人體的呼吸氣官，受傷甚至死亡（表一）[5]對植物的葉片造成脫水萎黃、灼傷等情形[3]，而二氧化硫又會轉化和水汽結合形成硫酸小滴的霧 (mist) 會使能見度降低，並侵蝕金屬、建築物、汽車等[6]，每年因爲二氧化硫所造成的損害，難以估計，亟需加以有效控制。

空氣污染問題的解決甚爲複雜，牽涉很廣，但不外乎觀察、分析、評估、預測、控制[7]，由觀測所得的資料往往不能直接提供有用的消息，需要加以分析、評估，而因爲採取有效行動去控制，往往須花費數月，甚至數年的時間，單就立法一事而言，立法若只根據現況（不作預報）則因法律從設定至實施常要數年，使得立法常在現況之後，因此預報的工作在整個的防治工作中佔據了一個無可取代的地位，而發展出一套有效的預報方式，也就成爲必須。

現在一般所作空氣污染濃度的預報，常是利用流體力學氣體流動的方程式加上能量方程式，把當時的氣溫風向等氣象因素再加上污染源的分布與排放量等資料而推算全面性的下一時間濃度分佈情況，但此因各種資料的取得受到經費、人力等現實因素的限制，以及大氣紊流的複雜性，不可能太密集而準確，所以所得的結果會有某種程度的誤差，不過它仍對全面性變化的趨勢提供了一個有效的工具。

對於局部性的變化而言，擴散模式既有上述的限制，本文採用另一途徑，直接把在偵測站測得的資料，加以分析，利用統計方法，找出適合該地的預報模式，因爲所有的資料皆是與該地的情況，具有很高的相關性，所以預報的結果自應比擴散模式爲佳，不過它仍不能應用在幾個關鍵性的大污染源（如大工廠）的偵測預報，若再配合擴散模式作全面性的預測，相信會使空氣污染的防治工作有極大的改善。

貳、統計模式理論

對於一物理量作一等時距的連續測量，則測量所得的數列叫作時間序列 (Time Series)，時間序列的分析法一般可分爲兩類[3] ㈠頻率域分析 (Analysis in frequency domain) 也叫作波譜分析 (Spectral Analysis)，係將時間序列的變化分解爲不同頻率變化的和，㈡時間域分析 (Analysis in time domain)，本文採用了 Box and Jenkins 在 1970 年[9]，所提出的一種時間序列分析法，來對不同的時間

序列建立預報模式。

由觀測所得的時間序列如果它的分配機率不因時間的移動而改變則稱爲嚴格穩定 (strictly stationary)，若於這序列的前二階力矩 (moment)，不因時間的移動而改變則稱爲二次穩定 (Second-order Stationary)，但若所得的序列是非穩定性的 (Non-Stationary) 則須藉數次差分以得一新的穩定性的時間序列。

一般來說我們對於一組時間序列經由 Box and Jenkins 所建議的方法可以建立一個包含有三個部份的隨機時間模式 (Stochestic madel)[9] 此隨機模式包括了自廻歸 (Auto-regressive 簡寫爲 AR)、積分 (Integral 簡寫爲 I) 與移動平均 (Moving Average 簡寫爲MA)，或稱爲 ARIMA 時間數列模式，其中積分 (I) 的部份是當該序列爲非穩定性時才有，所以一般而言，對於一組穩定性的時間序列，它的預報模式將只包括自廻歸與移動平均 (ARMA) 兩個部份，而對於非穩定性的序列我們就藉差分的過程使序列穩定下來，然後再求其 ARMA 模式最後合成 ARIMA 的模式。

對於一穩定性的時間序列 Z_t，而言，ARMA (p、q) 模式具有以下的關係：

$$[\sum_{j=0}^{p}\phi_j B_j](\tilde{Z}_t-\bar{Z})=[\sum_{j=0}^{q}\Theta_j B_j]\,a_t \qquad (1)$$

或可寫爲：

$$\phi(B)\ (\tilde{Z}_t-\bar{Z})=\Theta(B)a_t \qquad (2)$$

其中 $\phi(B)=1-\phi_1B-\phi_2B^2\cdots\cdots\phi_pB^p$

$\Theta(B)=1-\Theta_1B-\Theta_2B^2\cdots\cdots\Theta_pB^q$

此處B爲後移運算子 (backward shift operator) 即 $BZ_t=Z_{t-1}$，$B^mZ_t=Z_{t-m}$ 而 a_t 爲白噪音 (White noise) p、q 分別是 $\phi(B)$ 及 $\Theta(B)$ 兩多項式的次數。

對上面方程式的兩邊取期望值 (Expected Values) 則因白噪音 a_t 的平均值爲零，所以我們就發現對於一平均值不爲零的時間序列則需要先減去其平均值 $\bar{Z}$。此後我們就以 $Z_t=\tilde{Z_t}-\bar{Z}$。

因爲由 Jonkien 和 Watts[10] 的理論 ARMA (p、q) 模式的變異數 (Variance) 可寫爲：

$$V_{ar}(Z_t)=\sigma_a{}^2\int_{-\frac{1}{2}T}^{\frac{1}{2}T}|\sum_{\alpha=0}^{q}\Theta_\alpha e^{-i\,2\pi WT\alpha}|^2/|\sum_{\beta=0}^{p}\phi_\beta e^{-i2\pi WT\beta}|^2\ dw \qquad (3)$$

此處 T 是取觀測值前後的時間長度 (Sampling time interval)，W是頻率 (frequency) σ_a^2 是 a_t 的變異數，如果在分子部份的多項式，Θ_α, $\alpha=0,\cdots\cdots q$ 的長度是有限的則上式會收斂，但分母可以表爲 $(1-C_j\times e^{-i\,2\pi WT})^{m_j}$ 的乘積，其中 m_j 是第 j 個因子的次方，上式之變異數在 $|C_j|<1$ 時將會收斂，而因爲分母的多項式其根爲 $1/C_j$, $j=1, 2\cdots\cdots p$，所以這意味著 $\phi(B)=0$，這多項式的根都必須位在單位圓的外面，才會使變異數收斂而這就是 (Stationality) 穩定性的條件。

例如對 ARMA (1, 0) 模式

$(1-C_jB)\,\tilde{Z}_t=a_t$ 則

$$Z_t=C_jZ_{t-1}+a_t$$

$$Z_{t+1}=C_j^2Z_{t-1}+C_ja_t+a_{t+1}$$

$$Z_{t+2}=C_j^3Z_{t-1}+C_j^2a_t+C_ja_{t+1}+a_{t+2}$$

以此類推，當 $|C_j|>1$ 時則現在的值對越遠的將來反而越大，此不合理，而當 $|C_j|=1$ 時則其影響力保持定值不因時間而消退，具有累積的作用，此時會產生不穩定的序列，所以穩定性的要求使得 $\phi(B)=0$ 的解都必須位在單位圓外。

雖然穩定性對 ARMA (p, q) 的移動平均部份 $\theta(\beta)$ 沒有什麼限制，但它仍必須滿足可逆性 (Invertibility) 的要求，這乃是爲了使時間序列符合實際的物理現象。

例如考慮 ARMA (0, 1) 的情形：

$$Z_t=(1-\Theta_jB)\,a_t \text{ 則}$$

$$a_t=(1-\Theta_jB)^{-1}\,Z_t$$

$$=(1+\Theta_jB+\Theta_j^2B^2+\cdots\cdots\Theta_j^kB^k$$

$$+\cdots\cdots\Theta_j^kB^k)\,(1-\Theta_j^{k+1}B^{k+1})^{-1}Z_t$$

所以

$$Z_t=-\Theta_jZ_{t+1}-\Theta_j^2Z_{t-2}\cdots\cdots-\Theta^kZ_{t-k}+a_t$$

$$-\Theta^{k+1}a_{t-k-1}$$

若 $|\Theta_j|>1$ 則現代的 Z_t 會受到 Z_{t-k} 的影響，k 隨時間的增加而增加，意即越久遠以前的事件對現在的情況影響更大，此與一般的現象不合，所以若 $\Theta(B)$ 寫成 $(1-C_jB)m_j$ 的乘積，其中 m_j 是 $\Theta(\beta)$ 的第 j 個根的次數，則 $|C_j|<1$, $j=1,\cdots\cdots q$，使得該序列可逆，也就是說可逆性的要求使得 $\Theta(B)=0$ 的根都必須位在單

位圓的外面。

在討論過穩定性與可逆性的問題之後，將着手建立合適的模式，建立模式的過程如同圖一所示，可概述如下：

㈠利用統計方法鑑定模式。

㈡由已有的觀測數列來估計模式中未知的參數值。

㈢診斷並檢驗此模式是否適當，是否能正確的代表觀測時間序列，並合乎精簡的原則 (parsimony principle)。

㈣如果模式適當則可用於分析與預報，如果模式不適當則重複進行 1～3 的步驟直到尋獲適當的模式爲止。

由於空氣污染物的濃度受到氣象及人類活動的影響而具有週期性或季節性 (Seasonal)，現在我們分述於後。

在作時間序列分析之始我們卽必須算出該序列的平均值遲滯 k 的自相關函數 (Autocorrelation function 簡稱 a.c.f.) 及遲滯 k 的部份自相關函數 (Partial Autocorrelation function 簡寫爲 p.a.c.f.)，其求法分別見(9)。

但以上各值是由有限長度的序列所求出，並不全然就是理論上實際的值，有時在理論值消失之後仍然可能出現相當大的估計值，所以我們須要一個工具來指出那些值不爲零，所以我們就以 a.c.f. 及 p.a.c.f. 的標準離差 (Standard deviation) 來作爲判斷的依據，如果理論爲零，而估計值呈正常分布，則估計值的絕對值大於一倍標準離差的可能性爲三分之一，而在正負兩方面大於兩倍離差的可能性則只有二十分之一，所以我們把估計值大於兩倍離差者皆視爲理論值不爲零。

Aartlett[11] 證明了 a.c.f. 的估計標準離差爲

$$\sigma[p_k]=\frac{1}{n^{1/2}}[1+2\sum_{j=1}^{q}\gamma_i]^{1/2}\quad q<k \tag{4}$$

此處 γ_i 爲遲滯 i 的 a.c.f.。

另外 Quenouill，證明 p.a.c.f. 的估計標準離差爲：

$$\sigma[\phi_{kk}]=\frac{1}{n^{1/2}}\quad k\geq p+1 \tag{5}$$

在利用 a.c.f 及 p.a.c.f 的標準離差之後我們可找出理論值不爲零的 a.c.f 及 p.a.c.f 由其分布的情形，可推論判斷出，可能的 ARMA (p、q) 的模式，我們先

討論非季節性的情形。

一、非季節性 (Non-seasonal) 模式：

對於穩定性的非季節性模式，可用下列的原則來判斷：

㈠若 a.c.f. 逐漸消失 (tail off) 而 p.a.c.f. 在 $k \leq p$ 時較顯著， $k > p$ 時不顯著，則此時爲 AR(p) 模式，即

$$Z_t = \phi_1 Z_{t-1} + \phi_2 Z_{t-2} + \cdots\cdots + \phi_p Z_{t-p} + a_t \tag{6}$$

或可簡寫爲 $\phi(B)Z_t = a_t$

㈡若是 p.a.c.f. 漸漸消失而 a.c.f. 在 $k \leq q$ 時顯著， $k > q$ 不顯著，則此模式爲MA(q) 即

$$Z_t = a_t - \Theta_1 a_{t-1} - \Theta_2 a_{t-2} \cdots\cdots \Theta_q a_{t-q} \tag{7}$$

或可寫爲 $Z_t = \Theta(B)a_t$

㈢若 a.c.f. 於遲滯 $q-p+1$ 時開始呈現指數及阻尼正弦波混合型消退，而 p.a.c.f. 亦於 $q-p+1$ 呈現此現象，則此時之適用模式爲 ARMA (p、q)，即

$$Z_t = a_t - \Theta_1 a_{t-1} - \Theta_2 a_{t-2} \cdots\cdots \Theta_q a_{t-q} + \phi_1 Z_{t-1} + \phi_2 Z_{t-2} \cdots\cdots + \phi_p Z_{t-p} \tag{8}$$

或可寫爲 $\phi(B)Z_t = \Theta(B)a_t$

但有時我們可能會發現 a.c.f. 及 p.a.c.f. 並沒有如上所述的現象而沒有很快消退，此時意味著可能是一非穩定性的時間序列。

對一非穩性的時間序列我們要經過數次差分後產生一穩定性的新時間序列 W_t ($W_t = \nabla^d Z_t$, $d = 0, 1, 2\cdots\cdots$)。此處 $\nabla^d = (1-B)^d$ 而 d 爲使 W_t 成爲穩定性序列的最小差分次數，一般不會大於 2 。

對於 W_t 我們就可用前面所述的方法，得其合適的 ARMA (p, q) 模式

$$\phi(B)W(t) = \Theta(B)a_t \tag{9}$$

再把 $W(t) = \nabla^d Z_t$ 代入則得一完整的 ARIMA (p, d, q) 模式

$$\phi(B)\nabla^d Z_t = \Theta(B)a_t \tag{10}$$

二、季節性的模式 (Seasonal)

當時間序列具有週期性變化時，其 a.c.f. 及 p.a.c.f. 也會有週期出現，而此時

無法用簡單的差分來消除，此時就要採用季節性模式，此模式分爲兩部份。

㈠週期性的部份：

若我們觀察發現時間序列具有週期 S，則可把每相隔 S 的 Z_t 運用前面所說的方式來求取其 ARIMA 模式，若得

$$(1-\phi_1*B^s-\phi_2*B^{2s}\cdots\cdots\phi_{p_1}*B^{p_1s})\ (1-B^s)^{d_1}Z_t$$
$$=(1-\Theta_1*B^s\cdots\cdots\Theta_q*B^{q_1s})e_t \qquad (11)$$

其中 e_t 爲另一組時間序列，一般而言 e_t 不是白噪音，所以對於 e_t 我們仍須作如下操作。

㈡非週期性的部份：

上面所得的 e_t 也可以如同一般的季節性時間序列加以判斷，而得一合適的 ARIMA (p, d, q) 模式：

$$(1-\phi_1B-\phi_2B^2\cdots\cdots-\phi_pB^p)\ (1-B)^de_t$$
$$=(1-\Theta_1B\cdots\cdots\Theta_qB_q)a_t \qquad (12)$$

把週期性及非週期性兩部份綜合起來，就得一通用的相乘季節性模式 (General multiplicative seasonal model)。

$$\phi_p(B)\ (1-B)^d\phi_{p_1}*(B^s)\ (1-B^s)^{d_1}Z_t$$
$$=\Theta_q(B)\Theta_{q_1}*(B^s)a_t \qquad (13)$$

其中

$$\phi_p(B)=(1-\phi B\cdots\cdots-\phi_pB^p)$$
$$\Theta_q(B)=(1-\Theta_1B\cdots\cdots-\Theta_qB^p)$$
$$\phi_{p_1}*(B^s)=(1\phi_1*B^s\cdots\cdots-\phi_{p_1}*B^{p_1s})$$
$$\Theta_{q_1}(B^s)=(1-\Theta_1*B^s\cdots\cdots-\Theta_{q_1}*B^{q_1s})$$

我們稱此爲 $(p, d, q)\times(p_1, d_1, q_1)$ 的相乘季節性 ARIMA 模式，至此我們便完成了鑑定模式，在實際使用時用最少數目的參數來完成合適 ARIMA 模式是很重要的，此稱爲精簡原則 (Parsimony Principle)[13] 接著的工作便是要估計模式的參數值 (Estimation)。

我們可由理論利用圖表或公式先找出各參數 ϕ, Θ, ϕ^* 及 Θ^* 的起始值 (Starting Values)，代入模式中則可得一組同樣時間的預測值 Z_t，由 Z_t 與 $\tilde{Z}_t$ 的差得到一個殘差的平方和，利用非線性最小平方差法 (9)[14] (Non-linear least square

error method)，經過數次的遞代 (Iterations) 即可求出較精確的參數值，遞代的次數由我們所選的起始值與所要求的精確度所決定。

在求出各種係數的值後接著便須作橫式診斷 (Diagnostic checking)，以便對模式的適性 (Goodness of fit) 作診斷工作來看看所求得的模式是否能最佳地代表觀測數列。

第一個檢驗方法爲過度配合 (Overfitting) 此乃是在所求得的模式兩側各加一項，倘若原來的模式是恰當的則會顯示出加上去的項是多餘的，當然此法並不表示所得的模式爲最佳模式，不過正如聖經所說的「凡事要查驗、善美的要持守」，我們由上面的實驗中找出較佳的模式。

另一個方法是看 a_t 是否白噪音，首先把 a_t 的 a.c.f. 算出，則因估計的殘差，與 a_t 實際的餘差有如下的關係

$$\hat{a}_t = a_t + 0\left(\frac{1}{\sqrt{N}}\right) \tag{14}$$

所以若有一個以上的 a.c.f. 明顯地大於兩倍的 $1/\sqrt{N}$ 則考慮修改模式。

最後還要作殘差的總體自相關檢定，若在 k 項後 a_t 的 a.c.f. 可以忽視且令 $n = N - d - sd_1$，則定義下面的量 Q

$$Q = n\sum_{k=1}^{k}\rho_k^2(a_t) \tag{15}$$

Q 可用來和 $X^2(k-p-q)$ 比較此處 X^2 爲 chi-square 分配，可取90%或95%來比較，而對 a_t 作一總檢驗看是否爲一白噪音，若模式不太恰當，則可用殘差的 a.c.f. 來修正。

倘若在診斷模式之後並未發現模式有何不宜之處，則該模式可用來預報。

預報的方式是把該 ARIMA 模式展開，若 $Z_t(\ell)$ 表示爲在時間 t 時預報 $t+\ell$ 時間的值，則對式中各項可用下面的值代入該模式中而得到結果：

$$[Z_{t-j}] = E[Z_{t-j}] = Z_{t-j} \qquad j = 0,\ 1,\ 2$$

$$[Z_{t+j}] = E[Z_{t+j}] = \hat{Z}_{t(j)} \qquad j = 1,\ 2$$

$$[a_{t-j}] = E[a_{t-j}] = a_{t-j} = Z_{t-j} - \hat{Z}_{t-j} \qquad j = 0,\ 1,\ 2$$

$$[a_{t+j}] = E[a_{t+j}] = 0$$

換句話說，若該值爲已發生的事件則用已知值代入，若該值尚未發生則把其期

望值代入，如此一來，我們不僅可在時間 t 作預測而且可隨時因新資料獲得而作最新的預測 (Updating forcasting) 其方法是，首先我們定義一無窮的級數

$$\psi(B)=\sum_{j=1}^{\infty}\psi_j B^j \text{ 且令 } Z_t=\psi(B)a_t \text{ 則} \tag{16}$$

$$\phi(B)Z_t=\Theta(B)$$

會變成

$$\phi(B)\psi(B)=\Theta(B)$$

把多項式展開比較兩邊的係數則可發現

$$\psi_1=\phi_1-\Theta_1$$

$$\psi_2=\phi_1\psi_1+\phi_2-\Theta_2$$

$$\vdots \qquad\qquad \vdots$$

$$\psi_j=\phi_1\psi_{j-1}+\cdots\cdots+\phi_p\psi_{j-p}-\Theta_j$$

此處 $\psi_0=1$，對於 $j<0$ 之項 $\psi_j=0$，而且 $j>q$ 時 $\Theta_j=0$，最後可得

$$\psi_j=\phi_1\psi_{j-1}+\phi_2\psi_{j-2}+\cdots\cdots\phi_p\psi_j,\quad j>q \tag{17}$$

如此則因

$$Z_{t+1}(\ell)=\psi_l a_{t+1}+\psi_{t+1}a_t+\psi_{l+2}a_{t-1}+\cdots\cdots$$

$$Z_t(\ell+1)=\qquad \psi_{l+1}a_t+\psi_{l+2}a_{t-1}+\cdots\cdots$$

所以

$$Z_{t+1}(\ell)=Z_t(\ell+1)+\psi_l a_{t+1} \tag{18}$$

故隨著時間的前進每一個新發生的值都可以立刻用來得到一最新的預測。

至此爲止，對於建立一組時間序列的 ARIMA 模式的理論過程乃告完成。

叁、結 果 與 討 論

一、汚染特性的討論：

本文所用的資料係由中央氣象局在臺北市公園路所測得二氧化硫 (SO_2) 逐時的濃度變化，時間是自民國六十三年一月一日至六十六年年底，而偵測站的高度距地面高 2 公尺，位置距公園路中心約 45 公尺，距貴陽街約 80 公尺，距愛國西路約

220 公尺（見圖二）而且此地有許多的建築物介於馬路與偵測站之間，所以偵測站所測得的結果會比旁人所實際呼吸的濃度爲低，故需要加以校正，以利比較討論。

首先因爲偵測站的高度距地 2 公尺，約略比人的口鼻的位置稍高，但差別不大，所以高度的影響不加校正。

再者，如果把道路上汽車排放廢氣的情形，簡化爲一無窮長的線源，則根據 Turner (1970) 書[15] 的公式，倘若風向與道路垂直時則

$$X(x, y, O, H)=\frac{2q}{\sqrt{2\Pi}\ \sigma_z\ u}\exp[-\frac{1}{2}(\frac{H}{\sigma_z})^2] \qquad (19)$$

此處

x：下風距道路距離

y：與道路平行距 x 軸的距離

H：排放源高度在此爲零

σ_z：下風 x 處的垂直擴散參數

u：表示風速

q：線源的强度

X：濃度

因爲汽車排放廢氣的位置可視爲 H=O，故方程式可改寫爲：

$$X(x, y, o, o)=\frac{2q}{\sqrt{2\pi}\ \sigma_z\ u} \qquad (20)$$

爲了與路旁八公尺行人的情況比較，設風速爲 5 公尺／秒，則因此時風速屬於上級（表二）；Turner 的 σ_z 與風速的關係（圖三）再利用外差法估計 x=8 公尺，$\sqrt{\tau}=0.7$ 公尺，x=45 公尺，$\sqrt{\tau}=3.6$ 公尺，x=80 公尺，$\sqrt{\tau}=6.5$ 公尺，x=220 公尺，$\sqrt{\tau}=17$ 公尺，所以當風自正東方吹來時由式(20)可以發現路旁八公尺的濃度爲偵測站的五倍，而當風自正北方吹來時，則其差異擴大爲約 9 倍，當風自正南方吹來時，因距離更遠，所以其間的校正比例更大至約 24 倍，但一則因有建築物的影響，所以會有相當的誤差，再則因 SO_2 會因逆溫層的影響而有累積致不能看爲單純的線源擴散情形，其中建築物因爲有遮避的作用，會使路旁與偵測站間的濃度比加大，但因累積現象，則會使二者的濃度比接近，但相信 5～10 倍，當是一合理的估計，所以作爲以下各項討論時的參考：

㈠一日二十四小時年平均濃度的變化：

我們把民國六十五年，每天同一小時（例如早上八時）的觀測值求取年平均濃度（圖四），結果發現自午夜起濃度輕微地下降，到早上六時起，開始迅速地增加，至早上九時達到高峰，然後又迅速的下降，在下午二、三時降至最低，然後又開始緩慢爬升，入晚後變化不大至晚上十一時後輕微地下降。

據推測臺北市鬧區的二氧化硫可能主要來自柴油車輛的廢氣，以及市區旅社餐館燒重油，和市郊工廠燒重油的排放廢氣，分析一天二十四小時年平均濃度的變化則可發現晚上十一小時後因工廠收班，各項活動停止，車輛稀少，所以 SO_2 濃度下降，但因臺北市爲一盆地地形，晚上逆溫層相當低，SO_2 擴散不易，所以雖然城市的活動歸於沉寂，但 SO_2 並未顯著減少，當早上六時城市的活動又開始，早班車也開出，所以 SO_2 的濃度也開始急劇地增加，尤其到八、九時爲上班的高峰，燒柴油的各型公車、交通車大量行駛於路上，而因國內柴油含硫量高級柴油爲 0,5%，普通柴油高達 1.25%[16] 使得此時的濃度達到一高峰，如果應用前面 5—10 倍的校正參數，則此時路旁的濃度可能能達 0.15 ppm 至 0.31 ppm 已高於年平均濃度的許可量（表三）過了早上九時以後因陽光的加溫使得逆溫現象消失[17] 再加上已過了尖峰交通時間，所以 SO_2 污染的情形迅速好轉，至中午時更因午間活動的停頓所以達到一天中的最低峰，甚至比午夜也稍微低些，這可能是因晚間有逆溫層的關係，過了兩點以後因爲活動又慢慢增加，所以 SO_2 又開始恢復增加，但因此時空氣的擴散良好，所以下班的交通尖峰就沒有出現特別明顯的高峰，入晚後雖然活動漸漸沉寂，但對臺北盆地不利的逆溫層又籠罩在上空，所以 SO_2 的氣體一直無法有效的擴散出去。

㈡月平均濃度的變化：

自表四及圖五可發現一年中各月份的 SO_2 濃度在夏天七月起至秋天九月其平均濃度特別的低，這可能是因此段期間爲颱風季節，一次的颱風可以把累積的各種污染物一吹而走，等於大掃除，所以空氣特別乾淨，而夏日的炎陽使光化反應加速也使 SO_2 消失較快，另外因此時臺北市大都吹西南風，而偵測儀器的位置離南方的愛國西路有 220 公尺加上建築物的阻擋，所以量到的值很自然的會偏低，所以是否夏天的 SO_2 污染情形眞的較輕微仍有待進一步的探討。

㈢年平均濃度的變化：

同樣的由表四所示年平均濃度自民國六十三年起逐年下降，顯示出空氣污染的問題漸受到社會大衆的關心，政府的重視，而漸漸地改善，而另一個可能的因素是能源危機使得耗油量受到影響而 SO_2 排放量降低，但民國六十六年却又有輕微的回升，這可能是因該年的經濟情況自能源危機中復甦、工廠增產、市面繁榮、車輛增多所致，希望能很快地獲得控制。

我國現行的二氧化硫年平均濃度一般地區不得高於 0.05 ppm 而工業區不得高於0.075 ppm， 則偵測站所在的二氧化硫情況低於法規的標準之下，但因爲前面所曾討論的原因，若乘於 5—10 倍其值就值得重視了，這顯示出在路旁行人所呼吸的空氣其二氧化硫的年平均濃度很可能高於法規所許可的標準之上，雖然修正因子 5—10 ，並不是一個很可靠的估計 ，但我們猜想因爲偵測站所測的結果已經很接近法令的許可標準，所以路旁的情況應該已到了須要採取行動的地步。

二、統計預報模式：

㈠同一小時濃度逐日變化的模式

測量二氧化硫濃度的儀器，因爲故障或維護保養，測量的工作偶有中斷，自民國六十三年到民國六十六年的資料中以民國六十五年的資料最完備把該年每天同一小時（例如早上八時）的濃度值分出則會分別形成二十四個長度爲 365 項的新時間序列，它們的 a.c.f. 及 p.a.c.f. 利用電子計算機計算所得的結果分別繪於圖六到圖九，可看得出 a.c.f. 呈指數漸漸消退，而 p.a.c.f. 則在遲滯 2 卽小於兩倍離差，所以判斷可能的模式 ARMA (2, 0) 在利用非線性最小平方差法估計出各參數值，後列於表五，則可見每日濃度受前一日同一小時濃度的影響甚大，而再前一天同一小時之影響， 則較小， 這反應出臺北市二氧化硫濃度擴散的情形 ， 再進一步的檢視計算所得的殘差（表六）其 a.c.f. 皆近於零 ， 沒有比兩倍離差大者，且當取自由度 (Degree of freedom) 爲30時，由表五所列的 Q 值與 Chi-sguare 分配比較則自由度爲 30 時的值分別爲

χ^2_{30} (95%) =43.8　　χ^2_{30} (90%) =40.3

χ^2_{30} (75%) =34.8　　χ^2_{30} (50%) =29.3

χ^2_{30} (25%) =24.8　　χ^2_{30} (10%) =20.6

χ^2_{30} (5 %) =18.5　　χ^2_{30} (1 %) =15.0

當Q值愈小時則殘差的總體檢驗越顯示出殘差與白噪音相似，我們發

現計算所得的Q值分別皆小於 χ^2_{30}（90%）而大部份皆在 χ^2_{30}（50%）到 χ^2_{30}（10%）之間而中午十二時的Q值甚至可達 χ^2_{30}（10%）左右，這顯示殘差的總體檢驗證明了所得的諸模式皆能有效地代表該時間序列而殘差的標準離差（見表五）與平均值相比在10%左右，這顯示出在實際的預報時，本 ARMA（2,0）模式可相當準確而有效地預報逐日同一小時的濃度變化情形，這作爲採取各種應變措施的參考，來防止災害的發生是相當重要的，因爲一個不可靠的預報系統不僅使防治單位的警告失去權威而且若用來採取暫時關閉工廠的參考，則顯然會造成廠家額外的停工損失，並且招致怨言，所以爲了避免「該警告而不警告，不該警告而警告」，選擇一個可以信賴的模式是非常的重要，而 AR（2）可以滿足此項要求。

㈡連續地小時濃度變化模式

爲了比較冬季和夏季小時連續濃度變化之不同故分別取民國六十五年一月一日至一月十五日連續 360 小時及同年七月十六日至七月三十日連續 360 小時等兩組時間序列分別計算它們的 a.c.f. 及 p.a.c.f.（見圖十至圖十三）發現呈現出具有十二小時及二十四小時的週期，會有十二小時週期乃是因上班及下班的尖峰交通時刻，相差大約十二小時，但因尖峰交通時刻持續有兩個小時左右，且差距並非正好十二小時，所以此週期並不會比二十四小時的週期明顯，而在冬天時，此週期的影響比夏天時明顯，這可能是因夏天的夜晚，逆溫層很低，所以會產生干擾，而影響了人類活動的週期，至於二十四小時這週期的出現是很容易理解的，因爲人類的活動很自然的會有以一天爲一個循環，而氣象上的溫度、風速、風向也因地球自轉的緣故而會有二十四小時的週期出現。

我們取二十四小時的週期再來計算新的 a.c.f. 及 p.a.c.f.（見圖十四及圖十五）則可判斷季節性的相乘模式 $(1,0,1)\times(1,0,1)_{24}$ 可以考慮，結果估計出各參數後分別得民國六十五年一月一日至一月十五日的模式爲

$$(1-0.77B)\ (1+0.13B^{24})\nabla^{24}Z_t = (1+0.09B)\ (1-0.64B^{24})a_t$$

而七月十六日至七月三十日的模式爲

$$(1-0.75B)\ (1+0.22B^{24})\nabla^{24}Z_t = (1-0.11B)\ (1-0.44B^{24})a_t$$

其殘差的 a.c.f.（見表七）證實這兩個季節性相乘的 ARIMA 模式並無不適之處，且其殘差的標準離差與平均濃度相比，仍小於10%，故可用來作預報模式。

仔細觀察一月及七月的兩個模式，則可發現二者有許多相似之處只是二者的係

數略有出入，雖然此些許的差別並不會使得多天的模式無法應用在夏天的情形，但在實際的應用時，最好每隔一兩個月就修正一次係數，那麼會更佳地代表在不同氣象狀況下的情形，此項工作配合電子計算機的處理應該是可以輕而易舉地完成，而此種預報正是我們所最關心的也是最應該讓民衆知道以有所警覺，所以有必要儘量忠實地反應出可能的變化以維大衆健康。

㈢連續日平均濃度

把民國六十五年的小時濃度利用辛浦森 (Simpson) 的積分法換算成日平均濃度計算 a.c.f. 及 p.a.c.f.（圖六及圖七）則顯示出它與每日同一小時的情形相近，這是很合理的結果，將它的參數值利用非線性最小平方差法算出則可得到下面的模式

$$(1-0.61B-0.09B^2)\ (Z_t-2.303)=a_t \qquad (21)$$

其殘差的 a.c.f.（見表七）顯示出此爲一良好的模式而本模式顯示每日平均濃度的值受前一日的影響較小但仍不可忽視，再把日平均濃度與法令所規定一般地區不得大於 0.1 PPM 工作地區不得大於 0.15 PPM（表三）比較之下偵測站所在之地的 SO_2 濃度的日平均在法令之標準以下，但正如以前所討論的路旁行人所呼吸的空氣會比較差，所以是否路旁的日平均濃度不大於法令的許可濃度則有待進一步的探討。

再把民國六十三年至民國六十六年同一日（如五月二日）的日平均濃度相加，除以四而得一組新的時間序列，計算 a.c.f. 及 p.a.c.f.（圖十六及圖十七）則會發現有一明顯的七天週期，但這是前面連續日平均濃度所沒有的，這可能是連續的日平均濃度變化中各種短期的影響把它遮蔽了而把四年同一日的情況加以平均此乃一整年的作用 (Smoothing) 就會使得人類活動中七天（一星期）這樣的週期顯露出來，再把週期爲七天時的 a.c.f. 及 p.a.c.f. 求出（圖十八及十九）判斷爲相乘的 $(1,0,1)\times(1,0,1)_7$ 季節性模式，可得下面的模式

$$(1-0.65B)\ (1-0.1B^7)\nabla^7 Z_t=(1-0.14B)\ (1-0.88B^7)a_t \qquad (22)$$

此時殘差的 a.c.f. 示於（表七）再一次的顯示殘差爲一白噪音且其殘差的標準離差小於平均濃度的10%。

因爲有此模式的經驗所以雖然民國六十五年的逐日連續日平均濃度並未顯示出七天的週期但猜想應該也有七天的週期，嘗試地以相乘季節性模式 $(1,0,1)\times($

1,0,1)$_7$ 來估計其參數可得其模式

$$(1-0.72B)\ (1+0.03B^7)\nabla^7 Z_t=(1-0.1B)\ (1-0.92B^7)a_t \qquad (23)$$

其殘差的 a.c.f. p.a.c.f. 殘差的標準離差及Q的總體檢驗顯示此仍爲一良好模式，這顯示出七天的週期是存在的，但被各種短期變化所遮蔽了，而面對這種具有一個以上週期的情況，季節性相乘的 ARIMA 模式仍可有效地工作但假如能和波譜分析的技術配合相信會更好。

三、預報模式的通性

㈠以連續小時模式預報

利用民國六十五年一月一日至一月十五日的模式來預報結果示於圖二十可看得出在開始的幾項會有很好的結果但隨時預報的時間越遠則誤差會加大，這是很自然的結果，在此我們並沒有用到即時預報 (Updating forcast) 的方法能有這樣的結果已令人滿意了。

㈡日平均濃度的預報

與前面的方法相似地我們用民國六十五年的日平均濃度來作預報結果示於圖二十一則有一很好的結果，直到時間較遠時偏差才加大，相信在實際使用時，加上即時預報 (Updating forcast) 會有更好的結果。

㈢連續小時模式每一日同一小時模式之比較

用連續小時模式與二十四個每一日同一小時模式之預報示於圖二十二。可見用二十四個每一日同一小時模式之預報比用連續小時模式爲佳，與實際的情形較相近而這種優勢將會隨著預報時間的增加而增加，例如作十天的預報時每一日同一小時模式只是分別預報了十個步驟。但對於連續小時模式而言，其所作的預報即達二百四十個步驟 (time steps) 。而一般來說，預報的時間隔越長效果越差，所以在作長期預報時以二十四個每一日同一小時模式預報效果將更好。

㈣精簡原則的影響

雖然逐日同一小時的模式 ARMA (2, 0) 已被證明具有很好的結果，但爲了觀察精簡原則的影響，嘗試使用數個不同的模式來比較。

首先嘗試用一 ARIMA (3, 1, 1) 的模式，此模式本來的對象應是非穩定性的序列，在此使用它必然會表現出某些參數是多餘的，而實際選擇下午 5 時爲例，則其模式爲：

$$(1-0.26B-0.1B^2-0.07B^3)\ (1-B)z_t=(1-0.95B)a_t \qquad (24)$$

由移動平均 $\theta_1=0.95$ 接近於 1 的情形看來，正顯示出差分是多餘的，此乃因 z_t 本來就是平穩性的。所以與原來的猜想很接近，而其殘差的標準離差爲 0.053 ，反而比原來ARMA (2, 0) 時的 0.051 略差，此正顯示出增加參數不僅不會改善情況，反而更能使其殘差的分布變壞，但此處 0.053 與 0.051 相比事實上是沒有太大的差別，只是更複雜的模式是不必要的。

再以早上九時的情況爲例，原來的模式爲

$$(1-0.42B-0.12B^2)\ (z_t-3.18)=a_t \qquad (25)$$

若求 ARMA (2, 1) 則變爲

$$(1-0.17B-0.30B^2)\ (z_t-3.18)=(1+0.27B)a_t \qquad (26)$$

這意味著前一日的值對現在的值影響比前二日的值還小不太合理，再看其殘差的標準離差 0.077 與原來的 0.078 差不多，所以也沒有改善預報的條件，反而增加了一個不太合理的情況，所以增加一項參數是不太需要的。

由上面的兩個例子可看出精簡原則的影響，使用最少所需的參數不僅使得模式較簡單而且也不會比更多參數時爲差。

肆、結 論 與 建 設

本文的研究顯示自廻歸積分移動平均 (ARIMA) 統計預報模式，能對我們感到興趣的地方的空氣污染情況提供一個相當良好而有效的預報。雖然無法像擴散模式那樣對整個地區的情況與可能的發展作一全面鳥瞰性的探討，但對於一些關鍵的地區像松山地區的鋼鐵廠 。 西門閘區等人口集中地區 、 中山北路車輛較多的地區 ， 如果能設立各種不同污染物的偵測站 ， 則可針對該地區的濃度變化資料， 建立 ARIMA 統計預報模式，將可以在嚴重事故發生之前，有所警覺，採取必要措施來防止，例如：暫時關閉排放量大的工廠，疏導車輛、勸告病人、老人、小孩等抵抗力較差者避免進入污染情況嚴重的地區。

此外在本文的分析中對於具有週期性的情況利用季節性相乘的 ARIMA 模式雖可建立適合的模式，但因空氣污染的情況受氣象因素與人類活動的影響，可能有不止一個的週期，單單針對其中最明顯的一個週期，建立相乘的預報模式，難免忽略了其他的週期，我們建議如果能先用波譜分析的技巧分成幾個由不同頻率部份組

成的時間序列再分別建立合適的 ARIMA 模式，相信會有更好的代表性。而如果能再和擴散模式及動力預報模式合併應用，並且以風洞實驗及實測資料利用空氣污染評估的佳化理論[7] 來佳化模式的計算值則可以補足各種不同理論的弱點、發揮它們的優點，而建立一套完整的空氣污染防治的系統。

現在世界各大都市除了氣象情況的預報也一併將空氣污染的情形及可能的發展讓市民知道，以作爲民衆外出居家等的參考。我國目前在此方面仍有待急起直追，而近年來因政治穩定，工商繁榮，人口密集，汽車急速增加，工廠煙囪林立，市區、工業區的空氣品質越來越差，爲了避免賺得全世界賠上自己的性命，我們希望政府一本過去愛民的仁政，寬列空氣污染防治經費，支持學術機構研究各種空氣污染資料分析及防治的基本研究，增設偵測站，修訂更爲完善的法規，利用大衆傳播工具教導民衆注意自己的環境問題，並且由公營機構的工廠，運輸單位帶頭採取各項減少污染的措施，（如中油公司排除萬難，增加脫硫設備）雖然如此會增加開支，但相信它能維護國民健康，建立一個媲美先進國家的清潔社會，如此的投資實在是很值得的，在此期望我們的國民早日能無慮地呼吸清新、高品質的空氣。

參 考 文 獻

1. 楊建輝，1975：二氧化硫之控制，臺灣環境衛生，七卷一期，68-70。
2. 趙文雄，1964：臺灣地區空氣污染防治概況，臺灣環境衛生，六卷一期，29-33。
3. 劉俊一，1979：二氧化硫氣體對農作物影響之檢討，臺灣環境衛生，十一卷一期，80-102。
4. Martin Crawford, 1976: Air Pollution Control Theory, McGraw-Hill Book Company, New York.
5. 張乃文，1977：硫氧化物之污染及其防止對策，能源季刊，七卷二期，85-96。
6. 戚啓勳，1977：空氣污染的危害及其防範措施，能源季刊，七卷三期，97-104。
7. 梁文傑、李克堂，1880：臺北市一氧化碳污染與偵測網之佳化評估，機械工程學刊，一卷一期（待刊中）
8. 胡仲英，1977：應用 ARIMA 模式對臺北市月平均過度與總降水量的分析與預測，氣象學報，二十三卷三期，15-26。
9. G. E. P. Box, and G. M. Jenkins, 1976: Time Series Analysis forcasting and control, Holden-Day 575 pp.
10. Jenkins, G. and G. Watts, 1968: Spectra Analysis and Its Applications, Holden-Day, 523 pp.
11. Burtlett, M. S., 1946: On the theoretical specification of Sampling Properties of

表四　民國六十三年至六十六年月平均濃度，年平均濃度及每月四年平均濃度

單位 pphm

年 / 月	63	64	65	66	平均
1	3.70	3.19	2.98	2.31	3.05
2	4.40	3.31	1.31	2.13	2.79
3	4.73	2.35	2.47	3.32	3.22
4	4.54	3.05	2.38	3.59	3.37
5	5.55	2.81	3.24	2.54	3.54
6	4.89	2.69	3.11	3.82	3.63
7	2.75	2.45	3.25	1.72	2.30
8	3.00	1.97	1.45	1.35	1.94
9	3.33	2.25	1.69	1.22	2.12
10	3.50	2.68	2.68	2.58	2.86
11	3.09	2.58	1.90	3.03	2.65
12	2.07	2.74	2.55	4.25	2.90
平均	3.80	2.67	2.36	2.66	

表五　民國六十五年每一月同一小時濃度之模式，模式之形式為
$(1-\phi_1 \times B-\phi_2 \times B^2)z_t=a_t$

小　時	ϕ_1	ϕ_2	平　均	σ_2	Q
1	0.53	0.053	2.35	0.063	31.66
2	0.43	0.111	2.25	0.062	28.33
3	0.42	0.129	2.24	0.062	20.33
4	0.40	0.042	2.18	0.063	39.35
5	0.51	0.128	2.16	0.063	39.03
6	0.42	0.199	2.35	0.066	28.43
7	0.40	0.185	2.65	0.073	33.41
8	0.45	0.165	3.02	0.077	21.16
9	0.42	0.181	3.18	0.078	20.70
10	0.39	0.070	3.00	0.076	18.61
11	0.34	0.186	2.75	0.077	25.34
12	0.34	0.147	2.45	0.065	15.77
13	0.38	0.168	2.16	0.053	17.60
14	0.39	0.203	2.05	0.045	30.23
15	0.41	0.169	2.06	0.046	16.61
16	1.35	0.198	2.16	0.054	38.10
17	0.34	0.200	2.19	0.050	35.35
18	0.29	0.204	2.28	0.060	36.60
19	0.34	0.195	2.34	0.061	27.87
20	0.40	0.138	2.42	0.066	35.97
21	0.37	0.213	2.42	0.064	38.52
22	0.38	0.223	2.47	0.063	21.96
23	0.42	0.168	2.49	0.066	36.98
24	0.49	0.076	2.46	0.067	38.39

表六　二十四個每日同一小時模式殘差的 a.c.f.

	1	2	3	4	5	6	7	8	9	10
1	0.00	− 0.02	0.02	− 0.06	0.00	0.10	0.02	0.05	0.01	0.03
2	0.00	0.01	− 0.05	0.00	0.09	− 0.02	0.02	0.09	0.05	0.02
3	− 0.02	− 0.06	0.08	0.03	0.04	0.04	0.09	0.05	0.01	0.09
4	− 0.01	− 0.09	0.05	0.04	0.00	0.09	0.09	0.05	0.04	0.05
5	− 0.02	− 0.08	0.02	0.03	− 0.03	0.06	0.06	0.00	0.06	0.05
6	− 0.02	− 0.04	0.04	0.00	− 0.04	0.09	0.03	0.06	0.01	0.07
7	− 0.02	− 0.06	0.05	0.00	− 0.01	0.08	0.08	0.04	0.01	0.01
8	− 0.01	− 0.03	0.00	0.03	0.03	0.06	0.05	0.00	0.05	− 0.05
9	0.01	− 0.02	− 0.04	0.00	0.04	0.07	0.02	0.02	− 0.01	− 0.01
10	0.01	− 0.04	− 0.01	0.03	0.04	0.05	0.01	0.00	− 0.02	− 0.02
11	0.09	− 0.03	0.08	0.00	0.05	0.04	− 0.01	0.03	− 0.03	0.00
12	0.04	0.00	0.05	0.03	0.00	0.08	0.03	0.02	− 0.03	0.04
13	− 0.01	− 0.03	0.03	0.04	0.00	0.08	0.04	0.03	0.03	0.00
14	− 0.04	− 0.07	0.09	0.01	0.02	0.09	− 0.02	0.01	0.08	0.00
15	− 0.03	− 0.06	0.07	− 0.01	0.08	0.06	0.08	− 0.02	− 0.05	0.08
16	− 0.02	− 0.06	0.04	0.04	0.09	0.03	0.04	0.04	0.02	− 0.05
17	− 0.03	− 0.07	0.08	0.04	0.09	0.05	− 0.01	0.05	0.08	0.01
18	− 0.03	− 0.07	0.07	0.09	0.04	0.04	0.02	0.04	0.03	0.03
19	− 0.03	− 0.08	0.09	0.05	− 0.03	0.03	00.0	0.08	0.02	0.01
20	− 0.03	− 0.09	0.03	0.03	0.02	0.07	− 0.03	0.05	0.01	0.05
21	− 0.03	− 0.06	0.06	− 0.01	0.06	0.09	0.02	0.01	− 0.04	0.09
22	− 0.02	− 0.03	− 0.01	− 0.01	0.05	0.10	0.01	0.02	− 0.02	0.06
23	− 0.02	− 0.06	0.04	0.06	− 0.02	0.01	0.08	0.05	− 0.05	0.02
24	− 0.01	− 0.07	0.06	0.07	− 0.02	0.07	0.09	0.02	− 0.02	0.03

表六　二十四個每日同一小時模式殘差的 a.c.f.（續）

	11	12	13	14	15	16	17	18	19	20
1	− 0.03	0.10	0.01	− 0.04	− 0.03	−0.06	0.09	0.09	0.00	0.01
2	− 0.03	0.04	0.03	− 0.03	0.10	0.01	0.09	0.07	0.00	0.06
3	0.07	0.04	0.04	− 0.01	0.03	0.02	0.04	0.01	1.04	0.05
4	0.08	0.05	0.02	0.03	0.00	0.04	0.09	0.01	0.05	− 0.01
5	0.07	0.04	0.06	0.00	0.02	0.01	0.09	0.02	0.06	− 0.01
6	0.07	0.03	0.04	0.05	0.02	− 0.04	0.06	0.08	0.00	0.01
7	0.02	0.05	0.03	0.04	0.08	− 0.02	0.04	0.08	− 0.05	− 0.02
8	0.06	0.03	0.01	− 0.02	0.03	0.04	0.03	0.05	0.05	− 0.05
9	0.02	0.06	0.05	− 0.10	0.07	0.02	0.03	0.07	0.09	− 0.03
10	0.01	0.01	0.08	− 0.05	− 0.03	− 0.05	0.08	0.06	0.04	0.01
11	− 0.01	0.06	0.03	− 0.06	− 0.05	− 0.02	− 0.03	0.09	0.00	0.01
12	0.05	− 0.01	− 0.02	− 0.02	− 0.02	− 0.06	0.08	0.07	0.02	− 0.04
13	0.05	− 0.02	0.03	− 0.04	− 0.05	− 0.07	0.08	0.07	0.02	0.00
14	0.03	0.00	0.02	− 0.02	− 0.02	− 0.05	0.05	0.09	− 0.01	− 0.08
15	0.02	0.02	0.00	− 0.02	0.05	0.01	0.03	0.07	0.07	− 0.11
16	− 0.04	0.09	0.03	− 0.02	0.06	0.01	0.09	0.10	− 0.03	− 0.03
17	− 0.03	0.00	0.04	0.06	0.04	0.00	0.04	0.11	0.03	0.04
18	− 0.04	− 0.03	0.03	0.06	− 0.06	− 0.02	0.10	0.11	− 0.04	0.02
19	0.02	0.00	0.04	0.05	0.02	0.01	0.10	0.07	− 0.07	0.10
20	0.02	0.00	− 0.01	0.01	− 0.01	7.04	0.09	0.07	− 0.09	0.08
21	0.02	0.00	0.06	0.02	0.04	0.02	0.01	0.07	− 0.03	0.06
22	0.04	0.04	0.00	− 0.03	0.01	0.03	0.01	0.04	− 0.01	0.07
23	0.08	0.01	0.06	0.00	− 0.05	− 0.07	0.07	0.03	− 0.01	0.07
24	0.07	0.00	0.09	− 0.03	− 0.10	− 0.04	0.07	0.08	− 0.01	− 0.01

表六　二十四個每日同一小時模式殘差的 a.c.f.（續）

	21	22	23	24	25	26	27	28	29	30
1	− 0.01	0.01	0.01	0.04	0.06	− 0.04	0.05	0.01	−0.05	0.06
2	0.03	0.08	0.06	− 0.02	0.04	− 0.01	0.09	0.00	0.02	0.05
3	0.01	0.00	0.05	0.02	0.02	0.01	− 0.01	− 0.01	0.02	− 0.03
4	0.03	0.04	− 0.02	0.00	0.07	0.04	0.02	0.02	− 0.05	0.01
5	0.01	0.07	− 0.04	0.00	0.00	0.01	0.03	0.02	− 0.03	0.00
6	0.03	− 0.03	− 0.03	0.09	0.04	0.05	0.04	0.03	− 0.02	− 0.01
7	0.01	− 0.02	0.00	0.00	0.10	0·04	− 0.05	0.05	− 0.04	0.01
8	0.03	0.01	− 0.01	− 0.06	0.07	0.06	− 0.04	− 0.02	− 0.03	− 0.01
9	− 0.01	− 0.03	0.09	− 0.03	0.02	0.01	− 0.01	− 0.04	− 0.01	− 0.03
10	0.05	− 0.02	0.01	0.03	0.04	− 0.05	− 0.05	0.03	− 0.03	− 0.02
11	0.06	− 0.03	− 0.01	0.08	0.05	− 0.04	− 0.03	0.08	− 0.01	− 0.04
12	0.04	− 0.03	− 0.03	0.02	0.04	− 0.03	0.00	0.03	− 0.01	− 0.02
13	− 0.02	− 0.03	0.00	0.03	0.01	0.00	− 0.01	0.04	− 0.02	0.00
14	0.09	0.02	− 0.04	0.04	0.01	0.02	0.02	− 0.03	0.00	0.03
15	0.11	0.02	0.00	0.04	0.02	− 0.02	− 0.04	0.01	0.09	0.05
16	0.09	0.06	− 0.01	− 0.08	0.00	0.11	0.00	− 0.07	0.04	0.05
17	0.09	0.06	− 0.02	0.01	0.06	− 0.01	0.04	0.00	− 0.04	0.11
18	0.08	− 0.04	0.05	0.00	0.00	0.05	0.01	− 0.02	0.00	0.05
19	− 0.01	− 0.02	0.05	0.00	0.00	− 0.01	0.04	0.02	− 0.02	0.06
20	0.04	− 0.03	0.05	0.08	0.00	− 0.02	0.02	0.04	− 0.05	0.09
21	0.00	− 0.03	0.06	0.08	− 0.03	− 0.02	0.01	0.01	− 0.04	0.10
22	0.03	0.05	0.03	0.06	− 0.04	− 0.02	− 0.05	0.04	− 0.05	0.10
23	0.04	0.03	0.06	0.07	0.00	− 0.02	0.01	0.05	− 0.11	0.11
24	0.10	0.06	0.01	0.05	− 0.07	− 0.01	0.01	0.07	− 0.10	0.04

表七　四個不同模式的殘差之 a.c.f.

	1	2	3	4	5	6	7	8	9	10
A	− 0.02	− 0.04	− 0.06	0.02	− 0.03	0.09	0.09	0.00	0.00	0.00
B	0.00	− 0.03	− 0.07	0.03	0.04	− 0.06	0.00	0.09	0.08	0.01
C	− 0.01	− 0.05	− 0.00	0.09	− 0.02	0.05	0.07	0.03	0.03	0.00
D	− 0.01	− 0.06	0.01	0.09	0.00	0.07	0.05	0.04	0.03	0.08
	11	12	13	14	15	16	17	18	19	10
A	−0.10	0.01	0.04	0.06	− 0.04	0.06	−0.04	− 0.08	0.00	0.09
B	0.02	− 0.08	0.03	0.04	0.09	− 0.02	0.03	0.00	0.00	0.04
C	0.01	0.00	0.09	− 0.00	0.07	− 0.09	0.08	0.06	0.07	− 0.02
D	0.04	0.07	0.06	− 0.00	0.01	− 0.02	0.06	0.02	0.09	0.04
	21	22	23	24	25	26	27	28	29	20
A	0.03	− 0.05	− 0.02	0.04	0.03	0.08	− 0.01	0.04	0.09	0.06
B	− 0.08	− 0.04	0.06	0.06	0.04	− 0.01	− 0.02	− 0.03	− 0.07	− 0.06
C	0.03	0.05	0.06	− 0.01	− 0.04	− 0.04	0.06	0.00	− 0.07	− 0.02
D	0.02	0.01	0.10	− 0.03	− 0.01	0.00	0.04	− 0.03	0.06	− 0.04

其中 A.B.C.D. 分別爲下列四個模式

A：六十五年一月一日至十五日連續小時模式

B：六十五年七月十六日至三十日連續小時模式

C：六十五年日平均濃度模式

D：六十三年至六十六年同一日平均濃度模式

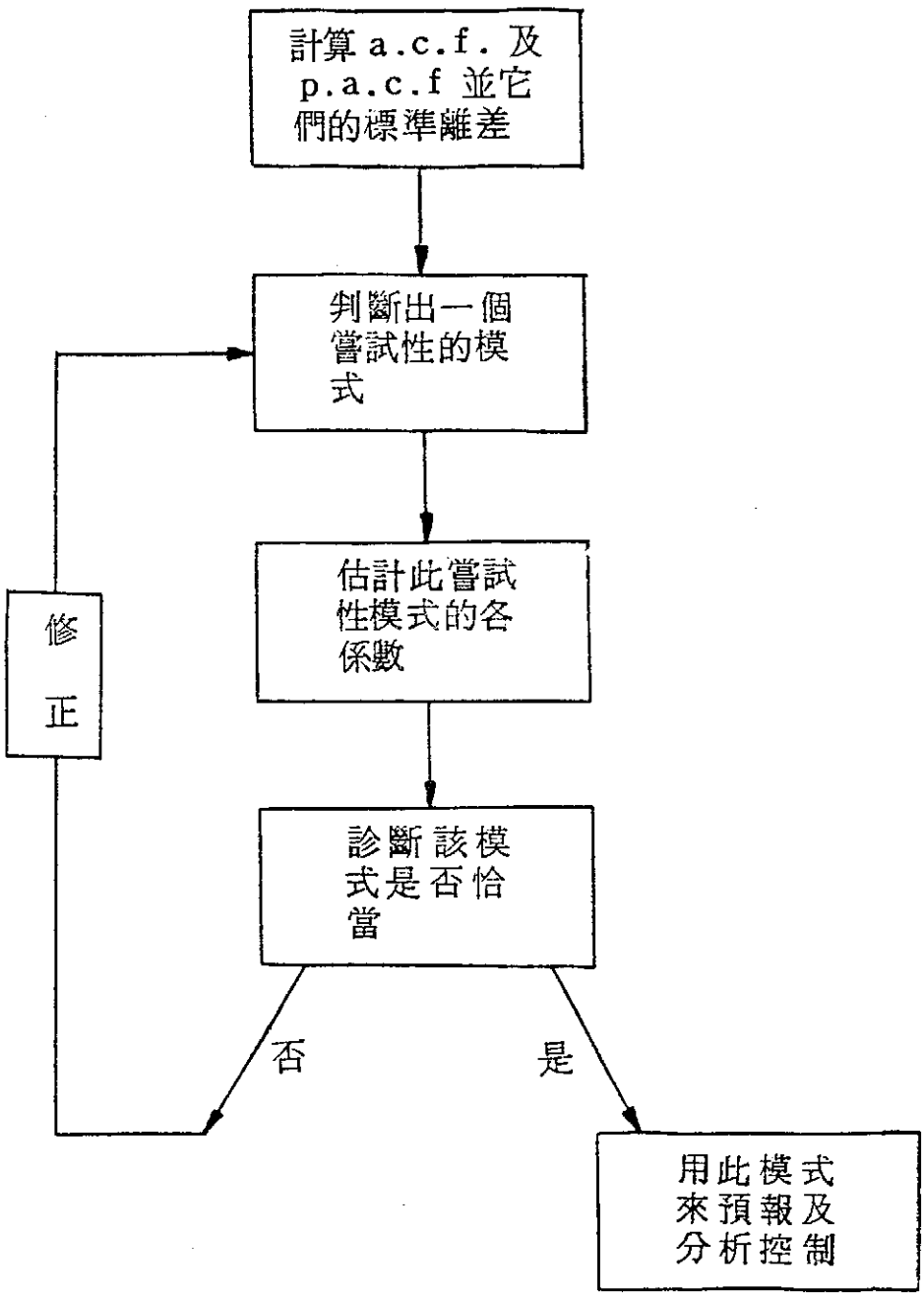

圖一　建立合適的 ARIMA 模式的各個步驟與流程圖

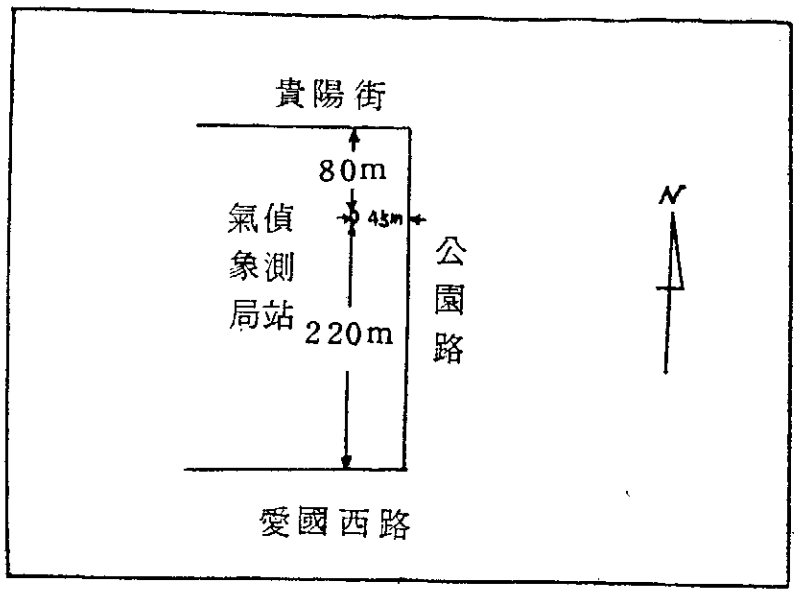

圖二　偵測站與附近道路的相關位置

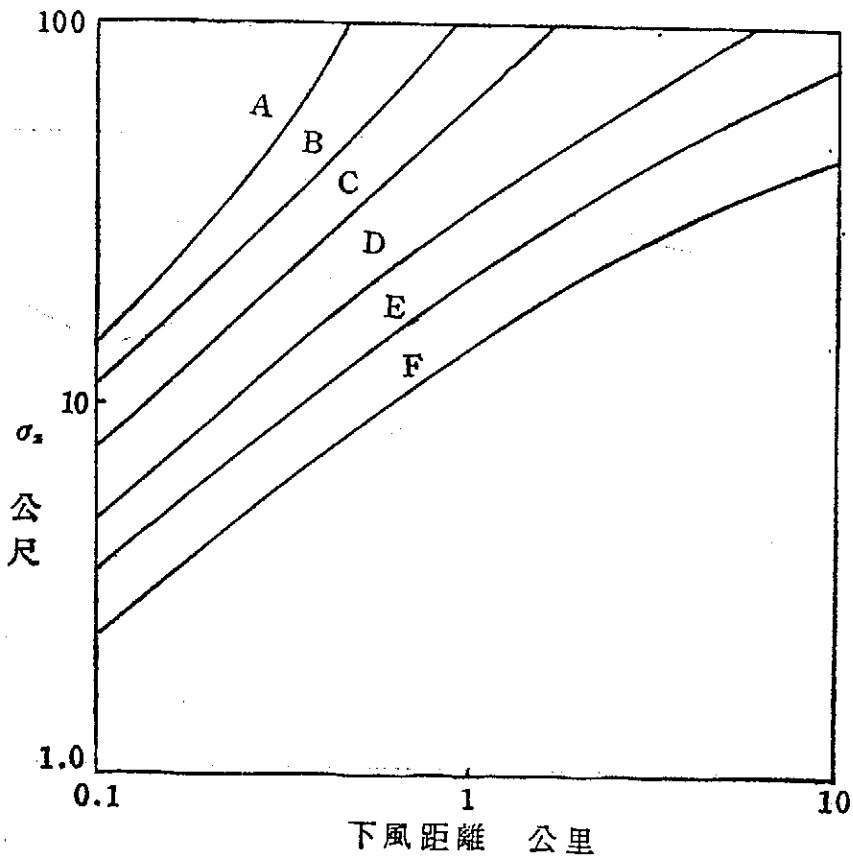

圖三　下風方向的垂直散佈係數（σ_z）

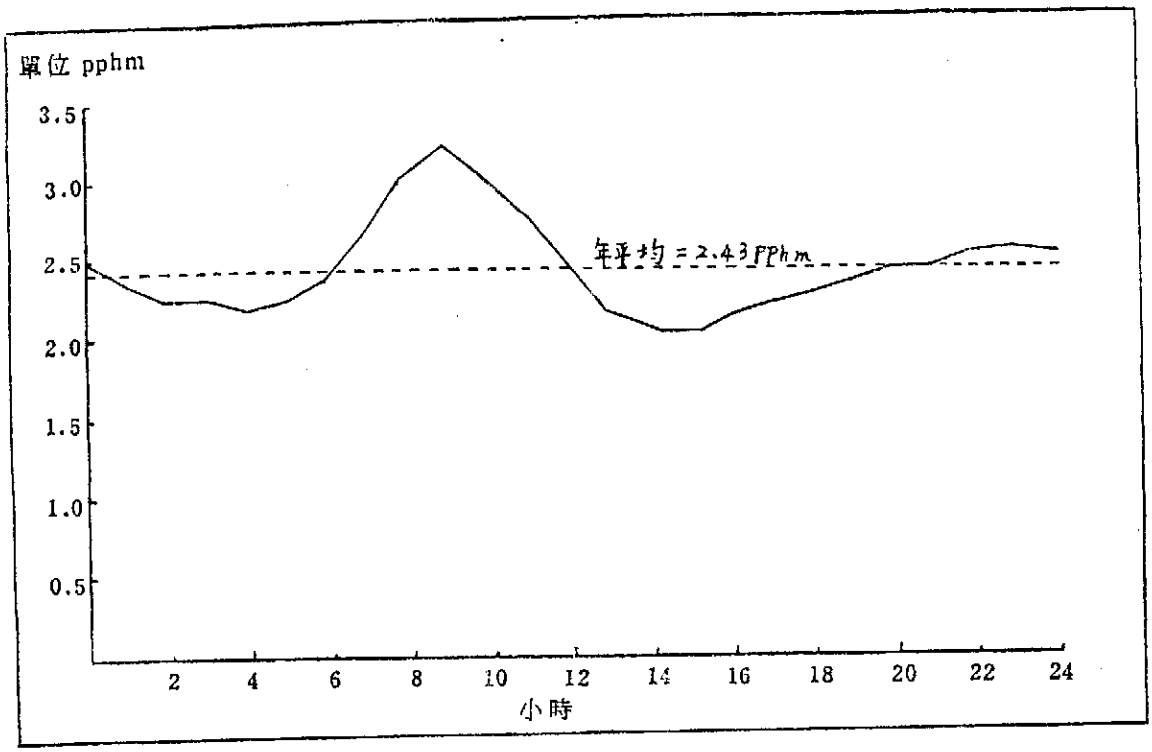

圖四　一日24小時的平均濃度（民國六十五年）隨著時間的變化橫軸表自凌晨一時起至午夜

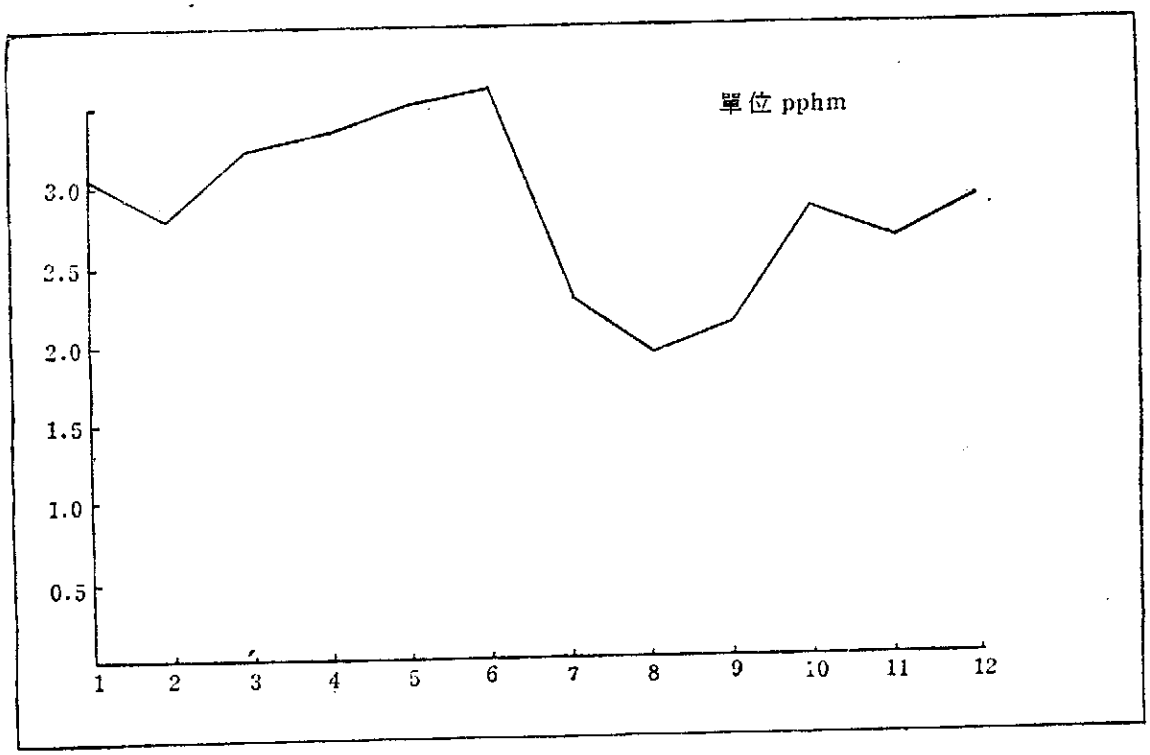

圖五　自民國六十三年至民國六十五年同一月份的月平均濃度之四年平均值

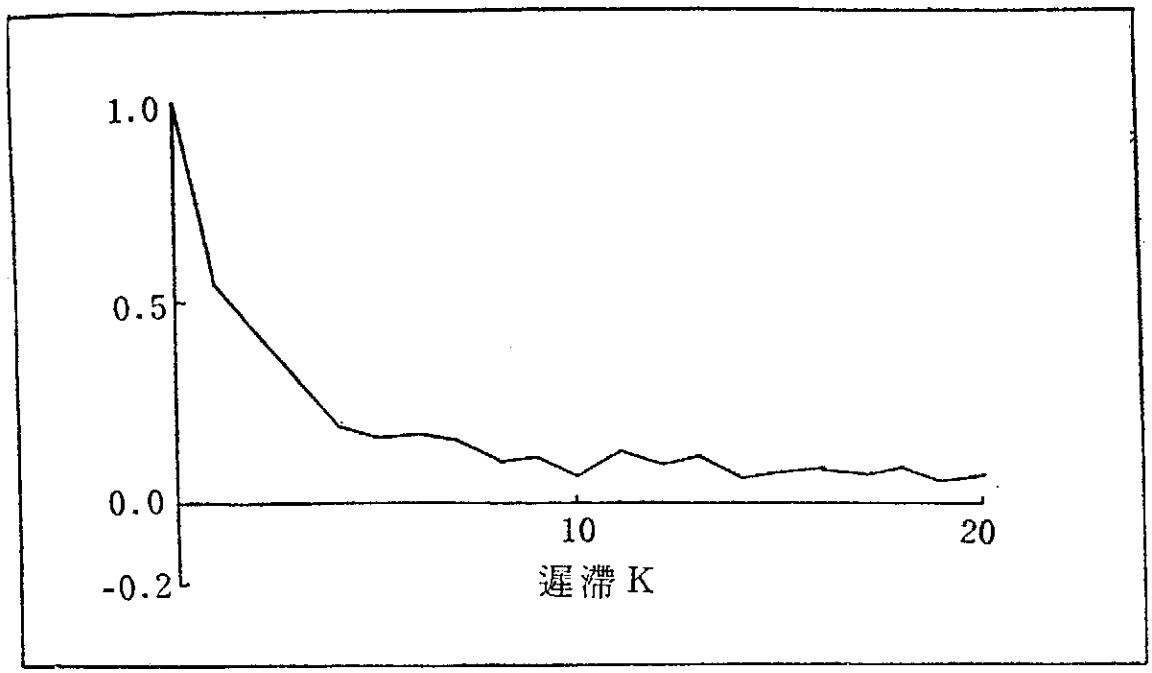

圖六　民國六十五年早上八時的小時平均濃度之 a. c. f.

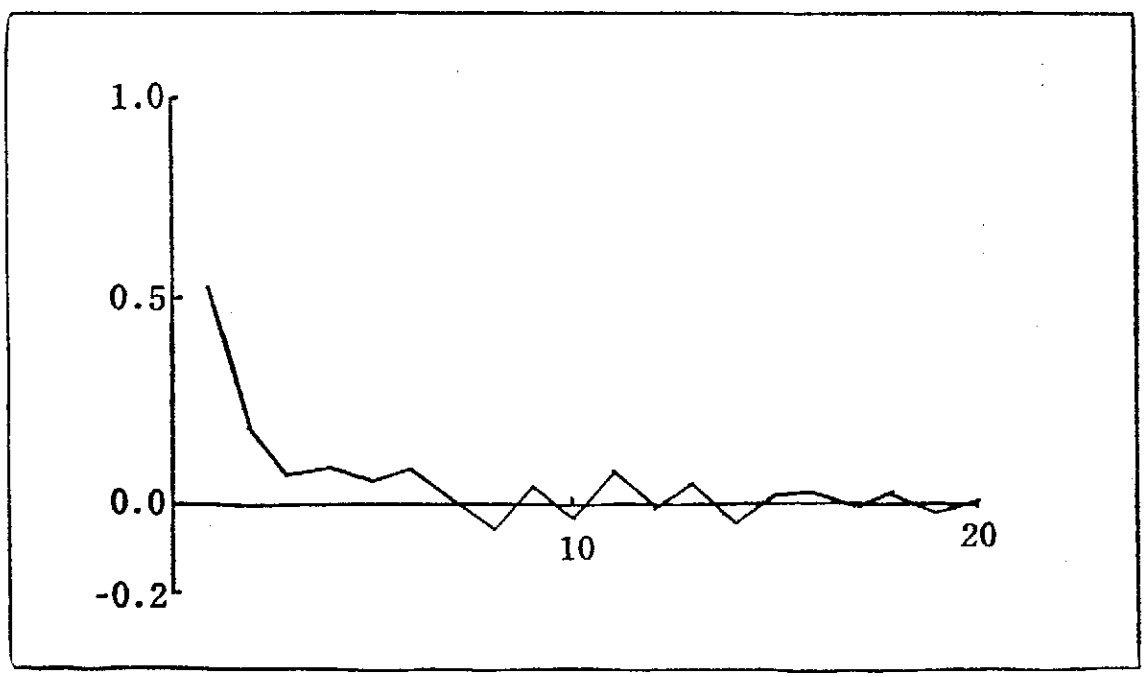

圖七　民國六十五年早上八時的小時平均濃度之 a. c. f.

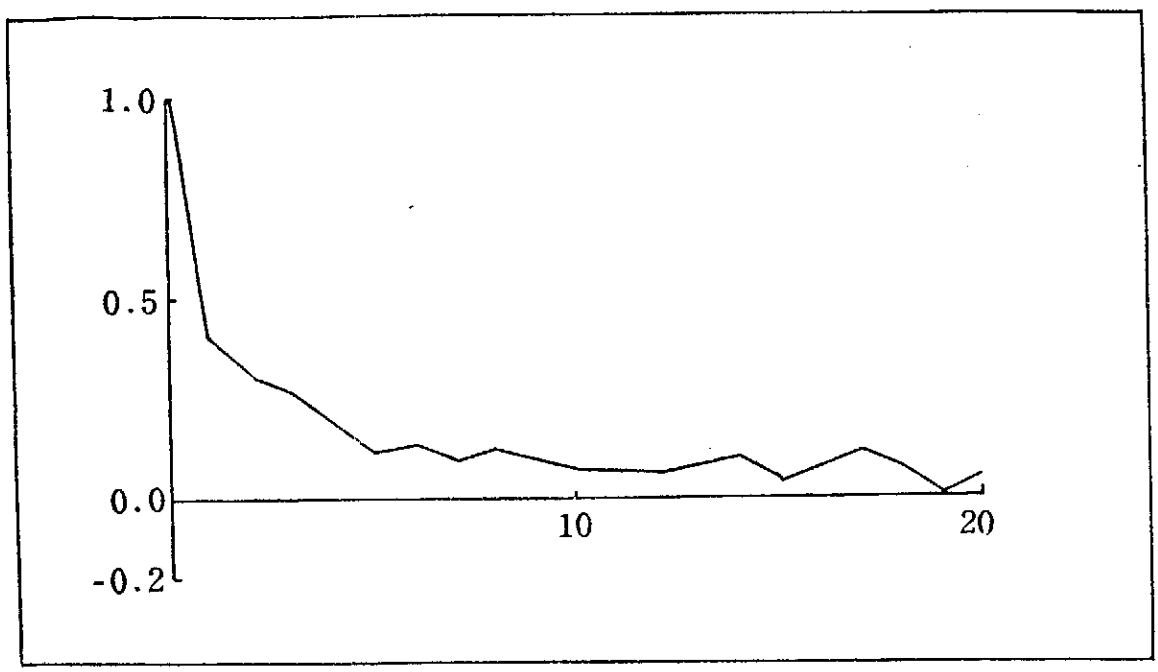

圖八　下午七時之小時平均濃度的 a. c. f.

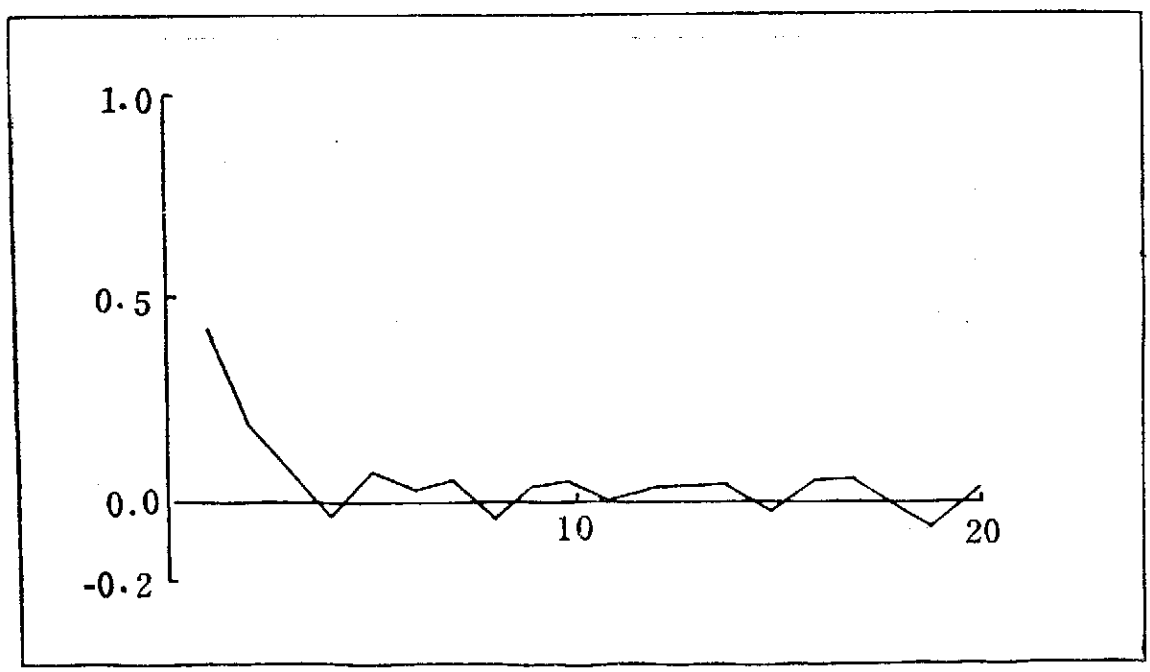

圖九　下午七時下時平均濃度的 p. a. c. f. 由圖六至九爲六十五年二十四個小時濃度模式 a. c. f. 及 p. a. c. f. 之代表其他的模式有相似外觀的 a. c. f. 及 p. a. c. f.

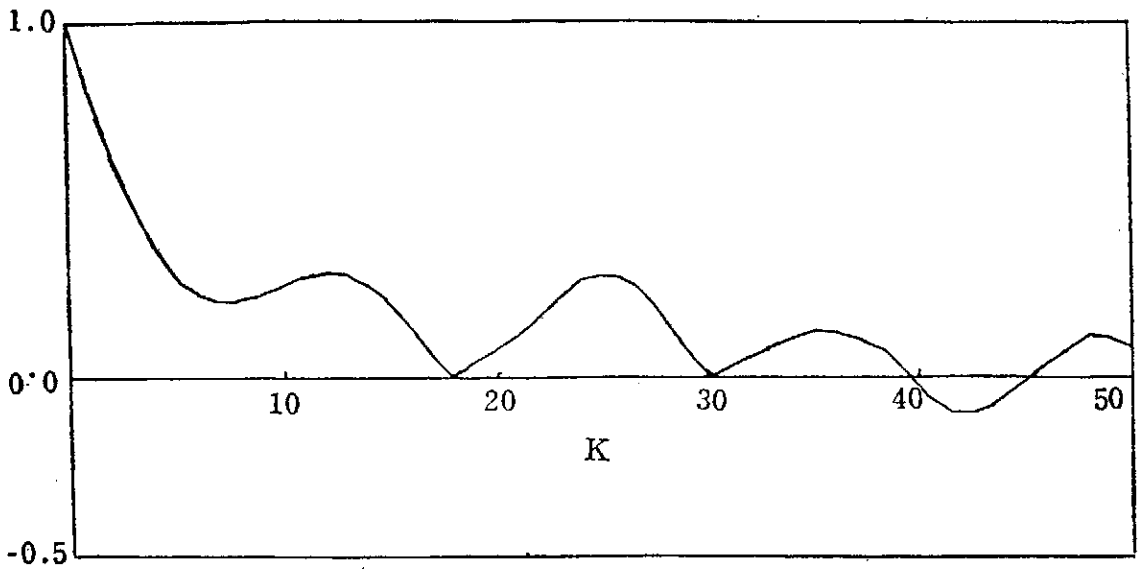

圖十　民國六十五年一月一日至十五日連續小時濃度變化的 a.c.f.

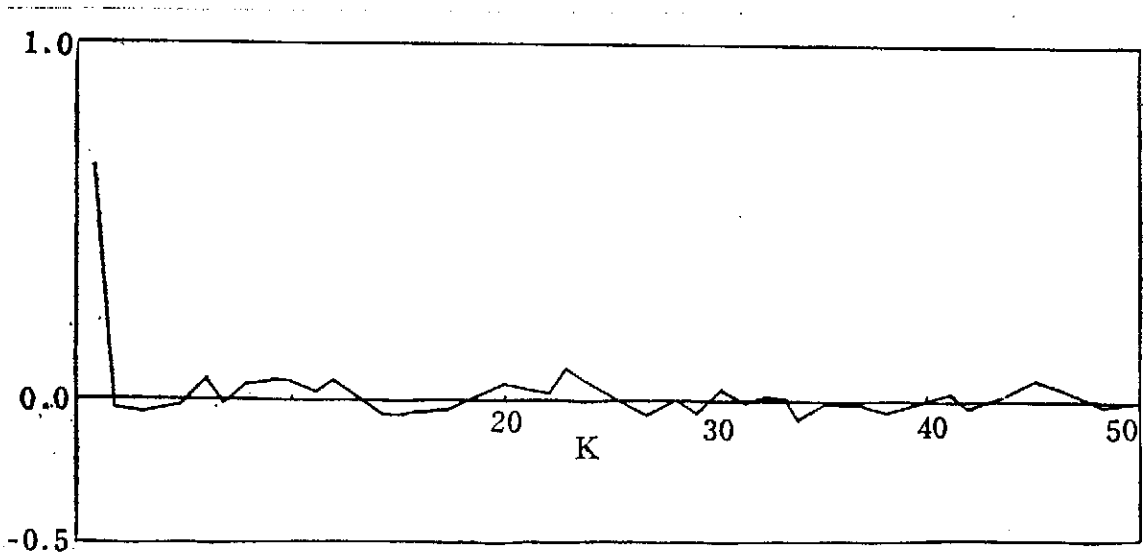

圖十一　民國六十五年一月一日至十五日連續小時濃度變化的 p.a.c.f.

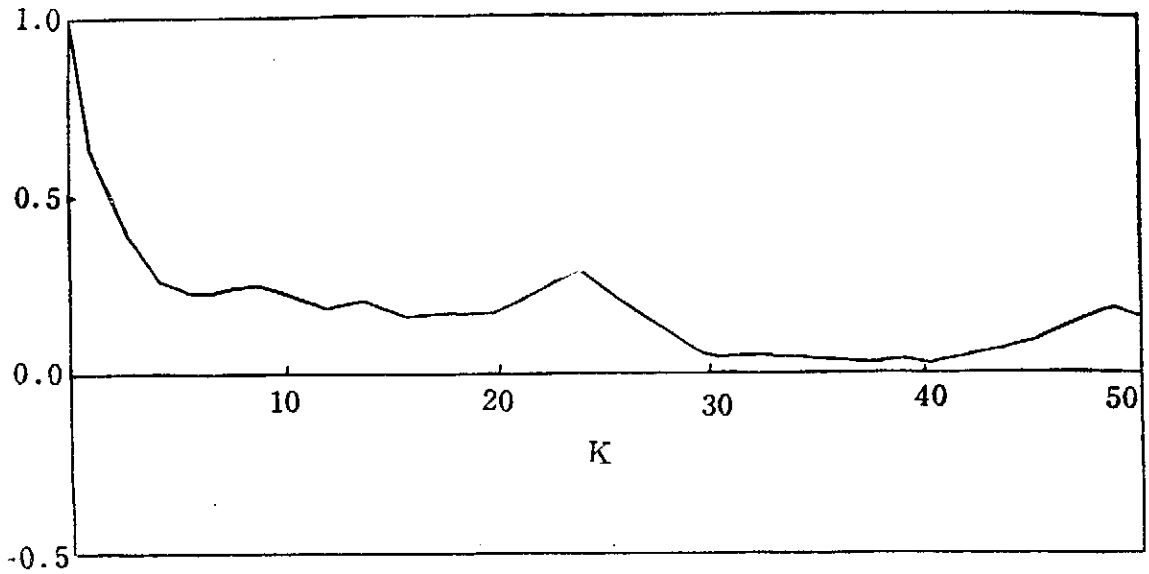

圖十二　民國六十五年七月十六日至三十日連續小時濃度的 a. c. f.

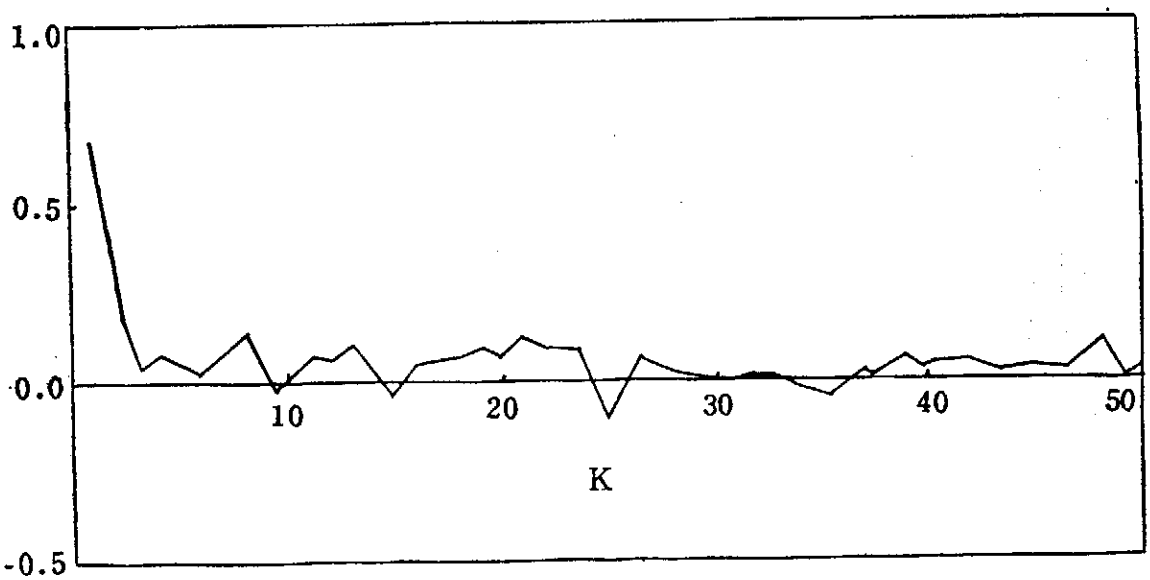

圖十三　民國六十五年七月十六日至三十日連續小時濃度的 p. a. c. f.

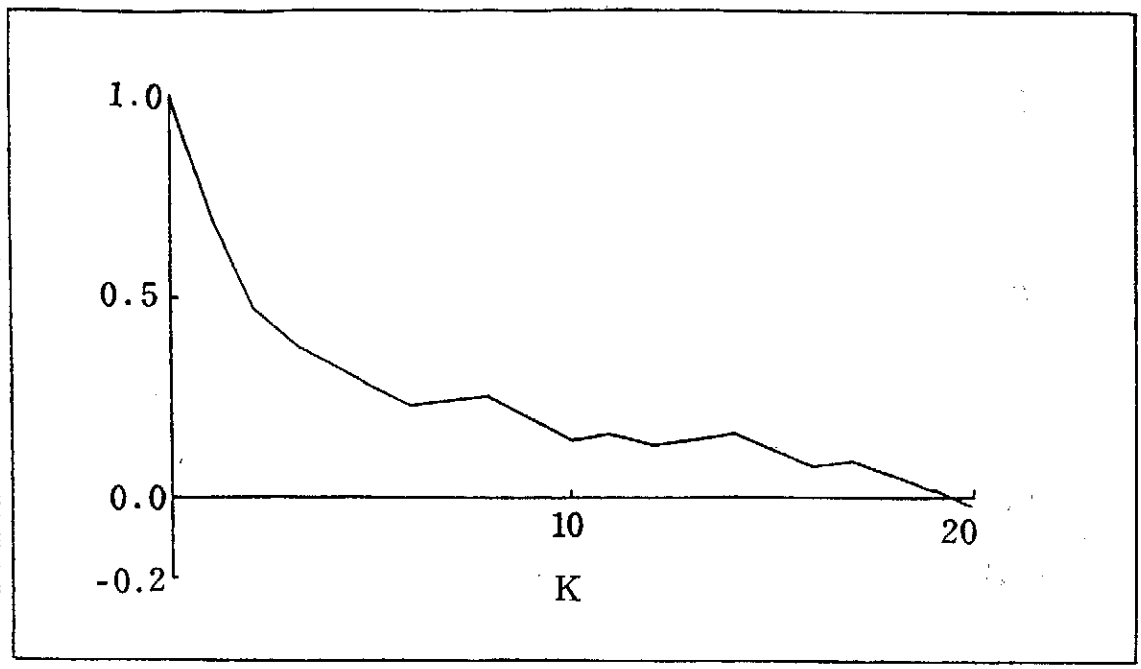

圖十四　把六十五年一月一日至十五日小時濃度 ∇^{24} 的差分後之 a.c.f. 七月十五日至三十日之那一組亦有相似的外觀

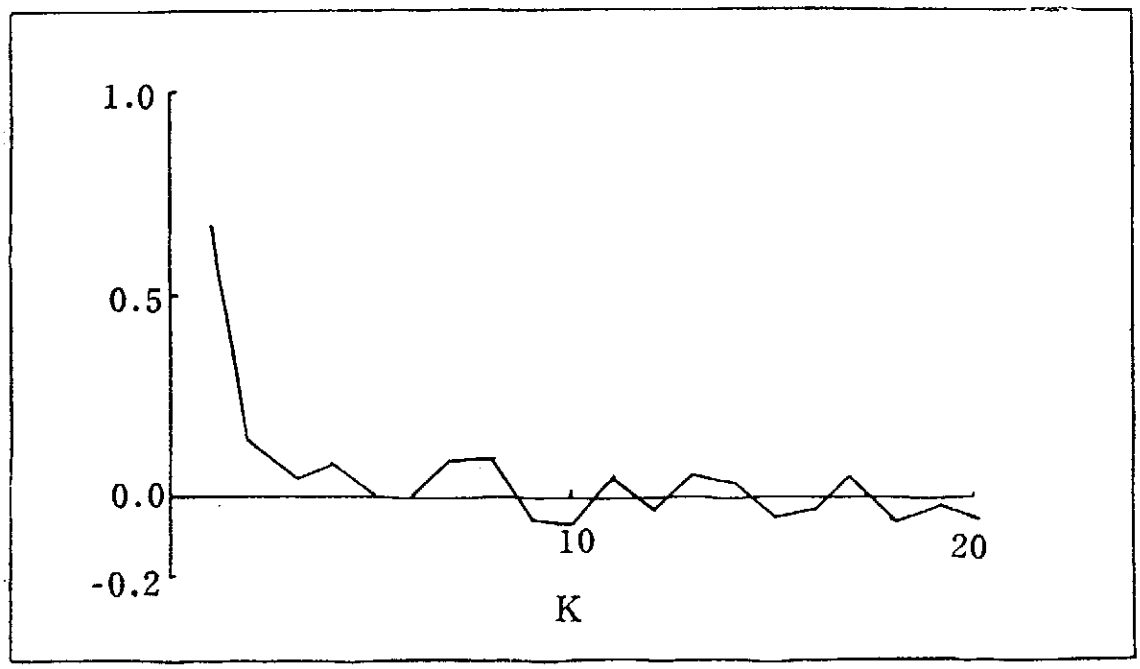

圖十五　把六十五年一月一日至十五日連續小時濃度作 ∇^{24} 後的 p.a.c.f.

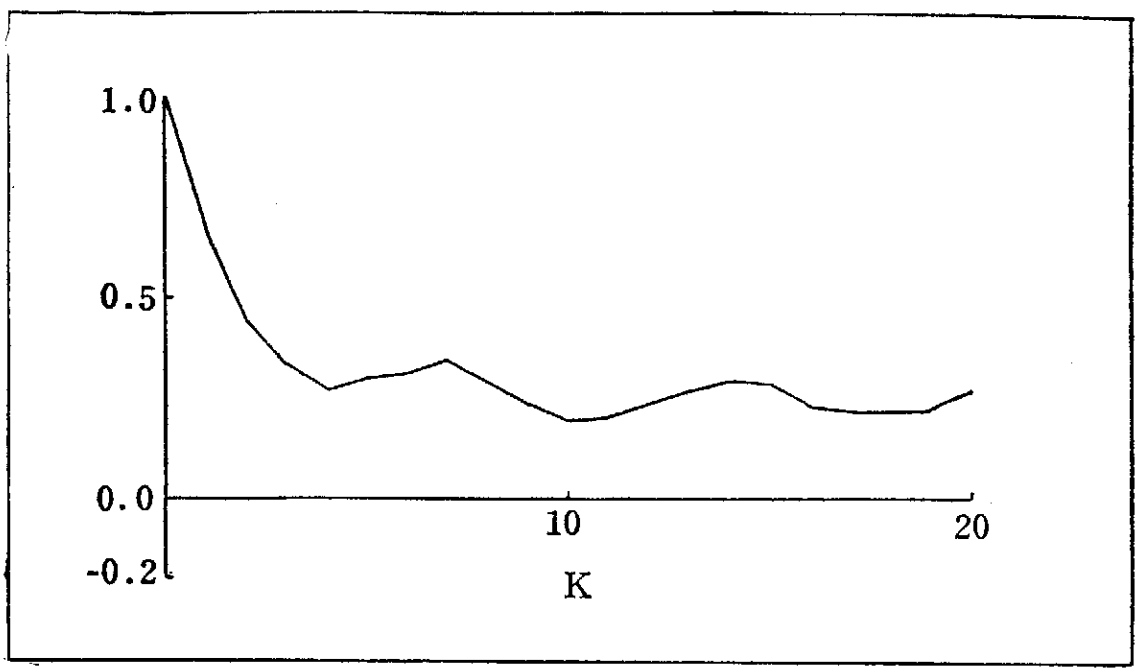

圖十六　六十三年至六十六年同一日四年平均之 a. c. f.

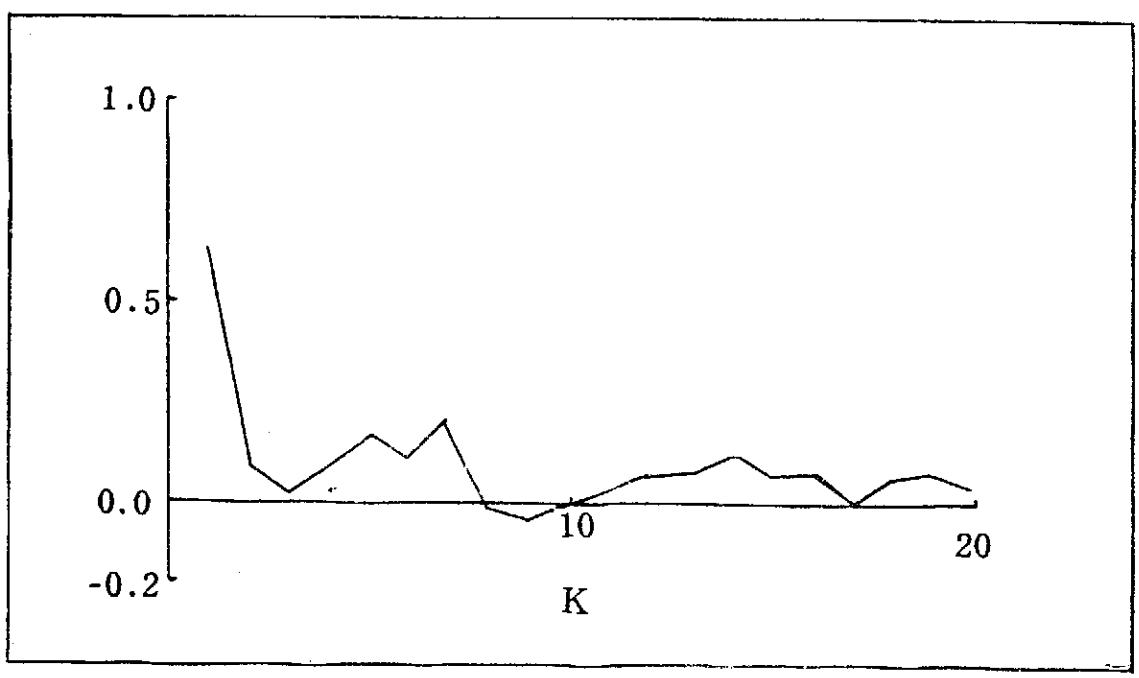

圖十七　六十三年至六十六年同一日四年平均之 p. a. c. f.

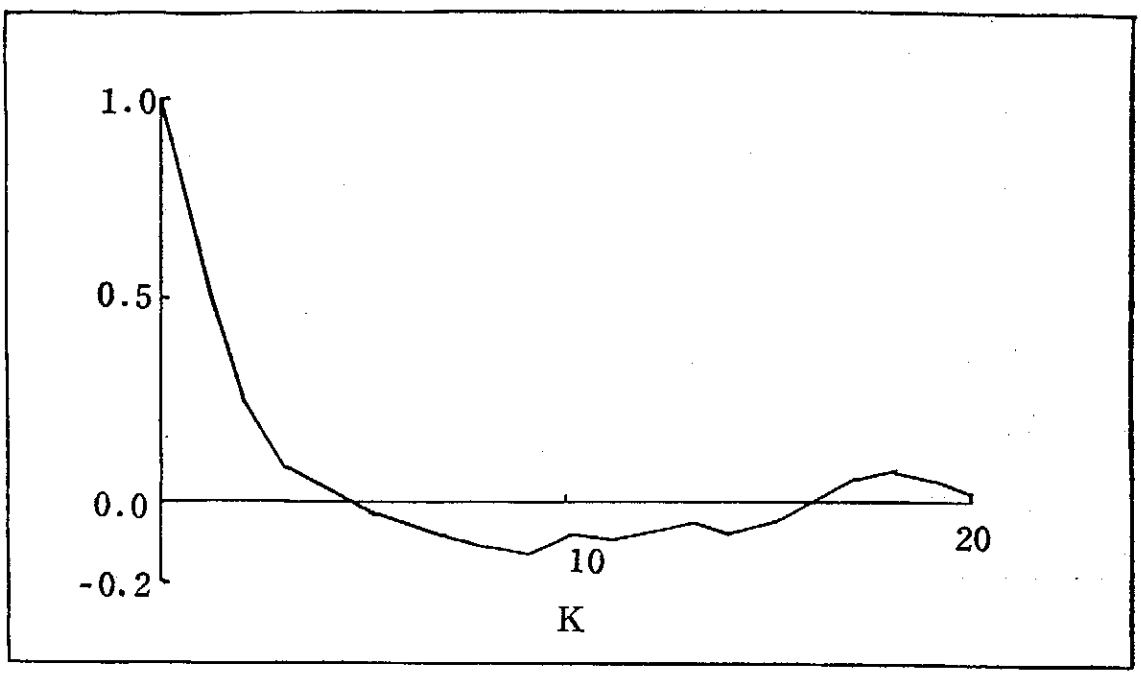

圖十八　六十三年至六十六年同一日四年平均 ∇^7 差分後的 a. c. f.

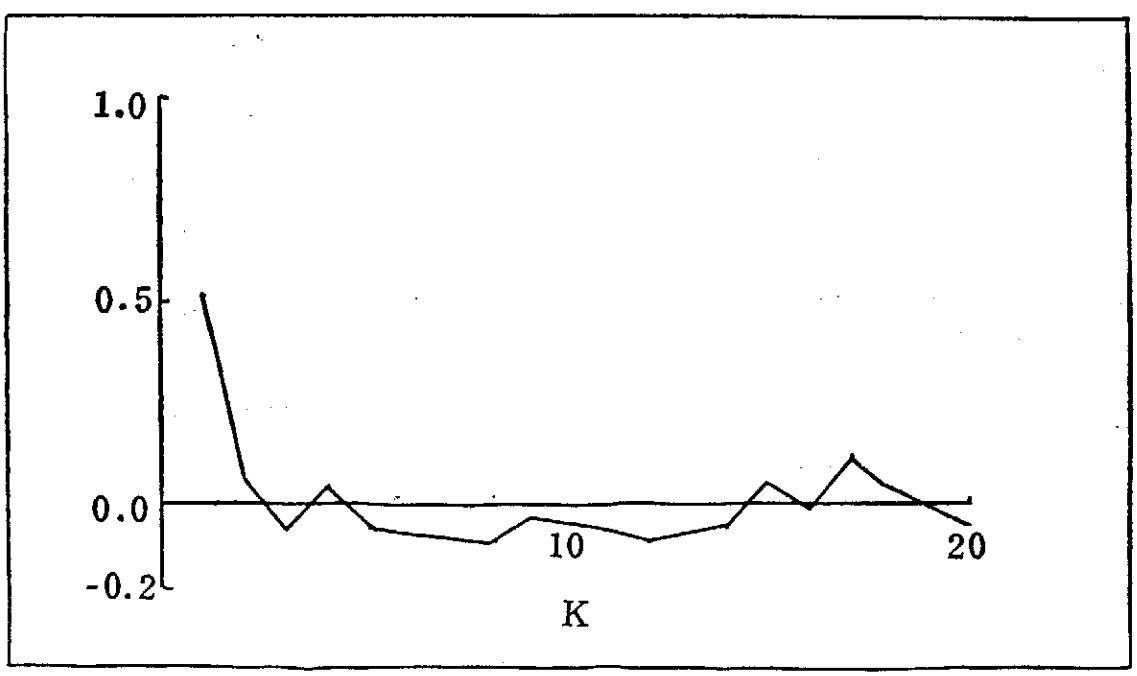

圖十九　六十三年至六十六年同一日四年平均 ∇^7 差分後的 p. a. c. f.

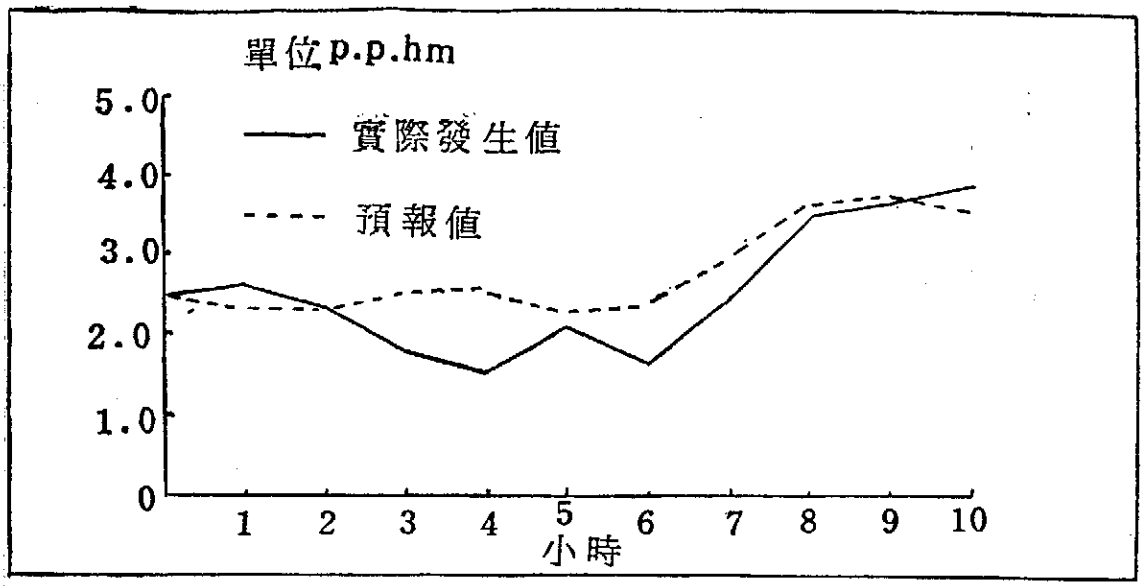

圖二十　自民國六十五年一月十六日起作十小時之預報

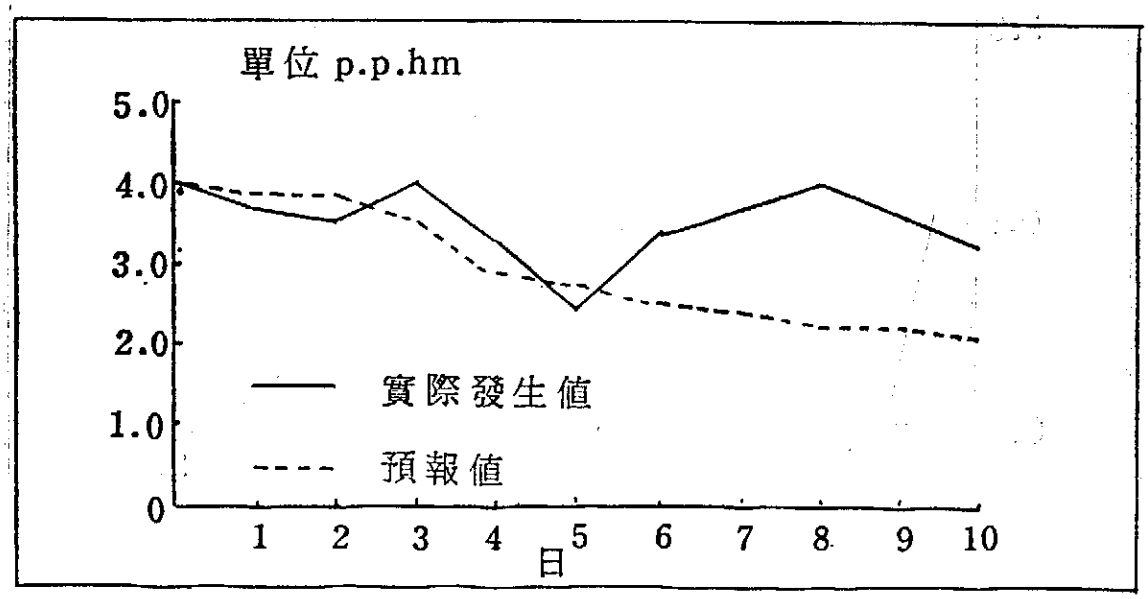

圖二十一　利用六十五年日平均濃度值作十天的預報

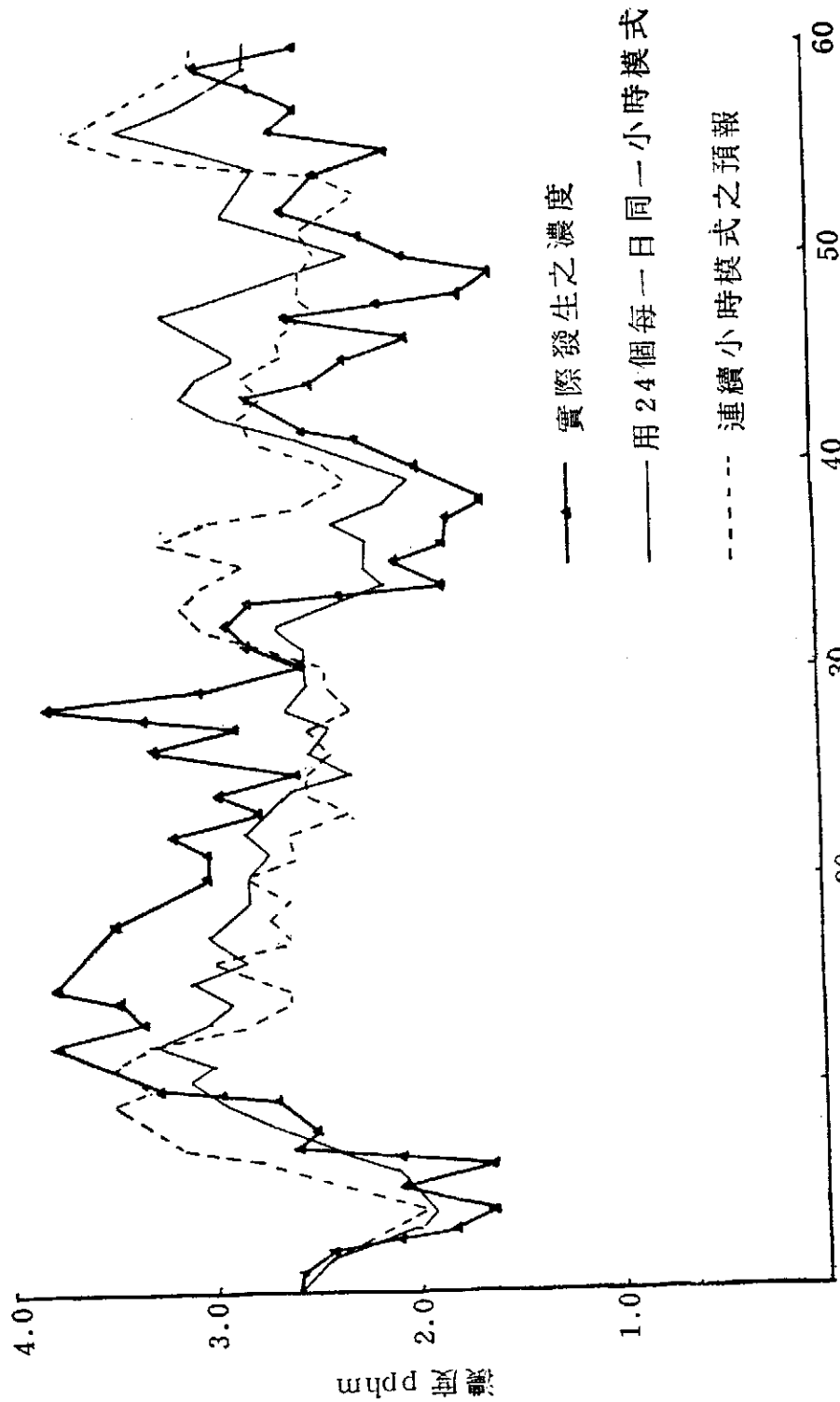

圖二十二　用二十四個每日同一小時濃度模式與連續小時濃度模式預報之比較

有限元素法之客觀分析

梁　文　傑

中央研究院物理研究所

國立臺灣大學機械工程研究所

謝　全　生

中國文化大學地學研究所

摘　　要

本研究直接以測站爲節點位置，建立一不等間隔之網格系統，以變分學原理，用地轉風平衡關係式爲弱勢動力約束條件，進行高層大氣定壓層之高度場與風場的變分客觀分析。本文用有限元素法得到分析方程式，這是聯立線性代數方程式，可以用高斯消去法求解。

本研究詳細討論有限元素法在氣象學上之應用，並且利用東亞和西太平洋地區的梅雨天氣資料進行個案研究。研究結果顯示，有限元素法求得之高度場能與實際大氣狀況和衛星雲圖相符合。與主觀分析和 Cressman 客觀分析之結果比較，本研究結果具備其他兩種方法之優點。本研究具有一般性，對不同之天氣系統，可用不同之約束條件予以分析。此外本研究亦詳細討論有限元素法未來在數值天氣分析與預報可能的發展與應用。

壹、導　　言

用客觀的數值方法來從事氣象變數場的分析，是近年來氣象學研究與日常作業最常用的方法，因其分析結果較主觀分析快速而且一致，不因操作員不同而影響其結果。客觀分析就是把分佈不規則的測站上各種氣象變數的觀測值內插到規則的有限差分網格系統上，以作爲分析大氣大規模運動或數值天氣預報起始值之用。作爲分析之用時，各變數之間的相關性必須列入考慮，否則用分析結果導出之氣象變數，如渦旋度、幅散度，會不合於實際大氣運動。作爲預報之用，更必須注意到分析場和使用的預報模式要保持一致性，假如這種內部一致的條件沒有獲得滿足，高頻雜波就會出現在預報模式內而無法正確的預報。這種氣象變數間的關係，作客觀分析必須加入考慮，變分客觀分析就是以各變數間的關係作分析時的約束條件，故祇有使用變分原理，客觀分析才能滿足各氣象變數的內部一致。

雖然很多研究客觀分析的學者一再强調內部一致的問題，可是直到1958年才獲得合理的解決。Sasaki (1958) 提出用變分原理來從事客觀分析的理論基礎，他的方法用途非常廣泛，能以各種約束條件來維持分析場的內部一致，這個方法後來被稱爲數值變分分析 (Numerical Variational Analysis, NVA)，或是變分客觀分析 (Variational Objective Analysis)，又叫做變分最佳分析 (Variational Optimization Analysis)。這個方法能將動力的、能量的、統計的或經驗的條件納入一個最佳的分析過程中。以從事氣象或海洋變數的分析。可是這種方法在其後十年間並無多大進展。直到1969年，Sasaki (1969, a. b) 指出這個方法的特點，約束條件的功能和濾波器的特性。Sasaki (1970) 又連續發表三篇文章，才奠定了變分分析的理論基礎，以及從事天氣分析的可行性。此後許多學者也從事變分客觀分析的研究與應用。最近變分分析更獲得進一步的發展。Groll (1975) 利用 Lewis (1972) 的模式來分析歐洲的天氣，並且發現利用約束條件確能濾除短波。Sasaki (1976) 利用能量守恒的積分條件來控制數值天氣預報積分運算中所產生的截斷誤差，可以避免短波和高頻雜波 (Noise) 的形成。因此變分分析除了能達成客觀分析目的外，更可以用來設計數值程式 (Numerical Scheme)。

一般氣象研究用變分客觀分析程式，都是先得到 Euler-Lagrange 方程式，然後再用有限差分方法求解，本研究考慮改用有限元素法來解 Euler-Lagrange 方程式。有限元素法發展的較晚，首先見於 Tuner, Clough, Martin 和 Topp (1956) 的論文上，用於解結構學和固體力學的問題。其後 Melosh (1963) 發現有限元素法是一種 Rayleigh-Ritz 的問題，祇要有變分原理的微分方程式都可以使用。Szabo 和 Lee (1963), Zienkiewicz (1971) 發現可用Weighted-Residual 法得到有限元素方程式，而使有限元素法的用途更爲廣泛，幾乎一般的微分方程式皆可用有限元素法求得數值解。

研究現行之客觀分析方法，發現因有固定網格距離之限制，使得測站與網格點不能在相同的位置上，因爲氣象測站的分佈太不規則。實際用於分析的氣象變數必須要在網格點上，使得網格點成爲一個虛構的測站，而用於分析的氣象變數值爲間接得來的觀測值。此一限制產生於所用的數值方法，即有限差分法，此法必須使用於有固定間距的有限差分網格系統上，網格點上之氣象變數因網格點並非測站，必須先將分佈不規則的測站所觀測得到的氣象變數值內插到規則的網格點上，才可使

網格點有氣象變數值，以作爲分析大幅度大氣運動或數值天氣預報之輸入值。內插的方法是將網格點周圍的測站上之值，做加權平均而後放入網格點。這種並非分析觀測值，而是加權平均後之結果，開始卽有所不同了，所得之分析結果或預報結果其精確度當然要大受影響。致力於改進分析方法或預報模式所得的效果，一定不及設法解除此種限制的效果。

爲求解除此限制，數值方法必須改進，卽要尋求一種不須要用固定間距的數值方法。此種方法必須用於不規則的網格系統，以適合分佈不規則的測站。在結構學和固體力學上，我們可以看到合於此種需要的數值方法，那就是有限元素法。使用有限元素法，沒有網格形狀和距離的限制，如能用於氣象學，則可達成測站卽是網格點，直接可用觀測值來分析或作預報。故本文研究使用有限元素法爲數值方法，討論此法在氣象學上之適用性，以期大幅度的改善客觀分析的品質，並嘗試探討有限元素法在氣象學問題的適用性。

現在一般高空測站上所觀測得到的氣象變數爲高度（或地面氣壓），溫度和風。不論用主觀分析或一般客觀分析法來從事這些變數的分析時，雖然會參考一些簡單的動力條件，如地轉風（水平方向）或溫度風（垂直方向）的關係式，可是實際上每個氣象變數仍爲獨立分析的。因此這些結果不能滿足變數間的相互關係，亦卽是這些變數之間不能保有內部的一致性，不能完全代表大氣大幅度之運動。若用於預報之模式爲輸入值，因爲變數之間不能保持一致會產生慣性重力波，終至影響積分之結果和預報的精確度。爲了解決這個問題，人們設計了許多由高度來求取其他變數的方法，這就是所謂初值化的問題 (Initialization)。假如高度值有誤差，這個誤差會立卽表現於風場上。測站上所得的各種氣象變數值，雖然其精確度有大小不同，可是在分析天氣時都是重要的資訊，要如何完全利用這些資訊來互相校正氣象變數，以求得滿足內部一致的氣象場，是研究改進客觀分析方法努力的目標。由研究結果顯示，變分分析能把動力的，能量的甚至統計的或經驗的條件一併納入一個最佳分析的過程中，以進行氣象變數的分析和校正，使校正後的氣象變數其間能維持內部一致，而且控制短波和高頻雜波的形成，使分析的結果能完全代表大氣大幅度運動。

本文基於上述之兩種理由，研究使用變分學和有限元素數值方法，期能一併解決這兩個問題。利用測站直接作爲網格點，然後對各變數同時進行變分分析，校正

變數使其間能滿足一致性。使校正後之氣象變數能代表大氣大幅度之運動，進而爲數值天氣預報模式的初始值之用，以改進數值天氣預報的精確度，更準確的預報大氣大幅度運動。

貳、研 究 方 法

進行本研究，首先將天氣資料打在卡片上，由計算機執行讀卡、驗卡之工作，然後定地圖座標，利用測站之經、緯度計算測站之座標值。同時利用有資訊的測站來建立本研究所使用之有限元素網格系統，把測站上之資訊直接放入節點上，完成有限元素法之資料輸入準備應用。最後用變分原理以地轉風近似關係式爲約束條件，來校正高度場與風場，使其保有力學的內部一致性。以下將分節討論本研究所用之變分原理和數值方法。

一、有限元素法之網格系統

本研究對高度 500 mb 層進行分析研究，對此層獨立分析研究，是一個二維空間 (2-Dimension) 的問題。使用有限元素法可用三角形或四角形元素來研究，其差別爲三角形元素多用於研究線性分布之問題，而四角形元素則分析二次函數分布較常用。本文以較簡單之分析過程，來探討本方法之適用性，僅假設風場和高度場在每一元素內爲線性元素函數，故可採用三角形元素來劃分整個研究範圍，建立三角形的有限元素網格系統，作爲分析研究之用。

劃分整個研究範圍成爲三角形元素的步驟包含下列兩點㈠以測站爲元素之節點 (Nodes)，連接各節點成爲三角形，各三角形的形狀和面積不需要相同，更不需要有相等的邊長。㈡將各個節點給予一個號碼，稱爲節點號碼 (Nodal number)，各個元素也給予一個號碼。步驟㈡特別重要，因其結果會影響計算機解方程組之速度，下面將會說明此點。

步驟㈠可以間接但較快的方式完成，先將研究範圍內節點連接成四角形，然後再劃對角線分成兩個三角形。但要注意對角線必須以較短的一條爲佳，因爲對角線較短所產生的兩個三角形，分析此種元素所得的結果，會比對角線較長而形狀狹長的三角形元素來得精確。同樣在劃分四角形時，也不限制其形狀和面積，當然更不須要其邊長爲固定值。

步驟㈡決定節點號碼和元素號碼中，要特別注意節點號碼的安置，因爲此種安

排的好壞對於求解之運程影響甚鉅。這與用有限元素法得到的聯立方程式係數矩陣之特性有關，係數矩陣有下列四個性質 (Segerlind, 1976) 1.稀疏性 (Sparse) 2.帶狀分布性 (Banded) 3.對稱性 (Symmetric) 和4.正性 (Positive definite)。性質1.就是係數矩陣中有許多項爲零，性質2.就是所有非零係數集中於主對角線之兩側，而且非零係數與零係數有一可與主對角線平行的分隔線，從主對角線到此分隔線之距離稱爲帶寬 (Bandwidth)，所有在此帶寬外之項其係數都爲零，因此可以不須要存入電腦的記憶位置內。因爲我們所使用的高速計算機，解聯立方程式祇須要這些在帶寬內的非零係數即可。故帶寬的減小一則可節省計算機可用的儲存空間，再則更可縮短計算機求解所用之時間 (CPU-Time)。帶寬是有限元素網格系統的一特性參數，計算之公式 (Segerlind, 1976) 爲

(1) $B=(R-1)\cdot NODF$

(1)式中B即爲帶寬。R爲全部元素之最大元素節點號碼差，受節點號碼之影響其大小。NODF 則是節點上變數之個數。在本研究，每一節點有一個變數，故 NODF =1。由(1)式看來，NODF 亦是元素之特性參數，是爲一固定值，故欲減小帶寬，就要使R值減小。要使R值減小，在編定節點號碼時就要注意不使每一元素最大節點號碼和最小節點號碼相差過大。由此可知編定節點號碼對計算之影響。

由步驟㈠㈡將研究範圍劃分成本研究所用之有限元素網格系統（圖1），共有92個節點，形成165個元素，其中R值等於27，依公式(1)的計算，每一節點上有一個未知數，得本研究所用之網格系統帶寬爲27。圖1上以阿拉伯數字表示節點號碼，再以阿拉伯數字加上小括號表示元素之號碼。然後把節點之測站號碼，經緯度和座標值依節點順序排列，打在卡片上作爲節點之輸入資點。再把元素之三節點號碼，從每一元素左下角開始以逆鐘方向順序記下來，也打成卡片作爲元素之資料，如此才完成建立有限元素網格系統之工作。

二、變分客觀分析與動力約束條件

進行變分客觀分析，我們所做的假設是

(2) $u\simeq\tilde{u},\ v\simeq\tilde{v},\ z\simeq\tilde{z}$

其中 u, v 是校正後 x, y 方向的速度分量，z 是校正後的高度值。$\tilde{u}$, $\tilde{v}$ 是觀測的 x, y 方向速度分量，$\tilde{z}$ 則是觀測的高度值。(2)式代表經變分客觀分析校正所得的 z, u, v 與觀測所得的 $\tilde{z}$, $\tilde{u}$, $\tilde{v}$ 相差很小，雖然如此，但若作爲預報模式之用，這

些氣象變數的微小改變其意義就非常的重大。因爲不但觀測值會有誤差，而且這些變數之間不能維持一定的關係，即沒有滿足力學的一致性，假如不加以校正，則在預報模式積分運程中，就會產生慣性重力波。此外，在作爲診斷 (Diagnostic) 用，如利用水平風速 u, v 計算垂直速度 ω 和渦旋量 ζ，這種些微的校正也屬必要的。

(2)式在變分理論中叫做弱勢約束條件 (Weak Constraints)，因此我們的變分公式爲

$$\delta J=\delta\iint\{\tilde{\alpha}^2(u-\tilde{u})^2+\tilde{\alpha}^2(v-\tilde{v})^2+\tilde{\beta}^2(z-\tilde{z})^2\}\frac{d_x d_y}{\sigma^2}=0 \tag{3}$$

其中 δ 是變分學的算符，$\tilde{\alpha}$, $\tilde{\beta}$ 分別是 x, y 方向速度分量和高度的觀測權重，σ 是投影變形因子 (image scale)。

(3)式中的變分原理其意義是很清楚的，大括號內是强迫校正值 z, u, v 分別與 $\tilde{\alpha}$, $\tilde{\beta}$ 成比例的趨近於原有的觀測值 $\tilde{z}$, $\tilde{u}$, $\tilde{v}$。換句話說，就是使校正值與觀測值兩者差的平方爲極小值，這和最小二乘方的意義相同。$\tilde{\alpha}$, $\tilde{\beta}$ 之觀測權重必須事先決定，因爲他們不是變分分析過程中的未知數。這些權重和觀測值的精度有極密切之關係。假如一觀測值的誤差很大，那麼它的觀測權重必會很小，這樣將使這個變數的觀測值較不影響最後分析的結果。反之若一變數的觀測值比較精確，那麼它就對最後的分析結果有甚大之影響。對於各種氣象變數觀測值的精度與所用之觀測儀器和觀測系統有關，這些在 Bengtsson (1975) 一書中有詳細的介紹。

又(3)式中的未知數 z, u, v 並非互相獨立的，而是藉著動力的關係而互相影響，此種關係即約束條件。本研究採用地轉風關係式作爲對 z, u, v 的約束條件，即以 u, v 代表 z 在水平方向梯度，所用的地轉風方程式爲

$$\frac{\partial z}{\partial x}=k_1\ v \tag{4}$$

$$\frac{\partial z}{\partial y}=k_2\ u$$

$$\text{其中}\quad k_1=-k_2=\frac{m\alpha g}{f} \tag{5}$$

(5)式中 m 爲比例尺，g 爲重力加速度，f 爲科氏力。(5)式用比例尺與投影變形因

子的意義是網格間隔是地圖上度量的。(4)亦爲一弱勢約束條件，故(3)式可增加爲

$$(6)\quad \delta J=\delta\iint\{[\tilde{\alpha}^2(u-\tilde{u})^2+\tilde{\alpha}^2(v-\tilde{v})^2+\tilde{\beta}^2(z-\tilde{z})^2]+$$
$$[\gamma^2(k_1\frac{\partial z}{\partial x}+v)^2+\gamma^2(k_2\frac{\partial z}{\partial y}+u)^2]\}\frac{dxdy}{\sigma^2}=0$$

(6)式中的第二個中括號是代表强迫校正後之 z, u, v 能滿足地轉風近似之關係式。

選擇地轉風近似關係式爲約束條件，還有一更重要之理由，卽可縮小測站所能測得之最小波長。亦卽節點所能分析之最短波長可以縮短。因本研究直接以測站爲節點，所得分析之最小波長受測站距離所支配。根據抽樣原理 (Sampling Theorem) (Stephens, 1971)，假如在測站上能測得某一變數之梯度，則這些測站所能測得之最小波長一定可以縮短，也就是說可定義幅度 (definable scale) 減小，因此更得以代表實際的觀測值。雖然氣象測站分布不均勻，用抽樣原理來討論比較困難，但其原理仍然一樣。

(6)式中所有的權重都假設爲常數，此外在(6)式內加入$\frac{1}{\sigma^2}$，表示所有的權重是在地球上而不是地圖上決定的。

由(6)式求出 Euler-Lagrange 方程式爲：

$$(7)\quad (\tilde{\alpha}^2+\gamma^2)u=\tilde{\alpha}^2\tilde{u}-\gamma^2k_2\frac{\partial z}{\partial y}$$

$$(8)\quad (\tilde{\alpha}^2+\gamma^2)v=\tilde{\alpha}^2\tilde{v}-\gamma^2k_1\frac{\partial z}{\partial x}$$

$$(9)\quad \tilde{\beta}^2z-k_1^2\gamma^2(\frac{\partial^2 z}{\partial x^2}+\frac{\partial^2 z}{\partial y^2})=\tilde{\beta}^2\tilde{z}+k_1\gamma^2\frac{\partial v}{\partial x}+k_2\gamma^2\frac{\partial u}{\partial y}$$

將(7)，(8)兩式代入(9)式，得高度場之分析方程式，爲

$$(10)\quad \tilde{\beta}^2z-k_1^2\frac{\tilde{\alpha}^2\gamma^2}{\tilde{\alpha}^2+\gamma^2}(\frac{\partial^2 z}{\partial x^2}+\frac{\partial^2 z}{\partial y^2})=\tilde{\beta}^2\tilde{z}+\frac{\tilde{\alpha}^2\gamma^2}{\tilde{\alpha}^2+\gamma^2}$$
$$(k_1\frac{\partial\tilde{v}}{\partial x}+k_2\frac{\partial\tilde{u}}{\partial y})$$

Euler-Lagrange 方程式之自然邊界條件爲 $\delta z=0$，卽高度場在邊界上不作校正，而以觀測值作爲校正值進行變分分析。

在(10)式中，令 $\tilde{C}=\frac{\tilde{\alpha}^2\gamma^2}{\tilde{\alpha}^2+\gamma^2}$，可簡化爲

$$(11)\qquad \tilde{\beta}^2 z - k^2 \tilde{C} \nabla^2 z = \tilde{\beta}^2 \tilde{z} + k\tilde{C}\left(\frac{\partial \tilde{v}}{\partial x} - \frac{\partial \tilde{u}}{\partial y}\right)$$

其中 $k = k_1 = -k_2$。

三、局部有限元素方程式和全域有限元素方程式

本研究首先把研究範圍分爲許多三角形元素，使用最簡單的二維線性三角形元素，每個元素具有三個節點。圖 1 顯示本研究的有限元素網格系統，共有 165 個元素，92個節點。在一元素中，某一變數 φ 可用線性內插多項式表示

$$(12)\qquad \varphi = \alpha_1 + \alpha_2 x + \alpha_3 y$$

其中 x, y 爲座標值，α_1, α_2, α_3 爲尙待決定的係數。代入元素三節點的變數值和節點座標，

$$(13)\qquad \begin{cases} \varphi = \varphi_i & \text{在 } x = X_i,\ y = Y_i \\ \varphi = \varphi_j & \text{在 } x = X_j,\ y = Y_j \\ \varphi = \varphi_k & \text{在 } x = X_k,\ y = Y_k \end{cases}$$

i, j, k 表元素之三節點，X_β, Y_β(β = i, j, k) 爲三節點之座標（圖 2）。

將(13)式代入(12)式，可得 α_1, α_2, α_3 的一組聯立方程式

$$(14)\qquad \begin{cases} \varphi_i = \alpha_1 + \alpha_2 X_i + \alpha_3 Y_i \\ \varphi_j = \alpha_1 + \alpha_2 X_j + \alpha_3 Y_j \\ \varphi_k = \alpha_1 + \alpha_2 X_k + \alpha_3 Y_k \end{cases}$$

可解得 α_1, α_2, α_3 爲

$$(15)\qquad \begin{cases} \alpha_1 = \dfrac{1}{2A}\left[(X_j Y_k - X_k Y_j)\varphi_i + (X_k Y_i - X_i Y_k)\varphi_j + (X_i Y_j - X_j Y_i)\varphi_k\right] \\ \alpha_2 = \dfrac{1}{2A}\left[(Y_j - Y_k)\varphi_i + (Y_k - Y_i)\varphi_j + (Y_i - Y_j)\varphi_k\right] \\ \alpha_3 = \dfrac{1}{2A}\left[(X_k - X_j)\varphi_i + (X_i - X_k)\varphi_j + (X_j - X_i)\varphi_k\right] \end{cases}$$

(15)式中 $2A = \begin{vmatrix} 1 & X_i & Y_i \\ 1 & X_j & Y_j \\ 1 & X_k & Y_k \end{vmatrix}$，爲(14)式之係數行列式之值，於編定元素之節點號碼能以逆時鐘方向順序，A卽爲此元素之面積。將(15)式 α_1, α_2, α_3 之值代入(12)式，經整理可寫爲

(16) $$\varphi = N_i\ \varphi_i + N_j\ \varphi_j + N_k\ \varphi_k = \sum_\beta N_\beta \varphi_\beta \quad (\beta = i,\ j,\ k)$$

其中 $$N_i = \frac{1}{2A}[a_i + b_i x + c_i y], \quad a_i = X_j\ Y_k - X_k\ Y_j$$
$$b_i = Y_j - Y_k$$
$$c_i = X_k - X_j$$

$$N_j = \frac{1}{2A}[a_j + b_j x + c_j y], \quad a_j = X_k\ Y_i - X_i\ Y_k$$
$$b_j = Y_k - Y_i$$
$$c_j = X_i - X_k$$

$$N_k = \frac{1}{2A}[a_k + b_k x + c_k y], \quad a_k = X_i\ Y_j - X_j\ Y_i$$
$$b_k = Y_i - Y_j$$
$$c_k = X_j - X_i$$

N_β 稱爲形狀函數 (shape function)，亦爲座標 x, y 之函數。

故每一元素之 z, u, v ， $\tilde{z}$, $\tilde{u}$, $\tilde{v}$ 可以形狀函數和節點值表示爲

(17) $$\tilde{z} = \sum_\beta N_\beta\ \tilde{z}_\beta \qquad z = \sum_\beta N_\beta\ z_\beta$$

(18) $$\tilde{u} = \sum_\beta N_\beta\ \tilde{u}_\beta \qquad u = \sum_\beta N_\beta\ u_\beta \quad (\beta = i,\ j,\ k)$$

(19) $$\tilde{v} = \sum_\beta N_\beta\ \tilde{v}_\beta \qquad v = \sum_\beta N_\beta\ v_\beta$$

本研究用 Galerkin 近似把 (11) 式轉換爲 局部有限元 素方程式 (local finite element equation) (Chung, 1978)，爲下列之式子：

(20) $$\iint[\tilde{\beta}^2\ z - k^2\ \tilde{C}\nabla^2 z - \tilde{\beta}^2\tilde{z} - k\tilde{C}\left(\frac{\partial\tilde{v}}{\partial x} - \frac{\partial\tilde{u}}{\partial y}\right)]N_\gamma\ dxdy = 0 \quad (\gamma = i,\ j,k)$$

在每一元素中，將 k 考慮爲一常數，爲三節點上 k_i, k_j, k_k 之平均值。將(17)，(18)，(19)式代入上式，計算出積分式，即可得到局部有限元素方程式。

本研究之局部有限元素方程式爲：

(21) $$\frac{\tilde{\beta}^2\ A}{12}\begin{pmatrix}2 & 1 & 1\\ 1 & 2 & 1\\ 1 & 1 & 2\end{pmatrix}\begin{pmatrix}z_i\\ z_j\\ z_k\end{pmatrix} + k^2\tilde{C}A\begin{pmatrix}b_i^2+c_i^2 & b_ib_j+c_ic_j & b_ib_k+c_ic_k\\ b_jb_i+c_jc_i & b_j^2+c_j^2 & b_jb_k+c_jc_k\\ b_kb_i+c_kc_i & b_kb_j+c_kc_j & b_k^2+c_k^2\end{pmatrix}\begin{pmatrix}z_i\\ z_j\\ z_k\end{pmatrix}$$

$$= \frac{\tilde{\beta}^2 \cdot A}{12} \begin{pmatrix} 2 & 1 & 1 \\ 1 & 2 & 1 \\ 1 & 1 & 2 \end{pmatrix} \begin{pmatrix} \tilde{z}_i \\ \tilde{z}_j \\ \tilde{z}_k \end{pmatrix} + \frac{k\tilde{C} \cdot A(b_i\tilde{v}_i + b_j\tilde{v}_j + b_k\tilde{v}_k - c_i\tilde{u}_i c_j\tilde{u}_j - c_k\tilde{u}_k)}{3}$$

每一個元素都有局部有限元素方程式，而且祇要每一元素爲片斷連續 (piecewise continuous) 即可積分，故可以將局部有限元素方程式擴大爲92個方程式，然後組合 (Assemblage) 起來就可以得到全域有限元素方程式 (global finite element equation)。組合之過程可參閱 Chung 1978 和 Segerlind 1976。全域有限元對稱方程式具有92個聯立代數方程式，解出此方程式就可得到每個節點在某一定壓層的校正高度值。

四、數值方法和計算步驟

全域有限元素方程式爲 92 個聯立代數方程式，其係數矩陣爲 92×92 的對稱方陣，所需計算機記憶和計算時間非常多。有限元素法得到的係數矩陣有前節所述的四個特點，使係數矩陣爲對稱的，其中非零項很少而且集中在對角線附近，也就是說係數矩陣具有一定的帶寬。考慮此一特性，使用特定的矩陣儲存方式，可以減少矩陣所需的計算機記憶。使用固定帶寬矩陣的儲存方式（林，1978），可以使本研究減少70%的記憶，因此計算機可輕易處理。此外在解聯立方程式方面，現在也發展許多有效的解法 (如 Fellipa 1975)，也可以節省許多計算機時間。

本研究求取校正值，其計算步驟如下：

1. 輸入節點和元素之資料；
2. 輸入節點上之氣象觀測值；
3. 計算(23)每一元素之局部有限元素方程式係數；
4. 以組合求得92個聯立代數方程式；
5. 解出92個節點之校正高度值；
6. 以校正後之高度值和觀測風速值代入(7)，(8)兩式，用 Galerkin 似法求取校正之風速分量 u 和 v。

參、研 究 結 果

一、資料來源及天氣狀況

本研究個案資料係1975年6月10日格林尼治零時之高空資料，計有220個測站的觀測資料，範圍約在10°N至60°N，70°E至160°E之間，此區域包括中國、蒙古、日本、中南半島、菲律賓及西太平洋地區。

所蒐集的高空資料包括高度、溫度、露點溫度、風向及風速等之觀測值，其垂直層次計有五層，即850 mb，700 mb，500 mb，300 mb，200 mb等定壓層，其中高度和風向風速每層均有，爲本研究所用。另外還有1,000 mb之高度值。

資料在傳遞之間，可能由於觀測偏差，編譯電碼不愼或通訊線路不穩定而產生錯誤。以中央氣象局臺北氣象測站到東京點間的通訊線路爲例，有10%到15%之高空測站資料錯誤或漏失（胡，1977），因此對氣象資料的輸入，應先加以檢定，並在可能的情況下予以更正 (Chen and Tsay, 1977) 以濾除可能的錯誤資料，並提高各測站觀測資料的可信度。

圖3爲實際500mb主槽線由日本海上空業已發展之低壓中心向西南延伸至臺灣東北，另一槽線由蒙古向西南延伸（略偏西南），較之700和850 mb上者稍微傾斜。巴士海峽，南中國海一帶有一反氣旋中心，故在500 mb上，臺灣附近盛行西北風。斜壓區位於北緯30度以北，噴射氣流在暖區，在此層上可見到典型的冷低壓（或槽）和暖高壓（或脊）型態。

此一時間，一連續的雲帶，涵蓋日本東南方、琉球、臺灣和華南一帶。根據NOAA-4衛星雲圖顯示（圖5），以臺灣北部一帶雲層最厚。對應另一條槽線在綏遠和陝西一帶亦爲雲帶所覆蓋。此外根據地面測站所作之雲量數字標示圖（圖4），亦與天氣狀況與衛星雲圖相符合。

二、權重之分析

進行變分分析，求數值之前，首先必須決定觀測權重 $\tilde{\alpha}$, $\tilde{\beta}$ 與動力權重 γ。使用於變分分析的權重函數，爲了避免不必要的錯誤，必須考慮到下面兩個因素 (a) 權重函數是代表觀測與理論值之誤差，換言之即爲觀測正確性之評估 (b) 權重函數必須與資料所代表之天氣形態相關，如鋒面區或高壓脊附近權重函數之表示。本文爲簡化計算過程，僅考慮前一項因素。即觀測權重 $\tilde{\alpha}$, $\tilde{\beta}$ 代表觀測的可靠度，若 $(u-\tilde{u})$, $(v-\tilde{v})$, $(z-\tilde{z})$ 等項愈趨近於零，亦即與理論值誤差很小，則其權重 $\tilde{\alpha}$, $\tilde{\beta}$ 應該愈大。動力權重是由 $(k_1\frac{\partial z}{\partial x}+v)$, $(k_2\frac{\partial z}{\partial y}+u)$ 的數量級決定，假如動

力權重愈大，代表大氣的運動趨向於地轉風平衡。雖然有三個權重，但只有二個互相獨立的權重，譬如 $\tilde{\beta}/\tilde{\alpha}$, $\gamma/\tilde{\alpha}$，另一個可假設爲 1。

本研究採用 $\tilde{\alpha}=1$，祇變動 $\tilde{\beta}$, γ 來調整觀測值與校正值間之差誤與地轉近似之數量級。因爲使用變分原理，並無法使(6)式中每一項皆爲最小值，而係考慮使各項差誤之總和爲一穩定的最小值 (Stationary Minimum)，故權重之調整是必要的。調整是使各項誤差的分佈符合物理意義，而所得校正值其分析場亦爲合理才可。

先使用 500 mb 一層作爲分析權重和各項誤差之關係。選用 $\tilde{\beta}^2$, γ^2 分別等於 10^4, 10^3, 10^2, 10^1, 10^0, 10^{-1}, 10^{-2}, 10^{-3}, 10^{-4}。然後以各別的三個權重值求解分析方程式，所得之校正值再與原觀測值求其均方根，爲：

(22) $$(\Delta u)_{r.m.s}=\left[\sum_{e=1}^{165}\iint(u_e-\tilde{u}_e)^2dxdy/165\right]^{1/2}$$

(23) $$(\Delta v)_{r.m.s}=\left[\sum_{e=1}^{165}\iint(v_e-\tilde{v}_e)^2dxdy/165\right]^{1/2}$$

(24) $$(\Delta z)_{r.m.s}=\left[\sum_{e=1}^{165}\iint(z_e-\tilde{z}_e)^2dxdy/165\right]^{1/2}$$

地轉近似的誤差值，則以下列式子求其均方根

(25) $$(\Delta G_1)_{r.m.s}=\left[\sum_{e=1}^{165}\iint\left(k_1\frac{\partial z_e}{\partial y}+v_e\right)^2dxdy/165\right]^{1/2}$$

(26) $$(\Delta G_2)_{r.m.s}=\left[\sum_{e=1}^{165}\iint\left(k_2\frac{\partial z_e}{\partial y}+u_e\right)^2dxdy/165\right]^{1/2}$$

然後將 $(\Delta u)_{r.m.s}$ $(\Delta v)_{r.m.s}$ 合併爲風速誤差項，$(\Delta G_1)_{r.m.s}$ 與 $(\Delta G_2)_{r.m.s}$ 合併爲地轉近似誤差項，其方法爲：

(27) $$(\Delta C)_{r.m.s}=\left[(\Delta u)^2_{r.m.s}+(\Delta v)^2_{r.ms}\right]^{1/2}$$

(28) $$(\Delta G)_{r.m.s}=\left[(\Delta G_1)^2_{r.m.s}+(\Delta G_2)^2_{r.m.s}\right]^{1/2}$$

所得之結果列表1 (a)～(c)，由表可知，觀測權重在一定範圍內確實與觀測誤差成反比，即 $(u-\tilde{u})$、$(v-\tilde{v})$ 與 $(z-\tilde{z})$ 項愈小，則其權重值愈大。而動力權重亦與動力約束條件成反比。

對於誤差分佈之決定，本研究採取下列之基本值：

$(\Delta u)_{r.m.s}$, $(\Delta v)_{r.m.s}\sim 2m/S$

$(\Delta z)_{r.m.s}\sim 10m$

如此選擇是假設 500 mb 層上，觀測風和理論值平均誤差爲 2m/S，而高度誤差爲 10 m。至於地轉近似項的誤差，在第一次估計時校正值 u, v, z 仍爲未知數，無法代入計算。本研究改爲採用觀測值 $\tilde{u}$ $\tilde{v}$, $\tilde{z}$ 來估計。以觀測之 $\tilde{u}$, $\tilde{v}$, $\tilde{z}$ 代入(29)(30)式計算其他轉近似差值，列於表 3 中。此差值表示觀測值不能滿足地轉近似的差誤，亦卽是觀測值不能保持內部一致的程度。故選擇地轉近似項的差誤，必須小於表 3 所列之值，才能滿足地轉近似平衡，而使變分分析能保持高度與風場之內部一致。

由表 1 中合於觀測誤差基本值和小於表 3 所列之值的權重爲 β^2 在 10^{-2}～10^{-1}, 而 γ^2 則在10^{0}～10^{-1} 之間。爲進一步研究各項誤差值在權重調整時如何移轉變化，將此範圍再細分爲10等分，重新求取權重和誤差值，所得之結果在表 3 中。並分析其經校正後的高度場和風場，期在此中能找到一個所需之權重，滿足變分分析的動力約束條件，而其分析場與實際天氣狀況、主觀分析、客觀分析與衛星雲圖相符合，以建立選擇權重的法則，供一般研究和日常作業時使用。

再利用表 2 之值劃成圖 6 (a)～(c)，圖 6 (a) 橫坐標爲 $\tilde{\beta}^2$ 之值，從左往右爲 0^{-1} 到 10^{-2} 分爲 10 等分，縱座標爲 $(\Delta z)_{r.m.s}$ 之值。圖中爲不同 γ^2 值的四條曲線，$(\Delta z)_{r.m.s}$ 之大小受 $\tilde{\beta}^2$ 與 γ^2 幾乎有相同之影響，與分析方程式完全相符。在圖 6 (b) 中，縱座標爲 $(\Delta C)_{r.m.s}$，圖中的四條線已爲直線，表示 $(\Delta C)_{r.m.s}$ 之值完全不受 β^2 之影響，而爲 γ^2 之函數，γ^2 愈大則 $(\Delta C)_{r.m.s}$ 也愈大，反之亦同，此結果亦與分析方程式完全符合。圖 6 (c) 縱坐標爲 $(\Delta G)_{r.m.s}$ 之值，爲比較方便橫坐標仍採用 β^2，隨著 β^2 減少，$(\Delta G)_{r.m.s}$ 有極小的遞減，而隨著 γ^2 的減小，此種遞減率愈來愈大。受 γ^2 之影響則完全成反比。$(\Delta G)_{r.m.s}$ 對於 β^2 之靈敏度較低，推斷其原因係地轉近似項中誤差比例所引起，因式中受 (Δu) 之數量級，卽約束 $k_1\frac{\partial z}{\partial x}$～v, $k_2\frac{\partial z}{\partial y}$～u，而高度之誤差比率約爲 10：6000，速度則爲 2：10，在誤差移轉之過程，較小之高度場會引起比例甚大之風場的誤差，進而使 $(\Delta G)_{r.m.s}$ 之值有甚大之改變，故在選擇權重，必須考慮此一因素。

利用表 2 及圖 6 (a)～(c)，本研究建立選擇權重之方法：首先決定 γ^2 之值，必不能過大以免 $\tilde{\beta}^2$ 對 $(\Delta G)_{r.m.s}$ 之變化影響過小，卽不可選用過小之地轉近似項

誤差值，但其上限又爲表3所限制，可得所須要之 γ^2 值。然後以所選之 γ^2 值用圖 6 (a) 與 6 (b) 以 $(\Delta C)_{r.m.s}$ 和 $(\Delta z)_{r.m.s}$ 基本值決定所須要之 β^2 值。如此則可得一具有合理的各項誤差分佈所須之三權重值。

三、本研究客觀分析場與天氣狀況、主觀分析和 Cressman 客觀分析場之比較

本研究以中央氣象局1975年 6 月10日格林尼治零時的高空定壓層之高度場分析圖作爲先決的比較。其次與主觀分析場和 Cressman 客觀分析場作進一步的驗證，包括高度場和風場。最後再以校正後之風場計算渦度場，比較和主觀分析與客觀分析之異同，決定本研究分析方程式之可靠性，並比較本研究客觀分析場之品質。

氣象局高空層 500 mb 天氣圖爲圖 3 ，本研究所分析得到之 500 mb 層高度場在圖 7 (c)，兩者之高度場非常相似。Cressman 客觀分析場作一綜合之比較，包括型態 (pattern)、位置和强度。爲比較之方便，將主觀分析場、客觀分析場和本研究客觀分析場依高度、風速 x 方向分量場、風速 y 方向分量場排列。圖 7 爲高度場，圖8爲風速的 x 方向分量場，圖9爲風速的 y 方向分量場，註角 a 代表主觀分析，b 代表 Cressman 客觀分析，c 則爲本研究客觀分析場。三種分析場比之結果，彼此非常相似，其中個別的相同和相異處，分別述敍於下：

圖 7 爲三種分析法在 500 mb 定壓層上的高度場，在 500 mb 其等高線的間隔 60 m。

500 mb 層，在型態三種分析大致相仿，中緯槽本研究則較 Cressman 客觀分析更近似於主觀分析。但在高低壓强度上，本研究與 Cressman 客觀分析的結果均弱於主觀分析。對應梅雨鋒的位置則三種分析均相同。在低緯度臺灣南部，本研究與主觀分析均有一封閉高壓，而 Cressman 分析則無。

由以上 500 mb 層之研究，可以發現本研究各高度場之型態與强度均較 Cressman 客觀分析更近似主觀分析。尤其是在低緯地區，與 Cressman 之分析最大差誤達 120 m，而與主觀分析僅差 30 m，故本研究高度場分析已改進了客觀分析的品質。

圖 8 爲三種分析在 500 mb 定壓層上風速 x 方向分量場的分析圖，圖 9 爲 y 方向分量場。風場的分析，在 500 mb，其等風速線的間隔爲 10 m/s。

500 mb 層，本研究與主觀分析之風場較相似，Cressman 客觀分析則在兩個方向分量場上均較高 5 m/S。

以 500 mb 層之分析，本研究與主觀分析正負值中心相差較少，不似 Cressman 客觀分析出現較高或較低之正負值中心，在中高緯度本研究與主觀分析較爲相似，在低緯度地區則與 Cressman 客觀分析較相似，但與主觀分析之平均差異較小。

本研究再進一步以校正之風場求解渦旋度場 (Vorticity)，與主觀分析和 Gressman 客觀分析之觀測風的渦旋度場作比較。先用各節點所求得之校正風速值，以Galerkin 近似法求得各節點上之渦旋度，再內插至圖 3 的網格系統上，分析其等值線和正負中心，其作法與分析高度場相同。

圖10爲三種分析在各定壓層上渦旋度場，註角 a. b. c 分別表示主觀分析場，Cressman 客觀分析場和本研究客觀分析場。渦旋度場的分析，各層均以 2×10^{-5} s^{-1} 爲等值線的間隔。

500 mb 層上，在日本附近的氣旋渦度場，位置較 700 mb 北偏，强度與型態三者相同。中緯槽位置上之反氣旋渦度場，Cressman 客觀分析最高值大過 10×10^{-5} s^{-1}，略較主觀分析與本研究偏高。低緯地區近爲反氣旋渦度場所涵蓋，三種分析均相同，亦與低緯度的高壓系統相符合。

綜觀整個系統，三種分析之渦度場的配置均大致能與槽脊線或高低壓系統的位置相配合，而本研究分析場之型態與强度均與主觀分析較爲近似。

綜合了以上三個階段的比較，本研究在高度場之分析，與實際天氣狀況型態相符合，而强度則高低壓中心值稍不足。然後與主觀分析和 Cressman 客觀分析相比較，不論在高度場、風場和渦度場，均比 Cressman 客觀分析較接近主觀分析之結果。可顯示本研究分析方程式可實際用於分析高空大規模天氣系統，而其結果與用主觀方法分析相差極微，確實改善了現行客觀分析之方法，當可視爲最佳之客觀分析。

肆、結　　論

本研究利用變分原理設計一個可以同時分析高度場和風速場的分析方程式，然後用有限元素法求解。以校正節點上氣象變數之觀測值，使校正後之氣象變數場能滿足約束條件，亦卽使氣象變數之間能維持力學的一致性，而得以完全代表大氣大幅度運動之特性。利用有限元素法做爲數值方法來處理變分客觀分析的問題，則是

本研究一項重要的嘗試，在本文之前尚未有人曾經做過。其特點是㈠以測站直接爲節點，解除固定網格距之限制而不必再虛構有限差分的網格系統。㈡有限元素法通常用變分法或 Galerkin 法得到有限元素方程式，所有的變分客觀分析問題選用有限元素法比較自然，因爲可由變分原理或 Galerkin 近似法直接得到有限元素方程式。由前一章結果顯示本研究之方法不但能適用於分析氣象場，而且較現行作業的客觀分析結果更好，計算速度更快，故使用此種方法必將是氣象學的新趨向。國內現在已有曾（1980）用有限元素法求大氣垂直速度。另外王（1979）用有限元素法以正壓模式預報 500 mb 高度場（私人信函，尚未發表）。

本研究僅作較簡單之假設，即假設高度場和風場在每一個元素內之分佈爲線性的元素函數。若要求更精確之分析場，可考慮將元素函數提高爲二次或三次以上的多項函數，如此更可以符合高度場和風場在每一元素內的分佈型態，對於整個研究範圍，也可以更合於大氣運動分佈之特性。其次可考慮加入溫度的分析，充分的利用觀測得到的資料，因爲溫度場可以代表高度場在垂直方向上的梯度，加入分析可使得到的校正場在水平和垂直方向上均能保持內部的一致性。再者更可考慮加入更多的約束條件，諸如動量方程式、靜水方程式、連續方程式和熱力學方程式等等，進一步的以變分原理校正各種氣象變數場，使這些氣象變數完全滿足原始方程式。

雖然使用有限元素法之變分客觀分析，較現行作業的有限差分客觀分析在建立網格系統是較爲複雜，但如能用有經驗的分析預報人員，以其對於各種天氣型態的認識，來建立有限元素網格系統，反較經計算建立有限差分網格系統容易，而且可以網格系統配合天氣型態，更適於分析氣象變數場，建立數種不同的網格系統以適應隨季節變化的天氣型態，而將這些網格資料存入電腦中以供選擇使用。再者利用此法所須之計算時間，較現行作業化的客觀分析節省許多，更適於氣象單位例行的日常作業化所用。

由本研究個案討論結果顯示，本方法已顯著的改進了客觀分析法所得氣象變數分析場之品質。而且各變數場間也已維持其內部一致之特性，故校正後之氣象變數可作爲氣象數值預報模式之初始值，其預報之結果，必能較現行有限差分法所預報更爲正確。

在數值程式的設計，微分方程式的 Galerkin 近似能自動滿足原方程式所具有的二次守恒律 (quadratic constervation law) (Fix, 1975)， 因此可以用有限元素

法設計數值程式，使滿足原方程式的守恒定律，以抑止在數值預報過程中雜波的產生。而且元素的大小可任意作緩慢變化，因此處理需要粗細網格併用的問題，不會在粗細網格交界處誘導出雜波而影響整個預報場，比有限差分法有效。此外，三角形的二維元素能與不規則的邊界密切吻合，對不規則邊界的問題用有限元素法來處理比較恰當。

以上所述諸點，可作爲繼續研究和發展之方向。

參 考 文 獻

林聰悟，１９７８：私人信函。

胡仲英，１９７７：高空天氣圖客觀分析之研究。大氣科學，第四期，１～１０

曾忠一，１９８０：用有限元素法求大氣垂直速度。大氣科學，第七期，１３～２０

劉玉龍，１９７９：客觀分析程式之驗證。中國文化學院地學研究所碩士學位論文。

Bengtsson, L., 1975: 4-dimensional assimulation of meteorological observations. GARP Publication Series No. 15, WMO-ICSU Joint Organizing Committee, 76pp.

Chung, T. J., 1978: Finite Element Analysis in Fluid Dynamics. McGraw-Hill, New York, 378pp.

Chen, T. J. G. and C. Y. Tsay, 1977: A detailed analysis of a case of Mei-Yu system in the vicinity of Taiwan. Tech. Rept. No. Mei-Yu-601, Dept. of Atmospheric Sci., National Taiwan University, Taipei, Taiwan, 249pp.

Fellipa, C. A., 1975: Solution of linear eq. with skyline stored symmetric matrix. Computer and Structures, 5, 13-29.

Fix, G. J., 1975: Finite element models for ocean circulation problems. SIAM J. Appl. Math., 29, 371-387.

Groll, A., 1975: On the initialization problem- a variational adjustment method. Mon. Wea. Rev. 103, 1089-1103.

Lewis, J. M., 1972: An operational upper air analysis using the veriational method. FNWC Tech. Note No. 72-3, 50pp., Also in Tellus, 24, 514-530.

Melosh, R. J., 1965: Basis for derivation of matrices for the direct stiffness method. J. American institute for Aeronautics and Astronautics, 1, 1631-1637.

Sasaki, Y., 1958: An objective analysis based on the variational method. J. Meteor. Soc. Japan, 36, 77-88.

Sasaki, Y., 1969a: Numerical variational method of analysis and predication. Proc. WNO/IUGG Symposium of Numerical Weather Prediction, Tokyo, Japan, Nov. 26-Dec. 4, 1968, Japan Meteor. Agency, Japan, III 23-25.

Sasaki, Y., 1969b: Proposed inclusion of time variation terms, observational and theoretical, in numerical variational objective analysis. J. Meteor. Soc. Japan, 47, 115-124.

Sasaki, Y., 1970a: Some basic formalisms in numerical variational analysis. Mon. Wea. Rev., 98, 875-883.

Sasaki, Y., 1970b: Numerical variational analysis formulated under the constrains as deterimined by long-wave equations and a low pass filter. Mon. Wea. Rev., 98, 884-898.

Sasaki, Y., 1970c: Numerical variational analysis with weak constraints and application to surface analysis of severe storm gust. Mon. Wea. Rev., 98, 899-910.

Sasaki, Y., 1976: Variational design of finite difference scheme for initial value problem of an integral constraints. J. Comp. Phy., 21, 270-278.

Segerlind, L. J., 1976: Applied Finite Element Analysis. John Wiley, New York, 422pp.

Stephens, J. J., 1971: On the definable scale reduction by simultancous observations, J. Appl. Meteor., 10, 23-25.

Szabo, Barna A., and George C. Lee., 1969: Derivation of stiffness matrix for problem in plane elasticity by Galerkin's method. Inter. J. of Num. Meth. in Eng., 1. 301-310.

Tuner. M. J., R. W. Clough, H. C. Matin, and L. J. Topp, 1956: Stiffness and deflection analysis of complex structure. J. Aero. Sci.,23, 805-824.

Zienkiewicz, O. C., 1971: The Finite Element Method in Engineering Science. McGraw-Hill, London, 1971, 521pp.

表 1. 500 mb 權重與各項差誤值 (a) ΔC (b) ΔZ (c) ΔG

(a) ΔC

$\tilde{\beta}^2$ \ γ^2	10^4	10^3	10^2	10^1	10^0	10^{-1}	10^{-2}	10^{-3}	10^{-4}
10^4	8.8	8.8	8.7	8.0	4.4	0.8	0.08	0.008	0.0008
10^3	8.8	8.8	8.7	8.0	4.4	0.8	0.08	0.008	0.0008
10^2	8.8	8.8	8.7	8.0	4.4	0.8	0.08	0.008	0.0008
10^1	8.4	8.4	8.3	7.6	4.3	0.8	0.08	0.008	0.0008
10^0	7.3	7.3	7.2	6.7	3.8	0.7	0.08	0.008	0.0008
10^{-1}	6.5	6.5	6.4	5.9	3.3	0.6	0.08	0.008	0.0008
10^{-2}	6.5	6.5	6.4	5.9	3.2	0.6	0.07	0.008	0.0008
10^{-3}	6.6	6.6	6.6	6.0	3.3	0.6	0.06	0.007	0.0008
10^{-4}	6.7	6.7	6.6	6.0	3.3	0.6	0.06	0.006	0.0007

(b) ΔZ

$\tilde{\beta}^2$ \ γ^2	10^4	10^3	10^2	10^1	10^0	10^{-1}	10^{-2}	10^{-3}	10^{-4}
10^4	0.001	0.001	0.001	0.001	0.001	0.0006	0.0006	0.0006	0.0006
10^3	0.01	0.01	0.01	0.01	0.01	0.001	0.0006	0.0006	0.0006
10^2	0.15	0.16	0.16	0.14	0.08	0.015	0.001	0.0006	0.0006
10^1	1.2	1.2	1.2	1.1	0.7	0.14	0.01	0.002	0.0006
10^0	4.9	4.9	4.9	4.7	3.5	1.1	0.16	0.016	0.002
10^{-1}	11.7	11.7	11.7	11.4	9.3	4.7	1.2	0.16	0.01
10^{-2}	20.3	20.3	20.3	20.0	18.1	11.4	4.9	1.2	0.16
10^{-3}	23.3	23.3	23.3	23.2	22.9	20.0	11.7	4.9	1.2
10^{-4}	23.7	23.7	23.7	23.7	23.6	23.2	20.3	11.9	4.9

(c) ΔG

$\tilde{\beta}^2$ \ γ^2	10^4	10^3	10^2	10^1	10^0	10^{-1}	10^{-2}	10^{-3}	10^{-4}
10^4	10.9	10.9	10.9	10.9	11.6	13.3	13.8	13.8	13.8
10^3	10.9	10.9	10.9	10.9	11.6	13.3	13.8	13.8	13.8
10^2	10.7	10.7	10.7	10.7	11.5	13.3	13.8	13.8	13.8
10^1	9.2	9.2	9.2	9.3	10.6	13.1	13.8	13.8	13.8
10^0	5.9	5.9	5.9	6.0	7.6	11.8	13.5	13.8	13.8
10^{-1}	4.2	4.2	4.2	4.3	5.4	8.7	12.1	13.6	13.8
10^{-2}	3.8	3.8	3.8	3.8	4.8	7.0	7.4	12.1	13.6
10^{-3}	3.7	3.7	3.7	3.7	4.8	6.8	7.4	9.1	12.1
10^{-4}	3.7	3.7	3.7	3.7	4.8	6.8	7.2	7.4	9.1

表 2. 500 mb 選擇權重參考之差誤值 (a) ΔC (b) ΔZ (c) ΔG

(a) ΔC

γ^2 / $\tilde{\beta}^2$	1.0	0.9	0.8	0.7	0.6	0.5	0.4	0.3	0.2	0.1
0.1	3.32	3.16	2.97	2.76	2.53	2.26	1.96	1.60	1.18	0.68
0.09	3.31	3.14	2.95	2.74	2.51	2.25	1.95	1.60	1.17	0.67
0.08	3.29	3.12	2.94	2.73	2.50	2.24	1.93	1.58	1.16	0.66
0.07	3.27	3.10	2.92	2.71	2.50	2.20	1.92	1.57	1.15	0.65
0.06	3.25	3.09	2.90	2.70	2.47	2.20	1.90	1.55	1.14	0.64
0.05	3.23	2.07	2.89	2.68	2.45	2.19	1.89	1.54	1.13	0.64
0.04	3.21	3.05	2.87	2.66	2.43	2.17	1.87	1.52	1.12	0.63
0.03	3.20	3.03	2.85	2.65	2.41	2.15	1.85	1.51	1.10	0.62
0.02	3.19	3.02	2.84	2.63	2.39	2.13	1.83	1.49	1.09	0.61
0.01	3.21	3.03	2.85	2.63	2.39	2.13	1.82	1.47	1.07	0.59

(b) ΔZ

γ^2 / $\tilde{\beta}^2$	1.0	0.9	0.8	0.7	0.6	0.5	0.4	0.3	0.2	0.1
0.1	9.3	9.2	8.9	8.7	8.4	8.1	7.6	7.0	6.2	4.7
0.09	9.7	9.5	9.3	9.0	8.7	8.4	7.9	7.3	6.4	4.9
0.08	10.0	9.9	9.7	9.4	9.1	8.7	8.3	7.6	6.7	5.2
0.07	10.5	10.3	10.1	9.9	9.6	9.2	8.7	8.0	7.1	5.5
0.06	11.1	10.9	10.6	10.4	10.0	9.7	9.2	8.5	7.5	5.9
0.05	11.7	11.6	11.3	11.0	10.7	10.3	9.8	9.1	8.1	6.4
0.04	12.6	12.4	12.1	11.9	11.5	11.1	10.5	9.8	8.7	6.9
0.03	13.7	13.5	13.3	13.0	12.6	12.1	11.6	10.8	9.7	7.8
0.02	15.4	15.2	14.9	14.6	14.2	13.8	13.1	12.3	11.1	9.0
0.01	18.1	18.0	17.7	17.4	17.1	16.6	6.0	15.1	13.8	11.4

(c) ΔG

γ^2 / $\tilde{\beta}^2$	1.0	0.9	0.8	0.7	0.6	0.5	0.4	0.3	0.2	0.1
0.1	5.40	5.5	5.7	5.8	6.0	6.3	6.6	7.1	7.7	8.7
0.09	5.34	5.5	5.6	5.8	6.0	6.2	6.6	7.0	7.6	8.6
0.08	5.29	5.4	5.5	5.7	5.9	6.2	6.5	6.9	7.5	8.5
0.07	5.24	5.4	5.5	5.7	5.9	6.1	6.4	6.8	7.3	8.3
0.06	5.18	5.3	5.4	5.6	5.8	6.0	6.3	6.7	7.2	8.1
0.05	15.2	5.2	5.4	5.6	5.7	5.9	6.2	6.6	7.1	8.0
0.04	5.05	5.2	5.3	5.5	5.6	5.9	6.1	6.5	7.0	7.8
0.03	5.00	5.1	5.2	5.4	5.5	5.8	6.0	6.4	6.8	7.6
0.02	4.91	5.0	5.1	5.3	5.5	5.8	5.9	6.2	6.6	7.3
0.01	4.83	4.9	5.1	5.2	5.4	5.7	5.8	6.1	6.5	7.0

表 3. 各定壓層第一次用觀測值估計地轉近似項差誤值

	850 mb	700 mb	500 mb	300 mb	200 mb
$(\Delta G_1)_{r\cdot m\cdot s}$	4.80	5.6	9.7	14.3	19.1
$(\Delta G_2)_{r\cdot m\cdot s}$	5.90	5.6	9.8	15.3	19.5
$(\Delta G)_{r\cdot m\cdot s}$	7.6	7.9	13.8	20.9	27.3

表 4. 使用本研究選用之權重各層各項之差誤值

(在 $\tilde{\alpha}^2=1.0$, $\tilde{\beta}^2=0.02$, $\gamma^2=0.2$)

	$(\Delta u)_{r\cdot m\cdot s}$	$(\Delta v)_{r\cdot m\cdot s}$	$(\Delta c)_{r\cdot m\cdot s}$	$(\Delta z)_{r\cdot m\cdot s}$	$(\Delta G)_{1r\cdot m\cdot s}$	$(\Delta G_2)_{r\cdot m\cdot s}$	$(\Delta G)_{r\cdot m\cdot s}$
850 mb	1.08	0.98	1.47	9.75	2.82	3.18	4.25
700 mb	0.96	0.96	1.36	9.93	3.13	2.93	4.29
500 mb	1.36	1.33	1.90	14.76	4.00	4.36	5.92
300 mb	1.78	1.85	2.57	18.42	6.41	6.26	1.96
200 mb	2.16	2.36	3.20	22.15	7.62	7.78	10.91

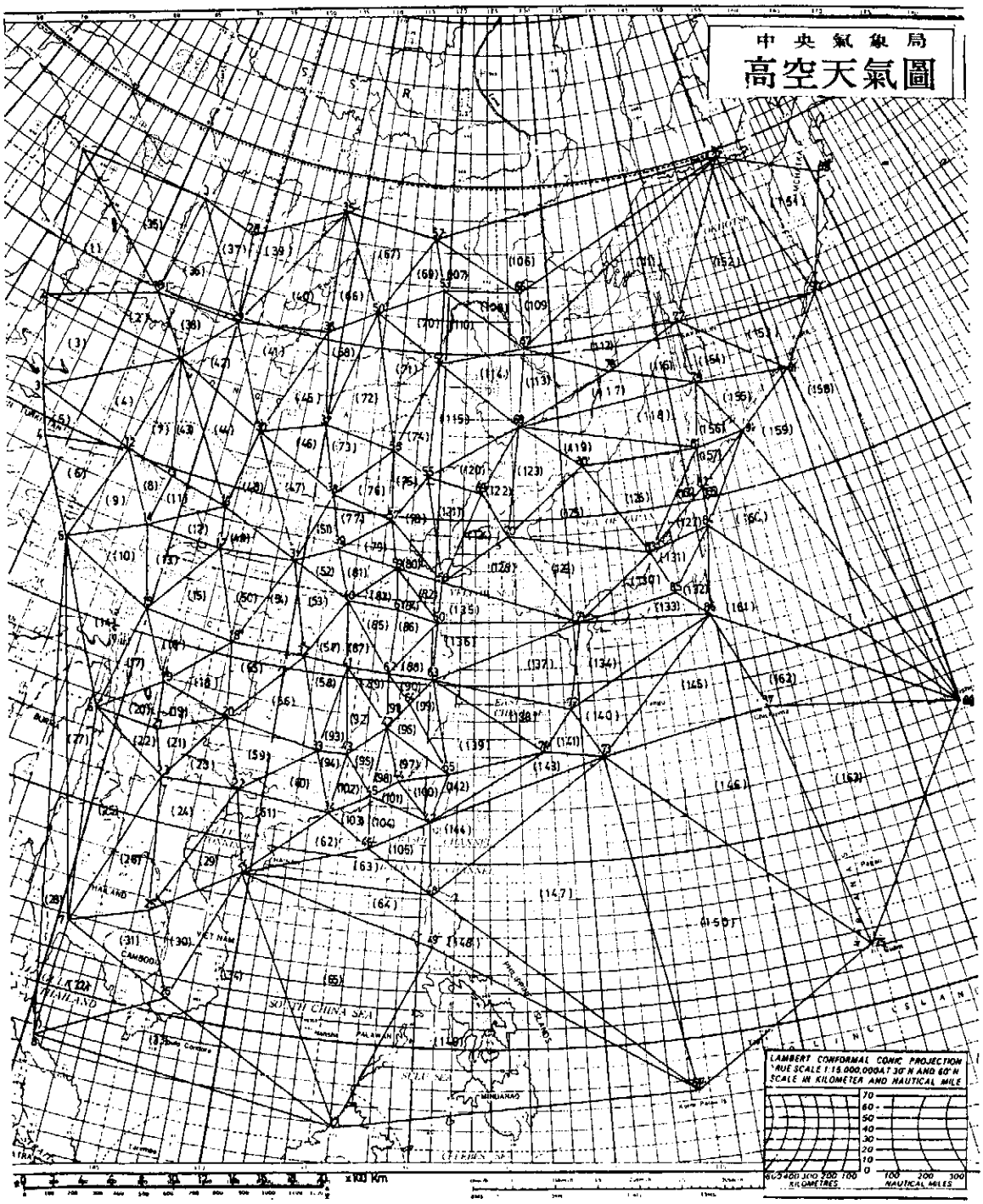

圖 1. 本研究所使用之有限元素網格系統，數字代表節點號碼，數字加小括號代表元素號碼

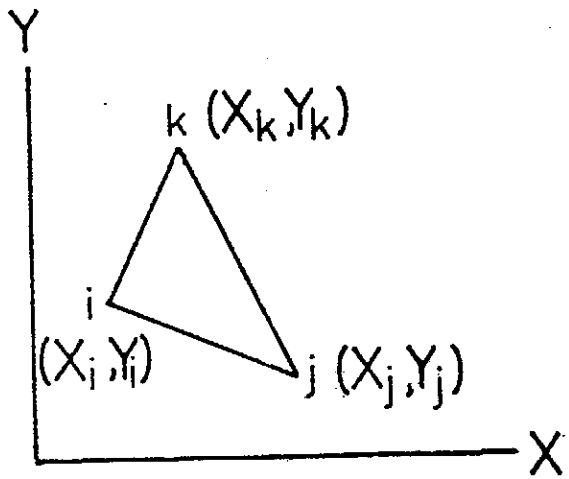

圖 2. 二維線性三角形元素

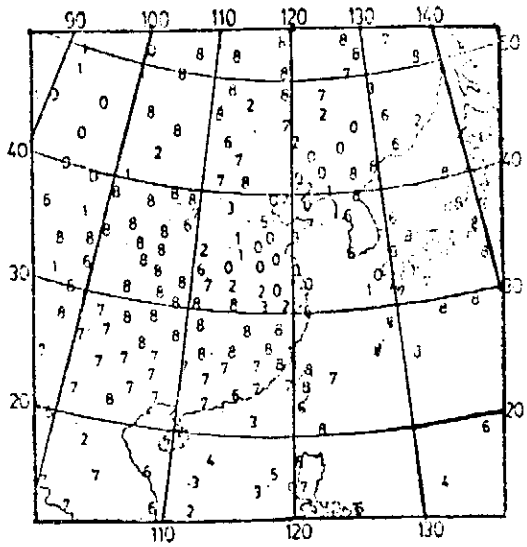

圖 4. 地面測站雲量記錄

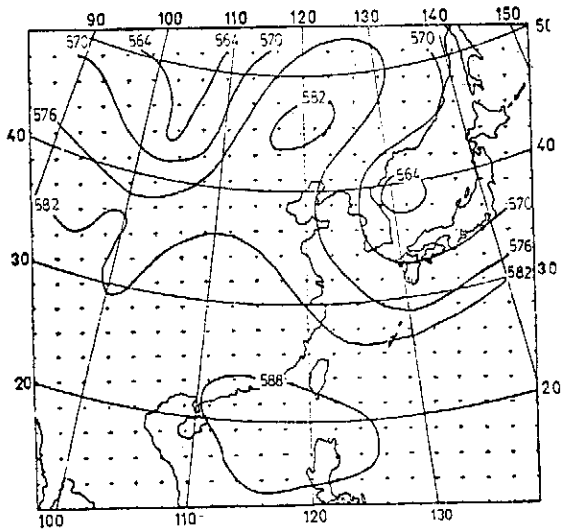

圖 3. 實際高空 500 mb 高度場，（單位：×10 m）

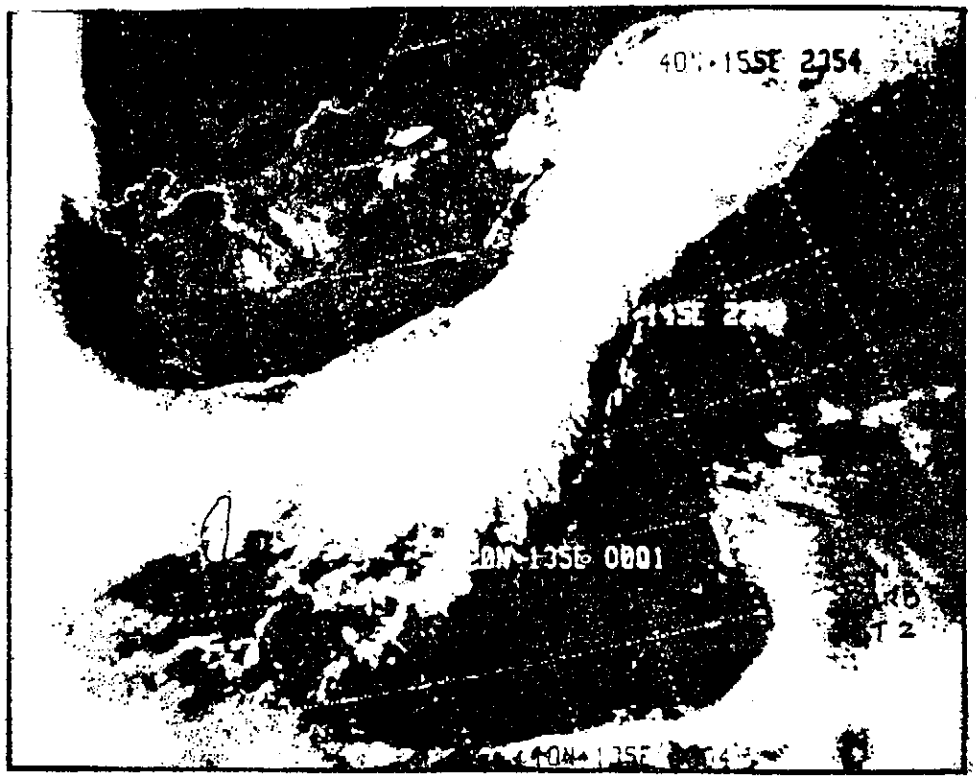

圖 5. NOAA-4 紅外光衛星照片，白色虛線表示經緯度以及海岸線，臺灣的位置用實線表示

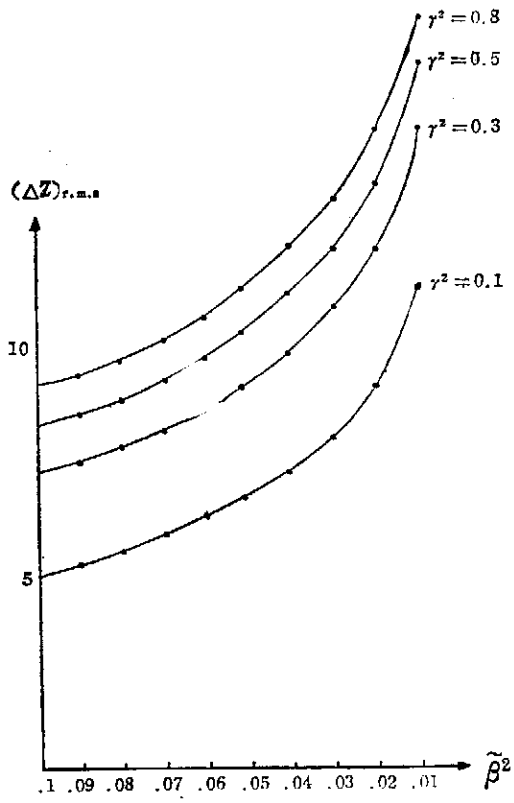

圖 6. 500 mb 選擇權重之參考圖
(a) ΔZ (b) ΔC (c) ΔG

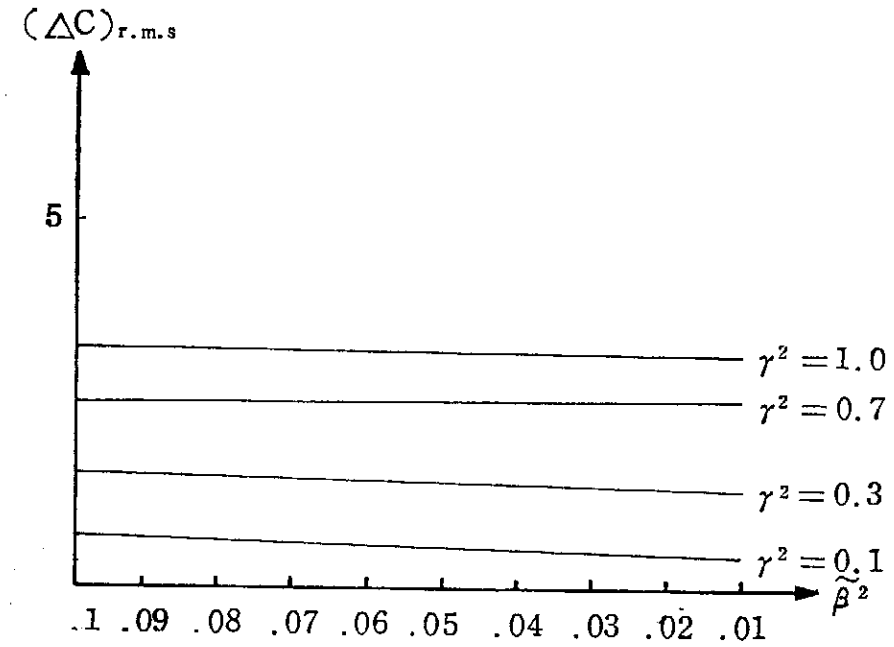
(△C)r.m.s
5
γ² =1.0
γ² =0.7
γ² =0.3
γ² =0.1
β̃²
.1 .09 .08 .07 .06 .05 .04 .03 .02 .01

(b)

(b)

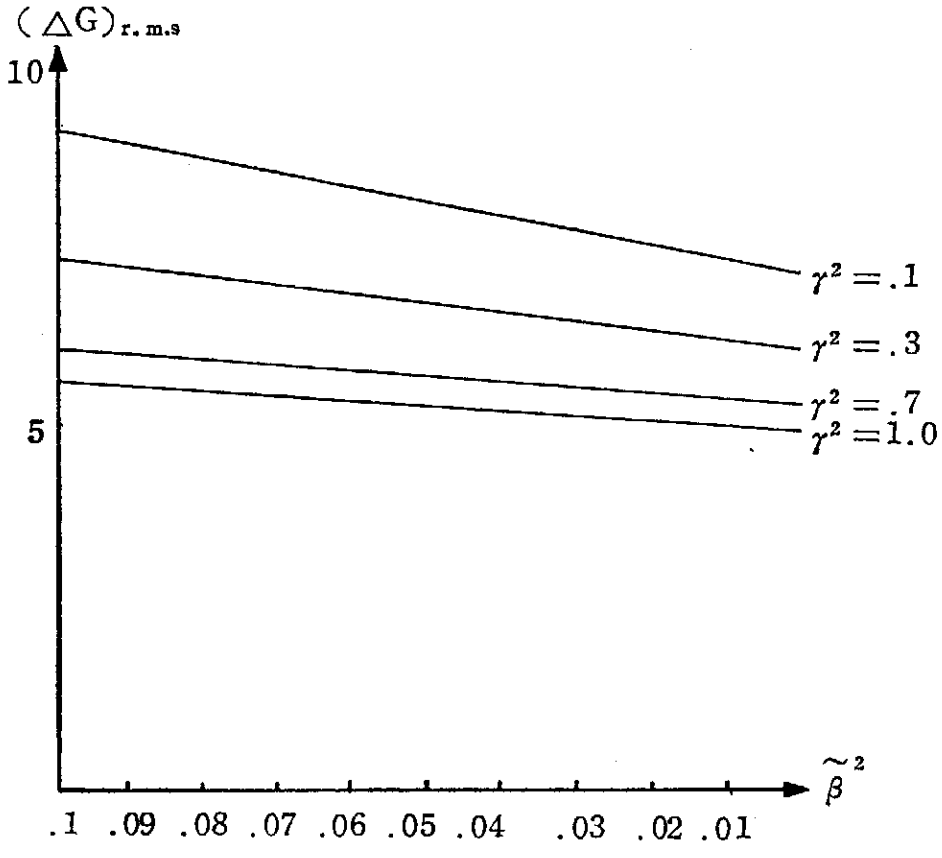
(△G)r.m.s
10
5
γ² =.1
γ² =.3
γ² =.7
γ² =1.0
β̃²
.1 .09 .08 .07 .06 .05 .04 .03 .02 .01

(c)

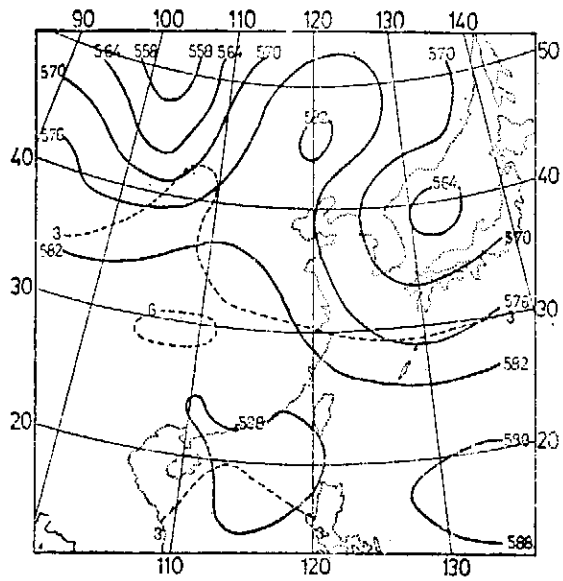

(a)

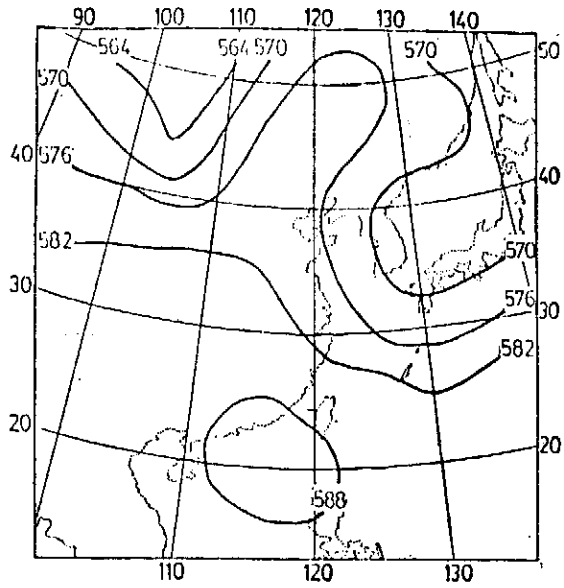

(c)

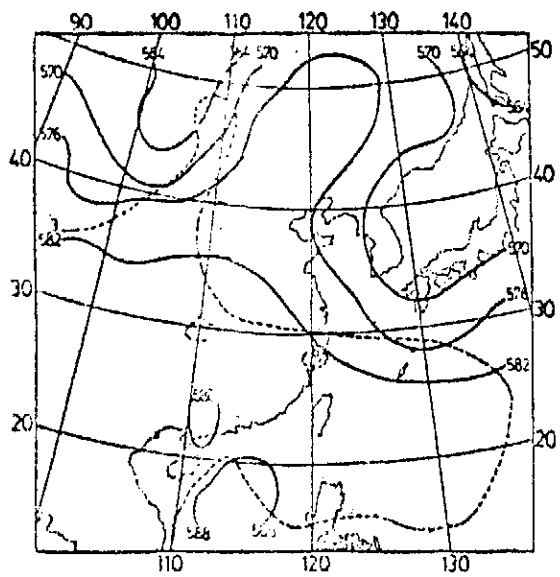

(b)

圖 7. 500 mb 高度場分析圖，（單位：×10m）

(a) 爲主觀分析

(b) 爲 Cressman 客觀分析

(c) 爲本研究分析結果

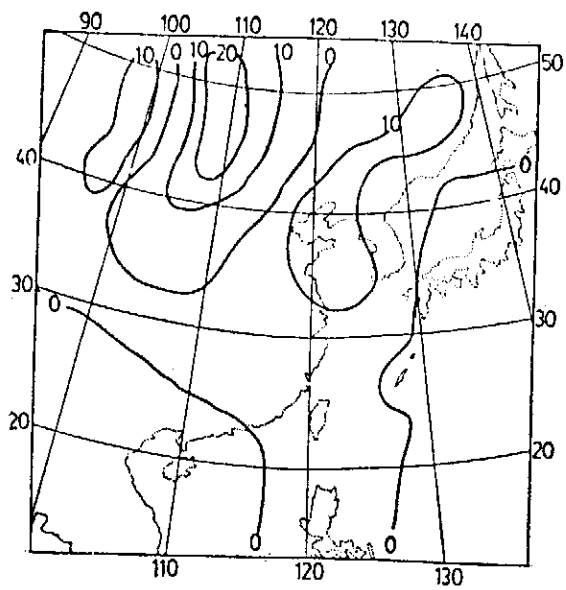

(a)

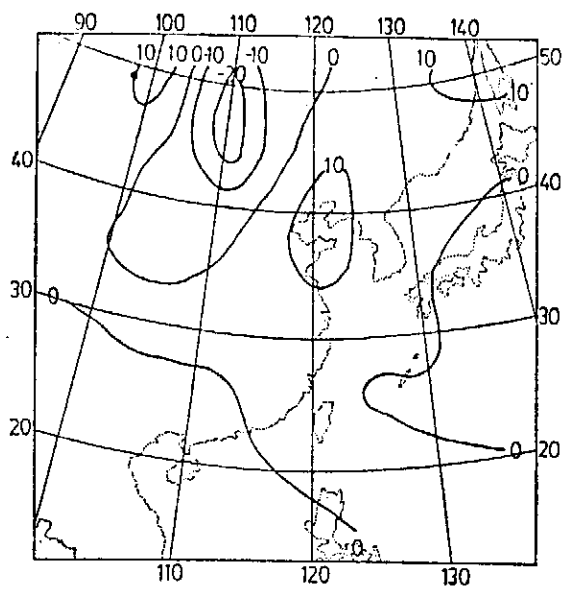

(c)

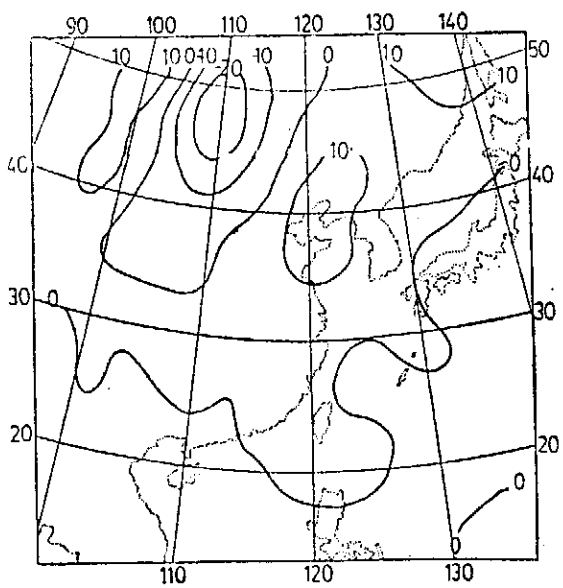

(b)

圖8. 500 mb x- 分量風速場，（單位：m/s）

(a) 爲主觀分析

(b) 爲 Cressman 客觀分析

(c) 爲本研究分析結果

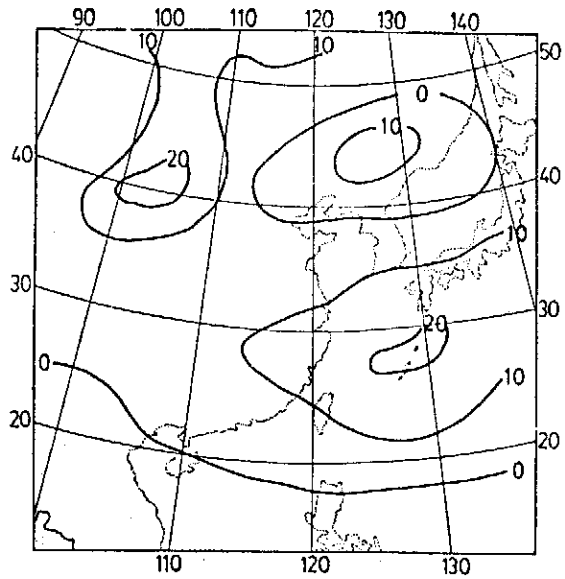

(a)

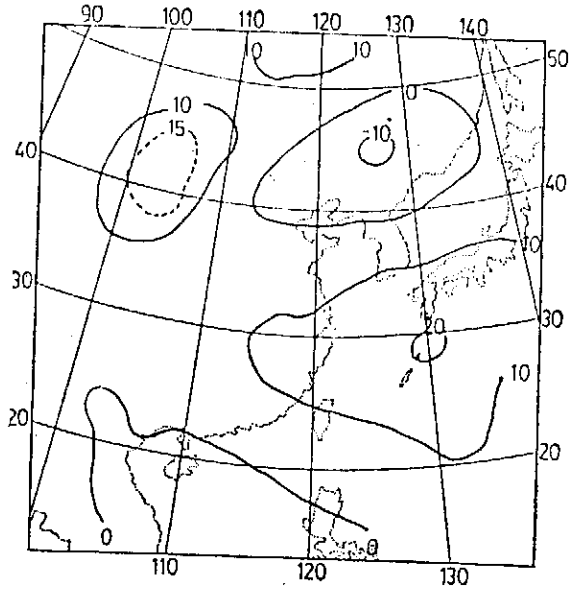

(c)

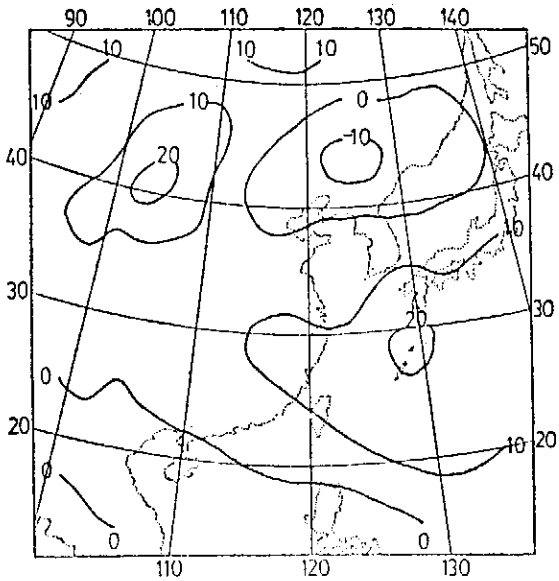

(b)

圖 9. 500 mb y-分量速度場 (單位：m/s)

(a) 爲主觀分析

(b) 爲 Cressman 客觀分析

(c) 爲本研究分析結果

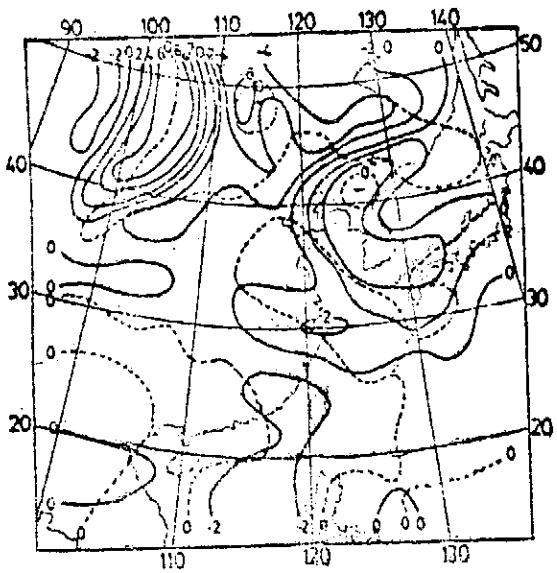

(a)

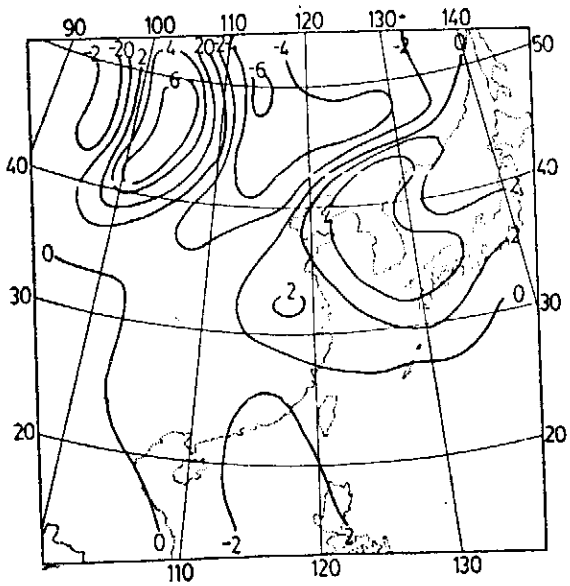

(c)

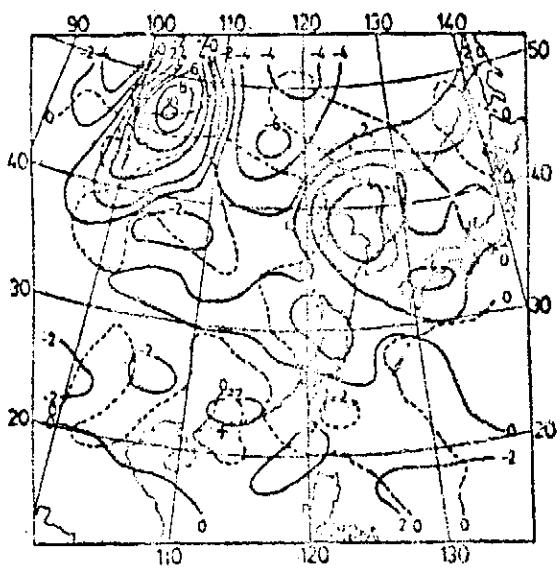

(b)

圖10. 500 mb 渦度場 (單位：$\times 10^{-5}S^{-1}$)

(a) 爲主觀分析

(b) Cressman 客觀分析

(c) 爲本研究分析結果

空氣污染之聚合平均佳化理論與應用

梁　文　傑

中央研究院物理研究所

國立臺灣大學機械工程研究所

楊　佩　華

國立臺灣大學環境工程研究所

摘　　要

本文利用佳化評估法與聚合平均近似法對高雄地區二氧化硫污染作一評估。佳化評估法乃利用變微分法結合擴散模式與測站資料的客觀分析法，能提供較一般評估法更具代表性的污染濃度分佈型態，聚合平均近似法則將約等強度的排放源聚爲一組，以簡單的算術平均值執行計算，能有效的減少計算機時間，尤其對排放源相當多的地區更爲適用。

本文因高雄地區排放源極多，且資料不全，全部排放源納入考慮實不可行，故先分區選取79個排放源，以兼顧全域的污染濃度分佈型態，再用觀測值修正所取排放源强度，來接近實際污染物排放總量，接著就用修正的79個排放源進行聚合平均佳化法的七種評估程序，探討聚合平均佳化法的特性及其可行性。文中分別討論其結果、比較誤差並對各種現象的原因加以研究。評估結果顯示聚合平均佳化法應用於高雄地區極爲成功，對利用數學模式評估空氣污染濃度分佈，本法提供了一簡單且代表性高的可行途徑，極具實用價值。

壹、前　　言

空氣是人類生存的基本要素，人類必須自空氣中吸取氧而將氧化作用所產生的二氧化碳呼出體外。由於吹風、下雨、沉澱、化學作用以及植物的吸收，人類呼出的廢氣理應很容易的被稀釋與排除。然而，隨著人類文明的進展，工業時代的來臨，工廠與車輛遍佈城市與鄉鎮的大街小巷，它們同人類一樣必須自空氣中攝取氧以供氧化、燃燒及其它工業過程之用，而將產生的廢氣（包括氣體與固體）排至大氣中。可是，由於它們驚人的排放量，造成的污染物無法被迅速的稀釋與排除，使得這些污染物所帶來的不良影響日趨嚴重，而城市與工業區的污染問題便是其中最爲顯著的例子。

城市與工業區的污染源包括有點源、線源與面源三類，大工廠可視爲點源污染，而小工廠因數目太多，若對每一個污染源的污染情形各別計算殊不經濟，一般皆取其總污染量除以總面積而將之視爲面污染源。此外，車輛的污染可視公路、鐵路（或地下鐵道與隧道）等爲線污染源。城市污染問題首先在於瞭解市區現在與將來可能的污染程度（亦即求取現在或預測將來的污染物分佈圖），以作爲都市計劃或污染程度控制的依據。求得污染物濃度分佈的方法一般可分爲兩積，第一種是在選定的各量測點實際量測空氣中污染物的濃度，並據之作將來濃度值的推測。第二種是利用數學模式將所有污染源的污染情形算出，並據此繪出城市現在與將來可能的濃度分佈曲線。理論上說，如果兩種方法都很理想，所求得的結果應該一致。但事實上由於量測與數學模式所牽涉到的許多問題，使得兩者間出入頗大。就以第一種方法來說，量測地點不同，其結果大不相同，使得量測值的意義不易確定。譬如，吹東風時（風由東向西吹），若測站在煙囪的東邊，則量得的濃度可能爲零。根據 Goldstein 等人[1] 藉各測站二氧化硫濃度的相關係數的研究，指出由一測站所測得的觀測值不一定可代表其周圍的污染情況。 Bryan[2]指出，若要測知一地區的污染情形每 0.65平方公里就需設一個測站。可是限於經濟與人力，實際作業下測站的數目顯然無法滿足如此的要求，使得實際量測所繪出的濃度曲線無法眞實的反映出量測區域的污染狀況。因此各國各大都市與工業區都以第二種方法（數學模式）來作污染程度的評估與預報，而第一種方法的結果僅用來作線性的統計校正（線性回歸）。但是污染源數目及每一時刻的排放量都無法準確的知道，使得模式的計算不易精確，更由於氣象資料、大氣紊流、都市地形與局部流動的複雜性、數值模式與數值方法等的誤差，經常使計算結果與眞實情況出入頗大。換句話說，求取城市污染物濃度分佈曲線的二種方法雖然都能反映部份的眞實狀況，却也都包含相當程度的誤差。因此如何充分利用數學模式與量測的所有訊息 (Information) 以獲取最有代表性的結果，顯然是一件極爲重要的事情。

Heimbach 與 Sasaki[3] 首先將變微分法 (Calculus of Variation) 引用到空氣污染的評估上，佳化 (Optimize) 排放源資料以提高觀測資料的一致性與代表性。然而， Heimbach 與 Sasaki 的方法僅限於測站數目多於污染源的數目，但在實際情況下污染源必遠多於測站的數目。更有進者，將此法應用於實際資料時，所算出污染源的佳化排放源有許多負值出現，就所試的各種結果顯示約有二分之一的污染

源其佳化值爲負值，使得污染源附近的佳化濃度值爲負值[4]，此種現象顯然極不合理。

梁[5]利用變微分法發展出兩種空氣污染評估的佳化理論(Optimization Theory)，分別爲强勢佳化理論與弱勢佳化理論。前者要求佳化值完全滿足擴散模式，後者只要求佳化值儘量滿足擴散模式。此種佳化理論可適用於任何測站與污染源數目，並使污染源的佳化排放值保持正值，不致發生 Heimbach 與 Sasaki 佳化方法的不合理現象。梁與李[4]和梁與李[6]分別應用强勢佳化理論於高雄地區二氧化硫與臺北市一氧化碳的污染評估，結果顯示可信性高，爲相當優秀的佳化理論。

此外，由於受到人力、物力、時間與知識的限制，作爲模式評估必須的氣象狀況、排放源及測站資訊的獲得均無法足够精確。且鑑於空氣污染日益嚴重，模式評估在目前急需應用於各都市及鄉鎮以建立空氣污染控制的基礎。因此，如何發展出一種簡化複雜模式計算的方法，於充分利用所有可得的資訊下，有效的減少計算時間，且能得到相當程度代表性的污染濃度分佈，對污染狀態簡單而迅速的得到適當瞭解，應屬當務之急。

Gustafson[7] 曾嘗試聚合平均近似法 (Aggregated-averaged Approximation Method) 的概念，以期達到此一目的。所謂聚合平均近似法，乃將强度相近的排放源聚爲同一組，以簡單的算術平均值代替此組各排放源强度以執行計算，可簡化大量且繁複（尤其對排放源極多情況下）的運算工作，計算機時間 (Computer Time) 可因此有效的節省。然而，Gustafson 爲使聚合排放源(Aggregated Source)代入模式計算後的測站模式值等於實測值，數值佳化法產生的三種方程式系統，除測站數目等於聚合排放源數目（稱 Even-determined System)[7]的情形有準確解 (Exact Solution) 外，不足擬定系統[5] (Under-determined System) 及過度擬定系統[5] (Over-determined System) 均有實際上應用的困難。前者測站數目少於聚合排放源數目的不足擬定系統，一般而言，具有無窮多個解，其中任何一解均能滿足該系統，此時方程式系統實爲不恰當配置系統[5] (Ill-posed System)。後者測站數目多於聚合排放源數目的過度擬定系統則陷於與 Heimbach 與 Sasaki 變分佳化法相同的困境中；即實際上測站數目大都少於排放源數目（分組數雖然可分到較測站數少，但又成爲不足擬定系統），且實際應用時，所算出污染源的佳化值有許多負值出現，使得污染源附近的佳化濃度值亦爲負值。由於分組後排放源數目減少，

各排放源的影響更形重大，則此種不合理的現象將會變得更加强烈與明顯。因此 Gustafson 假設一污染狀況作模擬所得結果不具代表性，當在意料之中。

本文嘗試將梁之强勢佳化理論與 Gustafson 之聚合平均近似法概念結合成爲聚合平均佳化法，使能充分發揮二者的特點；即不但能够節省大量計算機時間，並使結果不致發生不合理情形。此外，聚合平均近似法取平均值計算，所預期網格點濃度雖與不分組情形有所差異，在一般情形下，變動情形應該不大，污染濃度分佈曲線也應能保持未分組的型態（Pattern）。因此，本文應用於高雄地區二氧化硫污染評估的可行性是可預期的。文中對聚合平均佳化法應用於高雄地區的結果作詳盡的討論，以探討本法的特性及可行性，可作爲日後實際應用及繼續研究的參考。

本文中污染物以二氧化硫爲研究對象，因二氧化硫在高雄地區爲害最烈，且主要來自大量燃燒石化燃料的點源污染，符合本文點源擴散模式的使用。二氧化硫可作爲高雄地區空氣污染的良好指標，對其污染狀況的瞭解將極有助於高雄地區空氣污染的控制。

貳、佳化評估法、聚合平均近似法及聚合平均佳化法

一、佳化評估法

對已獲得若干污染濃度地面量測資料的地區，用數學模式評估環境空氣品質時，可選用適當的擴散模式，以量測資料爲校正條件，二者結合調整而獲得更具一致性與代表性的污染濃度分佈型態。

本文應用梁[5]所發展的强勢佳化理論，即求取完全滿足〔2〕式而使〔1〕式之誤差汎函數爲最小的佳化排放源强度（Optimized Source Strength）。

$$I=\frac{\sum_{i=1}^{n}(\hat{c}_i-\tilde{c}_i)^2}{\sum_{i=1}^{n}\tilde{c}_i^{\,2}}+\beta^*\frac{\sum_{j=1}^{N}(\hat{q}_j-\tilde{q}_j)^2}{\sum_{j=1}^{N}\tilde{q}_j^{\,2}}, \qquad 〔1〕$$

$$c_i=\sum_{k=1}^{N}v_{ki}q_k \quad (\text{或}c_i=\sum_{k=1}^{N}v_{ik}{}^{T}q_k), \qquad 〔2〕$$

式中　N：排放源數目，

n：測站數目，

$\hat{q}_j$：佳化排放源强度，　　q_k：泛指排放源强度，

$\tilde{q}_j$：排放源强度實測值，　　c_i：泛指計算點濃度值，

$\hat{c}_i$：佳化排放源經模式計算之測站濃度，

$\tilde{c}_i$：測站實測值，

v_{ki}：污染源N對測站 i 之擴散函數 (Dispersion Function)，

〔1〕式中的 β^* 可調整使佳化值全爲合理的正值。〔1〕式整理得：

$$\sum_{i=1}^{n}\tilde{c}_i^2\times I=\sum_{i=1}^{n}(\hat{c}_i-\tilde{c}_i)^2+\beta\sum_{j=1}^{N}(\hat{q}_j-\tilde{q}_j)^2,$$

式中
$$\beta=\frac{\sum_{i=1}^{n}\tilde{c}_i^2}{\sum_{j=1}^{N}\tilde{q}_j^2}\beta^*,$$

〔1〕式佳化值經導出爲[4]：

$$\hat{q}=(vv^T+\beta I)^{-1}(\beta\tilde{q}+v\tilde{c})。 \qquad 〔3〕$$

若再考慮污染物質量守恒關係 (Conservation of Mass)，即各測站觀測值總和等於各測站模式值總和：

$$\sum_{i=1}^{n}\hat{c}_i=\sum_{i=1}^{n}\tilde{c}_i. \qquad 〔4〕$$

則由變分法知，爲使〔1〕式最小且滿足〔4〕式條件可介入一未知參數 λ (Lagrange's Multiplier) 使得下式爲最小

$$\sum_{i=1}^{n}\tilde{c}_i^2\times I=\sum_{i=1}^{n}(\hat{c}_i-\tilde{c}_i)^2+\beta\sum_{j=1}^{N}(\hat{q}_j-\tilde{q}_j)^2+\lambda(\hat{c}_i-\tilde{c}_i).$$

上式取變微分並將〔2〕式代入得

$$\frac{\sum_{i=1}^{n}\tilde{c}_i^2\times\delta I}{2}=\sum_{k=1}^{N}\delta q_k[(\sum_{i=1}^{n}(\hat{c}_i-\tilde{c}_i)v_{ik}^T+\beta(\hat{q}_k-\tilde{q}_k)+2\lambda\sum_{i=1}^{n}v_{ik}^T].$$

故
$$\sum_{i=1}^{n}(\hat{c}_i-\tilde{c}_i)v_{ik}^T+\beta(\hat{q}_k-\tilde{q}_k)+2\lambda\sum_{i=1}^{n}v_{ik}^T=0$$

對每一 k。上式整理後得：

$$\sum_{i=1}^{n}(\sum_{j=1}^{N}v_{ki}v_{ij}^T\hat{q}_j-v_{ki}\tilde{c}_i)+\beta(\hat{q}_k-\tilde{q}_k)+2\lambda V_k=0，對每一 k， \qquad 〔5〕$$

式中　$V_k=\sum_{i=1}^{n}v_{ik}^T=\sum_{i=1}^{n}v_{ki}$.

令 $v=[v_{ki}]$，$v^T=[v_{ik}{}^T]$，$\hat{q}=[\hat{q}_{ji}]$，

$\tilde{q}=[\tilde{q}_{ji}]$，$\hat{c}=[\hat{c}_{i1}]$，$\tilde{c}=[\tilde{c}_{i1}]$，

$V=[V_{k1}]$，則〔5〕式可寫爲：

$$vv^T\hat{q}-v\tilde{c}+\beta(\hat{q}-\tilde{q})+2\lambda V=0,$$

或
$$\hat{q}=(vv^T+\beta I)^{-1}\ (v\tilde{c}+\beta\tilde{q}-2\lambda V), \qquad 〔6〕$$

式中 I 爲單位矩陣。將〔6〕式代入〔4〕式可得：

$$\lambda=\frac{\|v^T(vv^T+\beta I)^{-1}\ (v\tilde{c}+\beta\tilde{q})\|-\|\tilde{c}\|}{2\|v^T(vv^T+\beta I)^{-1}V\|}, \qquad 〔7〕$$

式中 ‖ ‖ 表示其中矩陣的元素和。將〔7〕3式代入〔6〕式中得佳化排放源强度，其較〔3〕式多考慮質量守恒關係，即

$$\hat{q}=(vv^T+\beta I)^{-1}\ [v\tilde{c}+\beta\tilde{q}-$$
$$\left(\frac{\|v^T(vv^T+\beta I)^{-1}\ (v\tilde{c}+\beta\tilde{q})\|-\|\tilde{c}\|}{\|v^T(vv^T+\beta I)^{-1}V\|}\right)V]. \qquad 〔8〕$$

將 $\hat{q}$ 代入〔2〕式得：

$$\hat{c}=v^T\hat{q}, \qquad 〔9〕$$

此即佳化濃度值。

二、聚合平均近似法

假設影響污染物擴散的因素（如氣象狀況、排放源强度）爲由不同準平衡狀態（Quasi-equilibrium State）的時間序列所構成[8]，且污染物爲化學惰性者，則對任何一位置 p，各污染源所造成的污染物濃度影響應可疊合相加（Superposition），總濃度爲

$$c_p=\sum_{j=1}^{N}q_jv_{jp}, \qquad 〔10〕$$

式中 N：排放源數目，

q_j：排放源强度，

v_{jp}：j 排放源單位强度對位置 p 所造成的污染濃度，即擴散函數（Dispersion Function）

即對每一所欲求位置 p 之濃度均須考慮N個排放源的影響，如N相當大，則計算甚爲浩繁。現將强度相近的排放源合爲一組，以其算術平均值代替之，則可聚成 n 個聚合排放源（r＝1, 2,……, n, n＜N）（圖（一）表示分組的示意情形），而可以下式表示：

$$c_p=\sum_{r=1}^{n}c_{rp} \qquad 〔11〕$$

其中

$$c_{rp}=\sum_{j=J_{r-1}+1}^{J_r} q_j v_{jp}$$

$$\approx \bar{q}_p \sum_{j=J_{r-1}+1}^{j_r} v_{jp}\,, \qquad 〔12〕$$

式中

$$\bar{q}_r=\sum_{j=J_{r-1}+1}^{J_r} q_j/(J_r-J_{r-1})\,.$$

以 $v_{rp}=\sum_{J_{r-1}+1}^{J_r} v_{jp}$ 代入〔12〕式則

$$c_{rp}\approx \bar{q}_r\ v_{rp}\,, \qquad 〔13〕$$

$$=Q_r\ v_{rp}/J_r-J_{r-1}\,, \qquad 〔14〕$$

式中

$$Q_r=\sum_{j=J_{r-1}+1}^{J_r} q_j\,。$$

以 $\bar{v}_{rp}=v_{rp}/J_r-J_{r-1}$ 代入〔14〕式得

$$c_{rp}\approx Q_r\ \bar{v}_{rp}\ 。 \qquad 〔15〕$$

將〔13〕及〔15〕式分別代入〔11〕式得下二式：

$$c_p\approx\sum_{r=1}^{n}\bar{q}_r\ v_{rp}\,, \qquad 〔16〕$$

$$=\sum_{r=1}^{n}Q_r\ \bar{v}_{rp}\,. \qquad 〔17〕$$

式中 $\bar{q}_r$：r 組中排放源强度平均值，

$\bar{v}_{rp}$：r 組中排放源强度平均值每一單位强度對位置 p 所造成的濃度，

Q_r：r 組中排放源强度和，

v_{rp}：r 組中排放源强度和每一單位强度對位置 p 所造成的濃度。

令 $c=[c_p]=[c_{p1}]$，$\bar{v}=[\bar{v}_{rp}]$，

$\bar{v}^T=[\bar{v}_{pr}]$，$Q=[Q_r]=[Q_{r1}]$，$\bar{q}=[\bar{q}_r]$

$=[\bar{q}_{r1}]$，$v=[v_{rp}]$，$v^T=[v_{pr}]$，

則〔16〕及〔17〕式分別可寫成〔18〕及〔19〕式的矩陣型式：

$$c \approx v^T \bar{q}, \qquad 〔18〕$$

$$= \bar{v}^T Q. \qquad 〔19〕$$

三、聚合平均佳化法

聚合平均佳化法乃爲取前二法優點而將之結合爲一的評估方法。於實際應用上，考慮二者各種可能結合過程，可分爲以下六種評估程序。爲便於文內討論時引用的簡便，各種評估程序皆以代號稱之。

1. 以各組中排放源强度和爲佳化對象且佳化時不考慮質量守恒的評估程序：

   僅聚合時〔18〕式相等於〔19〕式，但當將〔18〕式的 $\bar{q}$（各組中排放源强度平均值）及〔19〕式的Q（各組中排放源强度和）分別代入佳化評估法後，其佳化值再代回原式中，則因佳化的作用二式不再相等。此外，佳化評估法又有考慮質量守恒關係（式〔6〕），與不考慮質量守恒關係（式〔3〕）二種，故配合後共有四種評估程序。這第 1 種評估程序以下簡稱爲「Q程序」。依分組情況此程序又可分爲不分組Q程序、50組Q程序、30組Q程序、15組Q程序及 5 組Q程序。以下各程序分組命名均相似於此。

2. 以各組中排放源强度和爲佳化對象，但佳化時考慮質量守恒的評估程序：

   以下簡稱爲「QL 程序」（L（取 λ 讀音（Lambda））表示有考慮質量守恒關係）。

3. 以各組中排放源强度平均值爲佳化對象，佳化時不考慮質量守恒的評估程序：

   以下簡稱爲「$\bar{q}$ 程序」。

4. 以各組中排放源强度平均值爲佳化對象，佳化時考慮質量守恒的評估程序：

   以下簡稱「$\bar{q}$L 程序」

5. 將不分組排放源佳化後（不考慮質量守恒關係）的佳化值按大小排列再分組的評估程序：

   首先將不分組的排放源佳化，接著將其佳化值按大小順序排列（Sorting），再用聚合平均近似法，以下簡稱爲「S程序」。

6. 將不分組排放源佳化後（考慮質量守恒關係）的佳化值按大小排列再分組的

評估程序：

以下簡稱爲「SL 程序」。

除此之外亦計算僅利用聚合平均近似法而未經佳化程序的各種分組情形以進行比較，此種評估過程以下簡稱爲「N程序」。

叁、擴散模式與進行步驟

爲便於聚合平均佳化法之評估結果與一般方法之比較，本文所用擴散模式、氣象資料及排放源資料均與梁與李[4]所用相同。擴散模式爲求取點排放源長時期累積平均濃度的高斯擴散模式[9]：

$$\bar{C}_p = \frac{16}{2\pi} \sum_{m=1}^{N} \sum_{IV=1}^{6} \sum_{IL=1}^{6} \sum_{IT=1}^{6} \frac{P_{rob.}(K, IV, IL, IT)\, Q_m\, S(X_m, O; U_{IV}, IL)}{X_m} \quad \cdots\cdots (20)$$

氣象資料取自民國六十五年六月份。排放源資料及測站資料係前「臺灣地區公害防治先驅計劃工作實施小組」（行政院衛生署）在高雄地區量測結果。測站資料除續用梁與李[4]所用的 20 個測站資料外，本文另加入座標爲（1.1，16.4）與（2.6，16.2）的二個測站，即共有22 個測站。以上數學模式的說明及所用量測資料的詳細說明，均詳見[4]。

本文進行步驟可依次說明如下：

一、修正排放源强度，並將排放源按大小順序排列

由於分區選取的79個排放源總强度僅爲先驅計劃所有排放資料總强度的80%，乃將排放源乘上一修正因子$\frac{\Sigma\tilde{C}_i}{\Sigma C_i}$（其中$\tilde{C}_i$爲觀測值，$C_i$爲所選取79個排放源直接代入模式計算的未修正，未佳化測站模式值），以消除此差異。本文以後各種評估情形均用修正後的排放源强度。

二、計算各排放源對網格點及測站的擴散函數

由於聚合平均近似法對排放源按大小分組的特性，本法與直接將排放源代入模式計算者有一絕然不同處。即本法可事先將各排放源對網格點及對測站的擴散函數一次算出，儲存於磁碟或磁帶的記憶裝置中，需要時取出應用即可。亦即對於模式

計算中最耗計算時間（Computer Time）的擴散函數部份只要計算一次即可，對於實用上計算時間的節省相當可觀。此種即時（Real Time）計算的能力對污染的及時評估或預報提供良好的基礎。本文所謂的擴散函數爲〔20〕式中去掉排放源强度項的高斯擴散函數（Gaussian Dispersion Function）。

因梁與李[4]，用穩定度降二級的氣象條件，計算結果顯示南部地區的模式評估值較實測值偏高較多，本文乃將南部地區穩定度只降一級，其餘地區穩定度仍降二級，來計算其擴散函數，觀其變化。

三、進 行 分 組

分組即依排放源的編組情形將排放源、各排放源對網格點及測站的擴散函數予以聚合。分組後的資料存入記憶裝置，以備佳化及計算網格點濃度。本文分組共有5 種情形，即不分組、50組、30組、15組與 5 組。各分組情形見表㈠及表㈡。

四、進行各評估程序

進行第二章所述的七種評估程序。佳化過程的最佳 β 值，乃謂使誤差最小而佳化值仍爲合理正值的 β 值[5]，可以反覆法（Iteration）求得。

五、標準偏差（Standard Deviation）

爲比較各種評估程序結果的變化與優劣，以不分組佳化（考慮及不考慮質量守恒關係）所得的網格點濃度爲標準計算各評估程序網格點濃度與它的標準偏差（考慮質量守恒的 QL、$\bar{q}$L 及 SL 程序以下分組佳化考慮質量守恒的評估濃度爲標準，不考慮質量守恒的 Q、q 及 S 程序以下不分組佳化不考慮質量守恒的濃度爲標準），以下式計算：

$$SD=\sqrt{\frac{\Sigma(CS_{xy}-C_{xy})^2}{N-1}},$$

CS_{xy}：不分組佳化（考慮或不考慮質量守恒）的網格點濃度，x 爲橫座標，y 爲縱座標。

C_{xy}：各評估程序所得的網格點濃度，

N：網格點數目。

六、平均坡度（Average Gradient）

爲比較各評估程序所得污染濃度分佈的型態（Pattern）變化情形，又計算各種

表一　七種評估程序分50、30、15、及5組時69個排放源所屬組別

排放源依強度編號	各排放源所屬組別				排放源依強度編號	各排放源所屬組別			
	50 組	30 組	15 組	5 組		50 組	30 組	15 組	5 組
1	1	1	1	1	41	39	26	12	5
2	2	2	2	1	42	39	26	12	5
3	3	3	3	2	43	40	26	12	5
4	3	3	3	2	44	40	26	12	5
5	4	4	4	3	45	41	27	13	5
6	5	5	4	3	46	42	27	13	5
7	6	6	4	3	47	43	27	13	5
8	7	7	5	3	48	43	27	13	5
9	8	8	5	3	49	44	28	13	5
10	9	9	5	3	50	44	28	13	5
11	10	10	5	3	51	44	28	13	5
12	11	11	6	3	52	45	28	13	5
13	12	12	6	3	53	45	28	13	5
14	13	13	7	4	54	45	28	13	5
15	14	14	7	4	55	45	28	13	5
16	15	15	8	4	56	45	28	13	5
17	16	16	8	4	57	46	29	14	5
18	17	17	9	4	58	46	29	14	5
19	18	18	9	4	59	47	29	14	5
20	19	19	9	4	60	47	29	14	5
21	20	20	10	4	61	48	29	14	5
22	21	21	10	4	62	48	29	14	5
23	22	22	11	4	63	48	29	14	5
24	23	22	11	4	64	48	29	14	5
25	24	22	11	4	65	48	29	14	5
26	25	23	11	4	66	48	29	14	5
27	26	23	11	4	67	48	29	14	5
28	27	23	11	4	68	48	29	14	5
29	28	23	11	4	69	48	29	14	5
30	29	24	11	4	70	48	29	14	5
31	30	24	11	4	71	48	29	14	5
32	31	24	11	4	72	48	29	14	5
33	31	24	11	4	73	49	29	15	5
34	32	25	11	4	74	49	30	15	5
35	33	25	11	4	75	49	30	15	5
36	34	25	12	5	76	50	30	15	5
37	35	25	12	5	77	50	30	15	5
38	36	25	12	5	78	50	30	15	5
39	37	26	12	5	79	50	30	15	5
40	38	26	12	5					

表二　七種評估程序分50、30、15及5組時各組別所包括排放源數目

組　別	50　組	30　組	15　組	5　組	組　別	50　組	30　組
1	1	1	1	2	26	1	6
2	1	1	1	2	27	1	4
3	2	2	2	9	28	1	8
4	1	1	3	22	29	1	17
5	1	1	4	44	30	1	6
6	1	1	2		31	2	
7	1	1	2		32	1	
8	1	1	2		33	1	
9	1	1	3		34	1	
10	1	1	2		35	1	
11	1	1	13		36	1	
12	1	1	9		37	1	
13	1	1	12		38	1	
14	1	1	16		39	2	
15	1	1	7		40	2	
16	1	1			41	1	
17	1	1			42	1	
18	1	1			43	2	
19	1	1			44	3	
20	1	1			45	5	
21	1	1			46	2	
22	1	3			47	2	
23	1	4			48	12	
24	1	4			49	3	
25	1	5			30	4	

程序所得網格點濃度的平均坡度，以下式計算：

$$\sqrt{\frac{\Sigma(\frac{\partial C}{\partial x})^2+\Sigma(\frac{\partial C}{\partial y})^2}{N_{xy}}},$$

式中　C：網格點濃度，

N_{xy}：計算所用間距數目。

肆、結果與討論

一、穩定度的降低

梁與李[4]將六月份氣象資料的穩定度均降低二級作模式評估，評估結果除南部地區次濃度區模式值較實測值（圖二）偏高外，評估之污染濃度分佈型態及高濃度區的網格點濃度值均與實際污染狀況相當符合。根據梁與李[4]的討論，南部地區偏離市區穩定度應較接近實際所求得等級。爲使南部地區模式值降低以接近實測值，本文將南部地區接近氣象站的穩定度較求得等級只降一級，其餘氣象條件不變，來執行模式評估（降低一級穩定度的範圍包括四個排放源，恰爲依次編號1、2、3及4的四個最大排放源（表㈢），座標分別爲（7.3，3.9），(7.4，3.8），(7.2，4.0）與（7.2，4.0））。評估結果圖㈢成功的降低偏高的濃度，且整個污染濃度分佈型態與實測者相當符合，故以本文以後模式計算的氣象條件均本此；即南部地區四個排放源穩定度所求得穩定度降一級外，餘皆降二級。

將修正後排放源直接代入高斯模式評估（即不分組N程序）就得到相當具有代表性的污染濃度分佈曲線，除顯示該模式的可靠性外，分區選取排放源及再修正排放源的方法亦證明爲適當。

二、不分組Q程序與分組Q程序（佳化評估法特性）

不分組Q程序的排放源佳化值與未佳化前相較，除强度較小的排放源外（編號較大者）大致相等，故評估的污染濃度值二者亦極接近（參考圖㈢、圖㈣）。佳化值變動（調整）甚微小，究其原因，乃受佳化作用要求上限制的結果；即佳化值須全爲合理的正值。欲進行佳化程序的排放源若有强度相當小者，佳化時則僅容許有相當小的「調整」後就趨近於零。所以這些較小强度的排放源成爲「控制」佳化作用佳化值變化大小的重要因子（以下即稱作控制因子），故若欲進行程序佳化程序

表三 排 放 源 資 料

排放源編號	X軸座標 (Km)	Y軸座標 (Km)	所屬區別	煙囪高度 (m)	煙口斷面積 (m^2)	煙口排氣量 (m^3/min)	煙口平均溫度 (°C)	排放源強度 (g/sec)	修正排放源強度(註) (g/sec)
1	7.3	3.9	1	130	11.9	33,862	150	3,122.4	6,085.6
2	7.4	3.8	1	130	28.3	23,270	150	2,145.7	4,182.0
3	7.2	4.0	1	89	12.5	6,580	130	606.7	1,182.5
4	7.2	4.0	1	89	12.5	6,580	130	606.7	1,182.5
5	3.6	11.0	2	70	10.1	7,059	156	466.9	910.0
6	3.6	11.0	2	45	11.1	5,190	160	343.3	669.0
7	3.6	11.0	2	70	10.1	3,529	144	233.4	455.0
8	3.6	11.0	2	45	11.1	2,595	145	171.6	334.5
9	7.7	22.2	5	85	3.6	2,007	163	154.9	301.9
10	3.4	11.8	2	45	4.9	1,810	150	139.7	272.3
11	5.6	11.6	2	48	0.4	1,400	200	120.5	234.9
12	3.4	11.8	2	25	1.6	1,280	150	99.0	193.0
13	3.4	11.7	2	40	1.3	1,270	150	98.0	191.0
14	5.5	23.2	5	35	9.6	2,270	256	72.3	140.9
15	5.6	23.2	5	45	12.3	2,660	366	68.6	133.6
16	7.4	23.2	5	50	3.0	796	321	62.0	120.8
17	6.0	23.5	5	45	12.3	2,372	243	61.1	119.0
18	5.5	23.2	5	38	2.8	2,147	154	57.2	111.4
19	5.5	23.2	5	35	9.7	2,096	214	56.1	109.4
20	5.5	23.2	5	35	9.6	2,023	214	54.2	105.6
21	8.0	24.4	5	57	4.7	581	200	45.0	87.7
22	7.7	25.0	5	17	0.9	581	344	45.0	87.6
23	8.1	24.3	5	59	3.6	465	200	36.0	70.2
24	5.5	23.2	5	35	9.6	1,105	256	35.1	68.4
25	6.0	23.5	5	53	6.9	1,195	371	31.2	60.8
26	5.8	23.8	5	45	0.5	99	538	30.1	58.7
27	5.8	23.7	5	45	0.5	99	538	30.1	58.7
28	8.2	25.1	5	18	1.2	378	170	29.2	57.0
29	5.5	23.2	5	47	9.6	908	256	28.8	56.2
30	5.3	23.3	5	15	4.4	1,004	343	25.8	50.2
31	5.7	23.6	5	35	2.6	1,811	300	25.4	49.6
32	7.5	22.1	5	30	1.9	314	201	24.3	47.4
33	5.3	23.0	5	49	4.1	700	288	24.2	47.3
34	5.6	23.3	5	46	2.6	853	300	22.0	42.8
35	7.8	24.8	5	52	3.0	270	200	21.0	40.8
36	1.4	16.4	5	19	2.5	700	50	20.0	38.9
37	5.3	23.4	5	34	4.4	694	204	18.3	35.6
38	5.2	23.0	5	29	1.0	495	300	17.2	33.4
39	5.7	23.3	5	40	2.3	563	300	14.7	28.6
40	5.4	23.4	5	30	1.6	880	179	14.0	27.3

表三　排　放　源　資　料（續）

排放源編號	X軸座標 (Km)	Y軸座標 (Km)	所屬區別	煙囪高度 (m)	煙口斷面積 (m^2)	煙口排氣量 (m^3/min)	煙口平均溫度 (°C)	排放源強度 (g/sec)	修正排放源強度(註) (g/sec)
41	2.2	15.4	3	35	7.0	125	295	13.5	26.3
42	5.6	23.5	5	38	1.8	372	300	13.4	26.2
43	5.8	23.5	5	34	4.1	477	300	12.4	24.2
44	4.9	22.9	5	30	1.8	383	232	12.3	22.9
45	1.2	16.4	3	16	0.4	90	150	8.4	16.4
46	5.9	19.9	4	35	0.8	1,000	100	6.8	13.2
47	5.7	16.2	4	36	1.3	120	200	6.8	13.1
48	6.1	20.8	4	18	0.8	76	150	6.3	12.2
49	5.7	21.0	4	13	0.7	70	150	5.8	11.2
50	2.2	15.8	3	35	0.8	285	100	5.3	10.4
51	4.8	18.9	4	20	0.7	50	370	5.1	9.7
52	5.1	16.5	4	45	2.5	65	200	5.0	8.7
53	2.8	16.9	3	15	1.8	56	200	5.0	9.7
54	2.7	16.9	3	15	1.2	56	200	5.0	9.7
55	2.3	16.5	3	15	0.5	30	300	4.7	9.1
56	5.0	16.5	4	14	0.6	55	150	4.3	8.3
57	7.0	17.0	4	10	0.2	48	150	3.8	7.5
58	5.4	16.4	4	14	0.7	60	150	3.7	7.2
59	1.5	16.1	3	25	0.6	120	150	3.7	7.1
60	1.3	16.4	3	18	0.3	30	150	2.8	5.5
61	6.5	17.0	4	8	0.6	36	150	2.8	5.5
62	5.4	18.4	4	9	0.5	35	200	2.8	5.4
63	6.3	16.3	4	6	0.3	33	200	2.8	5.4
64	6.0	19.1	4	36	1.1	400	100	2.7	5.3
65	6.0	18.8	4	35	1.1	400	100	2.7	5.3
66	5.6	16.4	4	12	0.1	43	150	2.6	5.1
67	1.3	16.7	3	15	0.3	32	150	2.4	4.7
68	1.8	16.7	3	7	0.5	28	200	2.1	4.1
69									
70	1.0	15.0	3	35	3.6	4,833	90	2.1	4.0
71	5.6	17.7	4	30	0.3	300	100	2.0	4.0
72	6.7	17.5	4	38	0.3	300	100	2.0	4.0
73	6.5	17.0	4	9	0.1	24	200	2.0	3.8
74	5.9	20.0	4	10	0.1	23	150	1.9	3.6
75	6.0	16.0	4	30	0.2	24	150	1.9	3.6
76	6.7	20.0	4	16	1.5	275	100	1.9	3.6
77	4.1	19.5	4	33	0.1	250	100	1.8	3.5
78	7.2	16.9	4	15	0.2	23	150	1.8	3.5
79	5.6	18.1	4	8	0.1	22	200	1.7	3.3

註：修正係數 1.949

的排放源强度有相當小的，佳化值與未佳化值差異可能就不大了。佳化值變動幅度的大小，亦可由最佳 β 值得知，當 β 值愈大，佳化值愈接近被佳化值，β 當值相當大時佳化值即無變化[5]。據梁與李[4]之計算，當 β 值大於 1.0×10^{-4}，佳化值即無變化，而當 β 值小於 4.0×10^{-17} 時，模式評估的測站值即約等於實測值。查看表四，不分組Q程序的最佳 β 值爲 1.228×10^{-5} 故亦知佳化值變動甚微。然而，最佳 β 值的變化是「控制因子」控制佳化程序的結果，而非佳化程序的原因。亦即，最佳 β 值受控制因子的控制。

表四　四種佳化評估程序的最佳 β 值（S與SL過程為分別將不分組Q程序與不分組QL程序所得佳化值分組，不再經佳化程序）。

分　組	Q　程　序	QL　程　序	$\bar{q}$　程　序	$\bar{q}$L　程　序
不分組	1.288×10^{-5}	6.4298×10^{-6}		
50　組	1.0116×10^{-6}	6.5040×10^{-7}	1.1130×10^{-5}	$2.748\varsigma\times10^{-6}$
30　組	1.0525×10^{-7}	7.8801×10^{-8}	6.8989×10^{-6}	2.8988×10^{-6}
15　組	3.7365×10^{-8}	2.7818×10^{-8}	6.2083×10^{-6}	2.3123×10^{-6}
5　組	5.5927×10^{-10}	5.3805×10^{-10}	7.6373×10^{-8}	5.2445×10^{-8}

分組Q程序與不分組Q程序則呈較顯著差異。高濃度區仍然保持，但中部地區的次濃度區隨分組不同而有較大變化。分5組Q程序評估結果中部地區次濃度區完全消失（圖㈢、㈣、㈤、㈥）。探其所以，乃由於分組所用以計算的聚合排放源數目減少（$n<N$），單一聚合排放源强度的變化對網格點濃度的影響增大；即單一聚合排放源强度的變化對網格點濃度的改變更爲顯著，所影響的範圍也增大。由於佳化程序的「調整」作用受較小排放源强度之一者控制，該控制因子趨近於零時應使網格點濃度降低（尤以受該組排放源影響大的網格點濃度降低較多），但因佳化程序的調整作用使其它佳化排放源有的較未佳化時升高，有的降低，故總影響變得複雜。但在分組相當少時（如分5組）每一組强度的變化影響濃度分佈更大，應可由佳化值的變化及各排放源對網格點間擴散函數的分佈得知其濃度大致變化情形。分5組Q程序的控制因子爲第5組，當其趨近於零時其它各組調整並不大（表㈤），故該組的影響更形明顯，且該組包含排放源多（44個），影響範圍大，整個中部地

區濃度主要由該組所造成，當其佳化後趨近於零時，整個中部地區次濃度區因而消失，濃度分佈型態較其它分組情形乃較不相同。高濃度區受其它各組影響大仍然無顯著變化。同樣的，分 50、30 及 15 組的控制因子也是主要影響中部地區的小排放源，但因組數多，使濃度的變化不若分 5 組時那麼强烈，但仍可看出逐漸消失的趨勢。

表五　分 5 組各種評估程序的聚合排放源強度值（g/sec）

組別	各組強度和（Q或N程序）	Q程序	QL程序	各組平均強度（$\bar{q}$）（註）	Q程序	$\bar{q}$L程序	S程序	SL程序
1	10,268	10,272	10,272	5,133.8	5,134.2	5,134.2	10,268	10,268
2	2,365.1	2,341.3	2,340.4	1,182·5	1,182.5	1,182.6	2,365.1	2,365.2
3	3,561.7	4,471.7	4,489.2	395.7	478.9	496.3	3,562.9	3,566.4
4	1,724.5	1,686.4	1,689.2	78.4	76.8	77.7	1,723.5	1,728.4
5	507.0	0.09	0.3	11.5	0.001	0.002	429.3	515.0
控制因子		5	5		5	5		

由以上討論可知，將對某一區域影響重大（此可由擴散函數與排放源强度看出）的排放源聚合成一組，此組强度又較低時，經過佳化程序時，該組排放源可能成爲控制因子而使受其影響區域的評估濃度整個降低，甚而消失；以上分 5 組Q程序造成中部地區次濃度區的消失，卽是此種情形。

三、Q 程序與 $\bar{q}$ 程序及其最佳 β 值變化情形

Q程序已於二中有相當的討論，分組Q程序的最佳 β 值隨著組數增多而漸大（表四或圖七），卽對各種分組程序而言，組數愈多佳化值變動愈小，這就是受較小排放源爲控制因子作用的結果。組數愈少控制因子强度提高愈多，佳化時「可容許調整」的幅度就愈大，使得最佳 β 值愈小。

$\bar{q}$ 程序則因分組後控制因子强度提高較Q程序爲少，雖然分組數減少，β 值也降低，卻較Q程序降低的較和緩。

比較二種程序評估結果，除分 50 組時 q 程序在中部地區有較顯著濃度降低的情況外，二者幾乎沒有差別（圖(六)與(九)），即雖然佳化值調整的程度有若干差異，〔16〕與〔17〕式仍能獲得相近的結果。因此 Q 程序與 q 程序可說沒有太大的差別。

四、佳化時考慮質量守恆關係（Q、QL、$\bar{q}$ 及 $\bar{q}$L 程序的比較）

由於修正排放源時已將排放源強度乘上一修正因子（$\frac{\Sigma\tilde{C}_i}{\Sigma C_i}$，$C_i$ 為 N 程序測站模式值，C_i 為測站實測值），即修正後的排放源直接帶入模式評估所得的模式測站濃度就已滿足質量守恆關係(式〔4〕)。雖然經過佳化程序，但由於前述佳化作用受較小排放源為控制因子影響的特性，分組愈多時佳化與未佳化差異愈小。故在分組多時(如79、50組)考慮質量守恆關係與否根本無甚差異（圖(十)）。分組較小時（如30、15組）則中部地區次濃度區變化呈不同現象（圖(十一)、(十二)）。分 5 組時，因受最後一組強度值趨近於零的影響，整個次濃度區均消失，考慮質量守恆與否亦無差別（圖(十三)與(十四)）。但觀察表(四)或圖(七)，考慮質量守恆關係的各評估程序較不考慮者有較小的最佳 β 值，這可表示考慮質量守恆關係的評估程序能得到更佳的「調整」。再比較〔6〕式與〔3〕式，考慮質量守恆關係的〔6〕式較不考慮質量守恆關係的〔3〕式多了一項（$-2\lambda V$)。又參考表(六)或圖(七)，隨分組數目增加，λ 值負的愈來愈少（即 $-2\lambda V$ 逐漸變小）。也就是說，隨著分組數目的減少 β 值亦降低，而有較大的「調整」作用，但 λ 值的「修正量」卻又逐漸變小。因此，λ 項有「穩定」佳化調整作用的功能；此種穩定的功能使得佳化評估所得污染分佈型態更具代表性；當然，這也就是考慮質量守恆關係的本意。

表六　二種佳化時考慮質量守恆關係的評估程序 λ 係變化情形（SL 程序為將不分組 QL 程序所得佳化值分組，不再經佳化程序）

分　組	QL　程　序	$\bar{q}$L　程　序
不　分　組	-1.7907×10^{-3}	
50　組	-1.0748×10^{-3}	-1.5690×10^{-3}
30　組	-7.3869×10^{-4}	-1.5244×10^{-3}
15　組	-6.2149×10^{-4}	-1.1799×10^{-3}
5　組	-1.1804×10^{-5}	-7.8024×10^{-5}

五、分組的特性（聚合平均近似法特性）

由於分組佳化當組數少時會導致次濃度區濃度降低，甚而消失。現僅考慮分組之情況，以觀其變化，計有N、S及 SL 三種程序，結果分別示於圖㈣至㈥。

因爲分組後用平均值計算，對任一網格點而言，其濃度的變化與未分組時相較可能升高或降低，至於究竟是升高還是降低，或其變化大小有多少，則與擴散函數、排放源强度及分組方式均有關係，其間變化相當複雜，無法簡單預估其變化情形或作出一致性結論，故以下討論僅對分組的特性作一般瞭解。

設某位置 p 濃度值可以〔10〕式表示：

$$c_p=\sum_{j=1}^{N} q_j v_{jp} . \qquad 〔10〕$$

排放源聚合爲 n 組後〔10〕可以〔12〕式表示：

$$c_p \approx \sum_{r=1}^{n} \bar{q}_r \sum_{j=J_{r-1}+1}^{J_r} v_{jp} ,$$

式中 $$\bar{q}_r = \sum_{j=J_{r-1}+1}^{J_r} q_j / J_r - J_{r-1} ,$$

$$\begin{aligned} c_p \approx & \left(\frac{q_{J_0+1}+q_{J_0+2}+\cdots\cdots+q_{J_1}}{J_1-J_0}\right). \\ & (v_{J_0+1}+v_{J_0+2}+\cdots\cdots+v_{J_1}) \\ & +\left(\frac{q_{J_1+1}+q_{J_1+2}+\cdots\cdots+q_{J_2}}{J_2-J_1}\right) \\ & (v_{J_1+1}+v_{J_1+2}+\cdots\cdots+v_{J_2}) \\ & +\cdots\cdots\cdots\cdots\cdots\cdots \\ & +\left(\frac{q_{J_{n-1}+1}+q_{J_{n-1}+2}+\cdots\cdots+q_{J_n}}{J_n-J_{n-1}}\right). \\ & (v_{J_{n-1}+1}+v_{J_{n-1}+2}+\cdots\cdots+v_{J_n}) , \\ & =\bar{q}_1(v_{J_0+1}+v_{J_0+2}+\cdots\cdots+v_{J_1}) \\ & +\bar{q}_2(v_{J_1+1}+v_{J_1+2}+\cdots\cdots+v_{J_2}) \\ & +\cdots\cdots\cdots\cdots\cdots\cdots \\ & +\bar{q}_n(v_{J_{n-1}+1}+v_{J_{n-1}+2}+\cdots\cdots+v_{J_n}) \circ \end{aligned}$$

就第一組 $$\bar{q}_1(v_{J_0+1}+v_{J_0+2}+\cdots\cdots+v_{J_1})$$

而言，若有

$$(a)\ q_{J_0+1}=Q_{J_0+2}=\cdots\cdots=q_{J_1}\ 或\ (b)\ v_{J_0+1}=v_{J_0+2}=\cdots\cdots=v_{J_1},$$

則等號成立，即

$$q_{J_0+1}v_{J_0+1}+q_{J_0+2}v_{J_0+2}+\cdots\cdots+q_{J_1}v_{J_1}$$
$$=\bar{q}_1(v_{J_0+1}+v_{J_0+2}+\cdots\cdots+q_{J_1}),$$
$$=(q_{J_0+1}+q_{J_0+2}+\cdots\cdots+q_{J_1})\,\bar{v}_1.$$

若對第一組而言（a）及（b）情形不成立，且擴散函數 v_{J_0+1} 最重要（值最大），其餘者可略，則第一組可表爲

$$q_1(v_{J_0+1}+v_{J_0+2}+\cdots\cdots+v_{J_1})$$
$$\approx\bar{q}_1(v_{J_0+1}),$$

因同一組排放源强度相近，則第一組濃度較未分組時（即 $q_{J_0+1}v_{J_0+1}+q_{J_0+2}v_{J_0+2}+\cdots\cdots+q_{J_1}v_{J_1}$）增加或降低視 $\bar{q}_1$ 較 q_{J_0+1} 爲大或小而定，若 q_{J_0+1} 較大則降低，若 q_{J_0+1} 較小則升高。故第一組可能相同、升高或降低，其它各組情形亦同，總濃度的變化是大或小故不一定。即由於其間複雜的關係，無法簡單預測其變化。而一般上，由於各組間之加强及減弱作用下濃度較未組合時的變化應不致太大。但有以下二種極端情形值得注意。即當對該位置影響重大的擴散函數均包含於同一組中，使得該組平均擴散函數提高較小的擴散函數甚多，而擴散函數與排放源强度的分佈情形有如圖㈡極端情形時，聚合後升高量較降低量多的多，濃度就會升高相當大。

反之，若排放源强度與擴散函數在該組中有如圖㈡的另一極端情形，則聚合後降低量較升高量大的多，濃度就會有相當程度的降低。

由以上的討論知，局部濃度的升高或降低同時受擴散函數，排放源强分佈及分組方式的影響。若不發生圖㈢或圖㈢的極端情形，則局部濃度不致增强或減弱的相當劇烈。若能避免將影響重大的擴散函數分爲一組，同時排放源强度亦不致有升降太大的情形，則能獲得良好的評估結果。

由圖㈣至㈦可看出，對高雄地區而言，分50、30、15組的N、S及SL程序評估結果差異極微，誤差也相當小（參考表㈦），但分5組時中部地區的次濃度區（尤其座標（6，16）處）發生較大的局部增强現象。此可由上面討論的情形解釋之

，即中部次濃度區受第 5 組排放源的影響最大，而該組對發生較大增強現象的各網格點有相似圖㈢的排放源強度及擴散函數分佈情形。譬如，濃度增加最明顯的(6，16）網格點就是如此（參考圖㈢）。若要改變此處明顯局部增強的現象，可改變分組數目或編組情況。

六、標準偏差指標與平均坡度指標

一般說來，聚合平均近似法以平均值計算，產生的網格點濃度誤差應該不大，但若發生上述的極端情形，誤差就可能大爲增加。參考表㈦或圖㈣，N、S 與 SL 程序分50、30及15組時標準偏差（本文網格點濃度誤差用標準偏差表示）都很小。分15組時分別爲4.7%、2.8%與 2.7%，但分 5 組時因發生較劇烈的局部增強現象，誤差突升，分別達30.8%，26.9%與26.7%。

Q、QL、$\bar{q}$ 與 $\bar{q}L$ 四種分組後佳化的評估程序，雖較 S 及 SL 程序計算上簡便，因受前述佳化作用特性的影響，誤差的產生有其必然性。隨著分組數目的減少誤差有相當的增加，同時誤差的大小較 N、S 及 SL 程序也高得多（參考表㈦或圖㈣）。

表七　標準偏差（不考慮質量守恆關係的程序以不分組Q程序所得網格點濃度為標準，計算得標準偏差後除以標準網格點濃度的平均值，而以%表示。考慮質量守恆關係的程序以不分組 QL 程序所得的網格點濃度為標準，計算標準偏差後除以該標準網格點濃度平均值，以%表示）。

分組	N程序	Q程序	QL程序	$\bar{q}$程序	$\bar{q}L$程序	S程序	SL程序
不分組	4.1						
50 組	4.4	4.1	4.4	11.1	9.2	1.1	1.6
30 組	4.2	12.6	13.7	17.8	13.4	1.9	1.9
15 組	4.7	18.7	20.0	18.3	17.4	2.8	2.7
5 組	30.8	34.4	37.1	33.4	36.9	26.9	26.7

由於標準偏差對各評估程序分組下的規律性與特性，將之作爲判斷分組情形是否可接受的指標應是合理可行的。

對於污染濃度分佈型態（Pattern）相似的情況，網格點間濃度差異必也互相對應，污染區域的平均濃度坡度應可作爲判斷污染濃度分佈型態變化的參考。表(八)（或圖(三)）顯示各評估程序50、30、及15組時平均坡度變化不定，分 5 組時則有一致性坡度增大的趨勢；此與分 5 組時各評估過程處得污染濃度分佈變化較大的實際情況正相符合。

表八　平均坡度（單位 $\times 10^{-3}$ ppm）

分組	N 程序	Q 程序	QL 程序	q 程序	$\bar{q}$L 程序	S 程序	SL 程序
不分組	9.00	8.94	9.15				
50 組	8.99	8.79	9.09	8.66	9.23	8.92	9.10
30 組	8.98	8.87	9.41	8.55	9.49	9.11	8.93
15 組	8.95	9.19	9.96	8.56	9.81	8.90	9.12
5 組	10.59	9.87	9.90	9.66	9.90	10.47	10.66

七、綜 合 誤 差

以上所討論的佳化過程亦可自測站濃度誤差（式〔1〕第一項）、排放源誤差（式〔1〕第二項）及綜合誤差（式〔1〕的變化情形（參考表(九)）看出一些特性。首先，表中顯示各種分組情況下考慮質量守恒關係（QL 與 $\bar{q}$L 程序）較未考慮質量守恒關係（Q 與 $\bar{q}$ 程序）有較大的排放源誤差及較小的測站濃度誤差。此即表示考慮質量守恒關係可獲得更佳的調整效果及更正確的污染濃度分佈型態，因此前者最佳 β 值較後者爲小，綜合誤差亦然。再者，同一種佳化程序隨著分組數目的減少，排放源誤差增加甚多，而測站濃度誤差卻逐漸降低。此即表示，分組數目愈少控制因子强度「可調整的範圍」愈大，佳化排放源强度變化就相當可觀，隨著分組數目減少誤差幾乎以一個階次（Order）的速率增加。雖然表中顯示綜合誤差亦逐漸降低，但此時佳化排放源誤差，乃相對各未佳化聚合排放源而言，在分組數目不同情況下，其大小當不宜互相比較。但是隨著分組數目減少，測站濃度誤差也逐漸降低的事實與六所討論網格點濃度誤差隨分組數目減少而逐漸增大的情形恰恰相反。探其所以，除因中部地區測站數目較高濃度區測站數目稀少（參考圖(三)），

表九　各種佳化評估程序的誤差

分組 \ 誤差項 \ 程序		Q 程序	QL 程序	$\bar{q}$ 程序	$\bar{q}$L 程序
不分組	Ⅰ	0.26083	0.25933		
	Ⅱ	0.86998×10^{-6}	0.16990×10^{-5}		
	Ⅲ	0.27113	0.26996		
分 50 組	Ⅰ	0.25804	0.25806	0.25192	0.24584
	Ⅱ	0.11678×10^{-4}	0.18058×10^{-4}	0.12179×10^{-5}	0.56599×10^{-5}
	Ⅲ	0.27002	0.26998	0.26474	0.26056
分 30 組	Ⅰ	0.22744	0.22141	0.24133	0.24706
	Ⅱ	0.21825×10^{-3}	0.33386×10^{-3}	0.21839×10^{-5}	0.52076×10^{-5}
	Ⅲ	0.25080	0.24817	0.25551	0.26133
分 15 組	Ⅰ	0.21061	0.20477	0.23294	0.23219
	Ⅱ	0.64816×10^{-3}	0.95326×10^{-3}	0.28058×10^{-5}	0.77328×10^{-5}
	Ⅲ	0.23693	0.23365	0.24901	0.24870
分 5 組	Ⅰ	0.17024	0.16996	0.17346	0.17037
	Ⅱ	0.85639×10^{-2}	0.88198×10^{-2}	0.25228×10^{-3}	0.36710×10^{-3}
	Ⅲ	0.18016	0.17978	0.18223	0.17914

註：Ⅰ表測站濃度誤差項 $(\sum_{i=1}^{n}(\hat{c}_i-\tilde{c}_i)^2/\sum_{i=1}^{n}\tilde{c}_i^2)$（無因次）

Ⅱ表排放源强度誤差 $(\sum_{j=1}^{N}(\hat{q}_j-\tilde{q}_j)^3/\sum_{j=1}^{N}\tilde{q}_j^2)$（無因次）

Ⅲ表綜合誤差（即式〔1〕）（無因次）

以致計算測站濃度誤差時所佔權重（Weighting）較低，使隨分組數目減少該區局部濃度降低的事實所能表現出的誤差份量偏低的一部份原因外，主要由於隨著分組數目減少，排放源佳化值調整漸大，使得測站模式值與實測值相接近，但整個污染濃度分佈較未分組時因而也逐漸改變。然而重要的是，聚合平均佳化法僅以相當少數的佳化聚合排放源就可獲致代表性的結果，且各聚合排放源均爲合理正值，不致發生 Heimbach 與 Sasaki 濃度值爲負的情形；甚至到將所有排放源聚合成互相，佳化近似後的評估結果亦可得到污染濃度分佈大致上的瞭解，更足以顯示本法令人驚異的效果。

伍、結　　論

空氣污染的解決牽涉甚廣，但解決的過程不外乎觀察（或觀測）、分析、評估、預報與控制。評估與預報固爲污染控制的先決條件，但作好評估與預報並非易事。在實際作業時，由於經費、人力、時間與知識都極有限，而良好的評估與準確的預報需建立在這些脆弱的條件上，則如何竭力發揮所有可能得到的資訊，以獲取最具代表性的結果，顯然是必須盡力去作的一件要事。在空氣污染的評估與預報上，最重要的資訊來源便是實測資料與評估或預報模式，可惜由於各種因素的限制，兩者之間並不一致，甚且出入頗大，佳化理論卽成爲互相調整以譜出最具代表性污染濃度分佈的良好途徑。

Heimbach 與 Sasaki[3]利用變分法在量測濃度與評估模式間從事佳化，但其理論僅可用於測站數目多於污染源的數目，且其佳化後的污染源强度值常有負值出現，因此無法應用於實際狀況。梁[5]所發展的佳化理論藉著一個控制機制（β 值），使污染源强度值與污染濃度分佈值皆能爲正，且能適用於任何測站數目與污染源數目，尤以測站數目稀少時（此爲一般實際情況）更具成效。

此外，由於受到諸多因素的限制，模式評估所需各種資訊收集不能完全，量測無法精確，而空氣污染嚴重性日甚一日，模式評估必須廣泛應用在各都市及鄉鎭以建立空氣污染控制的基礎，因此如何發展出一種簡化龐大繁複模式計算的可行方法，於充分利用所有可得的資訊下，有效的減少計算工作，化浩繁爲簡易，且能得到具有相當程度代表性的評估結果，應屬當務之急。

Gustafson[7]作聚合平均近似法(Aggregated-averaged Approximation Method）的嘗試以期有效減少計算機時間。但其數值佳化亦採用相似於 Hemibach 與 Sasaki[3] 方式，卽在實測濃度與評估模式間從事佳化，故實用上有和後者相同的限制，且所造成不合理的濃度分佈可能更爲明顯及嚴重。

本文的研究卽本於以上二種方法的趨勢與需求，嘗試將梁[5]之佳化理論與 Gustafson[7] 的聚合平均近似法概念相結合，以充分發揮二者的優點，並探尋此種聚合平均佳化法（Aggregated-averaged Optimization Method）應用的特性與可行性。從本文應用上二法七種組合於高雄地區的實例中可看出結果相當令人滿意。一般來說，隨分組數目的減少，中部以濃度區因受較小排放源影響重大，有較大的

變化外，整個污染濃度分佈型態始終能保持穩定，呈現出極具代表性的評估結果。為比較各種評估程序的變化與優劣，本文以不分組佳化所得的網格點濃度為標準濃度，計算各評估程序網格點濃度與標準濃度的標準偏差，結果顯示隨分組數目減少，標準偏差亦逐漸增加，因此標準偏差應可作為分組數目可否接受的良好指標。

由於聚合平均佳化法取佳化平均值來執行計算以獲得近似的結果，本法似應能適當「容忍」模式評估所需資料的收集不全與精確不足，因此可廣泛應用於都市與鄉鎮中以獲得具有足够代表性的污染濃度分佈型態。然而本質上，資料仍應儘可能齊全與精確（尤其是測站濃度值為作為校正的依據，精確度的要求極為重要），才能得到更佳的效果，因此對於各地區污染狀況的量測及資料的收集登錄，實在刻不容緩。

本法更有一特點，即於分組前已將所用氣象條件下的所有排放源與網格點之間，及排放源與測站間的擴散函數（Dispersion Function）計算出來，儲存於記憶媒體（磁碟或磁帶）中，於分組時僅需取出計算即可。因此若能對所有氣象條件（如本文所用16個風向、6 級穩定度、6 級風速與 8 級溫度共有4608種氣象條件）的擴散函數予以計算出，並儲存於記憶媒體，則可用於空氣污染濃度分佈的即時（Real Time）計算上，也就是可提供空氣污染的隨時評估與預報。

參 考 文 獻

1. Goldstein, I. P., and L. Landovitz, 1977: Analysis of air pollution patterns in New York City. I. Can one station represent the large metropolitan area? II. Can one aerometric station represent the area surrounding it? Atmos. Envir., 11, 47-57.
2. Stern, A. C., 1968: Air pollution, Academic Press, New York, 425-463.
3. Heimbach, J. A. and Y. Sasaki, 1975: A variational technique for mesoscale objective analysis of air pollution. J. Appl. Meteor., 14, 194-203.
4. 梁文傑、李崇德，1979：高雄市二氧化硫污染與偵測網之佳化評估。中國工程學刊，第三卷第三期。
5. 梁文傑，1980：空氣污染評估的佳化理論。中國工程學刊，第三卷第二期。
6. 梁文傑、李克堂，1979：臺北市一氧化碳污染與偵測網之佳化評估。中國機械工程學刊，第一卷第一期。
7. Gustafson S. A., K. O. Kortanek, and J. R. Sweigart, 1977: Numerical optimi-

zation techniques in air quality modeling: Objective interpolation formulus for the spatial distribution of pollution concentration. J. Appl. Meteor., 14, 1243-1255.

8. Kenneth, L. C., 1977: Multiple-source plume models of urban air pollution-their general structure. Atmos. Envir., 11, 403-414.
9. Busse, A. D. and J. R. Zimmerman, 1973: User's guide for the climatological dispersion model. EPA-R4-73-024. Research Triangle Park, North Carolina, 155pp.
10. Turner, D. B., 1970: Workbook of atmospheric dispersion estimates. U. S. Department of Health, Education, and Welfare, Cincinnati, Ohio, 84pp.
11. Weber, E., 1970: Contribution to the residence time of sulfur dioxide in a polluted atmosphere. J. Geophys. Res., 75, 15, 2909-2914.
12. 梁文傑、吕世宗，1977b：臺灣電力公司候選火力電廠廠址對周圍環境空氣員質之評估。臺灣電力公司委託研究計劃研究報告，257pp.
13. ㈱行政院衛生署 1978：臺灣地區公害防治先驅計劃工作報告。行政院衛生署，臺北市，741 pp.
14. Garnett A., P. Read and D. Finch 1976: The use of conversion factors in air pollution studies: sulphur dioxide ppm-μgm^{-3}. Atmos. Envir., 10, 325-328.

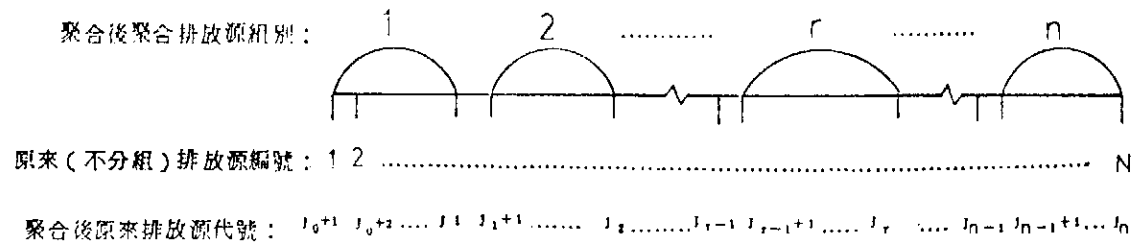

圖一　聚合平均佳化N個排放源聚合爲 n(n＜N) 組聚合排放源示意圖

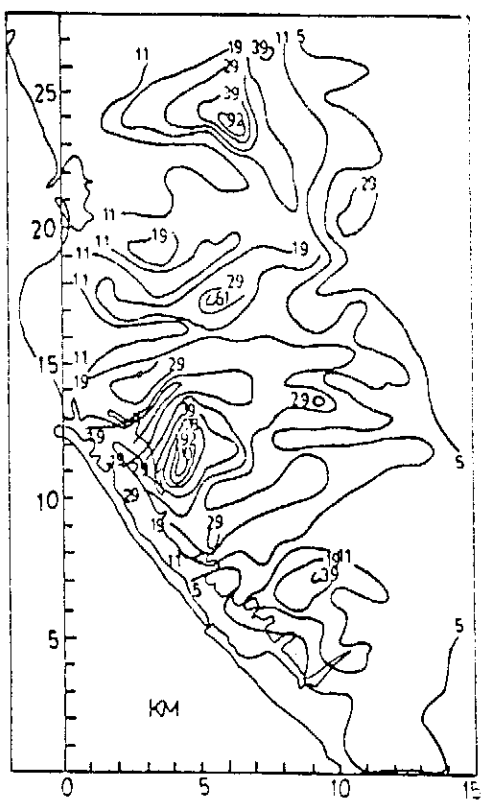

圖二　實際量測濃度分佈圖

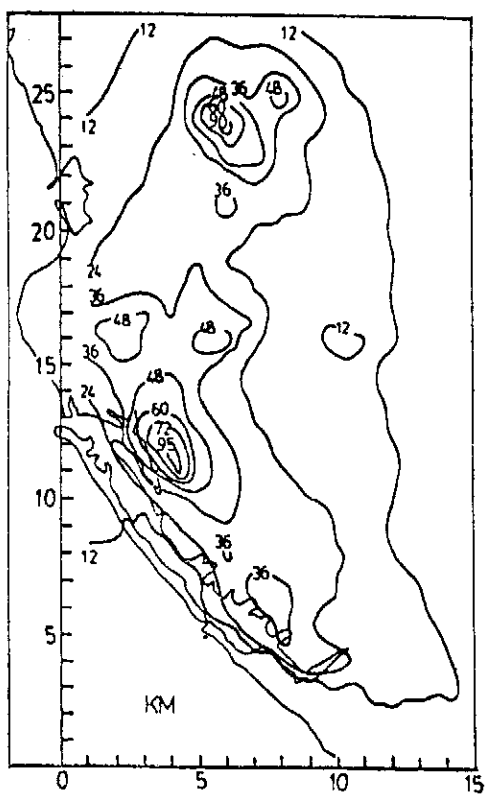

圖三　修正排放源直接代入模式評估（N程序）濃度分佈圖（穩定度南部地區降一級，其餘地區皆降二級）

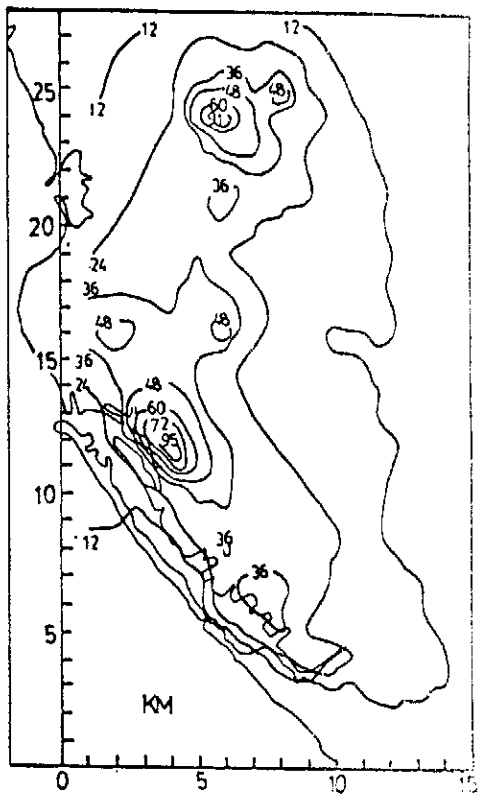

圖四　不分組Q程序濃度分佈圖

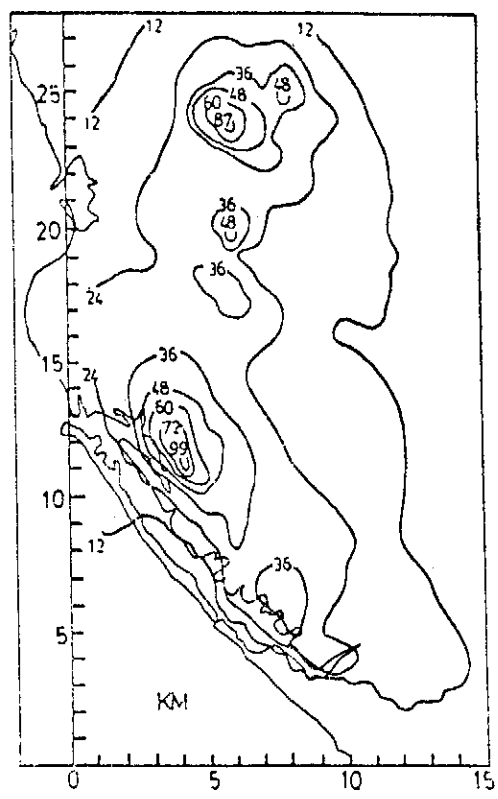

圖五　分15組Q程序濃度分佈圖

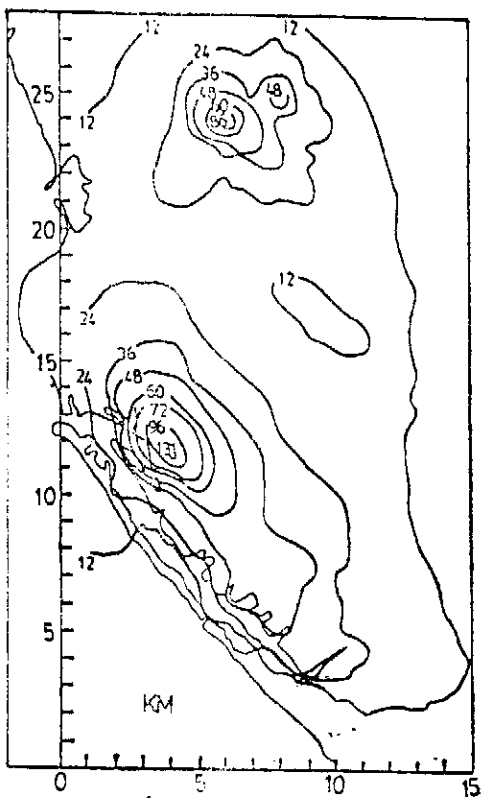

圖六　分 5 組Q程序濃度分佈圖

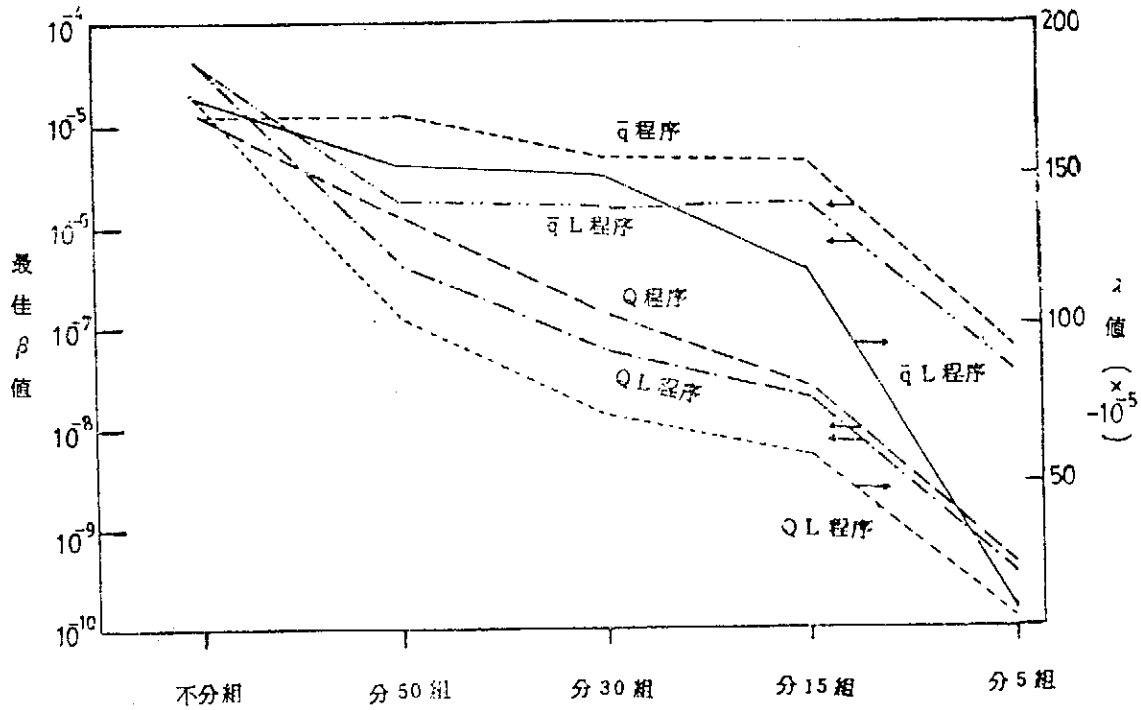

圖七　各種評估程序最佳 β 值變化的圖示情形及考慮質量守恒關係時 λ 值變化的圖示情形

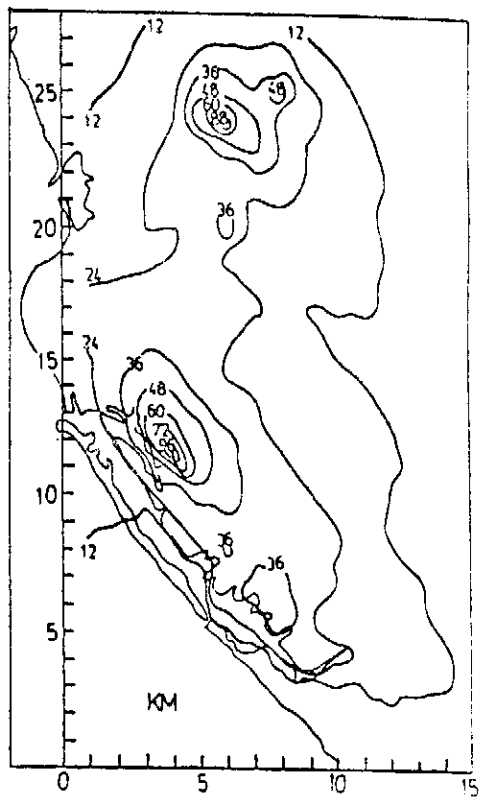

圖八　分15組 $\bar{q}$ 程序濃度分佈圖

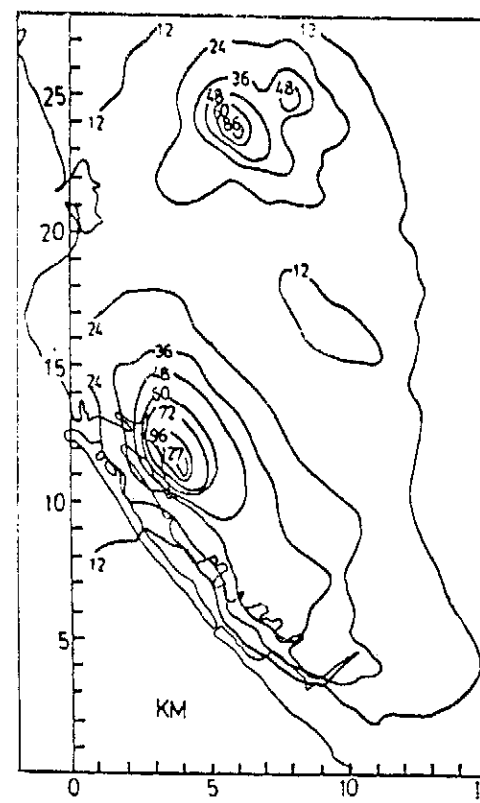

圖九　分 5 組 $\bar{q}$ 程序濃度分佈圖

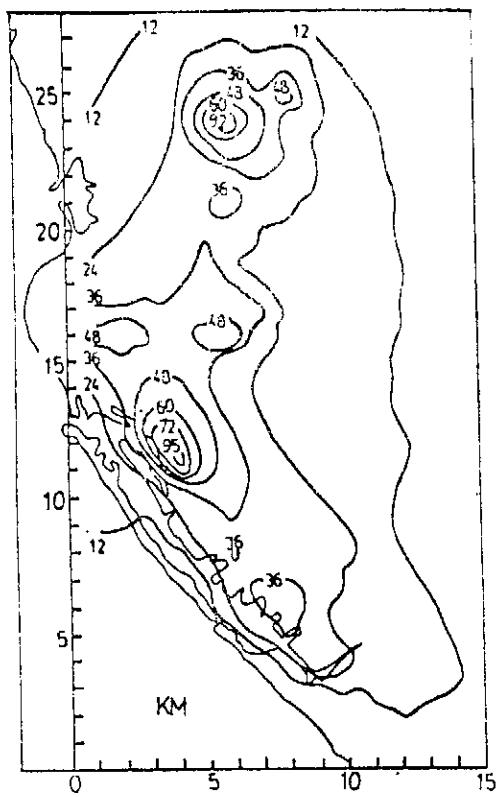

圖十　不分組 QL 程序濃度分佈圖

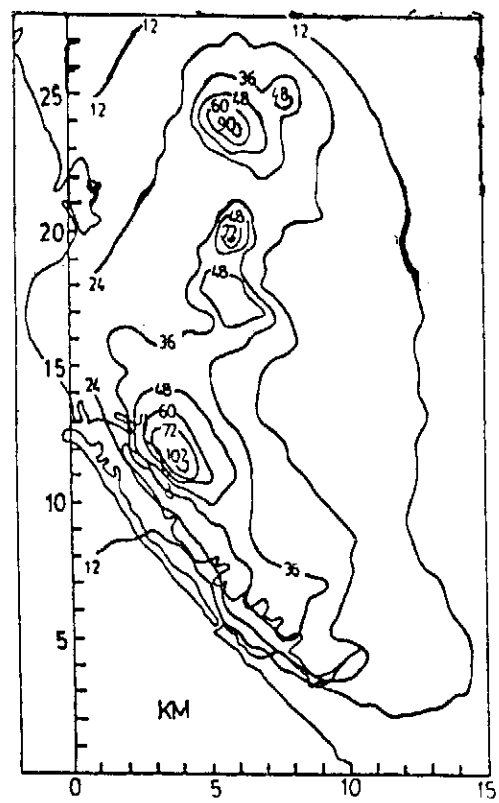

圖十一　分15組 QL 程序濃度分佈圖

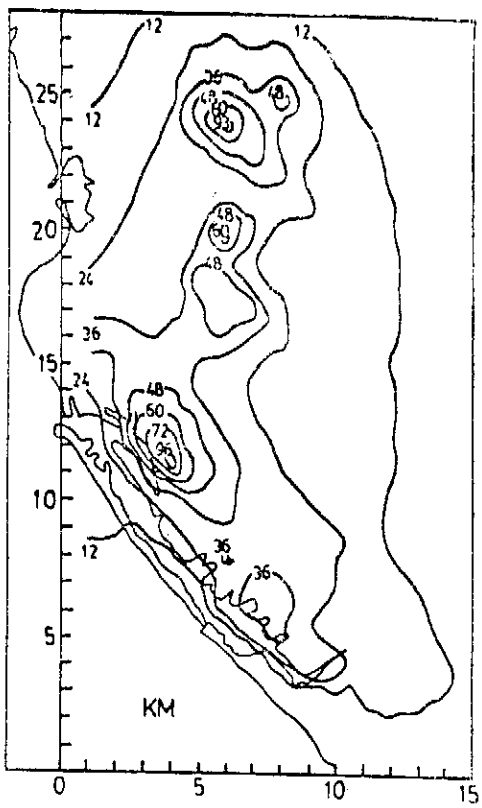

圖十二　分15組 qL 程序濃度分佈圖

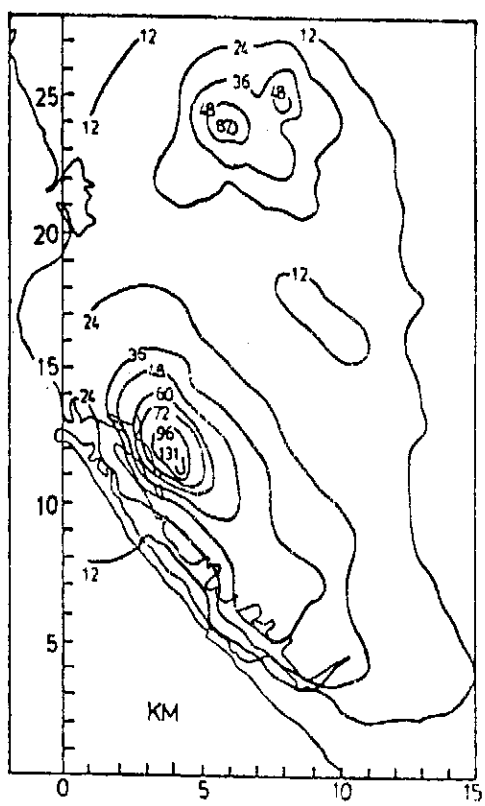

圖十三　分5組 qL 程序濃度分佈圖

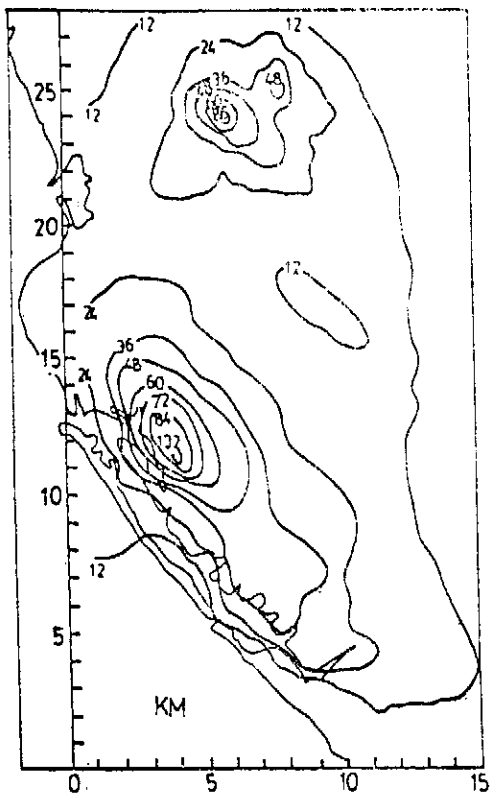

圖十四　分5組 QL 程序濃度分佈圖

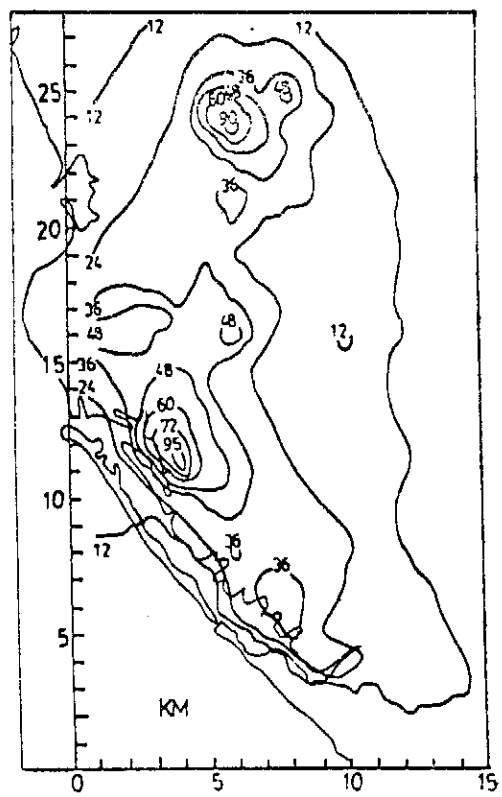

圖十五　分15組N程序濃度分佈圖

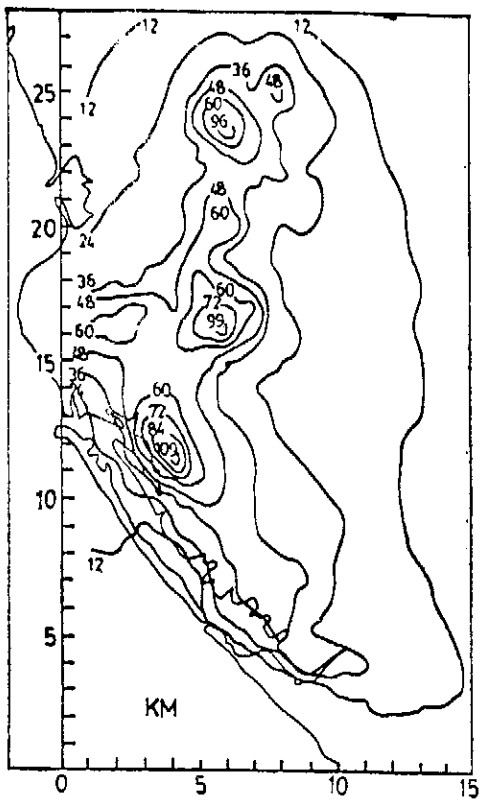

圖十六　分5組N程序濃度分佈圖

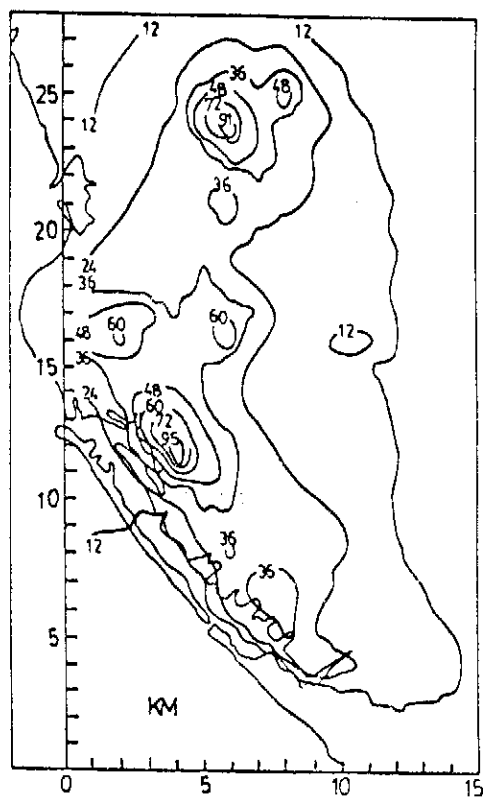

圖十七　分15組S程序濃度分佈圖

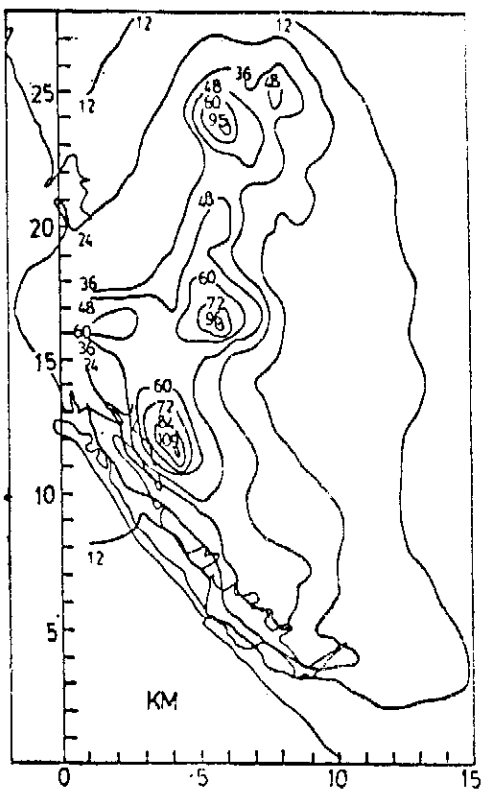

圖十八　分 5 組 S 程序濃度分佈圖

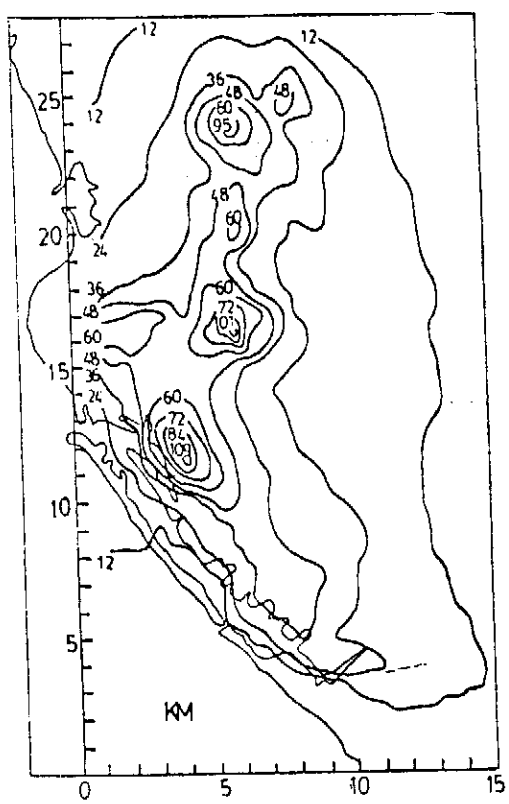

圖十九　分15組 SL 程序濃度分佈圖

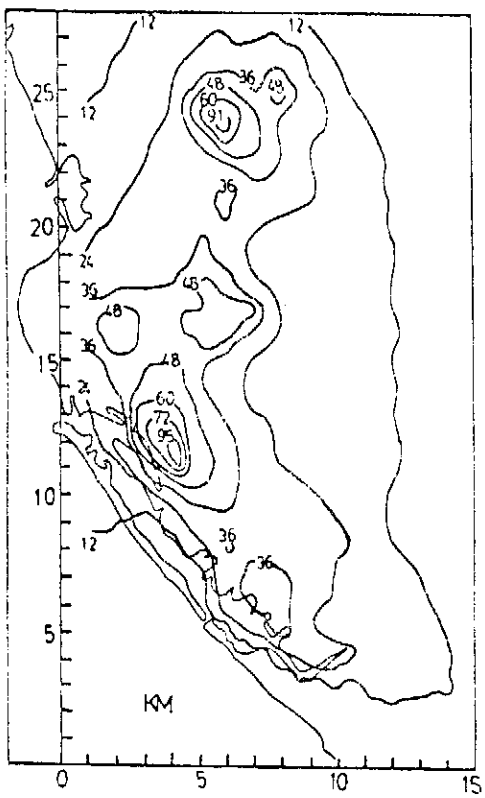

圖二十　分5組 SL 程序濃度分佈圖

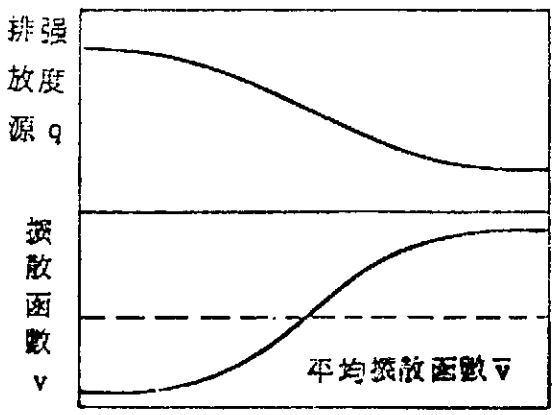

圖二十一　發生局部增强作用的極端情形示意圖

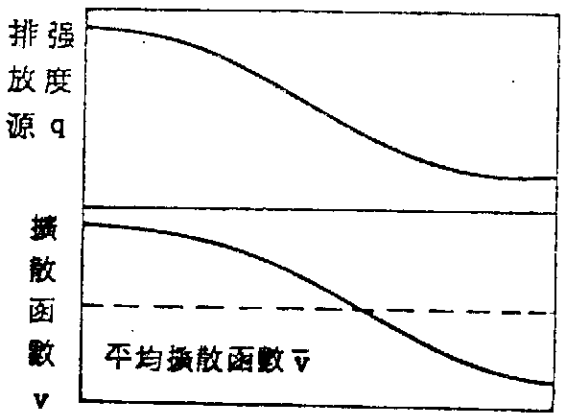

圖二十二　發生局部減弱作用的極端情形示意圖

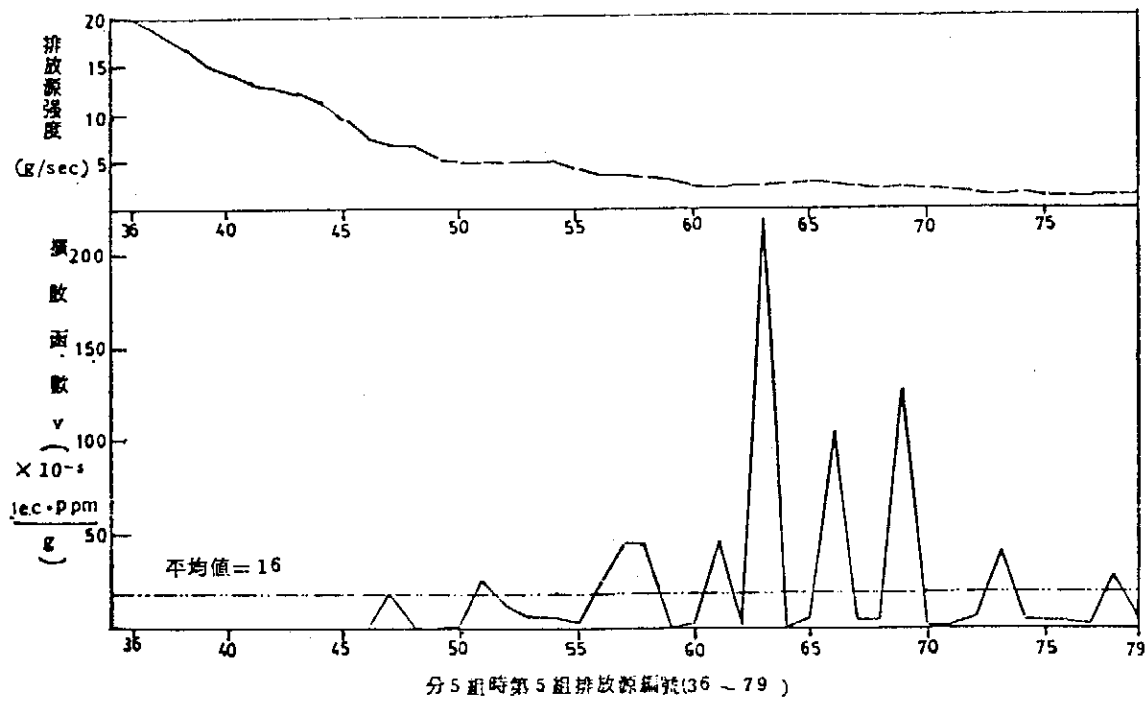

圖二十三　第5組（線號36～79）排放源強度值及各排放源對座標點（6, 16）的擴散函數S分佈圖示情形

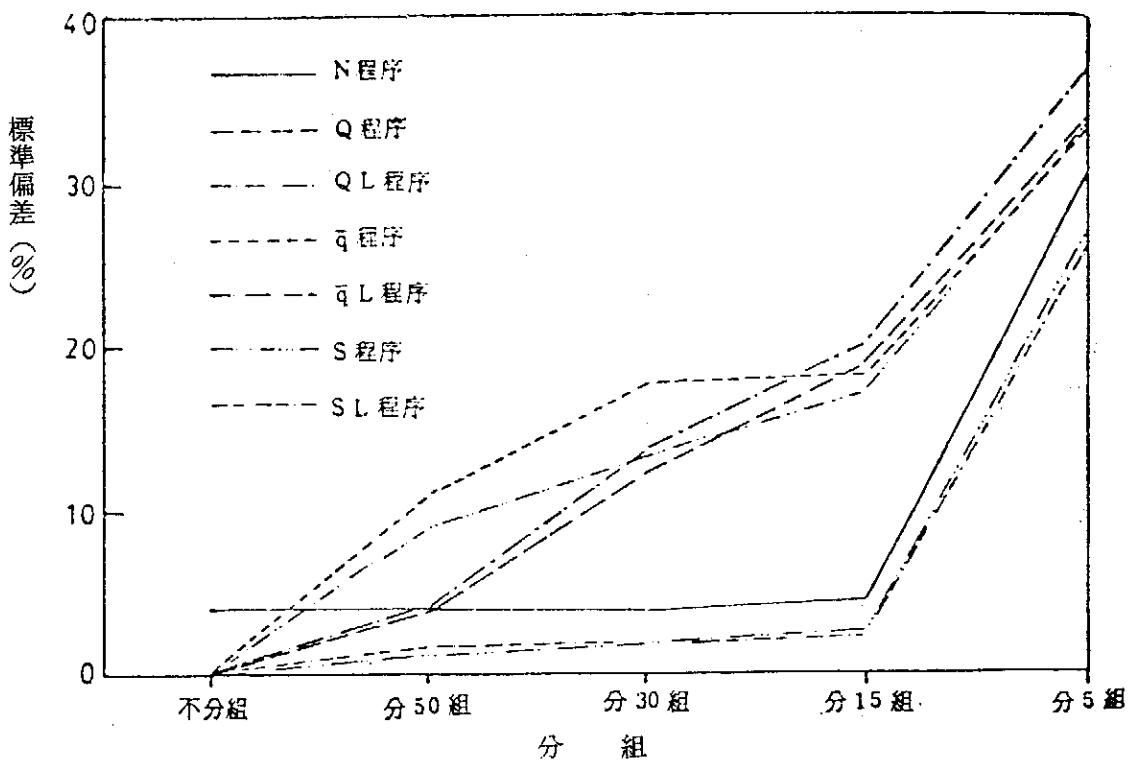

圖二十四　標準偏差（以%表示）圖示情形

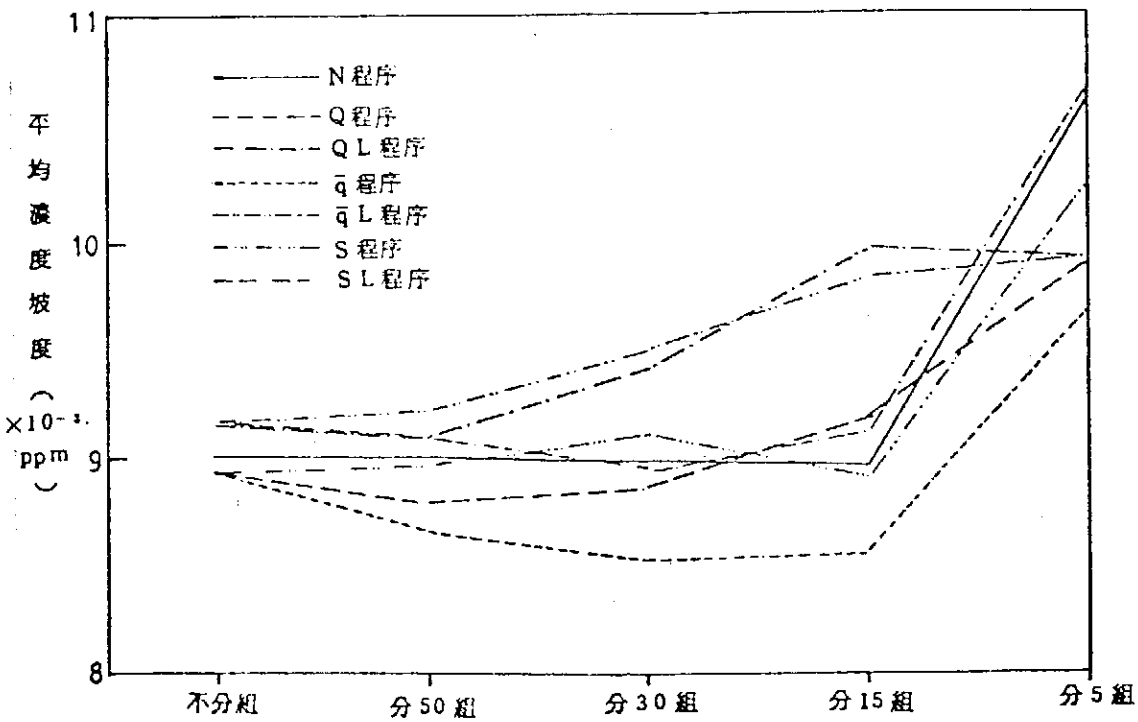

圖二十五　平均濃度坡度圖示情形

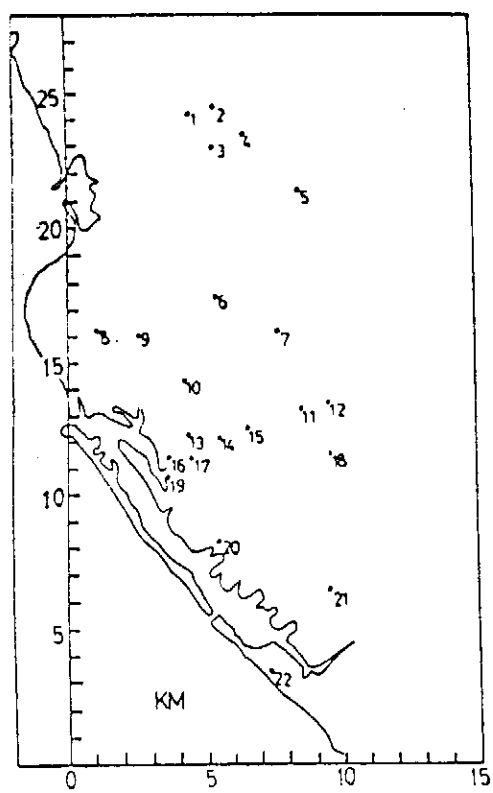

圖二十六　22個量測站分佈位置

$(\alpha, \alpha p)$ quasifree proton knockout reaction on ^{2}H, ^{6}Li, and ^{19}F+

A. NADASEN, T. A. CAREY, P. G. ROOS, N. S. CHANT,
C. W. WANG* (王 建 萬), and H. L. CHEN

Department of Physics and Astronomy,
University of Maryland. College Pork, Maryland 20742

Abstract

The $(\alpha, \alpha p)$ reaction on ^{2}H, ^{6}Li, and ^{19}F has been studied with 140 MeV α particles. Energy spectra for the ground state transition are presented at one angle pair for ^{2}H and ^{19}F, and three angle pairs for ^{6}Li. Distorted-wave impulse-approximation calculations provide good fits to the ^{2}H data, the ^{19}F data, and data at one angle pair for ^{6}Li. The other two angle pairs for ^{6}Li show significant deviations from the distorted-wave impulse-approximation suggesting contributions from processes more complicated than those included in the distorted-wave impulse-approximation.

* Inst. of Phys., Academia Sinica, Taipei, Taiwan, ROC.
+ Published in Phys. Rev. C. Vol. 19, No. 6, 2099 (1979).

Quasi-free $(\alpha, 2\alpha)$ reaction induced by 140 MeV alpha+ particles on ^{9}Be, ^{12}C, ^{16}O, and ^{20}Ne Targets

C. W. WANG* (王 建 萬), N. S. CHANT, P. G. ROOS
A. NADASEN, and T. A. CAREY

Department of Physics and Astronomy,
University of Maryland, College Park, Maryland 20742

Abstract

Measurements of the $(\alpha, 2\alpha)$ reaction on ^{9}Be, ^{12}C, ^{16}O, and ^{20}Ne targets at $E\alpha$ = 140 MeV were made at 20 angle pairs. The quasi-free knockout mechanism appears to dominate the reaction. The experimental data were analyzed with distorted-wave impulse approximation calculations. The factorization employed in the calculations was tested explicitly and found to be valid. The shapes of the calculated energy sharing spectra are in satisfactory agreement with the data. The predicted absolute cross sections were found to be very sensitive to the cluster-core bound state radius parameter, and a bound state radius $R = 2.52A_C^{1/3}$ fm is necessary to obtain absolute spectroscopic factors consistent with existing theoretical values. Several possible explanations for this excessive value are suggested. Comparisons are made with other alpha knockout and transfer reactions.

* Inst. of Phys., Academia Sinica , Taipei, Taiwan, ROC.
+ Published in Phys. Rev. C. Vol. 21, No. 5. 1705 (1980).

Variation of photovoltaic effect in vertical n/p-juction solar cells*

YU-TUNG YANG (楊 毓 東)

Physics Department, National Tsing-Hua University, Hsin-Chu, Taiwan, Republic of China

Abstract

Experiments reveal that the power output of an ordinary vertical silicon single-crystal solar cell changes with the local illumination. The dark current is found independent of the location of the local illumination if the illuminated part is only a small portion of the surface area of the vertical solar cell. If the vertical solar cell is fully illuminated, then the dark current may either increase or decrease with the nonhomogeneity or homogeneity of impurity concentration in the single crystal, respectively, and the short-circuit current is always increased. The energy conversion efficiency is different from place to place in a vertical solar cell and the exp(-x/L) law is only approximately followed because the impurity concentration is usually not uniform. The present experiments reveal the minute local variations.

* Published in J. Appl. Phys. **50**, 5047 (1979).

Diffusion and p-type conduction of magnesium impurities in germanium*

L. T. HO (何 倜 民)

Institute of Physics, Academia Sinica, Taipei, Taiwan, Republic of China

Abstract

Magnesium has been introduced into germanium by the diffusion technique. After heat treatment, the room-temperature carrier concentration of the sample is of the order of 10^{15} cm^{-3}. Conversion of the sample conductivity from n type to p type indicates that magnesium behaves like a substitutional double acceptor in germanium. A diffusion profile for magnesium impurities in germanium is presented.

* Published in Appl. Phys. Lett. **35**, 333 (1979).

Anisotropy of Magnetoresistivity in Ni-Rich Ni-Cu and Ni-Si Alloys*

YEONG DER YAO (姚 永 德)

Institute of Physics Academia Sinica
Nankang, Taipei, Taiwan, R.O.C.

Abstract

Measurements are reported on the anisotropy of the magnetoresistivity in Ni-Rich Ni-Cu and Ni-Si alloys as a function of applied magnetic fields (up to 12 KG) at liquid nitrogen temperature. Our results imply that Smit spin mixing type of mechanism is the dominant one in our Ni-Cu and Ni-Si alloy systems.

* Published in Chin. J. Phys. **18**, 39 (1980).

Electrical Resistivity and Crystallization of Metallic Glasses $Fe_{84}B_{16}$ and $Fe_{84}B_{13}Si_3$*

YEONG DER YAO (姚 永 德)

Institute of Physics Academia Sinica
Taipei, Taiwan, 115 R. O. C.
and
SHUI TIEN LIN
Department of Physics
National Cheng Kung University, Tainan, Taiwan, 700 R. O. C.

Abstract

Electrical resistivity (ρ) of metallic glasses $Fe_{84}B_{16}$ and $Fe_{84}B_{13}Si_3$ have been measured as a function of temperature (T) between 78 K and 1010 K. The ρ vs. T curves, obtained with specified warming and cooling rates, show that such curves are sensitive probes of the crystallization process. Within the experimental error, no anomalies in the behavior can be seen at the Curie temperature of each metallic glass.

* Published in Chin. J. Phys. **18**, 43 (1980).

Annual Report of the Institute of Physics, Academia Sinica, Vol. 10, 1980

An Artificial Upwelling Experiment—Laboratory and Field Investigation*

NAI-KUANG, LIANG, SHIANG-MAW TZENG, FUNG-I CHEN
YEONG-CHEN LIN and NAI-TSUNG LIANG (梁 乃 崇)

Abstract

A horizontal contraction & expansion tube and a long pipe was expected to pump the subsurface nutrient-rich seawater (Liang et al., 1978). The present paper is an advanced study in the same problem. Instead of contraction & expansion (C & E) tube, a tube-pair, which consists of two C & E tubes —one inner tube and one outer, is designed. The pumping ability has been tested both in laboratory and field. The pumping ability in field is greater than that of the laboratory, about 4-5 times. The reason may be due to scale effect and the big oscillations of the ocean current. Further field experiments pumping 150 m depth seawater to 30 m depth should be done for a long period in order to know the pumping ability and the bio-fouling problem.

* Published in Acta Oceanographica Taiwanica, Science Reports of the National Taiwan University, No. 10, pp. 67-80 (1979).

Percolation Theory and Experiments on Ultra Thin Metallic Films*

SHOU-YIH WANG and T. T. CHEN

Department of Physics, National Tsing Hua University
Hsinchu, Taiwan, Republic of China

and

N. T. LIANG (梁 乃 崇)

Institute of Physics, Academia Sinica,
Nankang, Taipei, Taiwan, Republic of China

Abstract

A short review of the conduction mechanisms and related features in discontinuous, quasi-continuous, and continuous films has been made. The $T^{-1/4}$ law of dc conductivity rederived by Ambegaokar et al is employed to illustrate the basic statistical spirit of percolation treatment. The 2D continuum percolation model is somewhat fully given and our work on ultra thin film using the 2D model are carefully reviewed. Mott transition and Anderson localization are restated. Controversy over percolation or non-percolation has been briefly described.

* Invited paper at the Solid State Physics Conference, Sponsored by the Chinese National Science Council during June 6 and 7, 1980 at National Tsing Hua Univ., Hsinchu, Taiwan, ROC.

A Proposed Dynamic Mechanism of Nerve Action Potential*

CHUN CHIANG (蔣 忻 儒)

Institute of Physics Academia Sinica
Nankang, Taipei, Taiwan, Republic of China

Abstract

The molecular processes involved in the nerve action potential are explained in sequence by the proposed model. Unlike the Hodgkin-Huxley equation, this model utilizes Newton's law of motion and the transient dipole barrier as the physical foundation for ion transport and never action potential; this provides a firm molecular basis for explanation of the action potential. In this model. it is the interplay of various autonomous forces acting on the sodium and potassium ions that gives rise to the potential. The oscillating after-potential can also be explained within the model without further assumptions.

* Published in Physiological Chemistry & Physics. Vol. 12, 1547 (1980).

Membrane Potential and Active Transport—An Information Theory Approach*

YUH YING L. WANG and WEI-KUNG WANG (王 唯 工)

Department of Physics, National Taiwan Normal University,
Biophysics Laboratory, Institute of Physics, Academia Sinica
Department of Zoology, National Taiwan University
Taipei, Taiwan, Republic of China

Abstract

A membrane potential stabilizing mechanism is proposed. Permeability is portrayed as controlled by a potential sensor. The active transport system is suggested to be a Maxwell demon able to recognize different ions, and modulate their passage into and out of the cell, without apparent reliance on energy. The idea that information is equivalent to entropy is used to resolve that paradox and contruct a model of the active transport system. The non-steady ionic state of muscle cell is deduced; that ionic concentration may determine the condition of muscle is also suggested.

* Published in Physiol. Chem. & Physics, **11**, 77 (1979).

Annual Report of the Institute of Physics, Academia Sinica, Vol. 10, 1980

Inhibition of dopamine formation by dopa, dopamine and apormorphine in presvnaptic nerve terminal*

WEI-KUNG WANG (王 唯 工), TSUNG-YUNG HAI and YI-CHIANG

Biophysics Laboratory, Institute of Physics
Academia Sinica, Taipei, Taiwan, Rep. of China

Abstract

Sprauge-Dawley Rats were illed by decapitation, Corpora Striata were dissected on ice and homogenized. After 1,000 g spin for 15 minutes, several 50 $\mu\ell$ portions of supernatant were incubated with 150 $\mu\ell$ of physiological medium which mimics the cerebrospinal fluid. A respirometer was used to supply the oxygen and give the continuous measurement of the $^{14}CO_2$ output from the tissue.

Inhibitory effects of dopa, dopamine and apomorphine on dopamine synthesis were studied. Drugs were added into crude synaptsomal preparation with L(1 - ^{14}C)-Tyrosine, and liberated $^{14}CO_2$ were measured for every 10 minutes. Special attention was paid to the time course of $^{14}CO_2$ liberation. The inhibitory effect of dopa on $^{14}CO_2$ liberation occured quickly. The different inhibition patterns indicate that dopamine and apomorphine inhibit the dopamine biosynthesis through a different mechanism from that of dopa.

We deduced that the dopamine presynaptic auto-receptor would regulate the synthetic rate of dopamine.

* Presented at 12th CINP Congress, Göteborg Sweden, 22-26 June 1980.

Annual Report of the Institute of Physics, Academia Sinica, Vol. 10, 1980

Study of Catecholamine Biosynthesis in Hypothalamus by a Continuous Measuring Method*

W. K. WANG (王 唯 工), T. Y. HAI and Y. CHIANG

Biophysics Laboratory, Institute of Physics. Academia Sinica
Taipei, Taiwan, Rep. of China

Abstract

Hypothalamus of rat was dissected and homogenated on ice. After 1,000xg spin for 15 minutes, several 50 $\mu\ell$ portions of the supernatant were incubated with 150 $\mu\ell$ of physiologival medium. A respirometer was used to supply the oxygen and give the continuous measurement of the $^{14}CO_2$ output from the tissue. The $^{14}CO_2$ liberated from (1 - ^{14}C) tyrosine was measured to indicate the formation of dopamine.

Crude synaptosomal preparations will release $^{14}CO_2$ from (1 - ^{14}C) tyrosine at rate of 0.05 p mole/min/mg, which is about one fourth of the rate from corpus striatum. When the preparation was incubated with 3-iodo-L-tyrosine at 5×10^{-4}M, about 50% of $^{14}CO_2$ release will be inhibited. In corpus striatum preparation, more than 90% of $^{14}CO_2$ release will be inhibited.

If we compare the amount of non-inhibited $^{14}CO_2$ release, both preparations from hypothanus and corpus striatum are about 0.02 p mole/min/mg. It suggested that these definite amounts of $^{14}CO_2$ release are from some unknown non-dopamine synthesis pathway, it is therefore necessary to study the inhibitory result by 3-iodo-L-tyrosine to identify the drug effect on catecholamine synthesis especially in the preparation of hypothalamus.

In hypothalamus, the effect of 3-iodo-L-tyrosine on catecholamine biosynthesis was about the same as that of DDC (Diethyl-dithiocarbamic acid), that is both DDC ($1=10^{-8}$M) and 3-iodo-tyrosine (5×10^{-4}M) will inhibited the $^{14}CO_2$ release about 50%. At the same time, both drugs inhibited the $^{14}CO_2$ release about the same in corpus striatum. These facts suggested that the inhibition of DDC is not limited to dopamine β-hydroxylase.

* Presented at XI International Congress of the International Society of Psychoneuroeudocriuology, Florence, Italy, June 16-20 (1980).

Annual Report of the Institute of Physics, Academia Sinica, Vol. 10, 1980

A Representation of an Instaneous Unit Hydrograph from Geomorphology*

V. K. GUPTA, E. WAYMIRE and C. T. WANG (汪 群 從)

Abstract

The channel network and the overland flow regions in a river basin satisfy Horton's empirical geomorphologic laws when ordered according to the Strahler ordering scheme. This setting is presently employed in a kinetic theoretic framework for obtaining an explicit mathematical representation for the instantaneous unit hydrograph (i.u.h.) at the basin outlet. Two example are developed which lead to explicit formulae for the i.u.h. These examples are formally analogous to the solutions that would result if a basin is represented in terms of linear reservoirs and channels respectively, in series and in parallel. However, this analogy is only formal and it does not carry through physically. All but one of the parameters appearing in the i.u.h. formulae are obtained in terms of Horton's bifurcation ratio, stream length ratio, and streamarea ratio. The one unknown parameter is obtained through specifying the basin mean lag time independently. Three basins from illinois are selected to check the theoretical results with the observed direct surface run-off hydrographs. The theory provided excellent agreement for two basins with areas of the order of 1100 sq. mi. but underestimates the peak flow for the smaller basin with 300 sq. mi. area. This relative lack of agreement for the smaller basin may be used to question the validity of the linearity assumption in the rainfall run-off transform ation which is embedded in the above development.

* To appear in Water Resources Research (1980).

A Geomorphologic Approach to Study Basin Hydrologic Response*

C. T. WANG (汪 群 從) and V. K. GUPTA

Abstract

Following the water flow paths, a river basin is divided into streams and catchments of different orders. Incorporating river basin geomorphology, the hydrologic responses of the river basin can be represented as a function of the basin geomorphologic parameters and holding time function.

When the basin holding time is intensity dependent, the geomorphologic hydrologic model introduced becomes quasi-linear. For some Illinois river basin studied, the model determines discharge due to compound storm events nicely.

* Appeared in Proc. Inter. Conf. on Water Resources Development, 397, May, 1980.

Annual Report of the Institute of Physics, Academia Sinica, Vol. 10, 1980

On the Wedge Effect on Planing Hulls*

CHUN-TSUNG WANG (汪 群 從)

Abstract

Assuming that the added lift of a trim flap can be approximated by imaging the trim flap to act like another planing surface with a mean wetted length equal to the flap length at a trim angle σ, planing equations developed by Savitsky can be modified to study the effects of trim flaps or wedges on planing bulls.

Analytical results obtained by solving eq. (4) (6) and (7) introduced compare nicely with experimental results.

* To appear in J. Hydronautics (1980).

Laboratory Study on the Two-Dimensional Flow of A Stratified Fluid Over an Obstacle*

ROBERT R. HWANG (黃 榮 樾) and SHAIN-WAY JANG

Institute of Physics Academia Sinica, R.O.C.

Abstract

This paper describes an experimental study of a stratified fluid of finite depth flowing over obstacles in which flow seperation and turbulence are induced on the lee side and of which the inviscid model is no longer useful. Varionus properties of the flow field, and in particular the criterion for the onset of gravitational instability in the lee waves are observed and analyzed. Results show that lee waves produced by obstacles in a stratified flow depend on the internal Froude number, Reynolds number of the flow field and two aspect ratio indicating the height and the half-width of obstacles β, and ε. It is also found that the existences of upstream influence and the flow seperation induced by the obstacle have great effects in some extent on the development of the lee-wave field.

* Presented at International Conference on Water Resources Development Taipei, Taiwan, Republic of China May 12-14, 1980.

Annual Report of the Institute of Physics, Academia Sinica, Vol. 10, 1980

Generalization of Kuo's Parameterization of Cumulus Convection*

WEN-JEY LIANG (梁 文 傑)

Institute of Physics, Academia Sinica and
Dept. of Mech. Eng., National Taiwan Univesity

(Manuscript received 18 September 1979, in final form 9 February 1980)

Abstract

The main purposes of this paper are to generalize Kuo's concept of parameterization of cumulus convection based on the moisture conservation equation and to reveal that several different schemes may be obtained by different assumptions for moisture local change term. Kuo's schemes and an extended scheme are then derived from the generalized formula. The cloud mass production rate in Kuo's formula is assumed to be constant throughout the whole convective layer, while that in the extended formula is allowed to be a function of height (or pressure). The diagnostic investigation of this extension is performed by utilizing the combination formula and the large-scale heat and moisture budgets. Compared with the observations, the results of the diagnosis show that the extended scheme gives better estimates on the latent heat released and the pressure of the cloud top. The diagnostic study also reveals that the adiabatic subsidence of the environmental atmosphere and the vertical transport of moisture inside the clouds are both significant in the parameterization of cumulus convection.

* Published in Meteorological Research, Vol. 2, No. 2, 101-115, (1979).

A Theory for Parameterization of Cumulus Convection*

WEN-JEY LIANG (梁 文 傑)

Institute of Physics, Academia Sinica and
Dept. of Mech. Eng., National Taiwan University

Abstract

In this study, a closed theory of the generalization of Kuo's parameterization of cumulus convection is developed by combining a one-dimensional cloud ense . Lle model. The theory is the extension of Kuo's (1965 and 1974) and Liang's (1 7) parameterization schemes. It includes the transport of the dry static energy whi.h is closely correlated to the baroclinity of the weather systems, and is able to appl to the middle latitudes as well as in the tropics. The theory is diagnosticated using the Marshall Islands data set, which is used in the budgets study by Yanai *et al* (1973). The results show that the estimations on the latent heat released, the cloud depth, the net entrainment rate and the cloud bulk properties are satisfactorily explained by the observations, and the physical phenommena revealed are consistent to the real situations.

* Published in Proceedings of the National Science Council, Vol. 4, No. 2, (1980).

The Variational Optimization of Wind Field for the Estimation of Vertical Velocity*

WEN-JEY LIANG (梁 文 傑)

Abstract

A variational optimization scheme of wind field is developed for the correction of vertical velocity field using kinematic method. The errors which appear in the vertical velocity field are classified as systematic errors and random errors. The systematic errors are suppressed by the use of two strong constraints, i.e., the integrated continuity equation and the global boundary condition. The random errors are filtered by including a low-pass filter simultaneously in the variational formation that the filtered field still satisfies above constraints. The upper boundary condition of the vertical velocity field is considered in terms of the spatial distribution of upward and downward motion. NASA AVE II data are utilized to verify the scheme. Results show that the magnitudes and general patterns of vertical velocity field are in good agreement with the synoptic weather system and radar reports.

* Published in Proceedings of the National Science Council, Vol. 4, No. 3, (1980).

The Optimization Theories for Air Pollution Estimation and Their Applications*

WEN-JEY LIANG (梁 文 傑)

Institute of Physics, Academia Sinica
and
Department of Mechanical Engineering
National Taiwan, University
Taipei, Taiwan, R. O. C.

Abstract

The optimization theories for air pollution are developed using variational approaches. The theories consist of the strong optimization theory and the weak optimization theory. The former requires the optimized values satisfying the utilized diffusion model, and the latter simply requires those values to approximate the model. Because the strength of the optimized sources should be non-negatitive, the constraints consist of the equalities and the inequalities. A control mechanism, which is adjusted by a weight parameter, is introduced to connect the inequatities to the optimization processes. An CO urban dispersion model with real data obtained from Taipei is utilized to investigate the plausibility of the theories. The results show that the schemes are very stable and the optimized concentration distribution are highly acceptable.

* Proc. of Fifth International Clean Air Congress, Buenos Aires, Argentina, Oct. 20-25, 1980.

Annual Report of the Institute of Physics, Academia Sinica, Vol. 10, 1980

Flow Past an Impulsively Started Circular Cylinder*

LAI-CHEN CHIEN (簡 來 成)

Institute of Physics Academia Sinica
Nankang, Taipei, Taiwan Republic of China

Abstract

Although there has been a large amount of literature on the unsteady viscous flow over an impulsively started circular cylinder, the existing solutions agree neither quantitatively nor qualitatively with one another. The potential flow-started initial conditions used by most scholars, do not take into account the initial boundary-layer structure of the flow. These investigations are inaccurate initially, and the effect of the inaccuracy on the solution at later times is unknown.

Because of the impulsive start, there is a singularity at the time $t=0^+$. This paper gives the accurate solution in neighborhood of the singularity by the analytic solution obtained by inner-outer expansion method to the third order. The viscous layer stream function and vorticity obtained by the method of asymptotic expansion at the small time are employed as initial conditions for numerical method, hopscotch method, is described for integrating the Navier-Stokes equations. The time development of the flow properties are obtained and plotted. No second bubble was found for Reynold number, based on radius, less than 250.

* Published in Proc. Natl. Sci. Counc. ROC, 4, 123 (1980).

Annual Report of the Institute of Physics, Academia Sinica, Vol. 10, 1980

Time Dependent of the Flow over an Impulsively Started Circular Cylinder*

LAI-CHEN CHIEN (簡 來 成)

Institute of Physics, Academia Sinica
Taipei, Taiwan, Republic of China

Extended Summary

Solutions of unsteady, incompressible, viscous flow over an impulsively started circular cylinder are presented for various Reynolds number. Most investigators used potential flow as their initial conditions for numerical integration. They computed the vorticity on the cylinder surface for $t=0^+$ using the stream function obtained from the potential flow theory and do not take into account the initial boundary layer structure of the flow. These investigations are inaccurate initially, and the effect of this inaccuracy on the solution at later times is unknown (Collins and Dennis, 1973b).

Accurate solution in the neighborhood of the singularity $t=0$, can be obtained either by developing an analytic solution, or a series solution for small time (Crank, 1975, p. 152). The calculation can then be continued with the aid of a suitable numerical method (Schlichting, 1979, p. 169). In this paper, the analytic solution is obtained by inner-outer expansion method to the third order for small time. Then the solution is continued by numerical integration.

Bar-lev and Yang (1975) got a perturbation solution by the method of matched asymptotic expansion to the third term. Initial flow properties were presented in detail. Unfortunately, there are some errors found in their third order inner solution. In this study, the complicated mathematical operations of the analytic solution is repeated with great care and checked in detail. The initial separation time and drag coefficient show closed agreement to Collins and Dennis (1973a, b).

The finite element Galerkin method is adopted for integrating the Navier-Stokes equations numerically for the larger time solutions using the viscous layer considered stream function and vorticity as initial conditions. The time development of the flow properties such as stream function, velocity components, vorticity distribution over the cylinder surface and drag coefficient are obtained and satisfactory in camprison with those of existing solutions. No second bubble was found for Reynolds number, based on diameter, less than 500.

* Presented at XVth International Congress of Theoretical and Applied Mechanics, August 17-23, 1980, Torento, Canada.

Annual Report of the Institute of Physics, Academia Sinica, Vol. 10, 1980

模型重量對波擊壓力之影響*

莊生命　汪群從　陳生平　林志清

摘　要

茲探討船底撞擊水面時的波擊壓力，本文系統化地進行十二組不同楔角、不同下墜高度、不同模型重量之下墜實驗，研討模型重量對波擊壓力之影響。提出經驗公式及重量影響修正曲線，供船舶結構設計參考。

* 詳見 NTU-INA-Tech. Rept. 106，臺大造船所，June 1979

用有限元素法求大氣垂直速度*

曾　忠　一

中央研究院物理研究所
國立臺灣大學大氣科學系

摘　要

本研究使用兩種網格系統，用有限元素法求得大氣的垂直速度，以與有限差分法的結果互相比較。研究結果顯示，有限元素法求得的垂直速度能與天氣系統相符，也能與有限差分法的結果互爲一致。有限元素法求得的垂直速度場，就大幅度的垂直運動型態而言，確能充份值而言，顯示本研究個案中的主要和次要的上升或下降運動。就各上升和下降氣流中心垂直速度的極端值而言，有限元素法和有限差分法的結果仍有若干差異，其差異起於使用資料的不同和網路系統的不同。此外本研究亦詳細討論有限元素法未來在數值天氣分析與預報上可能的發展與應用。

* 本文已發表於大氣科學第七期，第13頁至第20頁，民國69年5月。

Annual Report of the Institute of Physics, Academia Sinica, Vol. 10, 1980

臺北市一氧化碳污染與偵測網之佳化評估*

梁　文　傑

中央研究院物理研究所

國立臺灣大學機械工程研究所

李　克　堂

國立臺灣大學環境工程研究所

摘　　要

本文使用佳化理論來探討臺北市一氧化碳的污染情形。文中視車道爲有限線源，將高斯模式與測站上實際測定的濃度值相組合，以求出適合當地污染狀況的佳化排放源强度，再據而求出最能反映當地實況的一氧化碳佳化濃度分佈，並以佳化與未佳化模式在各測站的濃度計算值作統計特性的討論，以確知佳化結果的可信性，並根據佳化結果評估臺北市一氧化碳的污染狀況。此外，利用測站有效偵測圈與污染源分佈的關係，估計現有測站的偵測效率，又因夏季與冬季風向相異，故分別建議夏季與冬季增設測站的較佳位置與數目，估計其偵測效率，以作爲將來臺北市增設測站的參考。

* 中國機械工程學刊，第一卷第一期，(1980)。

組合模式數值天氣預報之研究*

梁　文　傑　　蕭　錫　璋

中央研究院物理研究所

胡　仲　英　　陳　熙　揚　　徐　月　娟

中　央　氣　象　局

摘　　要

本文係研究組合模式數值天氣預報的可能性。一方面以北半球準地轉模式從事粗網格網上的預報，一方面以此結果作爲邊界值從事有限區域內細網格網上原始方程式的預報。結果顯示對於大規模天氣系統的分布與運動狀態，此種組合模式的預報確能大大改進預報的精確度，唯每小時更新一次邊界值似應縮短以增强有限區域邊界處的播散效果。

* 大氣科學，第七期，21—37，(1980)。

Annual Report of the Institute of Physics, Academia Sinica, Vol. 10, 1980

高雄地區二氧化硫污染與偵測網之佳化評估*

梁　文　傑

中央研究院物理研究所

國立臺灣大學機械工程研究所

李　崇　德

國立臺灣大學環境工程研究所

摘　要

本文使用變微分法，以高雄地區的 SO_2 爲研究對象，將高斯擴散模式與實際量測的資料組合，以求出適合當地污染狀況的最佳 SO_2 排放源，再據而求出最佳 SO_2 濃度分佈。接著更利用此最佳濃度分佈狀況，對當地的排放源加以評估，舉出影響重大的排放源，以做爲污染控制方面削減排放源强度的依據，同時又對量測站進行評估，分別列出不受影響的量測站及受相同排放源影響的量測站，使對於不需要的測站能加以裁撤以節省人力、物力，但却又能獲得等量的資料，而在多個排放源影響區域則建議設立測站，以獲得重要的污染資料，達到最佳偵測網之設計。

中國工程學刊，第三卷第二期，（1980）。